UCRL-16877

c.2

UNIVERSITY OF CALIFORNIA

Lawrence Radiation Laboratory
Berkeley, California

AEC Contract No. W-7405-eng-48

A STUDY OF RESONANCE PRODUCTION AND DECAY AND ELASTIC SCATTERING IN $\pi^- p$ TWO-PRONG INTERACTIONS, 2.05 TO 3.22 GeV/c

Laurance David Jacobs

(Ph. D. Thesis)

August 16, 1966

7/18/86

TWO-WEEK LOAN COPY

This is a Library Circulating Copy
which may be borrowed for two weeks.
For a personal retention copy, call
Tech. Info. Division, Ext. 5545

UCRL-16877 c.2

Dedicated to the Memory of
Sulamith Goldhaber

DISCLAIMER

This document was prepared as an account of work sponsored by the United States Government. While this document is believed to contain correct information, neither the United States Government nor any agency thereof, nor the Regents of the University of California, nor any of their employees, makes any warranty, express or implied, or assumes any legal responsibility for the accuracy, completeness, or usefulness of any information, apparatus, product, or process disclosed, or represents that its use would not infringe privately owned rights. Reference herein to any specific commercial product, process, or service by its trade name, trademark, manufacturer, or otherwise, does not necessarily constitute or imply its endorsement, recommendation, or favoring by the United States Government or any agency thereof, or the Regents of the University of California. The views and opinions of authors expressed herein do not necessarily state or reflect those of the United States Government or any agency thereof or the Regents of the University of California.

A STUDY OF RESONANCE PRODUCTION AND DECAY AND ELASTIC SCATTERING IN $\pi^- p$ TWO-PRONG INTERACTIONS, 2.05 TO 3.22 GeV/c

Contents

Abstract v

I. Introduction 1

II. Experimental Methods

A. The Beam 2

B. Scanning 2

C. Measurement and Data Reduction 7

D. Decision Making and Ambiguous Events 10

E. Biases and Possible Errors 16

F. Determination of Cross Sections 17

III. Experimental Results

A. Cross Sections 28

B. Elastic Scattering 28

C. Three-Body States 61

D. $\pi\pi$ Scattering and the Absorption Model 115

E. Missing-Mass Hypotheses 154

Acknowledgments 159

Appendices . . . . . .

A. Relation between Proton Momentum and its Scattering Angle in the Laboratory System 160

B. Helicity Amplitudes for One-Pion Exchange 161

C. Absorption Calculation in a Linear Momentum Representation 173

D. Determination of η_{if} and β_{if} 183

E. Effective Scattering Amplitude 185

Footnotes and References 187

A STUDY OF RESONANCE PRODUCTION AND DECAY AND ELASTIC SCATTERING IN $\pi^- p$ TWO-PRONG INTERACTIONS, 2.05 TO 3.22 GeV/c

Laurance David Jacobs

Lawrence Radiation Laboratory
University of California
Berkeley, California

August 16, 1966

ABSTRACT

We present an analysis of 45 000 $\pi^- p$ interactions in the Alvarez 72-inch hydrogen bubble chamber resulting in two charged particles. The reactions $\pi^- p \rightarrow n\pi^+\pi^-$ and $\pi^- p \rightarrow p\pi^0\pi^-$ and elastic scattering have been studied at 2.05, 2.17, 2.36, 2.60, 2.86, and 3.22 GeV/c.

We find that the three-body interactions are dominated by production of the ρ meson. Nucleon resonances, although present, are not important. The f^0 is seen at the three higher energies.

We have used the OPE model, modified by absorption, to calculate and fit the production and decay angular distributions of the ρ and to estimate the s-wave contribution to $\pi\pi$ scattering. On the basis of the model and the observed (F-B)/(F+B) asymmetry in the $\pi^+\pi^-$ state, good agreement with the experimental data in the ρ region is found, if δ_0^0 is allowed to increase slowly through $\pi/2$. We do not require a resonant isoscalar s-wave amplitude.

We have fitted the diffraction peak in $\pi^- p$ elastic scattering to an exponential form and find that between 2.0 and 2.5 GeV/c the exponential slope varies. This behavior is linked to the presence of resonances in the s channel. The fast decrease of the secondary peak is linked to the exchange of the P' Regge trajectory in the t channel. Evidence is shown for production of the A_2^- in $\pi^- p \rightarrow \pi^- p$ + missing mass.

I. INTRODUCTION

The object of this work was envisaged as a systematic investigation of the bulk of the $\pi^- p$ interactions between 2.0 and 3.0 GeV/c--those resulting in two charged particles in the final state. Our attention was concentrated on the elastic processes (12 000 events) which constitute 1/4 of the $\pi^- p$ cross section, and the three-body states (14 000 events).

To derive elastic and total cross sections, it is essential to correct any bias against forward elastic scatterings. Since we are in the "intermediate" energy range, high enough for several partial waves to be important, but not high enough for us to approximate them by some asymptotic form, we are limited in our objectives. We confine our attention to the diffraction and secondary peaks in the differential cross sections and relate them to t-channel (exchange of Regge trajectories) and s-channel (nucleon resonance) effects.

For the three-body reactions, we are led to the absorptive modification of the one-pion exchange model. We devote much discussion to this topic and show that it gives good agreement for the production and decay of the quasi-two-body state $\pi^- p \rightarrow N_\rho$. We also attempt to use the absorption model to learn more about $\pi\pi$ scattering, and in particular the nature of the isoscalar s-wave phase shift, δ_0^0. We find that it passes through 90° near the ρ, but too slowly for it to be resonant.

Evidence of the f^0 and the A_2^- is seen in $n\pi^+\pi^-$ and $\pi^- p$ missing mass respectively, but other resonant states, such as nucleon isobars, are unimportant. No other enhancement in the $\pi\pi$ states is observed.

II. EXPERIMENTAL METHODS

A. Beam

The data in this experiment were obtained during two separate extensive exposures of the Alvarez 72-inch hydrogen bubble chamber to a separated π^- beam. The first run, $\pi 72$, with beam energies 1.55 to 2.36 GeV/c, took place at the Bevatron in early 1962; the second, $\pi 63$, started in March 1963 and ran for about 18 months and covered beam energies from 1.85 to 4.2 GeV/c. Both beams were designed for the corresponding K^- experiments; they are not discussed here.

From these extensive exposures, we selected film at beam energies 2.05, 2.17, and 2.36 GeV/c from $\pi 72$, and 2.60, 2.86, and 3.22 GeV/c from $\pi 63$. In Fig. 1, we have used the elastic scattering events to show the distribution of measured beam momenta in the experiment.

B. Scanning

The definition of the topology of interest here is quire straightforward. It is a two-pronged event (event type 22), the signature of an interaction resulting in two charged particles. These form about 2/3 of the $\pi^- p$ total cross section at our energies. Since the other interest in this film was the study of strange particles,[1,2] the number of beam tracks per picture was held to 15 to 20. In the 72-inch chamber, on the average, this results in a two-prong event in every picture. Further, these interactions have a visible proton 1/3 of the time and a stopping proton 1/6 of the time. It is also obvious that many pictures will have several two-prongs, an undesirable state of affairs.

In general, this is an experiment to study millibarn-type phenomena as distinct from microbarn-type phenomena. About a third of the two-prong cross section is elastic scattering, most of which is situated in the diffraction peak. The inelastic cross section has peaks in certain regions of phase space, characteristic of resonances of which the ρ meson is the most important. The ρ, f^0, and nucleon isobars all have observable cross sections on the order of millibarns. In contrast, the total strange-particle cross section is about 1 mb. Resonances

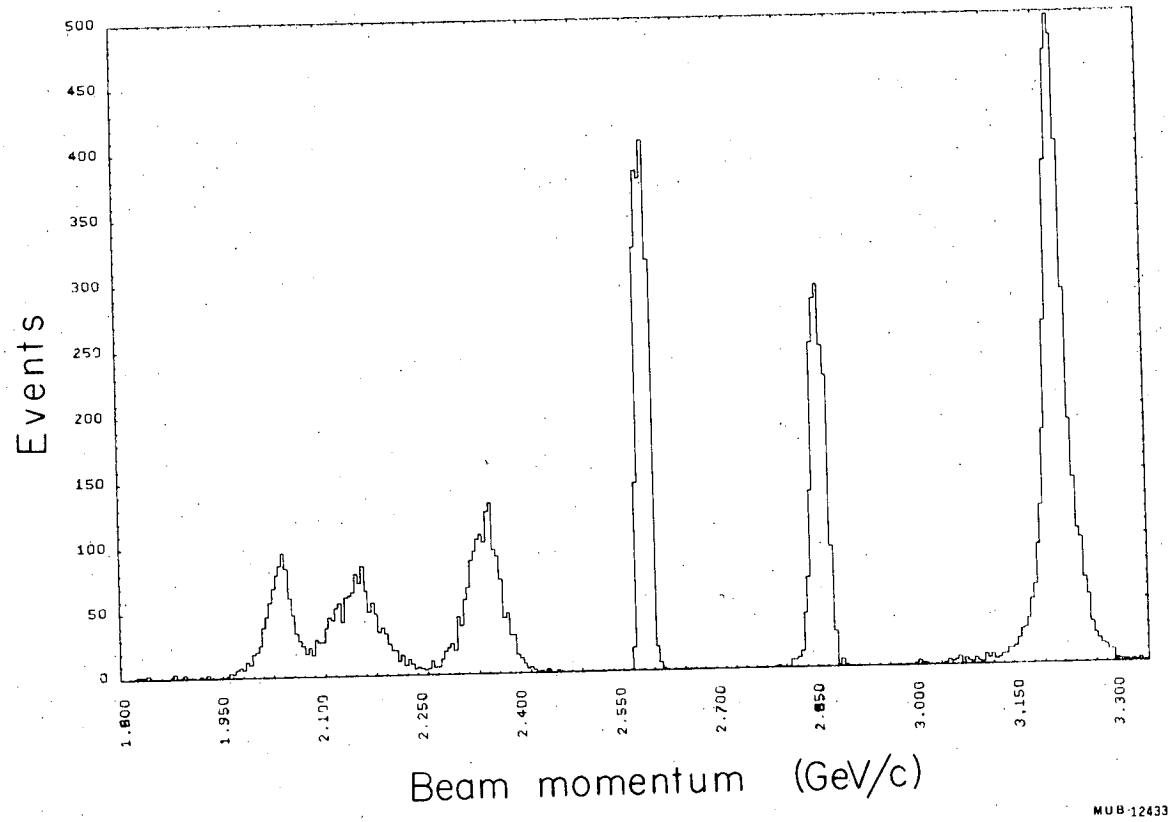

Fig. 1. Fitted beam momenta for elastic scattering events.

decaying into strange particles are in the microbarn region. In particular, resonances observed decaying into $\overline{K}K$, such as the ϕ,[2] K_1K_1,[3] or the S^*.[4] can be produced in our interactions, decaying into K^+K^- or $\pi^+\pi^-$. However, their low-cross sections make it very hard to observe them in two-prongs, or to describe their branching ratios into all π final states, unless the ratios are very large. In the decay to K^+K^-, the K's do not decay and they have to be differentiated from π's by ionization alone. In the decay to $\pi^+\pi^-$, the resonance is like a microbarn pimple on the $\pi\pi$ millibarn cross section.

What are rare among two-prong events, however, and can be found only in this topology are backwards elastic scatterings. One is tempted to bias the scanning somehow in order to find these interesting events. Nevertheless, in this experiment we have attempted an unbiased scan to amass data and statistics in a relatively painless and clean manner. Our discussion of exotica must necessarily be limited.

With our plethora of two-prongs, we can afford to discard events, provided that it is done in an unbiased way, if this gives us a cleaner sample and otherwise makes life easier.

Consequently, our scanning instruction has these general features. Only frames were scanned that had

(a) no more than 20 beam tracks,

(b) no bunching of beam tracks, and

(c) no extraneous tracks emanating from the window area.

For cross-section purposes, all skipped frames were recorded as such. For incoming tracks to be called beam tracks, they had to come through the window and be within 5° of the other beam tracks. We accepted interactions only away from the window area, for good measurement of the beam track, and not at the downstream end, to avoid trouble with turbulence, poor ionization, and short tracks.

A portion of the events, 50% of those at 2.05 and 2.17 GeV/c and all at 2.36 GeV/c, was originally scanned and measured in the π72 experiment. It was found that the kinematic fitting programs assigned more than one hypothesis to about 50% of the events, necessitating reexamination of the film by scanners to resolve ambiguities. Since this consists

of deciding whether the ionization of the positive track is consistent with a pion or a proton that has the fitted momentum, the operation is a trivial one. We felt, however, that due to the large number or resolvable ambiguities, such a reexamination of this particular class of events was wasteful and time-consuming and that it should have been possible to include the ionization information in the first scan.

Accordingly, scanners were instructed to record the interactions as beam-track 10, 20, 30, etc., the lowest number being assigned to the interaction at the left on the scanning table. Those events with obvious protons were numbered 14, 24, 34, etc.; stopping protons, were 15, 25, etc. How this information was used is described in the section on ambiguous events.

Most of the stopping protons are from elastic scattering events. Events with low values of momentum transfer to the proton are subject to scanning bias. The range of the proton is a few centimeters (see Fig. 2); the negative particle follows almost the same trajectory as the incident pion with very little deviation; in those events with the scattering plane perpendicular to the scanning table, these effects are so accentuated that events are unobservable. We attempt to correct for this, as is explained in the section on biases, but in order that our cutoff in Δ^2, the momentum transfer squared, be conservative, scanners were exhorted to look out for small-angle scatterings. A method of finding them was suggested. All "beamlike" tracks that appear to be diverging at the downstream end of the chamber were to be traced back to the main body of the chamber, where a dark, short, stopping proton track might be observed. It should be remembered that events with very low values of Δ^2 may be observed in this way. A proton of 140 MeV/c momentum, corresponding to a kinetic energy of 10 MeV, has a range of 1 cm, or 2/3 cm on the scanning table. Since

$$\frac{\Delta^2}{\mu^2} = \frac{2m_p T_p}{\mu^2} = \frac{2\times 0.938\ T_p}{0.018\times 10^3} \approx \frac{1}{10} T_p ,$$

where T_p is measured in MeV; this corresponds to a Δ^2 value of 1 μ^2.

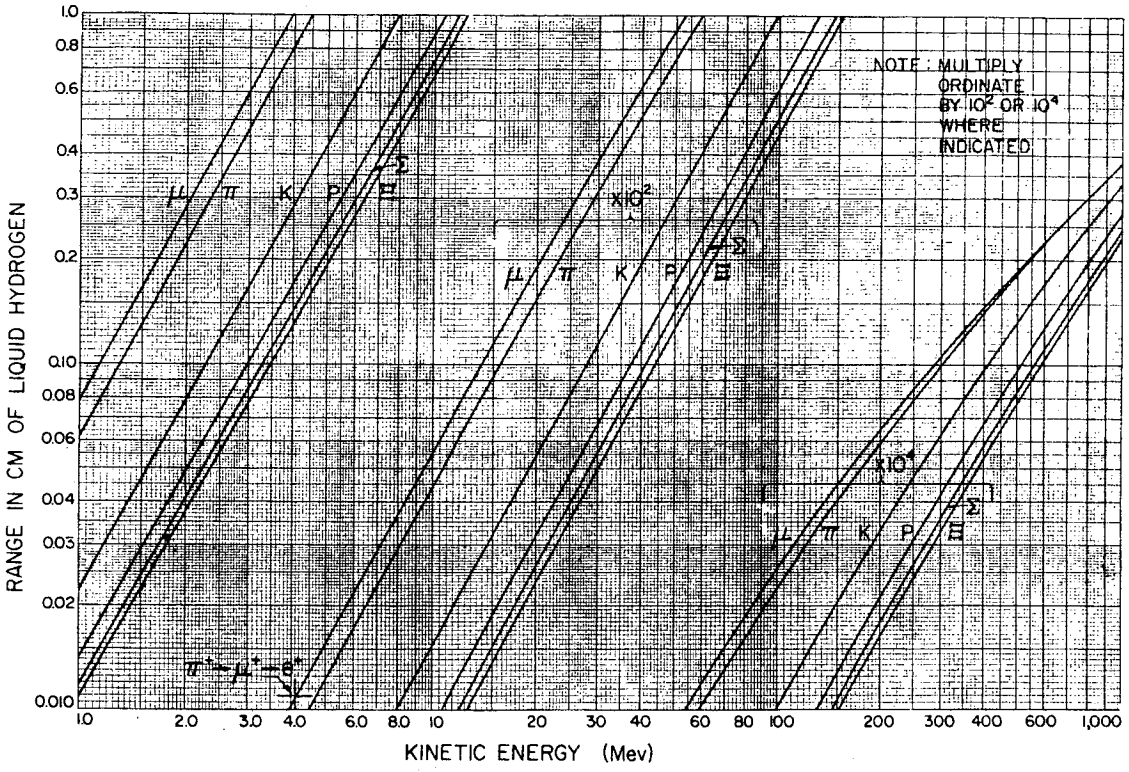

Range-energy curves for liquid hydrogen bubble chamber, based on experimentally determined range of 1.103±.003 cm for μ^+ from π^+ decay. Liquid hydrogen conditions: T = 27.6 ±.1° K; P = 48±5 psia; ρ = (5.86±.06) 10^{-2} g/cm^3. Mass ratios used: M_μ/M_p = 0.1127; M_π/M_p = 0.1488; M_K/M_p = 0.526; M_Σ/M_p = 1.270; M_Ξ/M_p = 1.408. (by Glenwood Clark and William Diehl)

MUB-124

Fig. 2

In theory, protons with a projected length of 1 mm on the scanning table are observable.

C. Measurement and Data Reduction

In Fig. 3, we represent on a flow chart the $\pi 63$ data-handling systems to be described below.

The transition of the events from the bubble chamber film to data summary and SUMX tapes is initiated by the recording of the "indicative" scanning data on IBM cards. Program LYRIC[5] (which replaced LINGO[6]) converts these cards to tape and originates a Master List, and is then used at various stages to update or correct the Master List, generate measurement lists as either paper output or magnetic tape, give a summary or tally of the events, and check the status of an event in order to detect human or programming error during any operation involving data handling.

The $\pi 72$ events and about 1/3 of the 3.22-GeV/c events were measured on the Franckenstein projection microscope. The rest of the events were measured on SMP's.[7] The measurement tapes are input to PANAL,[8] a measurement editor program. At measuring time, about 1% of the events were rejected by the measurers, either for reasons of scanner error or for event and fiducial unmeasurability. The PANAL tapes are input to PACKAGE,[7] where a further 3% of the events are lost during the PANG track-reconstruction process. These losses are due to measurement errors, and are revealed when measured points are out of order along a track, measurements in two views do not correspond, or measured points are found to lie outside the chamber. In the processing of 2.60-GeV/c data, 1/3 of events were rejected for these three reasons. This was due to changes in the optical constants of the chamber, which were subsequently accounted for by a new consistent set of parameters. About 1.5% of the remaining events fail to fit any reaction hypothesis tried by KICK. Examination of these events on the scan table shows them to have, for the most part, secondary interactions soon after the main interaction. A further 4% of those with a fitted hypothesis had χ^2 values greater than the maximum accepted. For well-measured

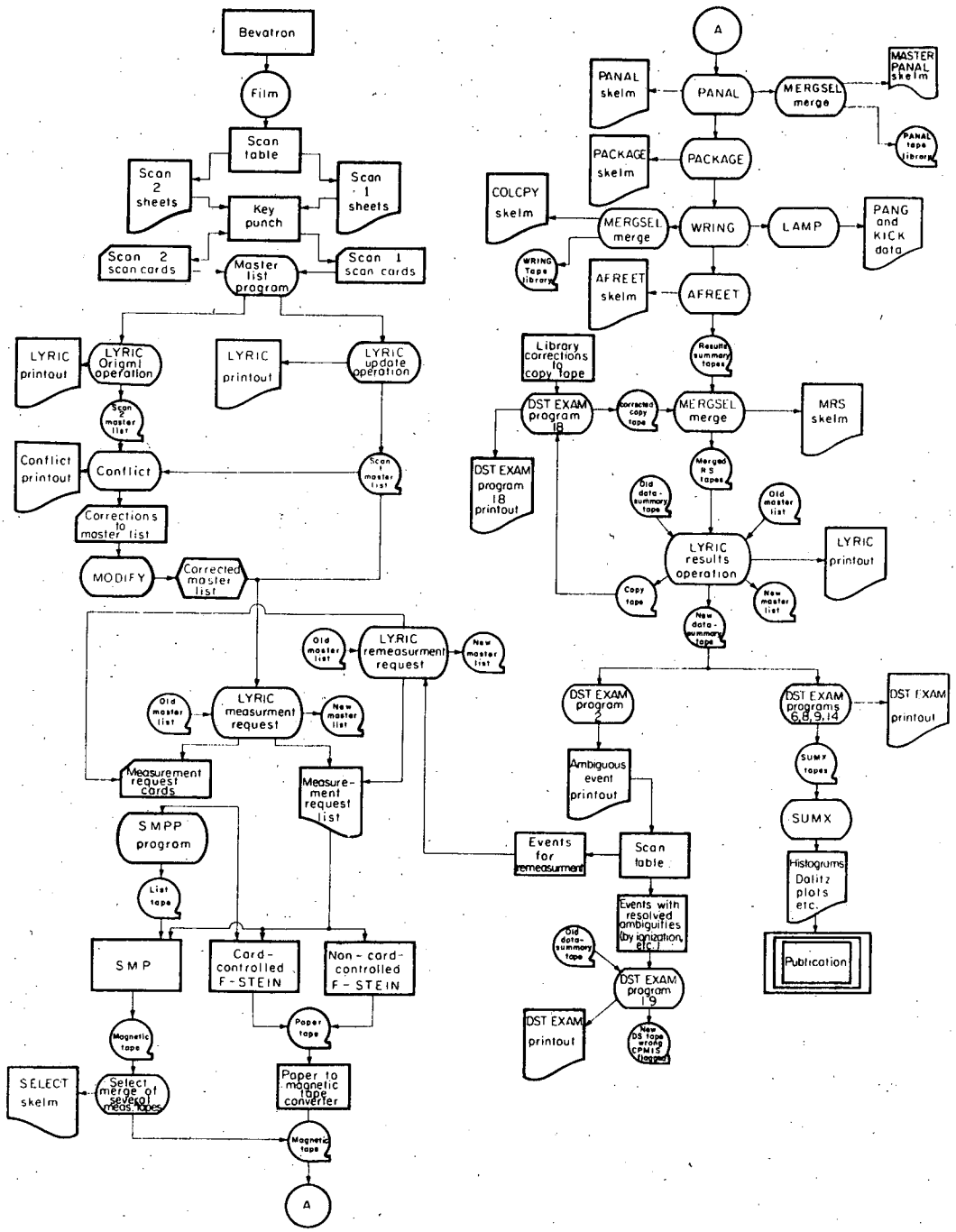

Fig. 3. Schematic diagram of the Alvarez π63-K63 data-handling system.

events with the correctly assigned hypothesis, we expect only 0.5% to lie outside these upper χ^2 limits. A good part of these events also have secondary interactions. Other obvious reasons are steeply dipping tracks, tracks with small angle and virtually undetectable scatterings, and elastic scatterings with very short stopping protons. This last category features prominently among all the failing events, as expected, and is the only one to contribute a bias. In general, no second measurement of the failing events was instituted. At 2.86 GeV/c all failing events were remeasured, mainly with the aim of trying to recover some of the short-recoil elastic scatterings. It was found, however, that in frames with appreciably more than one event there was always the likelihood of a good event's being measured again, whilst the failing event nearby was overlooked. At 3.22 GeV/c, although an unbiased scan was undertaken, because the initial interest at this momentum was the reaction $\pi^- p \rightarrow \pi^- p \pi^0 \pi^0$, only events with obvious protons were measured at first. When the rest of the events were being remeasured on the film, the failing events from the first sample also were remeasured. Again, this affected mainly the elastic scatterings.

The PACKAGE output tapes were condensed via two further Alvarez-system programs WRING and AFREET, into so-called Results Tapes. At this point LYRIC was called on once again to merge these tapes with the final Data Summary Tape (DST). Only events agreeing with the Master List went on the DST; the others had undergone trivial but almost untraceable bookkeeping errors and were usually discarded. In this experiment, since we were dealing with one simple event type and the measuring was done on SMP's controlled by a LYRIC-generated measurement tape, this leakage was not important, less than 1%.

The format of a DST and the use of the decision-making and "physics output" program DST-EXAM are the standard as used in the Alvarez experiments π63 and K63, and are described in Ref. 9. Suffice it to say here that the tape contains measured and fitted information according to the various hypotheses found acceptable in PACKAGE, and that the program acts upon this information according the χ^2 calculated in PACKAGE to yield a best hypothesis, on the basis of which it calculates

various kinematic quantities--e.g., effective masses of particle pairs, momentum transfers, and angular correlations. These quantities are output as condensed summary tapes, which are input to SUMX,[10] a data-summarizing program. We use SUMX to analyze the data in terms of histograms and scatter plots. All the data processing described was carried out on the IBM 7094 and 7044.

D. Decision Making and Ambiguous Events

Three fits are attempted by PACKAGE: elastic scattering $\pi^- p \rightarrow \pi^- p$, a four-constraint fit, and the three-body final states $\pi^- p \rightarrow \pi^- p \pi^0$ and $\pi^- p \rightarrow \pi^- \pi^+ n$, where we have one constraint on the momenta of the outgoing particles. In addition there are the hypotheses in which more than one undetected neutral particle is produced, $\pi^- p \rightarrow \pi^- p$ + neutrals and $\pi^- p \rightarrow \pi^- \pi^+$ + neutrals.

Other hypotheses are available, e.g., $\pi^- p \rightarrow K^+ K^- n$, $p K^- K^0$, $K^+ \pi^- \Lambda$. In the $\pi 72$ experiment these hypotheses were tried and it was found that almost every event could fit at least one of these strange-particle states. To separate out those events that are genuine is a hard matter, and is best attempted after most of the events have been fitted to the non-strange hypotheses. A good place to seek them is in the missing-mass hypotheses.

The hypotheses that we do consider divide naturally into two classes: those with a proton in the final state and those with a neutron. About 50% of the events have a single unambiguous hypothesis according to the fitting programs. The acceptable χ^2 for 4C fits was taken to be 30: for 1C fits the figure was 13. However, the decisions are made on the basis of the confidence level, the distributions of which should be flat if χ^2 is calculated correctly. To achieve this in practice we have to multiply our calculated χ^2 by a correcting factor to compensate for our inability to predict it properly.[11] For one constraint this number is 0.8; for the four constraints it is 0.6. We exhibit the confidence levels for $\pi^- p \rightarrow p \pi^0 \pi^-$, $n \pi^+ \pi^-$, and $\pi^- p$ in Fig. 4.

A useful yardstick for classifying ambiguous events was whether the confidence level of the second most favored hypothesis was greater

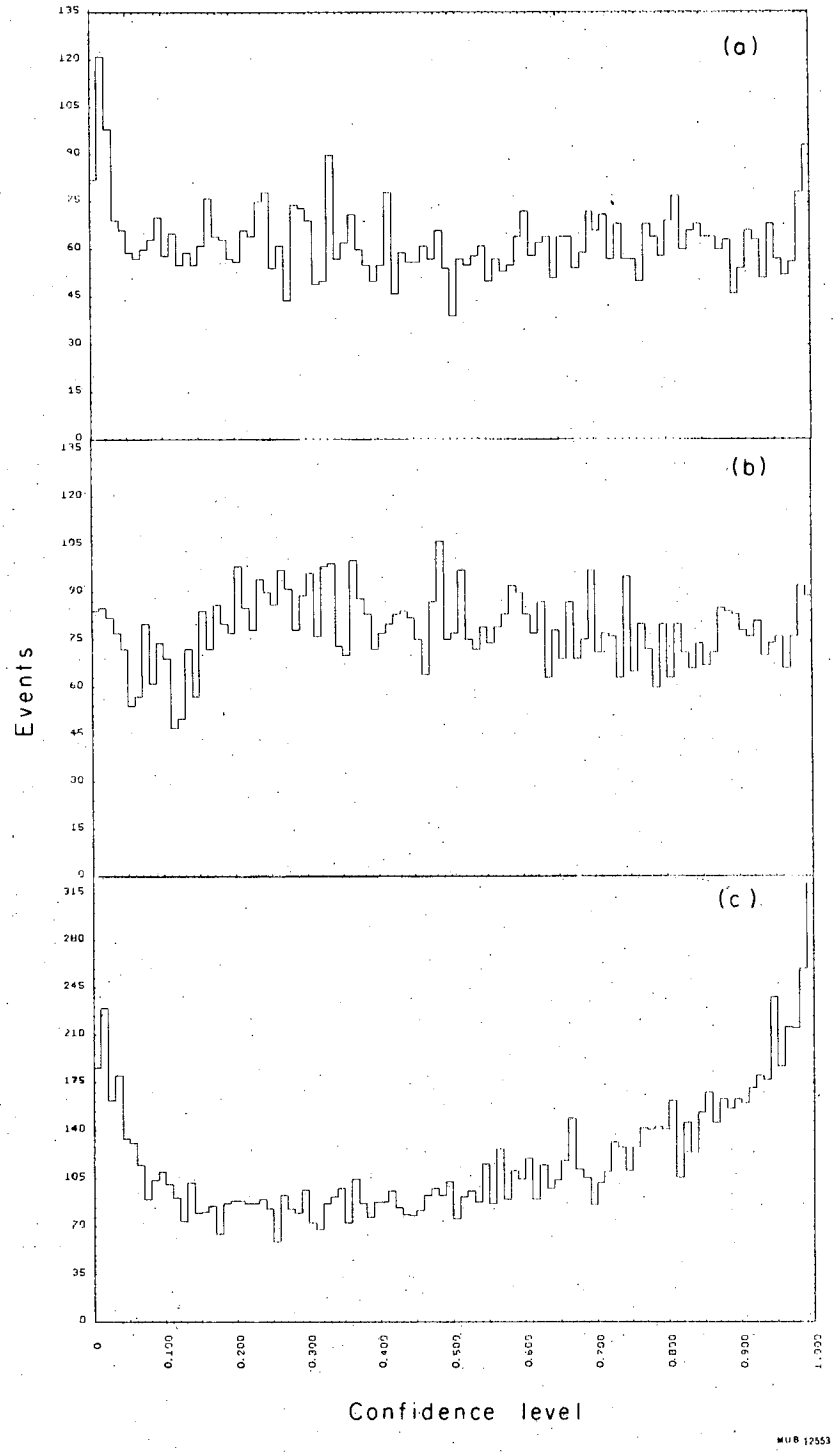

Fig. 4. Distributions of confidence levels;
(a) $p\pi^0\pi^-$
(b) $n\pi^+\pi^-$
(c) π^-p

than 1/3 of the best confidence level. Ambiguous events, in which the momentum of the positive track was less than 1 GeV/c, are resolvable on the scanning table. Here we used the information contained in the beam track number. On the basis of a scanner's indication that a proton was obviously present in the final state, all neutron hypotheses were discarded.

An initial sample of ambiguities was examined on the scanning table. It was decided that only the positive identification of a proton could be used. Thus, we did not define an "obvious pion." It became clear that in several instances frames with more than one two-prong would have events measured with the wrong beam track number. For those events with heavily ionizing protons, we merely lost the extra information and the event was looked at by a scanner in the usual way. However, events with lightly ionizing positives with an "obvious proton" appellation had to be treated with care.

DST-EXAM program 2 outputs a subset of ambiguous events. These are potentially resolvable events in which the ionization of the disputed track is appreciably different for the rival hypotheses, the point of view being taken that a ratio of 1.5 is distinguishable. With this in mind, we acted on the scanners' information only if the ratio of the ionization corresponding to a proton to the ionization of a pion was greater than 2.0. This was quite conservative, since a nondipping proton has twice minimum ionization at 730 MeV/c momentum. In addition, the dip of the positive track had to be less than 70° (80° for stopping protons.) For genuinely resolvable proton events this worked quite satisfactorily. Lightly ionizing positives failed these tests. The only doubtful region was for pions with momenta of the order 500 MeV/c. Since in addition the events would have to be ambiguous and mislabeled, any misidentification should have at most a second-order effect.

DST-EXAM program 19 writes a new DST. It deletes wrong hypotheses according to the decisions made during the re-examination of events on the scanning table. The information is punched on IBM cards. In addition it tests the beam track number, predicted ionizations and dip and automatically resolves "obvious proton" events.

There still remain the unresolvable ambiguous events. As the beam momentum increases from 2 to 3 GeV/c more momentum is available to the final particles, with correspondingly less difference in ionization between the particles. At 2.05 to 2.36 GeV/c, 7.8% of events are ambiguous; at 2.60 to 3.22 GeV/c, the figure is 9.8%. However, for elastic scatterings the figures are 0.45% and 0.85%. The regions of ambiguity for elastic scatterings is in the backwards hemisphere in the center-of-mass system, i.e., when the proton has momentum in the laboratory system greater than 1500 MeV/c. We shall have cause to return to this point in discussing biases in the data.

To distinguish $\pi^- p \rightarrow \pi^- p \pi^0$ from $\pi^- p \rightarrow \pi^- p$ + neutrals, and similarly for $\pi^- p \rightarrow n\pi^+\pi^-$, the following prescription[12] was adopted in DST-EXAM: The missing-mass hypothesis was alloted a reasonable confidence level, 0.2. However, this is modified depending on the values of missing energy and momentum and on how well the momenta of the tracks are measured. If the missing mass is less than the minimum--i.e., the mass of a neutron or a π^0, as the case may be--we introduce a factor with a Gaussian behavior, $\exp[-(x-\sigma)^2/\sigma^2]$, where x = (missing energy) - (minimum missing energy), and σ is the measured error of x.

If there is a good fit corresponding to the missing mass--e.g., $n\pi^+\pi^-$ in the case of $\pi^+\pi^-$ missing mass--there is a further factor $[1 - P_{fit}]$, where P_{fit} is the probability or confidence level for the corresponding fit. In Fig. 5 we show the missing-mass plot for both fitted and unfitted events. The separation of events is reasonable.

Without the help of ionization we cannot separate the two missing-mass hypotheses. If there is sufficient missing energy to make a neutron and a π^0 under one hypothesis or two π^0's under the other, neither can be preferred. In the fits we must rely on the confidence levels alone. In Fig. 6 we show that the separation is not at all bad.

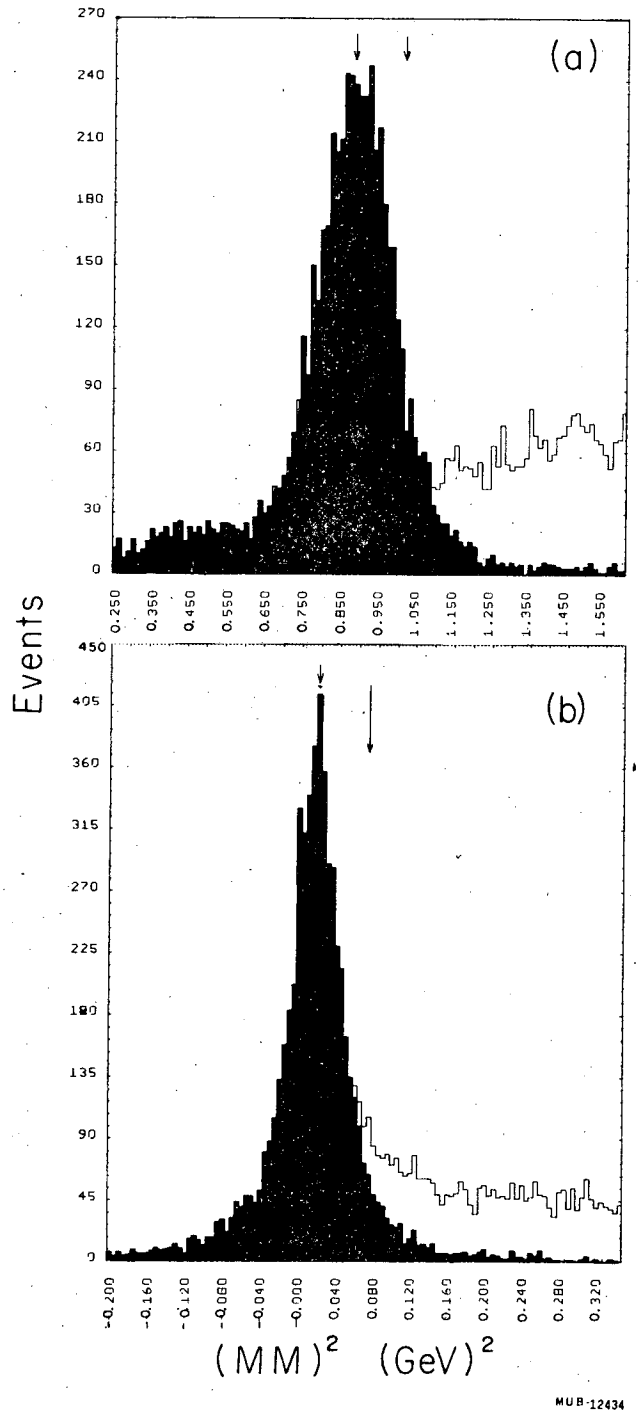

Fig. 5. Missing mass squared. Events shown as shaded correspond to three-body fits.
(a) $\pi^+\pi^-$ missing mass. Arrows indicate m_n^2 and $(m_n+m_{\pi^0})^2$.
(b) π^-p missing mass (excluding elastic scatterings). Arrows indicate $m_{\pi^0}^2$ and $4m_{\pi^0}^2$.

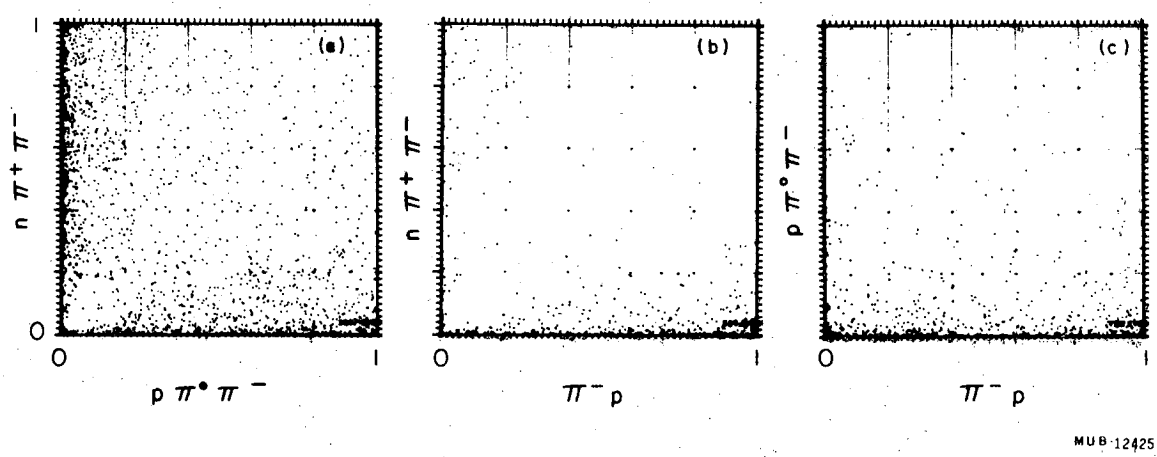

Fig. 6. Confidence-level scatter plots for ambiguous events.
(a) $n\pi^+\pi^-$ vs $p\pi^0\pi^-$.
(b) $n\pi^+\pi^-$ vs π^-p.
(c) $p\pi^0\pi^-$ vs π^-p.

E. Biases and Possible Errors

The bubble chamber is an excellent unbiased detector of particle interactions. Naturally, the interactions have to take place in the finite volume of the chamber, and any decaying particles must have decayed before they leave the chamber. Our chamber is longer than it is wide, and some spatial asymmetry is thereby introduced. More important is that we really observe the events projected onto three planes, the angles between which are less than 15°. But within limits, unlike spark chambers and counters, we do not have different efficiencies for various kinematic regions. This is excellent if we want to study angular correlations or cross sections as a function of effective mass, for example.

In carrying out the experiment we naturally introduce biases in scanning and measuring and in the assumptions that are implicit in the kinematic analysis. The events may favor certain kinematic regions, e.g., low Δ^2. There are two classes of bias: those we can forsee and take account of, and those that reveal themselves in the course of an experiment. We can do nothing, of course, about the ones that do not reveal themselves.

On events measured on the SMP's only a limited portion, $\approx$ 20 cm of the beam track, can be measured. However, in fitting the events we use the beam averaged momentum. A sample of beam tracks is measured accurately on the Franckensteins to determine the central beam momentum, P_{ave}, and its spread. The beam-averaged momentum is $P_{pang}\,\alpha + P_{ave}\,(1-\alpha)$, where P_{pang} is the measured beam momentum as calculated in PANG and α is a comprehensive factor that contains both the error in measurement and the spread in nominal beam momentum. Under these conditions the short beam track does not contribute any appreciable error. What was more serious was the unexpected effect of being able to measure only a limited portion of an outgoing fast track. We shall return to this soon.

That the missing masses corresponding to the fits are distributed about the mass of the missing particle shows that there are no serious systematic biases or shifts introduced in the measuring or fitting. An

incorrect beam average or contamination from other hyptheses would result in displacements from the correct central value, or skew distributions. The full width at half-maximum is 0.05 $(GeV)^2$ for the π^0 and 120 MeV for the neutron.

Contamination of other hypotheses by elastic scatterings was found to occur. In certain kinematic regions the fitting programs prefer the wrong inelastic process, sometimes unambiguously so.

A trivial case is the fitting to $\pi^- p \rightarrow n\pi^+\pi^-$ of elastic scatterings with stopping protons. Before applying the general ambiguity operation as described above, we made histograms of the effective masses of $\pi^+\pi^-$ and $n\pi^+$. The offending events are in the first bin in the $n\pi^+$ plot, since they approach the mass of the proton. On the $\pi^+\pi^-$ mass plot they are observed as a sharp peak at about 900 MeV at 2.86 GeV/c. This falls to about 780 MeV at 2.05 GeV/c. The effect is almost completely removed by applying the beam track criterion. As a further check all the remaining events in the suspect region were examined; it is believed that all this class of misidentified events has been set right.

At this point one somewhat worrying point should be mentioned. At the lower momenta of the run, any misidentified events that may somehow remain are in the body of the ρ peak, but may get interpreted as evidence of the 2π decay of the ω. This is further complicated by the belief that the $\pi^- p \rightarrow n\omega$ cross section is appreciably larger at 2 GeV/c than at about 3 GeV/c. However, the original misidentified events had an apparent Δ^2 of less than $4\mu^2$, as well as falling into one bin on the $n\pi^+$ plot, and the final histograms show no evidence of this (e.g., Fig. 57c).

Another class of elastic scatterings fitted the $\pi^- p \rightarrow \pi^- p\pi^0$ hypothesis. The situation here is less easy to understand, since we are dealing with the tail of a χ^2 distribution which allows about 1.5% of the elastic scatterings to fall in the wrong category.

We find it convenient to discuss separately the case for Δ^2 less than and greater than 20 μ^2. The first inkling of something wrong came from the comparison of the plot of the $\pi^0\pi^-$ effective mass with that for $\pi^+\pi^-$ (see Fig. 48). There seems to be a rise in the number of events as we approach the minimum-mass end.

Selecting events with $\Delta^2 < 20\,\mu^2$, and $m_{\pi^0\pi^-}$ less than 505 MeV, we made a scatter plot of the $\pi\pi$ decay angle and Treiman-Yang azimuthal angle. The surprising finding emerged that the events clustered about zero azimuthal angle, and the scattering angle tended to be large.

Other pieces of evidence were that on a missing-mass plot for $\pi^- p \rightarrow \pi^- p \pi^0$ there was evidence for a clustering about zero missing mass. For twelve events with an appreciably nonzero Treiman-Yang angle, we plotted the laboratory-system scattering angle against the momentum (lab) of the proton. In Appendix A we show that, for low values of this momentum and for elastic scatterings only, there is a linear relationship between these two quantities. Inelastic events lie on a curve for a given $\pi\pi$ mass which is above the straight line for elastic scatterings. Ten of the twelve events lay along the line and were appreciably below the curve for $m_{\pi\pi} = 2\mu$.

We remeasured on Franckensteins some 225 events; of these 9% failed, 50% fit elastic scatters, and 6% went into the $\pi^- p$ missing mass category, leaving 35% to fit the original hypothesis. Although the offending events lay below about 450 MeV, we measured events below about 505 MeV. We expect any genuine events to have a larger mass spread when measured again, and do not wish to introduce artificial discontinuities in the mass spectrum due to remeasurement. We accepted the second measurement in preference to the first. Our justification is this. On a random sample of events there is no statistical reason to choose one or the other measurement. However, we hypothesize that the anomalous behavior of these events is their being elastic scattering events, and that they are falling into the wrong category either because a small percentage does this statistically in any case or because large errors are made in some of the measured quantities (e.g., beam momentum, momentum of the outgoing π^-, or the lab scattering angle); then, if we believe our second measurement is at least as accurate as the first, we can expect fewer events to be in the bad χ^2 tail.

On comparing the output from the second measurement with the first we drew the following conclusions. The enhancement near 280 MeV

was mainly a creation of the SMP's. On those events which fit elastic scatterings on the second measurement the momentum of the outgoing π^- was consistently higher than when measured with the SMP's. This was directly related to the greater track length measured by the Franckensteins. In the most extreme cases a 3-GeV/c π^- was measured as 1.5 GeV/c, giving an energy and momentum imbalance of 1.5 GeV. A spurious π^0 with the same $\vec{\beta}$ as the π^- satisfies the energy-momentum relations, and the $\pi^0\pi^-$ system has low mass and its "decay" is naturally coplanar with the production plane.

For events with $\Delta^2 \geq 20\,\mu^2$ the effect is similar. The most striking feature is that the (F-B)/(F+B) asymmetry in the $\pi\pi$ scattering angle is strongly negative for events with $\pi\pi$ mass less than 600 MeV. If we choose $\pi^-p\pi^0$ events with $\cos\theta < -0.5$ and azimuthal angle less than 50° we obtain the Chew-low plot shown in Fig. 7. Of 230 events in this category and with $\Delta^2 \geq 20\,\mu^2$, 13% fail, 28% fit elastic scatterings, and 15% fit other hypotheses, leaving 38% still fitting $\pi^-p \rightarrow \pi^-p\pi^0$ on a second measurement. Those events which fit elastic scatterings were characterized by π^0's of momentum less than 300 MeV/c when fitted as $\pi^-p \rightarrow \pi^-p\pi^0$. Both the outgoing π^- and proton have high momentum. Errors in measurement of the order of 10% lead to an energy and momentum imbalance of a few hundred MeV and admit the inelastic hypothesis; 6% of the remaining inelastic fits were ambiguous with elastic scatterings. They had the same characteristics as genuine elastic scatterings. Of the 60 unambiguous fits, several also had π^0's with about 300 MeV/c momentum. The elastic scattering χ^2 ranged from 90 to 500. Examination of some of these events made it plausible that these were elastic scatterings that "failed" because of turbulence in the chamber or small scatterings in the outgoing tracks. If this was so, we were losing some elastic scatterings with high Δ^2, and there was very little that we could do about it.

Given a $\pi^-p\pi^0$ final state with either Δ^2 in the region 5 to 10 μ^2, and a 1500 to 2000 MeV/c π^- with a nearly parallel π^0 having almost the same momentum, or Δ^2 large and the π^0 slow, then if we make a

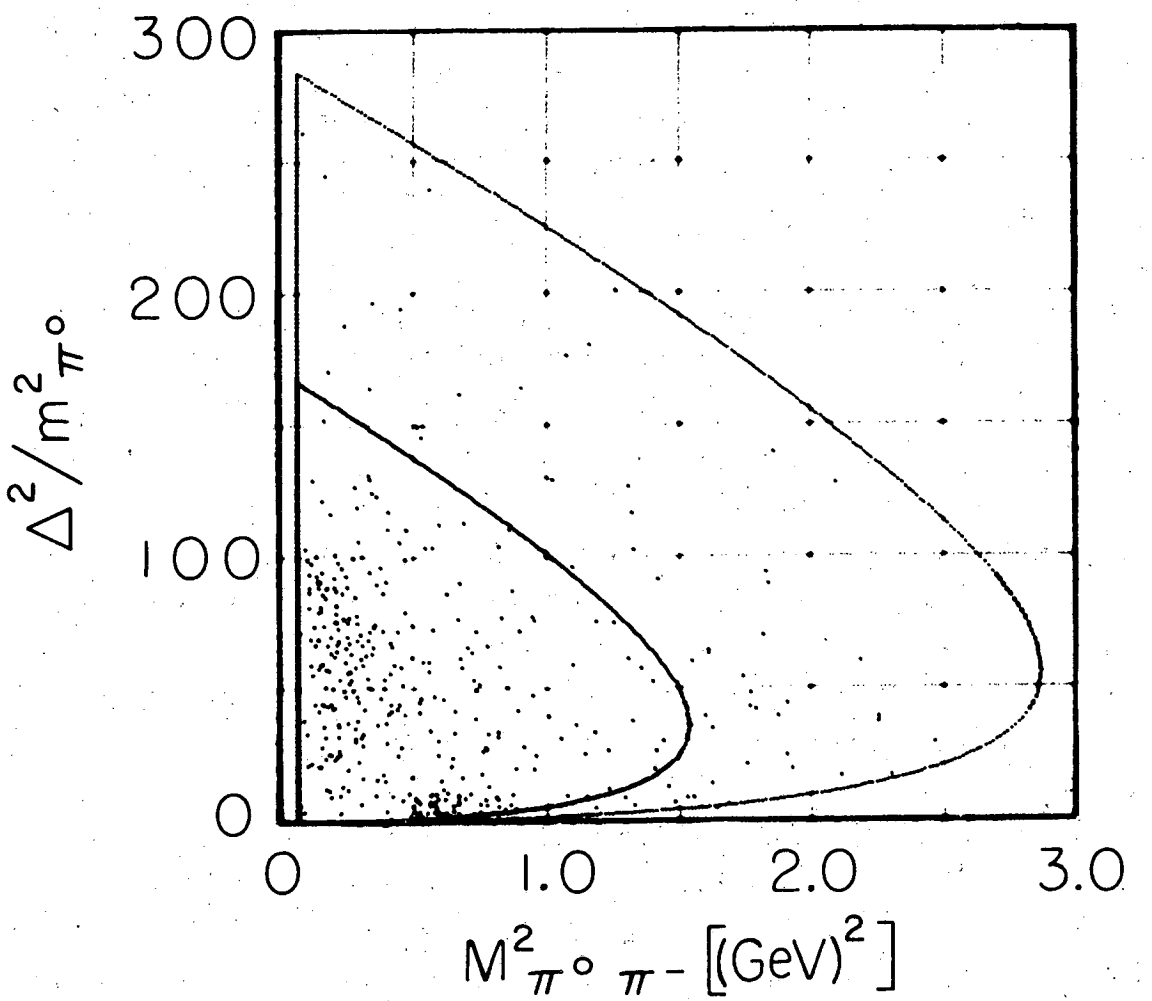

MUB-12535

Fig. 7. Chew-Low plot for $\pi^- p \rightarrow p\pi^0\pi^-$ at 2.05 to 3.22 GeV/c with $\cos\theta < -0.5$ and $\phi < 50°$. The clustering of events with $\Delta^2 > 20\ m_{\pi^0}{}^2$ and $m_{\pi\pi} > 500$ MeV is due to misfitted elastic scatterings.

Lorentz transformation from the Laboratory frame to the $\pi\pi$ rest frame we will rotate the direction of the incident π^- away from the outgoing. In fact, the angle between the two can exceed 90°. Thus arises the apparent strong backward asymmetry in the $\pi\pi$ scattering angle.

Parameterization and Correction of Scanning Bias

We attempted to parameterize the scanning bias against short protons in terms of the range of the proton. This range is synonymous with the measured length of the proton when the proton stops in the chamber. We use the range in preference to the length, so as to include nonstopping protons. For a given range interval we observed the distribution of the scattering plane about the direction of the beam. The reference plane was defined as that of the beam and the Z axis, the vertical axis of the chamber. The distribution is flat but due to scanning errors is observed as having dips when the scattering plane is parallel to the reference plane. We set up as a model that the visibility of the events depends on the range R and linearly on the sine of δ, the dihedral angle, between the planes.

We postulate that

$$\frac{\partial^2 N}{\partial \delta \partial R} \propto \text{Maximum of} \begin{Bmatrix} H(R) + \sin\delta \\ 0 \end{Bmatrix},$$

where H(R) increases monotonically with the range and hence with the momentum transfer. H(R) must be very large for large R. By parameterizing in this form we avoid singularities when H(R) is equal to 0.

In Fig. 8 we show the observed distributions and the corresponding fits up to ranges of 16 cm--which corresponds to a Δ^2 value of $5\,\mu^2$. Above this value we expect very little scanning bias; see Fig. 9, which shows a scatter plot of R against δ. Figure 10a shows a cubic least-squares fit to H(R). The linear fit did not increase fast enough, and the quadratic fit began to decrease when R was greater than 16.

If we assume that there is no scanning bias against events that scatter in the horizontal plane of the bubble chamber, and that this is

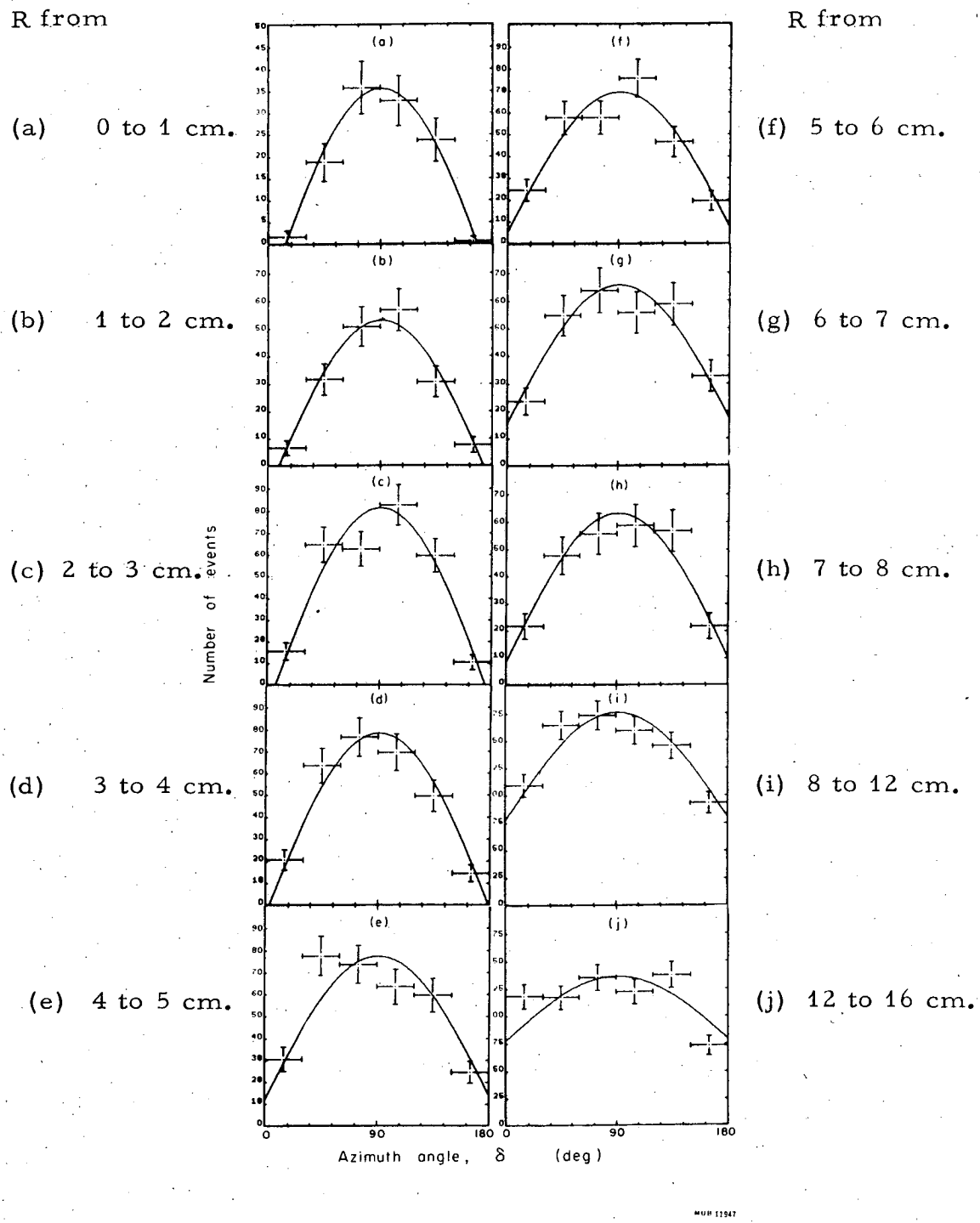

Fig. 8. Azimuthal distribution of elastic scattering plane about beam direction for various ranges of the recoil proton. Fitted curve is proportional to $H(R) + \sin\delta$.

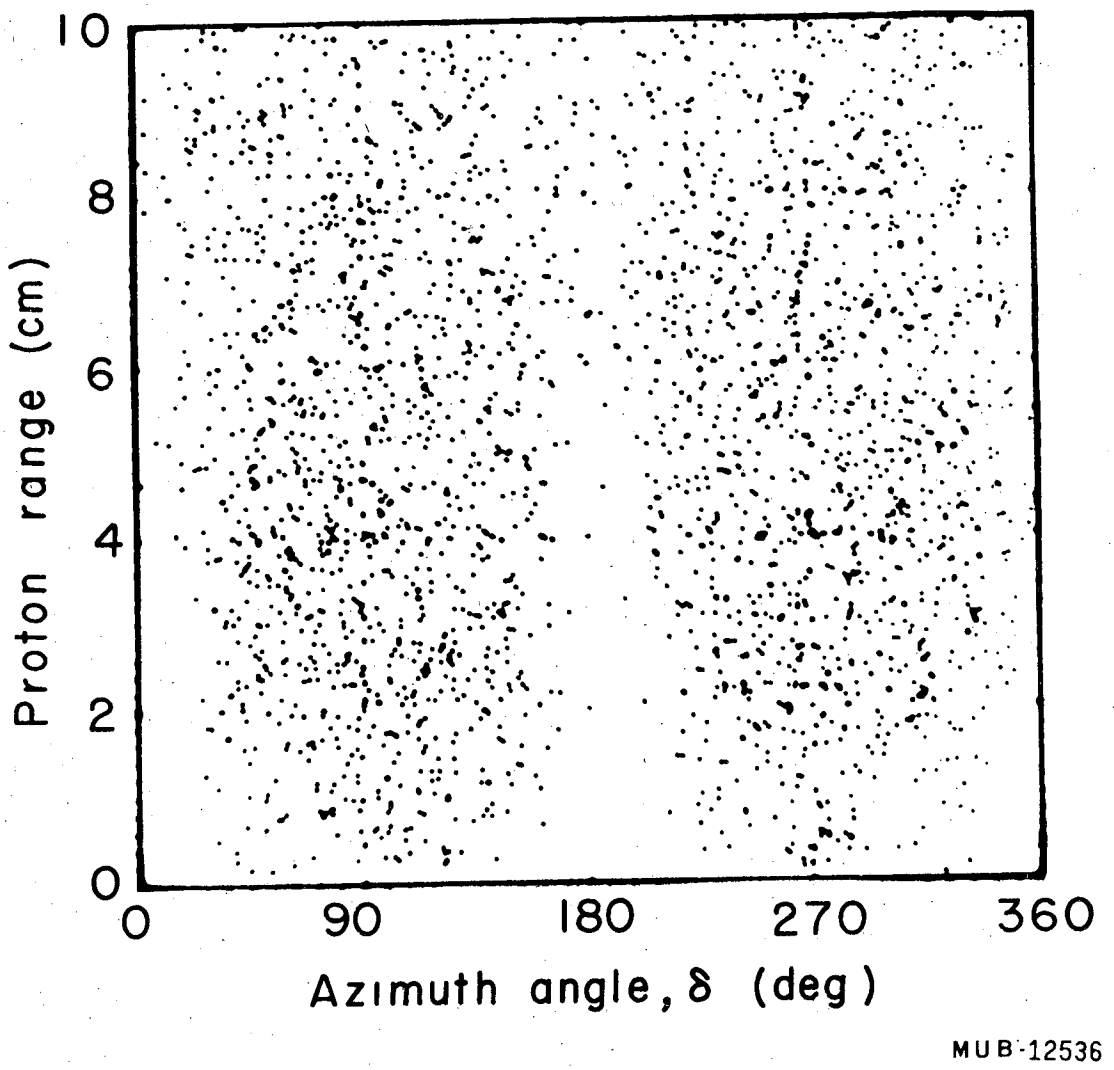

Fig. 9. Scatter plot of δ versus R, range of the recoil proton for elastic scattering events.

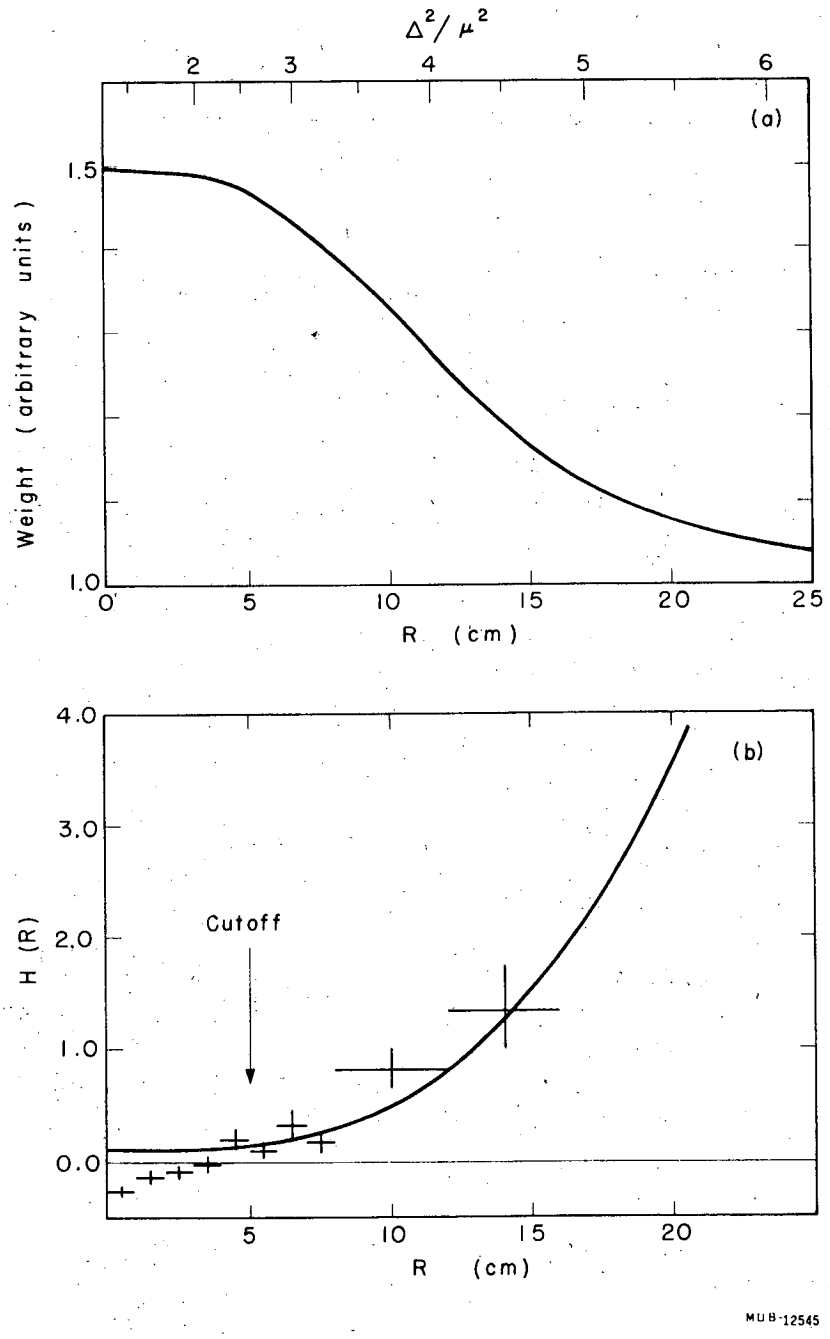

Fig. 10. (b) Experimental values of H(R) with cubic fit, $H(R) = 0.01\ (9.8 + 0.22R - 0.11\ R^2 + 0.048R^3)$.
(a) Weighting function $(H(R)\pi + \pi)/\ H(R) + 2)$.

true above some minimum value of R, then we say that we observed the number

$$\int_0^{\pi} [H + \sin\delta]\, d\delta = H\pi + 2$$

when in fact there were

$$\int_0^{\pi} [H + 1]\, d\delta = H\pi + \pi .$$

For an event with range R our efficiency is $(H\pi + 2)/(H\pi + \pi)$, and to correct this we weight each event by the reciprocal of the efficiency. In Fig. 10b we plot the weight as a function of R and Δ^2. We use the weight to correct all proton events since it is, according to our formulation, a function of the range of the proton.

F. Determination of Cross Sections

Knowing the average distance, L, a beam particle travels in liquid hydrogen, one can determine the total interaction cross section by the formula

$$\sigma = 1.008/N_0\, dL ,$$

where N_0 is Avogadro's number and d is the density of liquid hydrogen, taken here as 0.0586 g/cm^3. In practice, the procedure consists of scanning a large number of frames, counting the number of entering beam tracks, and recording the total number of interactions observed in the same fiducial volume and under the same acceptance conditions as in the two-prong scan. This information plus a knowledge of the path length (118 cm) in the fiducial volume, an estimate of the μ^- contamination in the beam, and the correction due to unobserved elastic scatterings yields a value for the mean free path. At 2.86 GeV/c we obtain an observable total cross section of 29.2 mb, corresponding to $L = 97.1 \pm 3$ cm. We compare this with the value 32.7 mb interpolated from the results of Citron et al.[13] A correction to our value amounting to about 11.5% is indicated.

To determine our two-prong cross section we have normalized our total number of interactions, corrected for unobserved small-angle scatterings, to the precisely determined value of Diddnes et al.[14] for the $\pi 72$ energy range and of Citron et al.[13] for the higher beam momenta.

A beam scan had been undertaken in the $\pi 72$ experiment. Every fifth frame of about a dozen rolls at each of three momenta--2.05, 2.17, and 2.36 GeV/c--was scanned. Frames with too many tracks were excluded. There was no fiducial volume restriction. In order to find out how many of these interactions were two-prongs a special USER subroutine was written for LYRIC, which read the Master List and totted up the events on the frames that had been beam scanned. It also read data cards on which were punched the total number of interactions corresponding to those frames that the two-prong scanner had looked at, and frame numbers that the beam scanner had ignored. LYRIC in reading the Master List ignored these frames in the totting up. Because of the different fiducial volumes of the two scans a correcting factor had to be introduced.

This procedure was also carried out for the 2.86-GeV/c events, but the same fiducial volume was used.

For the 2.60-GeV/c and 3.22-GeV/c film a somewhat different cross-section scan was performed. Six rolls were selected with less than the average number of beam tracks per frame. Every suitable frame was scanned and the interactions on a frame were subdivided into zero-prongs, two-prongs, and other interactions. In this way the proportion of two-prongs was obtained directly. This method, both simple and direct, was used on the 2.05- and 2.17-GeV/c film. Consistency was found between the two methods.

No correction was made for events overlooked by scanners. A two-prong rescan of a few rolls indicated scanning efficiencies of $89 \pm 4\%$. The two-prong cross section contains this factor in both the numerator and denominator. If we assume that the cross-section scan is subject to the same efficiency, the net effect on the value obtained is negligible, but it will introduce most of the error (5%) in our determination. The total number of interactions used ranged from about 2000 to 4000, introducing statistical errors of 1.6 to 2.3%.

To determine actual cross sections, as against observable cross section, we derived the total elastic scattering cross section, using both the weighting function that we have derived and the exponential dependence of the differential cross section in the diffraction region (as is described in the section on elastic scattering). The scanning bias involves a correction of 13%. The exponential dependence gives a further correction of 21%, making a total correction to the elastic scatterings of 37%. The actual total and two-prong cross sections are 10% larger than the observed. In the section immediately following we present the numbers obtained.

III. EXPERIMENTAL RESULTS

A. Cross Sections

In Table I we exhibit the numbers of events fitting the five hypotheses

$$\pi^- p \rightarrow n\pi^+ \pi^- , \tag{1}$$

$$\pi^- p \rightarrow p\pi^0 \pi^- , \tag{2}$$

$$\pi^- p \rightarrow \pi^- p , \tag{3}$$

$$\pi^- p \rightarrow \pi^+ \pi^- + \text{neutrons}, \tag{4}$$

$$\pi^- p \rightarrow \pi^- p + \text{neutrals} \tag{5}$$

at the six different beam energies.

At each momentum interval we have normalized the corrected total number of events to the total two-prong cross section as obtained in the cross-section scan. Reaction (2) has a 5% correction for short protons: we have already made reference to the elastic scattering correction. The values obtained for the total two-prong and reaction cross sections, and events per microbarn, are shown in Table II.[15] Statistical errors vary between 1.5 and 4.5%. Due to the way in which absolute cross sections were obtained, we believe that there is about 5% uncertainty in the normalization caused by the spread in scanning efficiencies. Consequently, we attach this error to all cross sections shown.

B. Elastic Scattering

Introduction

In this experiment we obtain two pieces of information on the πN scattering amplitudes, the total elastic cross sections, and the differential cross sections for the process $\pi^- p \rightarrow \pi^- p$. The most complete information available would involve knowing the polarizations of the initial and final nucleons and the elastic and differential cross sections not only for our reaction but also for the pure isospin 3/2 reaction, $\pi^+ p \rightarrow \pi^+ p$, as well as for charge exchange, $\pi^- p \rightarrow \pi^0 n$.

Table I. Number of events at each momentum, all final states.

Beam momentum (GeV/c)	Number of events					
	$n\pi^+\pi^-$	$p\pi^0\pi^-$	π^-p	$\pi^+\pi^-$ neutrals	π^-p neutrals	Total
2.05	864	624	1045	960	463	3956
2.17	951	701	1177	1158	576	4563
2.36	1005	901	1551	1481	820	5758
2.60	1418	1122	2003	2171	1170	7884
2.86	982	1727	1725	1609	1153	6196
3.22	2540	1939	4326	4735	3586	17126
Total	7760	6014	11827	12114	7768	
						45483

Table II. Partial cross sections.

	Events per μb	Cross sections (in mb) ± 5%					
		$n\pi^+\pi^-$	$p\pi^0\pi^-$	$\pi^- p$	$\pi^+\pi^-$ neutrals	$\pi^- p$ neutrals	Total
2.05	0.159	5.5	4.15	9.0	6.1	2.9	27.7
2.17	0.178	5.3	4.15	8.7	6.5	3.2	27.8
2.36	0.233 [0.254]	4.3	3.9	8.55	6.4	3.4	26.6
2.60	0.345	4.1	3.4	7.8	6.3	3.4	24.9
2.86	0.286	3.4	2.7	7.7	5.6	4.0	23.4
3.22	0.839	3.0	2.4	7.25	5.6	4.25	22.5
Total	2.04						

Until now, elastic scattering in this energy range (2.05 to 3.22 BeV) has been very hard to interpret. Orthodox partial-wave analyses become increasingly difficult to carry out even below 2 BeV. The terms in a $\cos\Theta$ or Legendre polynomial expansion of the angular distribution are, in general, dependent on a large number of partial waves. With good statistics, in an experiment measuring the differential cross sections and polarizations of both $\pi^- p$ and $\pi^+ p$ elastic scattering at graduated intervals of the incident beam momentum, Duke at al.[16] were able to pick out the important partial waves up to about 1.6 GeV/c and determine the spins and parities of the $N^*_{\frac{1}{2}}(1688)$ and $\Delta(1920)$. Yokosawa,[17] by extending partial-wave solutions at lower energies, was able to reproduce the $f_{7/2}$ resonant amplitude at 1920 MeV and to fit polarization data at 1.70 to 2.50 GeV/c with a resonant $g_{7/2}$ amplitude at 2190 MeV. In the same paper, he also discusses an alternative approach to elastic scattering, namely by the optical model.

A good discussion of the applicability of the optical model to πp elastic scattering will be found in Perl and Corey,[18] which contains many references to previous work. At 2 GeV/c, orbital angular momenta larger than 3 must be considered. Each value of the orbital angular momentum can couple with the spin 1/2 of the nucleon to give two values of the total angular momentum. We thus have two amplitudes associated with two phase shifts which, because of the inelastic processes that are known to occur, are complex. To describe the elastic scattering at our energies would need 20 or more parameters. This is not feasible. The optical model makes specific physical assumptions as to the behavior of the phase shifts with increasing l, the orbital angular momentum. In the most simple form of the model (see Simmons[19]) we have one parameter L. The nucleon appears as a black absorbing disk for orbital angular momenta $l \leq L$, i.e., the first L-phase shifts are purely imaginary and the rest are zero. The model may be refined by introducing an interaction radius over which the absorption decreases. Perl and Corey argued that, rather than imposing a prior shape on the nucleon--e.g., a Gaussian behavior--and employing

an impact parameter representation to convert the summation over partial waves into an integral, we could keep the summation and find the shape of the nucleon from the angular distributions, since we were dealing with comparatively few partial waves. They attempted fits to elastic scattering from 1.33 to 2.92 GeV/c, using the formula

$$\frac{d\sigma}{d\Omega} = \left|\frac{1}{2iq} \sum_{l=0}^{L} (2l+1)\,(a_l - 1)\,P_l(\cos\Theta)\right|^2 , \qquad (6)$$

where the a_l are the real parameters to be determined.

In an attempt to correct the model for its deficiencies, namely the assumptions of zero spin-flip amplitudes and zero real amplitudes, the authors added to the above series an extra set of terms $\sum_{i=0}^{i\,max} b_i (\cos\Theta)^i$. Despite this addition, the fits give only fair agreement with the data, failing to give the exact shape of the secondary peaks.

Since this is to our knowledge the most ambitious application of the optical model, we have not attempted to fit the data to any optical model but are content to present the data and mention some physical hypotheses which would seem to have more success in explaining them.

Presentation of data

In Figs. 11 through 16, we display the six differential cross sections, which are tabulated both in terms of momentum transfer squared and the c. m. scattering angle, $\cos\Theta$, in Tables IIIa and IIIb.

We find it convenient and instructive to consider the differential cross sections as being made up of four separate regions, of which only the first two can be discussed, with some certainty by us. The four regions are the forward diffraction peak, the second maximum, the large-angle region ($\cos\Theta \leq 0$), and the events at 180°.

Diffraction region

If we define the diffraction region as extending from zero momentum transfer up to $\Delta^2 = 40\ m_{\pi^0}{}^2\ [0.72\,(\mathrm{GeV})^2]$, we see that the points seem to lie on a straight line on the semilogarithmic scale. This suggests an obvious parameterization

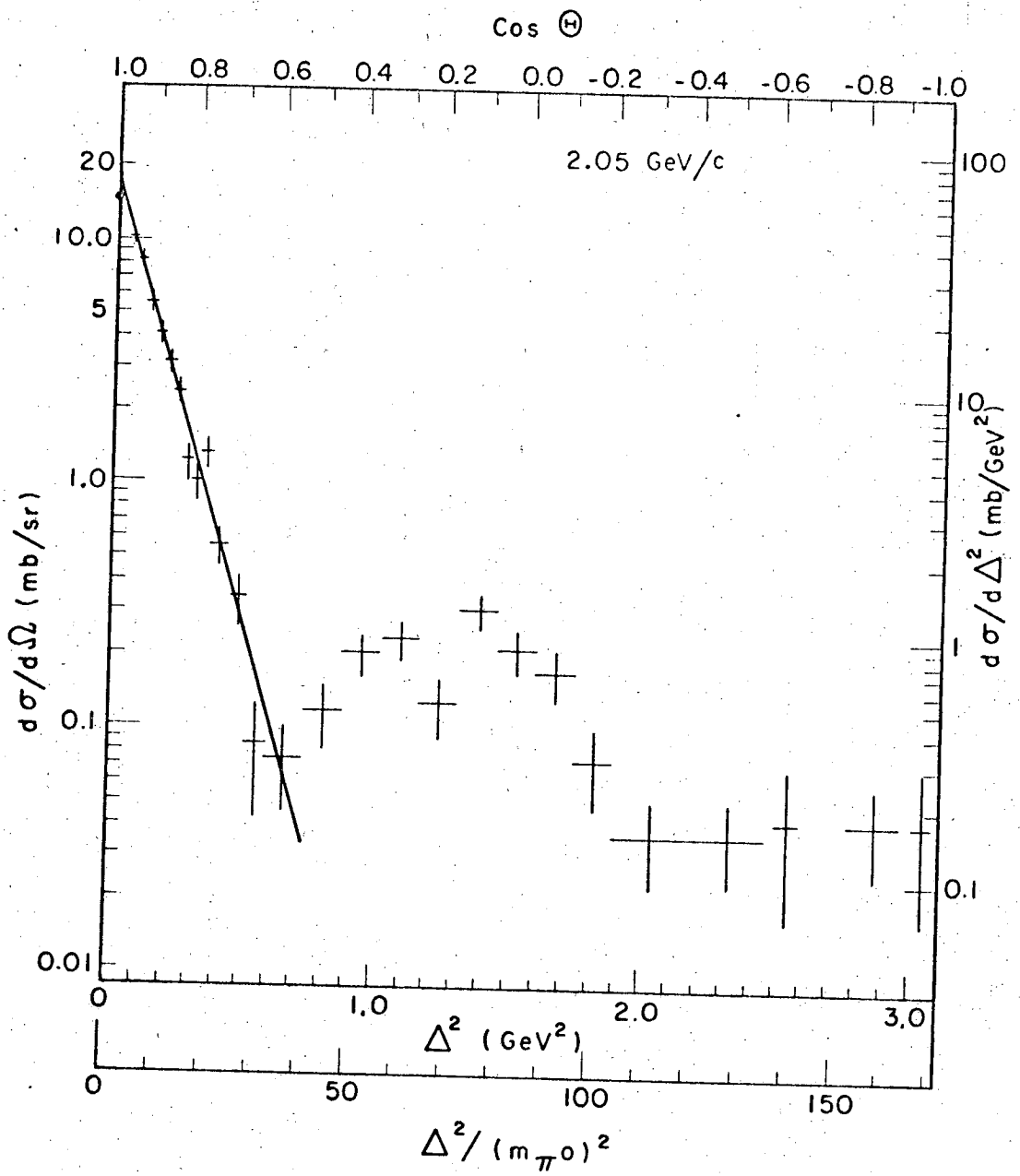

MUB-11942

Fig. 11. $\pi^- p$ elastic scattering differential cross sections showing the optical point and exponential fit to the diffraction peak at 2.05 GeV/c, 1045 events.

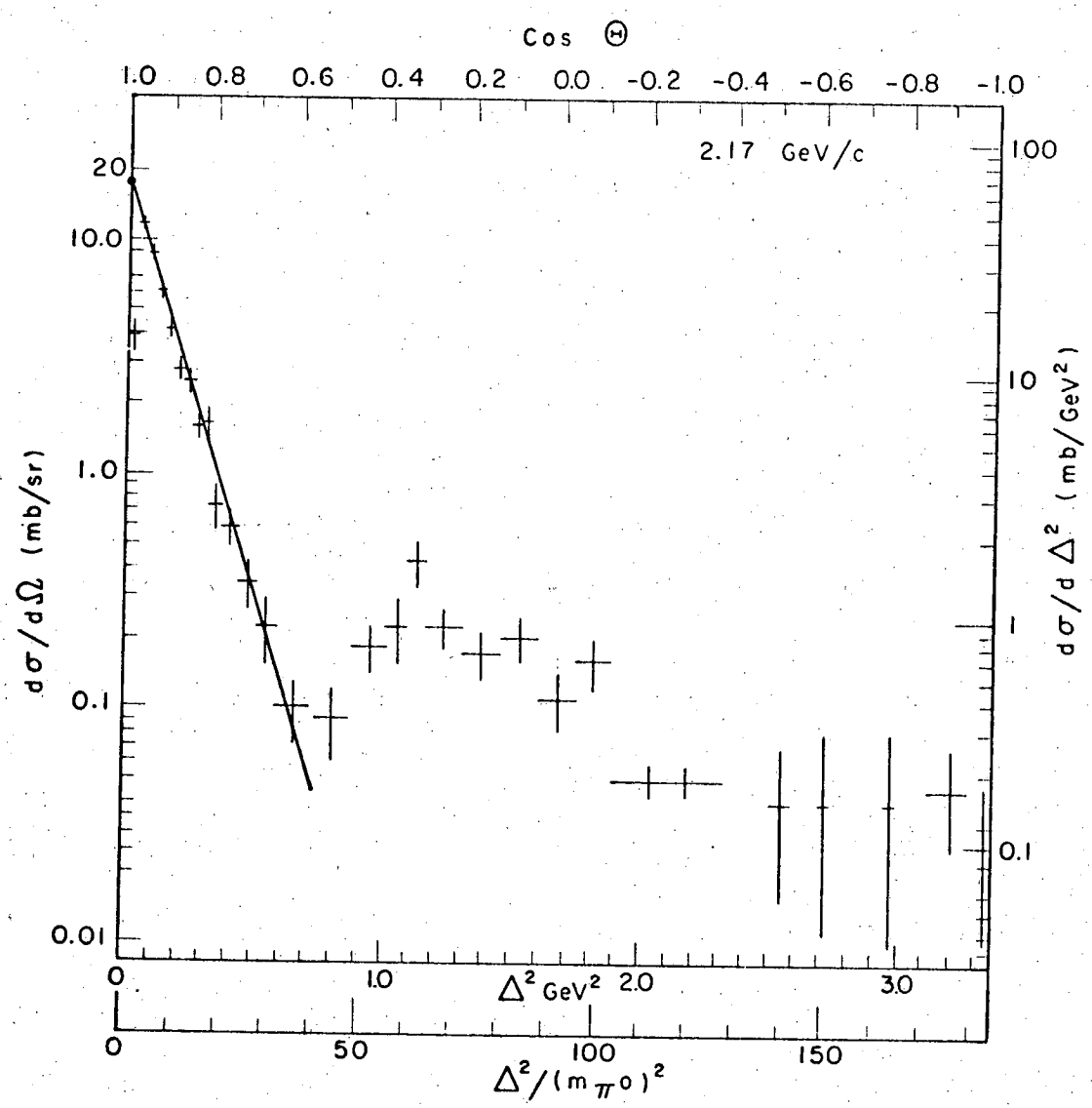

MUB 11943

Fig. 12. $\pi^- p$ elastic scattering differential cross sections showing the optical point and exponential fit to the diffraction peak at 2.17 GeV/c, 1177 events.

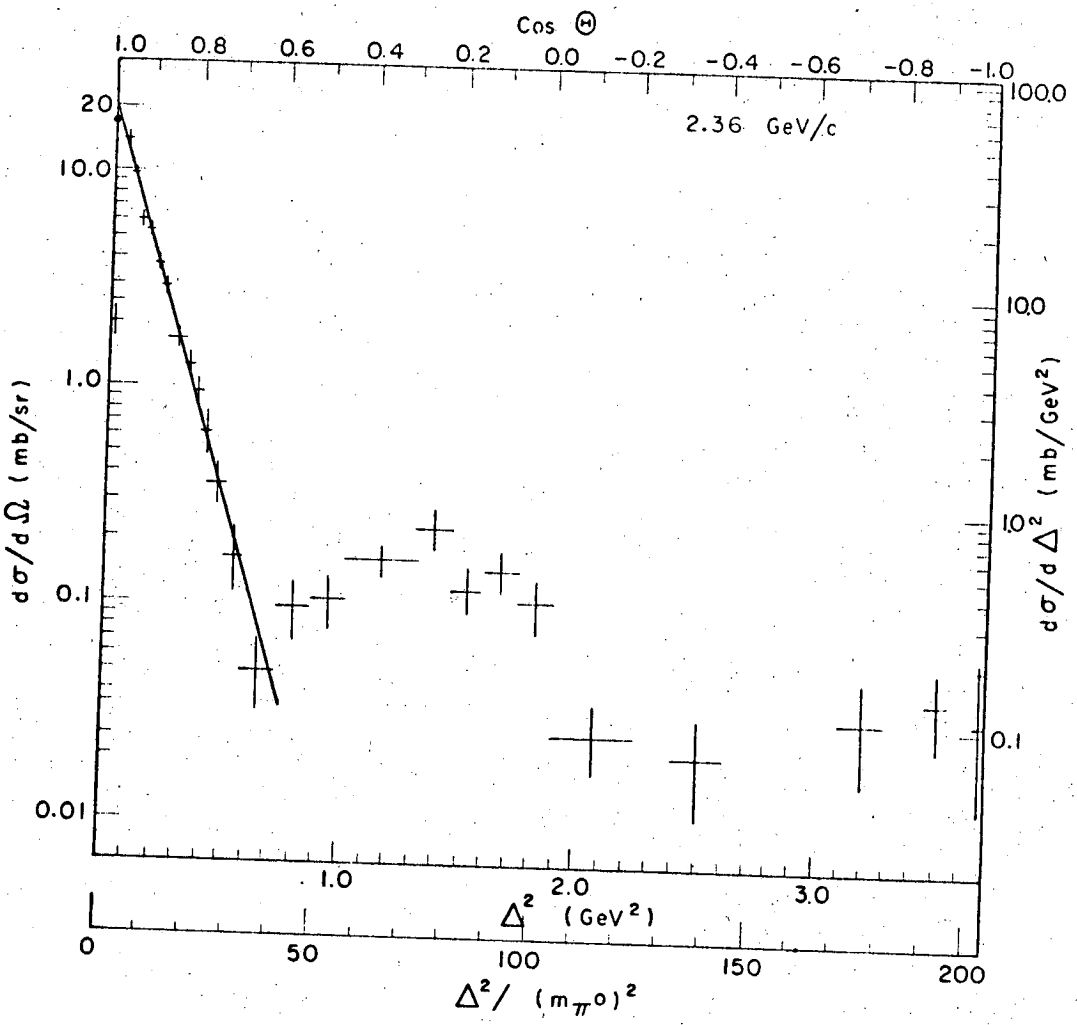

MUB 11941

Fig. 13. $\pi^- p$ elastic scattering differential cross sections showing the optical point and exponential fit to the diffraction peak at 2.36 GeV/c, 1551 events.

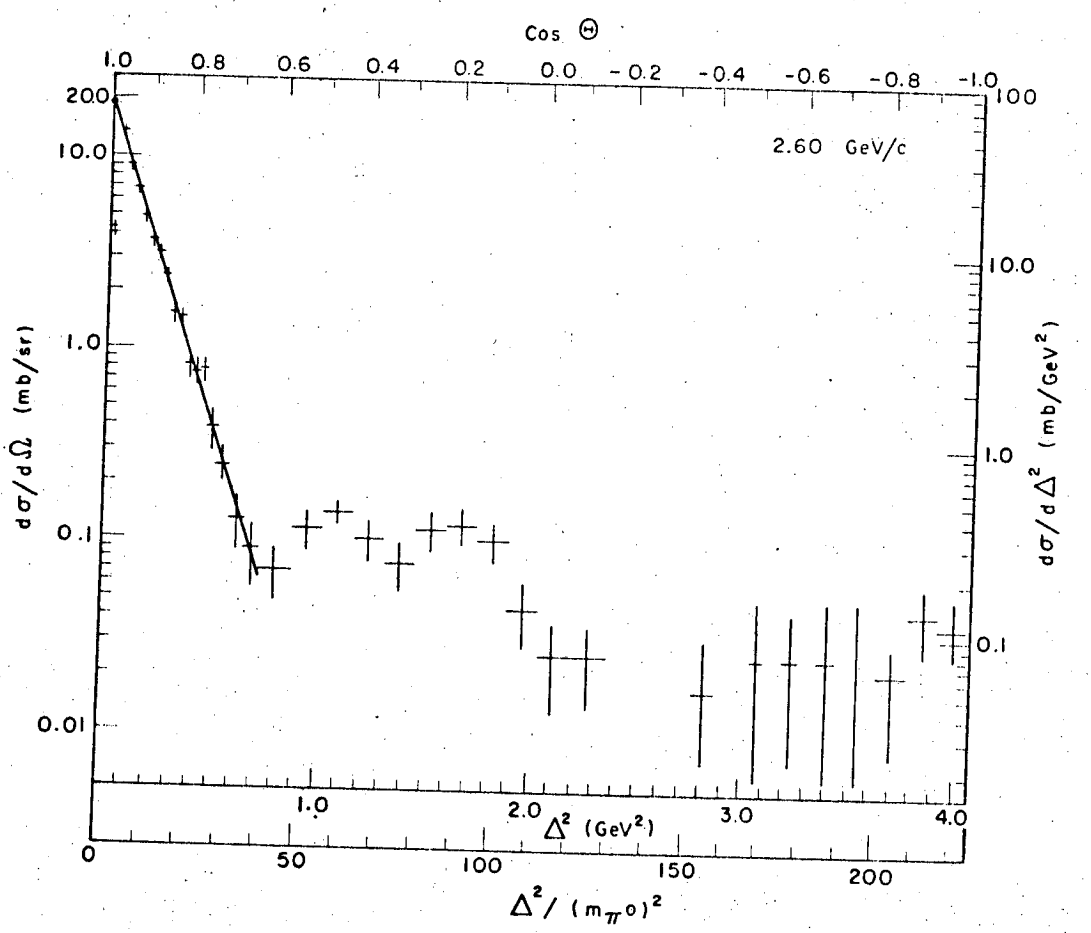

MUB-11945

Fig. 14. $\pi^- p$ elastic scattering differential cross sections showing the optical point and exponential fit to the diffraction peak at 2.60 GeV/c, 2003 events.

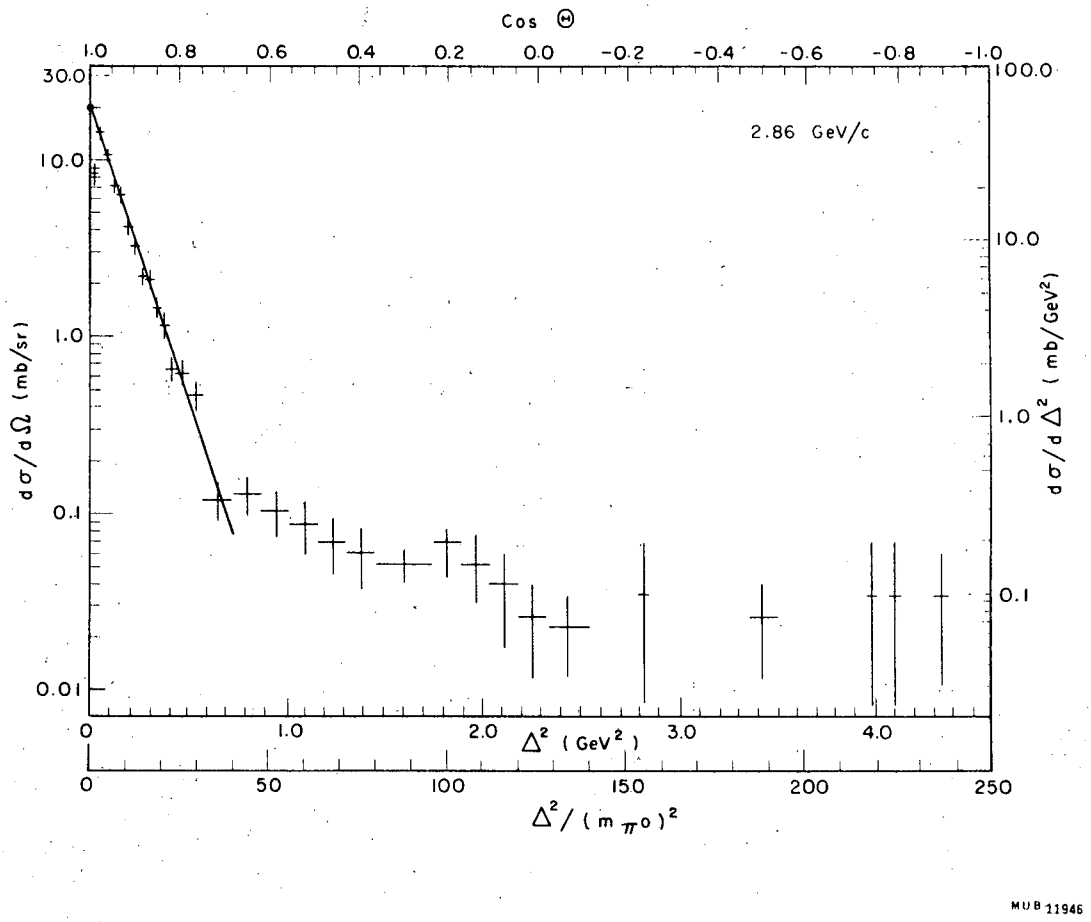

Fig. 15. $\pi^- p$ elastic scattering differential cross sections showing the optical point and exponential fit to the diffraction peak at 2.86 GeV/c, 1725 events.

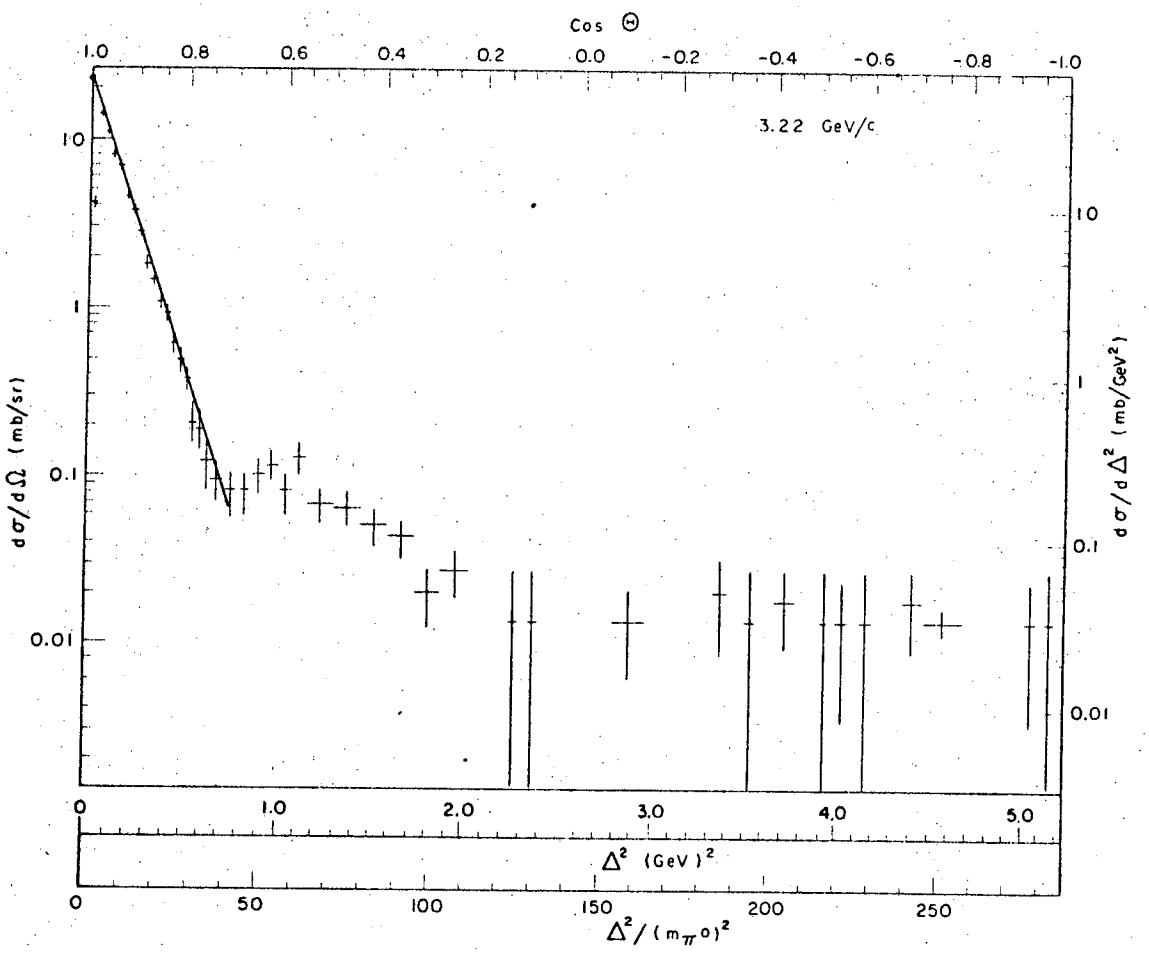

MUB 11944

Fig. 16. $\pi^- p$ elastic scattering differential cross sections showing the optical point and exponential fit to the diffraction peak at 3.22 GeV/c, 4326 events.

Table IIIa. $\pi^- p$ differential cross sections in mb/(GeV)^2.

$\Delta^2/m^2_{\pi_0}$	2.05 GeV/c		2.17 GeV/c		2.36 GeV/c		2.60 GeV/c		2.86 GeV/c		3.22 GeV/c	
	$\frac{d\sigma}{d\Delta^2}$	Error	$\frac{d\sigma}{d\Delta^2}$	Error	$\frac{d\sigma}{d\Delta^2}$	Error	$\frac{d\sigma}{d\Delta^2}$	Error	$\frac{d\sigma}{d\Delta^2}$	Error	$\frac{d\sigma}{d\Delta^2}$	Error
2	41.4	3.2	44.4	2.8	46.7	2.7	41.3	2.15	39.8	2.9	34.8	1.3
4	33.6	2.6	33.5	2.4	32.4	2.0	27.5	1.6	29.7	2.0	26.2	1.0
6	22.4	1.8	23.0	1.9	20.0	1.6	20.7	1.3	19.8	1.4	19.35	0.8
8	16.6	1.7	15.7	1.6	17.8	1.5	14.9	1.1	17.9	1.3	16.6	0.75
10	12.8	1.5	10.5	1.3	12.4	1.3	11.3	0.95	11.7	1.05	11.0	0.6
12	9.7	1.3	9.4	1.2	9.8	1.1	9.7	0.9	8.9	0.9	9.2	0.55
14	5.0	0.9	6.0	1.0	5.6	0.7	7.3	0.8	6.0	0.8	6.8	0.5
16	4.1	0.8	6.2	1.0	5.6	0.7	4.7	0.6	5.8	0.75	4.4	0.4
18	5.5	1.0	2.8	0.65	4.2	0.6	4.45	0.6	4.0	0.6	3.55	0.3
20	2.4	0.6	2.2	0.6	3.1	0.5	2.5	0.45	3.15	0.55	2.6	0.3
22	2.1	0.6	2.3	0.6	2.0	0.4	2.3	0.4	1.8	0.4	2.2	0.3
24	1.4	0.3	1.3	0.3	1.2	0.25	1.8	0.3	1.7	0.3	1.3	0.15
28	0.3	0.2	0.85	0.3	0.5	0.2	0.95	0.2	1.3	0.25	0.7	0.1
32	0.3	0.1	0.2	0.1	0.05	0.05	0.4	0.1	0.3	0.1	0.4	0.1
36	0.3	0.1	0.5	0.2	0.3	0.1	0.3	0.1	0.3	0.1	0.2	0.1
40	0.5	0.1	0.3	0.1	0.4	0.1	0.2	0.1	0.4	0.1	0.2	0.04
48	0.8	0.2	0.7	0.2	0.35	0.1	0.4	0.1	0.3	0.1	0.3	0.05
56	0.9	0.2	1.2	0.2	0.5	0.1	0.4	0.1	0.2	0.1	0.25	0.05
64	0.5	0.2	0.85	0.2	0.5	0.1	0.3	0.1	0.2	0.1	0.2	0.05
72	1.3	0.2	0.65	0.2	0.75	0.1	0.2	0.1	0.2	0.1	0.15	0.04
80	0.9	0.2	0.8	0.2	0.4	0.1	0.4	0.1	0.15	0.1	0.1	0.04
88	0.7	0.2	0.4	0.1	0.5	0.1	0.4	0.1	0.15	0.1	0.1	0.04
96	0.5	0.1	0.65	0.2	0.35	0.1	0.3	0.1	0.2	0.1	0.05	0.02
104	0.3	0.1	0.2	0.1	0.1	0.06	0.1	0.05	0.15	0.1	0.1	0.02
112	0.04	0.04	0.2	0.1	0.05	0.04	0.08	0.04	0.1	0.05	0.0	0.01
120	0.04	0.04	0.2	0.1	0.03	0.03	0.08	0.04	0.1	0.04	0.01	0.01
128	0.3	0.1	0.0	0.04	0.03	0.03	0.02	0.02	0.1	0.04	0.01	0.01
136	0.1	0.1	0.1	0.05	0.1	0.05	0.0	0.02	0.02	0.02	} < 0.004	
144	0.0	0.04	0.04	0.04	0.0	0.03	0.0	0.02	0.0	0.02		
152	0.2	0.1	0.0	0.04	0.0	0.03	0.04	0.03	0.02	0.02	0.02	0.01
160	0.1	0.1	0.04	0.04	0.0	0.03	0.0	0.02	} < 0.008		0.02	0.01
168	0.4	0.4	0.1	0.1	0.03	0.03	0.02	0.02			} < 0.004	
176			0.1	0.1	0.1	0.05	0.04	0.03				
184			0.4	0.4	0.05	0.04	0.02	0.02	0.1	0.04	0.02	0.01
192					0.1	0.05	0.02	0.02	} < 0.008		0.01	0.01
200					0.06	0.06	0.06	0.03			0.03	0.02
208							0.14	0.05			0.0	0.01
216							0.12	0.05	0.02	0.02	0.02	0.01
224									0.02	0.02	0.01	0.01
232									0.05	0.03	0.00	0.01
240									0.0	0.02	0.03	0.02
298									0.02	0.02	0.04	0.02
256											0.02	0.01
264											0.01	0.01
272											0.02	0.01
280											0.02	0.02
288												

Table IIIb. $\pi^- p$ differential cross sections in mb/steradian.

CosΘ	2.05 GeV/c		2.17 GeV/c		2.36 GeV/c		2.60 GeV/c		2.86 GeV/c		3.22 GeV/c	
	$\frac{d\sigma}{d\Omega}$	Error	$\frac{d\sigma}{d\Omega}$	Error	$\frac{d\sigma}{d\Omega}$	Error	$\frac{d\sigma}{d\Omega}$	Error	$\frac{d\sigma}{d\Omega}$	Error	$\frac{d\sigma}{d\Omega}$	Error
0.98												
0.96	10.20	0.8	11.80	0.75	13.50	0.70	12.95	0.55	13.75	0.70	12.70	0.35
0.94	9.00	0.7	9.70	0.65	9.40	0.55	8.40	0.45	8.20	0.50	8.10	0.30
0.92	6.90	0.6	6.35	0.55	5.80	0.45	5.60	0.40	6.25	0.45	5.69	0.25
0.90	4.65	0.5	5.05	0.50	5.28	0.40	4.34	0.35	4.00	0.35	3.57	0.18
0.88	3.85	0.45	2.70	0.35	3.60	0.35	3.28	0.28	2.75	0.28	2.42	0.16
0.86	3.40	0.40	3.25	0.38	2.65	0.30	2.38	0.23	2.22	0.25	1.59	0.12
0.84	2.05	0.30	2.20	0.31	1.80	0.24	1.62	0.19	1.59	0.21	1.05	0.10
0.82	1.80	0.30	1.75	0.28	1.52	0.22	1.45	0.18	1.00	0.17	0.70	0.08
0.80	1.10	0.25	1.38	0.25	1.15	0.19	0.92	0.15	0.58	0.13	0.44	0.065
0.78	1.15	0.25	0.67	0.17	0.90	0.17	0.65	0.12	0.67	0.14	0.26	0.05
-0.76	1.10	0.25	0.58	0.16	0.65	0.14	0.46	0.10	0.55	0.12	0.22	0.05
0.72	0.50	0.10	0.53	0.07	0.31	0.07	0.30	0.06	0.22	0.06	0.10	0.02
0.68	0.40	0.10	0.29	0.05	0.14	0.05	0.16	0.04	0.13	0.04	0.08	0.02
0.64	0.13	0.06	0.18	0.04	0.02	0.02	0.07	0.03	0.17	0.05	0.12	0.02
-0.60	0.13	0.06	0.05	0.02	0.06	0.03	0.05	0.02	0.06	0.03	0.10	0.02
0.52	0.05	0.03	0.15	0.04	0.09	0.03	0.13	0.03	0.11	0.03	0.095	0.015
0.44	0.14	0.04	0.08	0.03	0.10	0.03	0.13	0.03	0.08	0.02	0.07	0.013
0.36	0.21	0.05	0.25	0.05	0.17	0.04	0.10	0.02	0.06	0.02	0.05	0.010
0.28	0.23	0.05	0.30	0.06	0.17	0.04	0.08	0.02	0.04	0.02	0.02	0.008
0.20	0.16	0.05	0.23	0.05	0.22	0.04	0.11	0.03	0.07	0.02	0.015	0.005
0.12	0.25	0.06	0.19	0.05	0.12	0.03	0.13	0.03	0.04	0.02	0.002	0.002
0.04	0.30	0.06	0.17	0.04	0.13	0.03	0.08	0.02	0.06	0.02	0.002	0.002
-0.04	0.14	0.04	0.13	0.04	0.09	0.03	0.02	0.01	0.02	0.01	0.000	0.002
-0.12	0.19	0.05	0.16	0.04	0.03	0.02	0.03	0.01	0.02	0.01	0.01	0.005
-0.20	0.08	0.03	0.09	0.03	0.02	0.01	0.02	0.01	0.00	0.01	0.002	0.002
-0.28	0.09	0.03	0.06	0.03	0.01	0.01	0.00	0.01	0.01	0.01	0.01	0.005
-0.36	0.04	0.02	0.01	0.01	0.01	0.01	0.01	0.01	0.00	0.01	0.002	0.002
-0.44	0.03	0.02	0.06	0.03	0.02	0.01	0.01	0.01	0.01	0.01	0.01	0.005
-0.052	0.01	0.01	0.00	0.01			0.01	0.01	0.01	0.01	0.002	0.002
-0.60	0.09	0.03	0.02	0.02	< 0.008		0.01	0.01	< 0.004		0.01	0.005
-0.68	0.01	0.01	0.01	0.01			0.01	0.01			0.002	0.002
-0.76	< 0.006		0.01	0.01	0.02	0.01	0.01	0.01	0.01	0.01	0.01	0.005
-0.84			0.00	0.01	0.02	0.01	0.02	0.01	0.01	0.01	0.01	0.005
-0.92	0.06	0.03	0.02	0.02	0.02	0.01	0.04	0.02	0.01	0.01	0.002	0.002
-1.00	0.04	0.02	0.06	0.03	0.02	0.01	0.04	0.01	0.01	0.01	0.005	0.003

$$\frac{d\sigma}{dt} = \left[\frac{d\sigma}{dt}\right]_{t=0} e^{At} , \qquad (7)$$

where $-t = \Delta^2$.

We have taken a conservative cutoff at the lower end of 2.5 $m_{\pi^0}{}^2$ and have made least-squares fits[20] to the logarithms of the distributions with upper limits 20 $m_{\pi^0}{}^2$ and 40 $m_{\pi^0}{}^2$. In Table IV, we have tabulated the two sets of A which are consistent with each other within the errors assigned. $P(\chi^2)$ is the χ^2 probability of the fit to relation (7) above. In Figs. 17 through 22, the best fit is shown on a semilogarithmic plot for the set 2.5 to 40 $m_{\pi^0}{}^2$. These values were used to derive the elastic cross sections shown in Table II and the zero-angle differential cross sections shown in Table IV. All the curves extrapolate through or just above the optical point. This is in keeping with the findings of other experiments[21-23] at these energies, and with dispersion-relation calculations that any real amplitude is small in the forward direction.[24] We also feel that it implies that no serious error has been made in the estimates of the efficiencies and overall normalizations. Interpreting the numbers as giving us some idea of the upper limit of the magnitude of $\alpha = \mathrm{Re}\, f(0)/\mathrm{Im}\, f(0)$, we obtain the values shown in Table IV.

It is apparent from Table IV that the values of A at the lower three energies are significantly larger than the upper three. In order to say something more definite, we have presented a compilation of A values from 1.34 to 18.4 GeV/c in Table V, and in Fig. 23 plotted them against $\log_e s$, where s is the square of the total c.m. energy. As is now well known, in its dependence on the beam momentum the diffraction peak displays no obvious monotonic behavior, and A remains within the range 7.5 to 7.8 $(\mathrm{GeV})^{-2}$. However, on the basis of our data points at 2.05, 2.17, 2.36, and 2.60 GeV/c, and those of Esterling et al.[25] at 1.70, 1.88, 2.07, 2.27, and 2.50 GeV/c, we believe that there is a strikingly fast variation of A between 2.0 and 2.5 GeV/c. Below 2.0 GeV/c, the peak broadens $[A \sim 7.0\ (\mathrm{GeV})^{-2}]$, then narrows quickly over a few hundred MeV/c, finally broadening again to 7.8 $(\mathrm{GeV})^{-2}$ at 2.6 GeV/c.

Table IV. Diffraction region.

Beam	Δ^2 0 to 20 $m_{\pi^0}^2$		Δ^2 0 to 40 $m_{\pi^0}^2$							
Momentum (GeV/c)	A [(GeV)^2]	P(χ^2) (%)	A [(GeV)^2]	P(χ^2) (%)	$\left(\frac{d\sigma}{d\Omega}\right)_0$ (mb / Sr)	$\frac{q^2\sigma_T^2}{16\pi^2}$	$\left(\frac{d\sigma}{dt}\right)_0$ [mb /(GeV)^2]	$\frac{\sigma_T^2}{16\pi}$	$1 + X^2$	$\lvert a \rvert$ [a]
2.05	8.30± 0.52	36.2	8.48± 0.33	38.8	16.8± 0.6	15.5	67.9± 2.4	62.8	1.08 ± 0.035	0.28± 0.06
2.17	8.59± 0.46	12.9	8.20± 0.30	85.0	16.9± 0.6	17.1	63.8± 2.2	64.6	0.99 ± 0.035	0.00± 0.17
2.36	8.47± 0.41	26.7	8.48± 0.27	1.8	19.7± 0.5	17.5	67.2± 1.9	60.0	1.25 ± 0.03	0.35± 0.04
2.60	7.70± 0.34	45.4	7.88± 0.22	95.7	18.7± 0.5	18.5	57.3± 1.4	56.9	1.01 ± 0.025	0.10± 0.09
2.86	7.81± 0.37	17.5	7.57± 0.23	31.8	20.5± 0.6	20.0	56.0± 1.5	54.8	1.02 ± 0.03	0.14± 0.08
3.22	7.80± 0.25	12.6	7.87± 0.15	86.8	23.0± 0.4	22.3	55.2± 0.9	53.5	1.035 ± 0.015	0.19± 0.05

[a] Errors quoted are statistical only. Within the systematic errors the values of $|a|$ are consistent with zero.

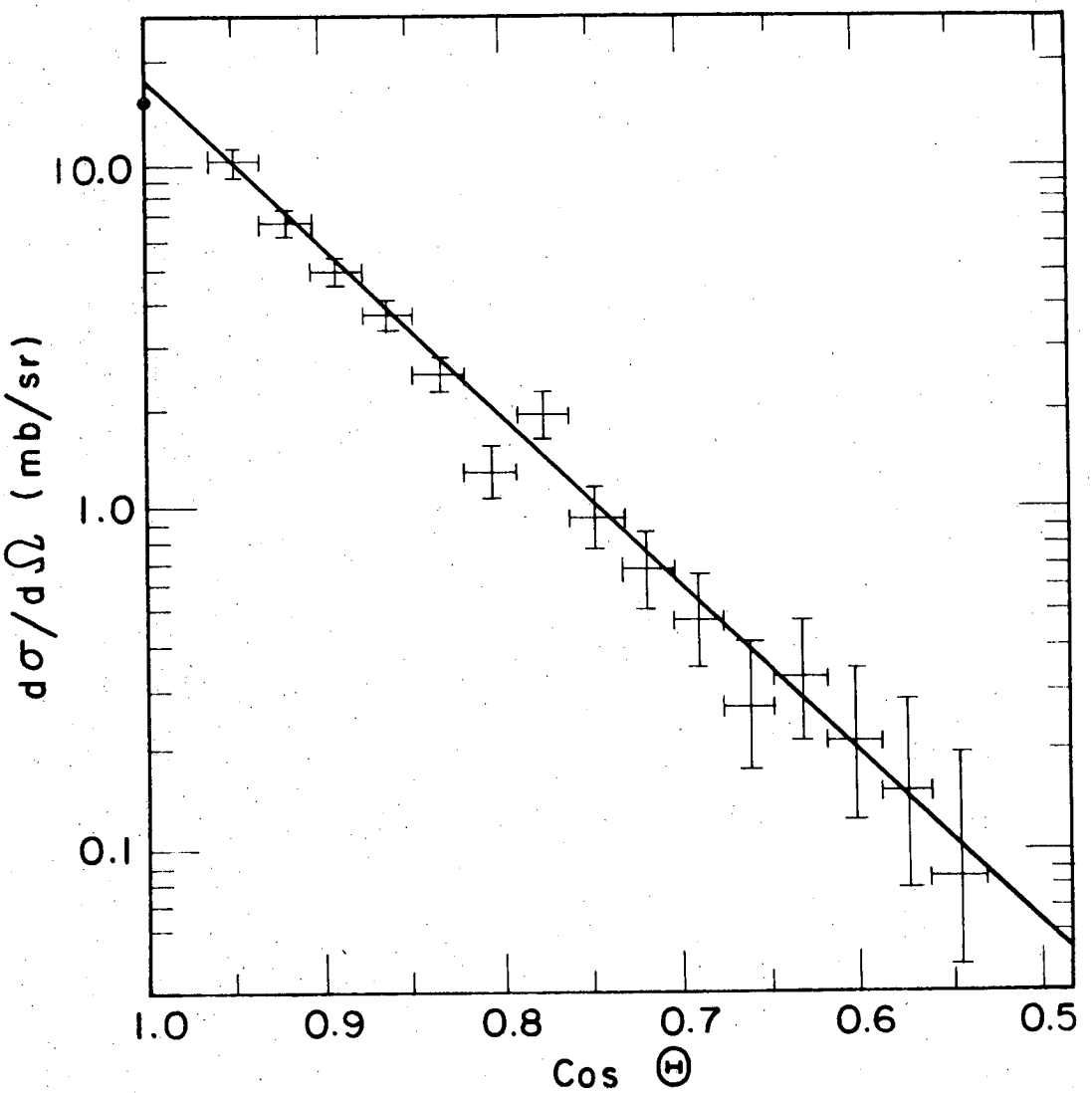

MUB 11936

Fig. 17. $\pi^- p$ elastic scattering diffraction peak. ● shows the optical point at 2.05 GeV/c, $A = 8.48 \pm 0.33\ \mathrm{GeV}^2$.

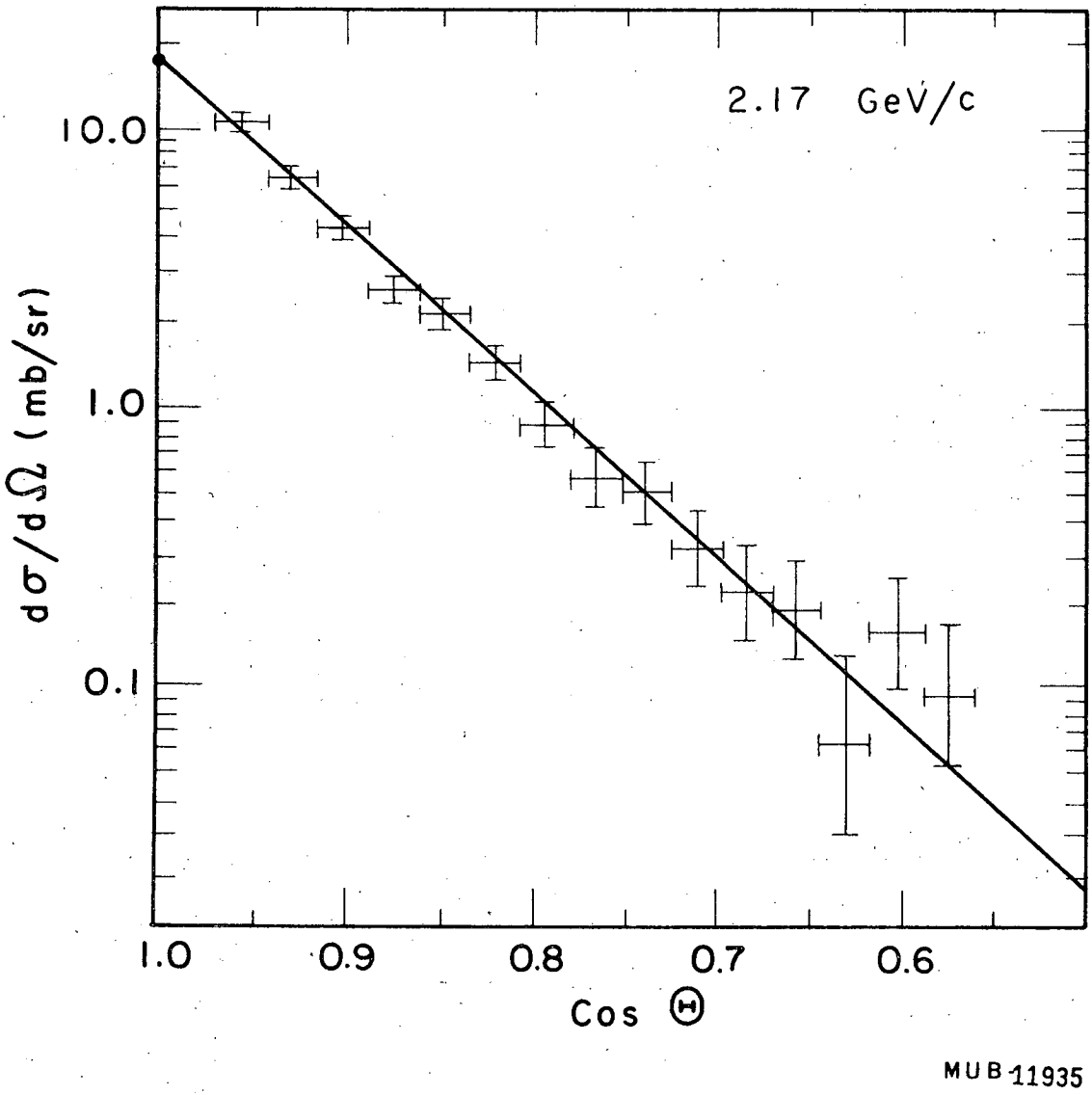

Fig. 18. $\pi^- p$ elastic scattering diffraction peak. ● shows the optical point at 2.17 GeV/c, $A = 8.20 \pm 0.30$ GeV^2.

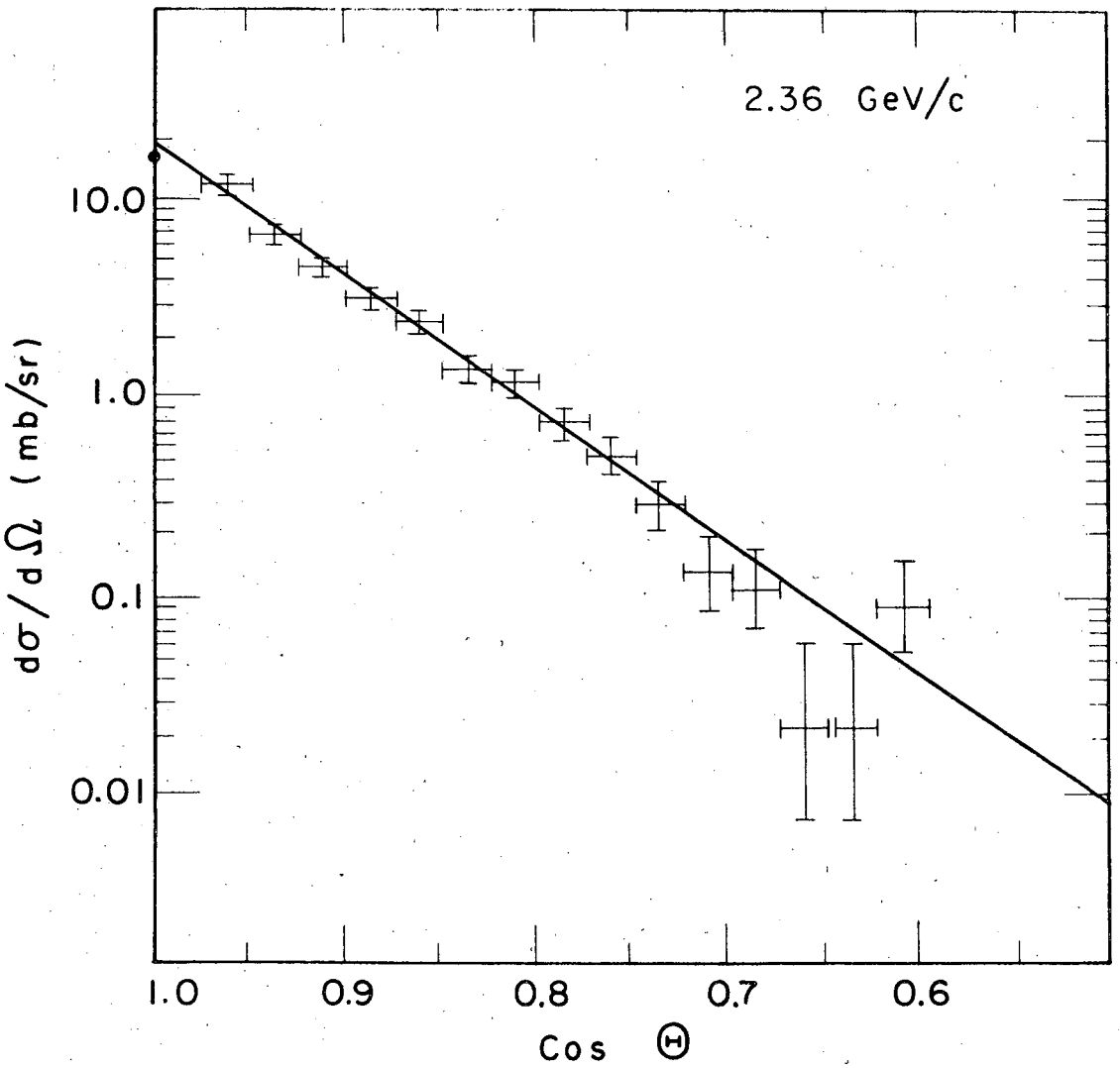

MUB-11939

Fig. 19. $\pi^- p$ elastic scattering diffraction peak. ● shows the optical point at 2.36 GeV/c, $A = 8.48 \pm 0.27$ GeV^2.

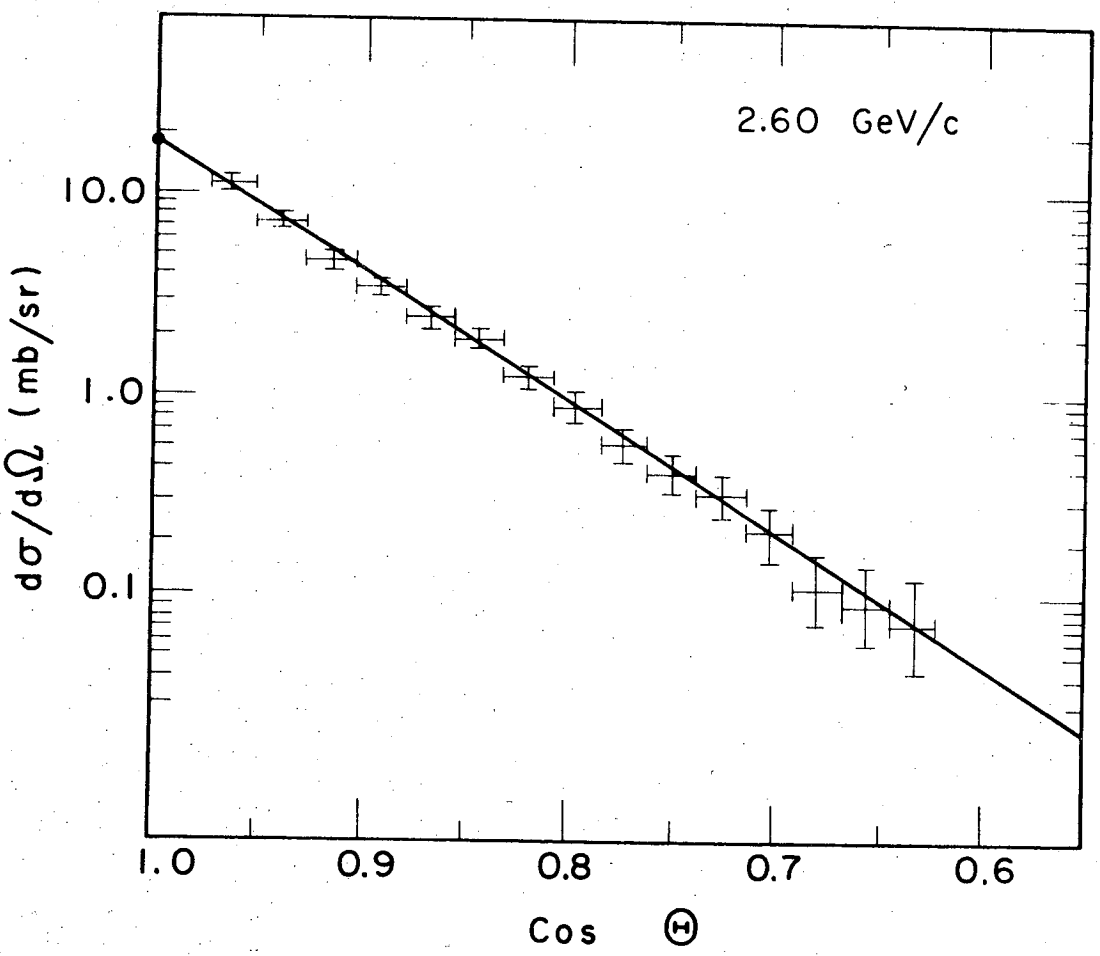

MUB-11940

Fig. 20. $\pi^- p$ elastic scattering diffraction peak. ● shows the optical point at 2.60 GeV/c, $A = 7.88 \pm 0.22$ GeV^2.

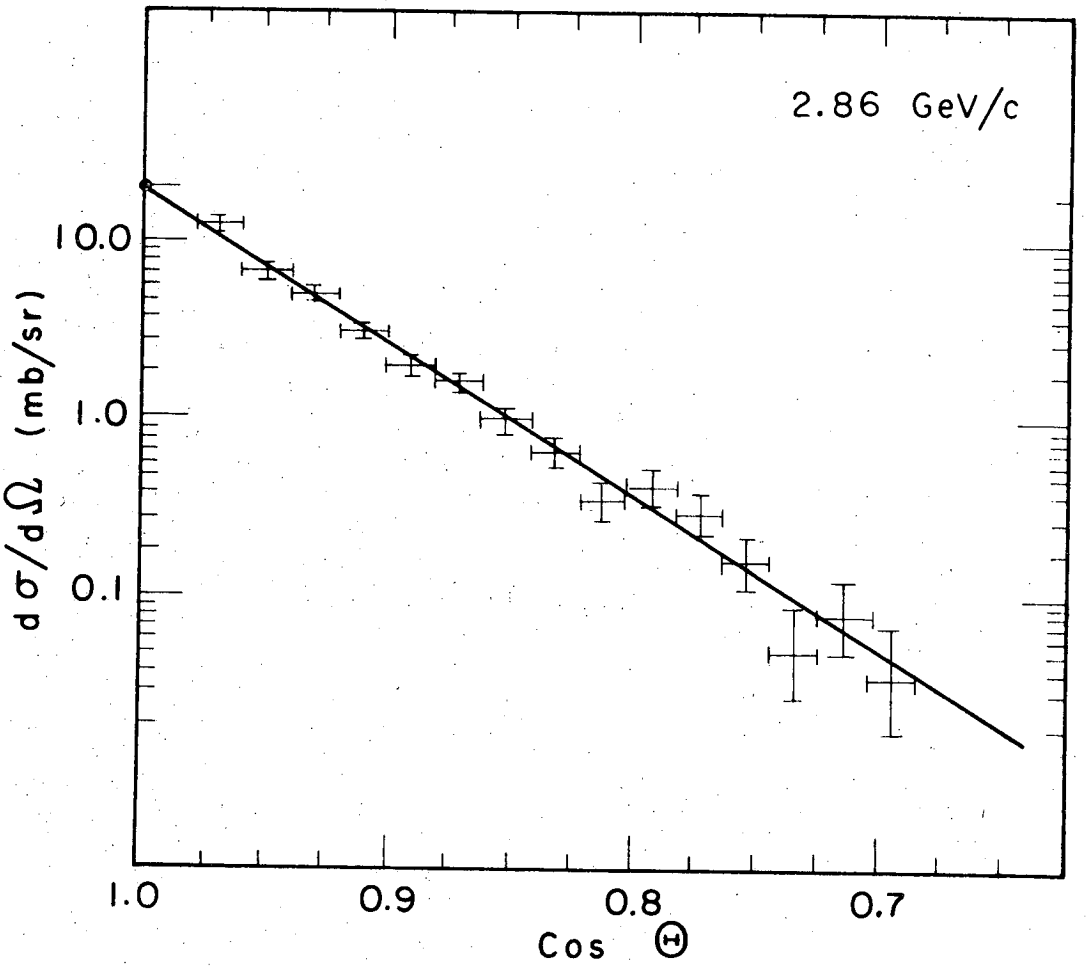

MUB-11937

Fig. 21. $\pi^- p$ elastic scattering diffraction peak. ● shows the optical point at 2.86 GeV/c, A =7-57± 0.23 GeV^2.

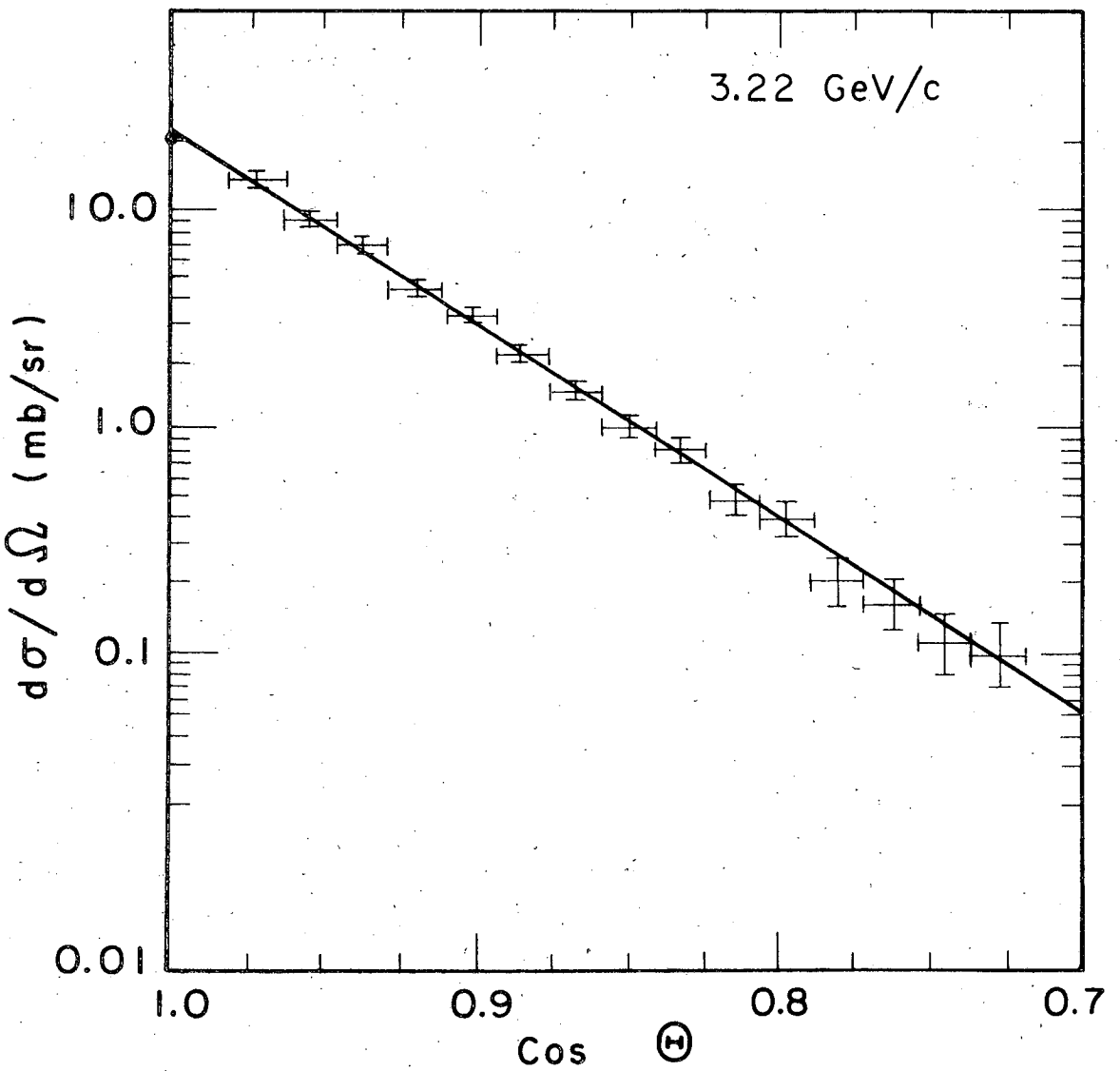

MUB-11938

Fig. 22. $\pi^- p$ elastic scattering diffraction peak. ● shows the optical point at 3.22 GeV/c, $A = 7.87 \pm 0.15$ GeV^2.

Table V. Compilation of A values for $\pi^- p$ elastic scattering.

Beam momentum (GeV/c)	A [(GeV)$^{-2}$]	Beam momentum (GeV/c)	A [(GeV)$^{-2}$]	Beam momentum (GeV/c)	A [(GeV)$^{-2}$]
1.34	7.5± 0.4	2.17	8.20± 0.30	3.63	7.95± 0.40
1.48	7.5± 0.4	2.27	8.88± 0.20	4.0	8.53± 0.49
1.59	7.2± 0.5	2.36	8.48± 0.27	4.13	8.4 ± 0.3
1.70	7.1± 0.5	2.50	8.16± 0.20	4.95	7.8 ± 0.3
1.70	7.06± 0.2	2.50	7.60± 0.12	6.0	7.68± 0.2
1.88	7.62± 0.2	2.60	7.88± 0.22	8.5	7.52± 0.09
2.01	7.94± 0.16	2.86	7.57± 0.23	10.0	7.50± 0.34
2.05	8.48± 0.33	3.0	7.65± 0.10	12.4	7.68± 0.09
2.07	8.25± 0.20	3.15	7.9 ± 0.3	18.4	7.53± 0.21
		3.22	7.87± 0.15		

(For other experiments see Fig. 23 and Ref. 27.)

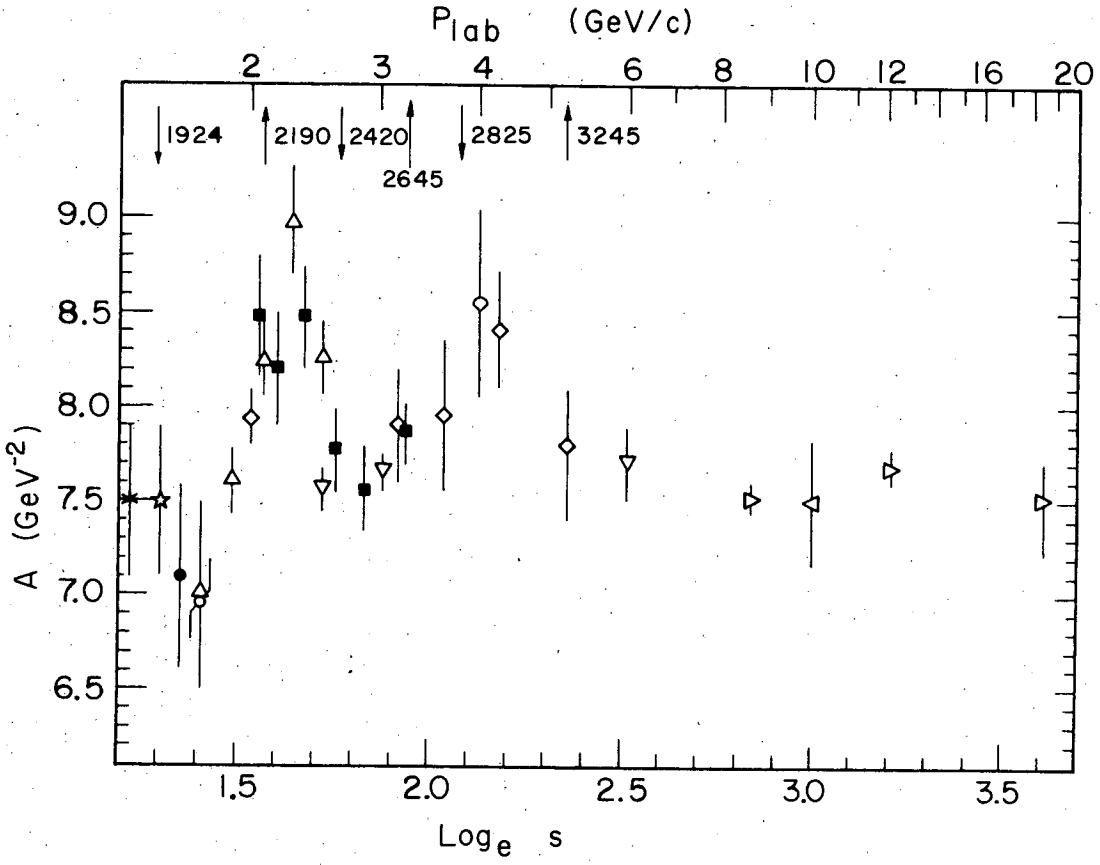

MUB 11553

Fig. 23. Variation of A, exponential slope in $\pi^- p$ elastic scattering, with c.m. energy. The position of known isospin 3/2 nucleon resonances is indicated by 1/2.

- □ This work: 2.05, 2.17, 2.36, 2.60, 2.86, 3.22 GeV/c.
- × Bertanza et al., 1.34 GeV/c.
- ☆ Chretien et al., 1.48 GeV/c.
- ● S.O.B.B., 1.59, 2.75 GeV/c.
- ○ Allen et al., 1.70 GeV/c.
- △ Esterling et al., 1.70, 1.88, 2.07, 2.27, 2.50 GeV/c.
- ◇ Damouth et al., 2.01 GeV/c;
  Perl et al., 3.15, 4.13, 4.95 GeV/c;
  Perl, Lee, and Marquit, 3.63 GeV/c.
- ▽ Coffin et al., 2.50, 3.00, 4.00, 6.00 GeV/c.
- Bondar et al., 4.0 GeV/c.
- ▷ Harting et al., 8.5, 12.4, 18.4 GeV/c.
- ◁ Brandt et al., 10.0 GeV/c.

Two physical theories lead naturally to the exponential behavior of the forward peak, Regge poles[26] and a version of the optical model. We briefly relate the salient features of each theory and attempt to derive the implications of the behavior of A.

The contribution from one Regge trajectory to the scattering amplitude is given by

$$f(s,t) \approx \xi(t)\,\beta(t)\,[\cos\Theta_t]^{\alpha(t)}\,, \tag{8}$$

where $\alpha(t)$ is the Regge pole trajectory function,

$\xi(t)$ is the signature function, and

$\beta(t)$ is the residue or coupling function;

$\xi(t)$ determines the real and imaginary parts of $f(s,t)$. If the signature of the trajectory is defined as $\tau = \pm 1$, which is equal to $(-1)^J$, in the boson case, for those real particles lying on the trajectory, then

$$\xi(t) = \frac{1 + \tau e^{-i\pi\alpha(t)}}{\sin \pi\alpha(t)}\,. \tag{9}$$

The Θ_t is the scattering angle in the c.m. for the crossed process i.e., t-channel scattering; $\cos\Theta_t$ is a linear function of s. For small values of t we may approximate

$$f(s,t) \approx \xi(t)\,\beta(t)\,[s/s_0]^{\alpha(t)}\,. \tag{10}$$

With a linear behavior for $\alpha(t)$,

$$\text{i.e.,}\ \alpha(t) = \alpha(0) + \alpha' t, \tag{11}$$

and an exponential behavior for $\beta(t)$,

$$\text{i.e.,}\ \beta(t) = \beta(0)\,e^{\eta t}\,, \tag{12}$$

we obtain a contribution to the differential cross section,

$$\frac{d\sigma}{dt} = \left[\frac{d\sigma}{dt}\right]_{t=0} e^{2\eta t}\left[s/s_0\right]^{2\alpha' t}\,. \tag{13}$$

We draw the conclusion that diffraction scattering can be described by one trajectory, the Pomeranchuk P with $\alpha P(0) = 1$ and that

$$A = 2\eta P + 2\alpha' P\,[\log s - \log s_0]\,. \tag{14}$$

From Fig. 23,[27] the evidence at high energies for $\pi^- p$ scattering is that the slope of the trajectory $\alpha' p$ is small. (This puts the onus for the peak shrinkage in pp scattering on the residue factor.) However, the Regge argument seems to have little relevance to the anomalous variation of A at our energies.

In the optical model, if we assume some smooth variation with l of a_l in Eq. (6), we can write the scattering amplitude as an integral over impact parameter b,

$$f = iq \int_b^\infty J_0 \left(2q\, b \sin\tfrac{1}{2}\Theta\right) [a(b) - 1]\, b db. \tag{15}$$

If we assume a Gaussian behavior for $a(b) - 1 = e^{-(b^2/\langle b^2 \rangle)}$ (16)

$$\frac{d\sigma}{dt} = \left[\frac{d\sigma}{dt}\right]_{t=0} e^{\frac{1}{2}\langle b^2 \rangle t}, \tag{17}$$

and we identify $A = 1/2 \langle b^2 \rangle$, as a measure of the mean-square radius of the $\pi^- p$ interaction.

We may thus interpret the variation in A as saying something about the scattering in a high orbital angular momentum state (l = 4 or 5). When A is small, the radius of interaction has decreased and there is little scattering in the relevant l state, i.e., δp is small. Correspondingly, when A is large, δ_l is large. This behavior is typical of that expected from an interference between a real background and a resonant amplitude.[28]

In fact, the variation of A has a distinct resemblance to the behavior of the total cross section in this region.[14] In neither case can we distinguish the fact that there are, in reality, two (possibly three) resonant amplitudes between 2.0 and 2.5 GeV/c of presumably opposite parities. It is tempting to try to correlate both the forward differential cross section and α with the behavior of A. However, due to possible errors in normalization as well as statistical errors, the variation of α is not significant. The variation in $|f(0)|^2$ reflects the increase in the total cross section. An argument by Lynch[29] suggests that a highly inelastic resonance i.e., $x < 0.5$-- will increase the cross section and

therefore $[f(0)]^2$ as the first power of x, but will increase the elastic cross section only quadratically in x and the effect will be to sharpen the diffraction peak at the resonance. He notices an effect similar to ours in K^-p elastic scattering from 1.43 to 2.45 GeV/c presumably associated with the $f_{7/2}$ resonance at 2040 MeV and the $g_{7/2}$ resonance at 2140 MeV.[30] A peak sharpening is observed in π^+p elastic scattering in the region of the $\Delta(1920)$. It will be interesting to see if there is a similar effect in the region of the $\Delta(2460)$.

Lastly, in Table VI, we list the parameters C, γ, (b), and $L = \langle b \rangle / q$ for elastic scattering. These are of interest in connection with the theory of the absorption model of peripheral interaction, which is dealt with in Section IV, where we define C and γ.

The second maximum

The presence of a secondary maximum is a prominent feature of π^-p elastic scattering from about 1 GeV/c.[16] Simmons attempted to explain the second peak as a second diffraction maximum.[19] His simple formula, which is just Eq. (6)

with $a_l = a$ for $l \leq L$

and $a_l = 1$ for $l > L$,

fails to reproduce either the main or the secondary peak. Moreover, since the peak persists over such a wide beam energy interval and occurs roughly at the same place in momentum transfer squared, we reject this explanation.

Coffin et al.[27g] showed that the secondary maximum decreased with increasing beam momentum. In Fig. 24 with some of the curves from this work, we see how data at four of our energies show the same general behavior. Somewhat arbitrarily, we have defined the secondary region to lie between 40 and 110 $m_{\pi^0}^2$. In $\cos\Theta$, this corresponds to, for example, the interval 0.3 to -1.0 at 1.59 GeV/c, 0.5 to -0.3 at 2.05 GeV/c, 0.7 to +0.35 at 3.22 GeV/c and 0.73 to 0.4 at 4 GeV/c. The numbers of events and values of $\sigma^{II} = \int_{-2.0}^{-0.72} \frac{d\sigma}{dt}\, dt$, the cross section, are shown in Table VII.

In Figure 25, we have plotted σ^{II} against s on a log-log scale for our six points. We observe that our data and those of other published

Table VI. Absorption parameters for π-p elastic scattering.

Beam momentum (GeV/c)	σ_T (mb)	$C = \frac{\sigma_T}{4\pi\omega}$	q (MeV/c)	$\gamma = \frac{1}{2Aq^2}$	$L = \sqrt{\frac{2A}{q^2}}$
2.05	35.0	0.84	882.0	0.076	3.6
2.17	35.5	0.87	912.3	0.073	3.7
2.36	34.2	0.83	958.5	0.064	4.0
2.60	33.3	0.87	1013.0	0.062	4.0
2.86	32.7	0.89	1071.4	0.058	4.2
3.22	32.3	0.84	1145.1	0.048	4.6

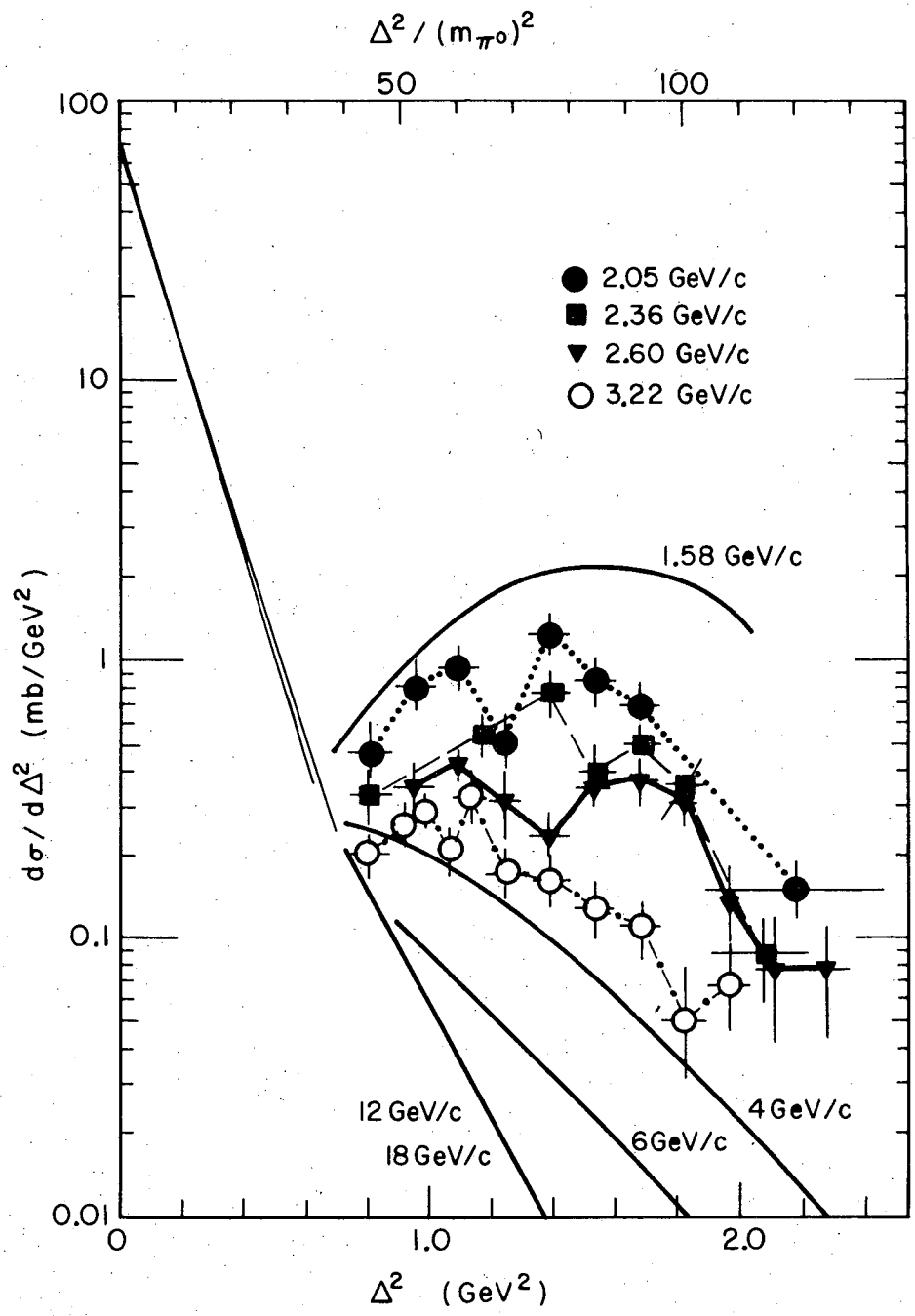

MUB-11556

Fig. 24. Behavior of secondary maximum in $\pi^- p$ elastic scattering with increasing beam momentum. Curves are taken from Coffin et al.

Table VII. $\pi^- p$ elastic scattering cross sections away from diffraction peak.

P_{lab}	Region II Secondary Peak Δ^2 40 to 110 $m_{\pi^0}^2$		Region III $\cos\Theta$ -0.3 to -0.68		Region IV $\cos\Theta$ -0.68 to -0.88		Region V $\cos\Theta$ -0.88 to -1.0	
(GeV/c)	Number of events	σ^{II} mb	Number of events	σ^{III} μb	Number of events	σ^{IV} μb	Number of events	$\frac{d\sigma^V}{d\Omega}$ μb/sr
2.05	143	0.90± 0.08	12	76± 21	1	6± 6	7	58± 22
2.17	150	0.84± 0.07	13	73± 20	1	6± 6	7	52± 17
2.36	141	0.55± 0.05	3	12± 7	4	15± 8	6	32± 13
2.60	139	0.40± 0.03	6	18± 7	7	20± 5	10	38± 12
2.86	75	0.26± 0.03	3	10± 6	2	7± 5	3	15± 8
3.22	168	0.20± 0.02	10	11± 3	10	11± 3	3	5± 3

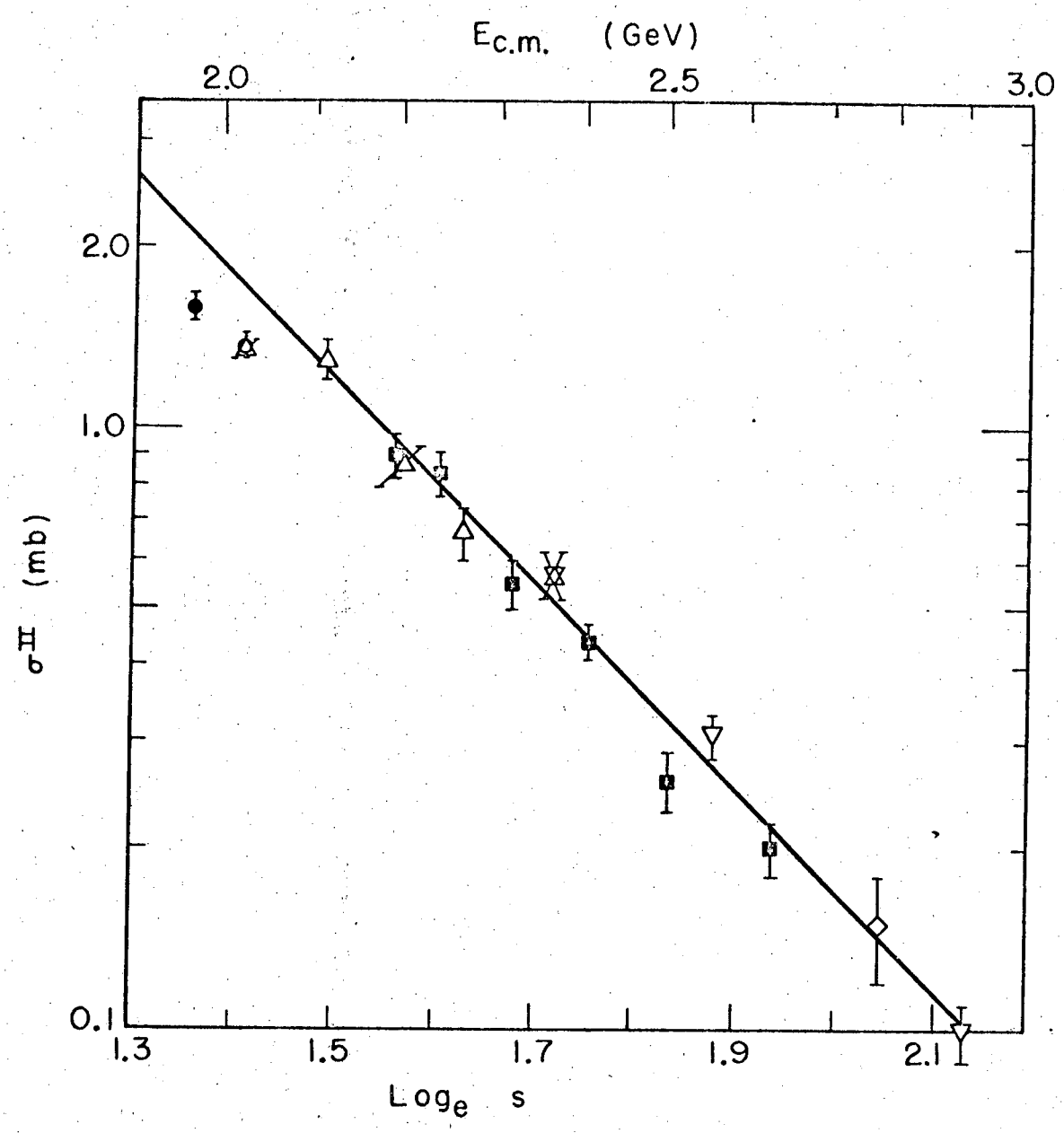

MUB-11555

Fig. 25. Variation of $\sigma^{II} = \int_{-2.0}^{-0.7} dt \left[\frac{d\sigma}{dt}\right]$ as a function of s. Straight line corresponds to the relation $\sigma^{II} \propto s^{-3.95}$. See Fig. 23 for key to symbols.

work in this region above 1.8 GeV/c fall (within errors) on a straight line. A least-squares fit corresponds to the relation $\sigma^{II} \propto s^{-3.95 \pm 0.3}$.

In searching for a model that may give rise to this behavior, we remark that although s-channel effects are important, it is hard to see how they could generate this fast energy variation. One advantage of integrating over a t interval is that we smooth out the effect of any ripples in the differential cross section associated with resonances.

In Regge theory, the contribution to the differential cross section from one pole according to Eq. (10) is of the form

$$\frac{d\sigma}{dt} \propto \left(\frac{s}{s_0}\right)^{2\alpha(t)-2} .$$

This suggests that in this particular area of s-t space we are observing the effect of one trajectory. A similar energy-dependent shrinkage, which has been explained by the exchange of the ρ trajectory, has been discussed by Sonderegger et al.[31] Exchange of nucleon and isobar trajectories in the u channel can account for the backward $\pi^{\pm}p$ scattering observed by Brody et al.[32]

Three trajectories dominate the t channel in πN scattering,[33] the Pomeranchuk P, the second vacuum P', and the ρ. We believe that there are grounds for suggesting that the second maximum is the contribution of the P'.[34] Confirmation of this can be possible only with more experimental and theoretical work.

Measurements of the polarization of the proton by Suwa et al.[35] and Chamberlain et al.[36] indicate a large negative polarization in the region of the second maximum, whose behavior is strongly energy-dependent. This suggests that a spin-flip amplitude is responsible for the peak.

Extrapolating the diffraction peak to $t \approx -1.35$ gives rise to a small contribution to the cross section. Since the slope of the P trajectory is small, we would expect to have the same energy variation as for the slope of the diffraction peak, if the P caused the second maximum.

Since the slope $\alpha'_\rho \approx 0.85$ and the intercept $\alpha_\rho(0) \approx 0.55$ of the ρ trajectory are thought to be close to those for the P', we cannot use the energy variation to eliminate the ρ. However, although we expect the ρ to have an important effect on the polarization, its contribution to the cross section is small. The second maximum in charge exchange is an order of magnitude smaller than that for $\pi^- p$ elastic scattering, and is in accordance with its being the difference between $\pi^- p$ and $\pi^+ p$ elastic scattering, which also shows a second maximum with an energy dependence similar to the $\pi^- p$ case.[37] This would seem to rule out the possibility of the peak's coming from the interference between the ρ and another trajectory, since the amplitudes have opposite signs in $\pi^- p$ and $\pi^+ p$ scattering.

Although it is possible that the effect is due to an interference between two amplitudes--e.g., the P and the P'--if we assume that the shrinkage is due to the P' alone, we can estimate the slope of P' trajectory needed to explain the energy dependence.

Assuming that $\alpha_{P'}(0) \approx 0.7$, we have

$$\alpha_{P'}(-1.35) \approx -1.0 \pm 0.15$$

$$\approx \alpha_{P'}(0) - 1.35\alpha'_{P'},$$

$$\alpha'_{P'} \approx 1.25 \pm 0.15.$$

This is a much faster variation than that needed by Rarita and Phillips[32, 34, 38]. The trajectory will go through zero at $-t \approx 0.56\ \mathrm{GeV}^2$; $t \approx 1.05\ \mathrm{GeV}^2$ corresponds to a particle with spin 2. There is no reason, however, why the trajectory should not flatten out as t increases.

Backward region

The backward hemisphere should be a good place to isolate the effect of any s-channel resonances. Near 180° we might observe the Regge effects of the u channel. We tried to illustrate these effects by choosing intervals in $\cos\Theta$ in which the data seemed to accumulate. In Table VII we have listed the cross sections for $\cos\Theta$ intervals -0.3 to -0.68, -0.68 to -0.88, and -0.88 to -1.0. Although, in contrast to the previous region, there seems to be a nonsmooth variation of the cross section with energy (see Fig. 26), our statistics are too meagre for us to say anything definite.

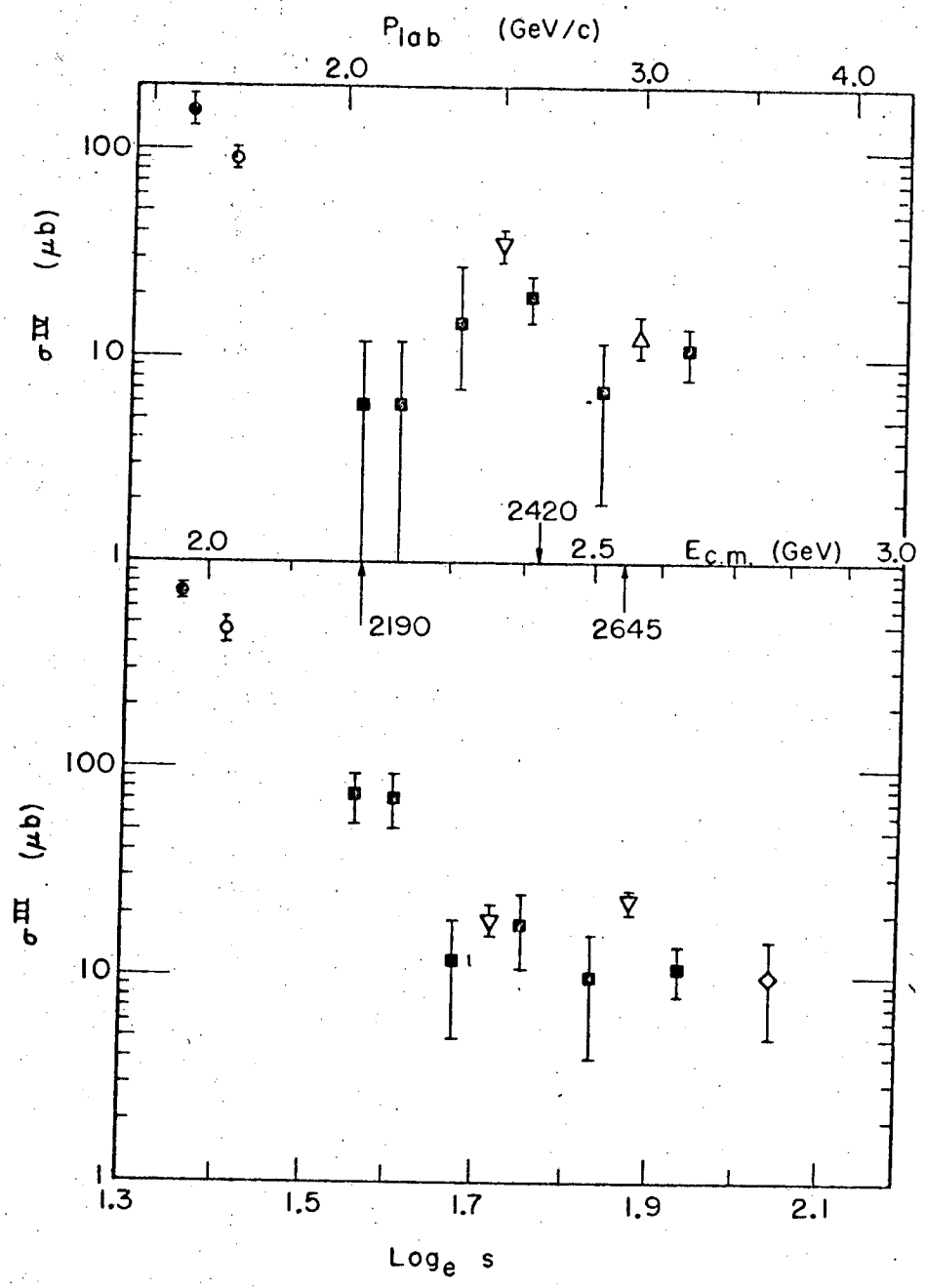

MUB-11554

Fig. 26. Variation of σ^{III} and σ^{IV}, the cross sections, between $\cos\Theta = -0.3$ to -0.68 and -0.68 to -0.88 respectively. Log-log scale is used to permit direct comparison with Fig. 25.

Total elastic cross section

Finally, in Fig. 27, we show how the total elastic cross section, like other $\pi^- p$ two-body reactions in this energy range,[39] falls monotonically. This is understandable in view of the competing many-body channels which become available to the $\pi^- p$ system as the beam energy increases. Above 7 GeV/c the elastic cross section falls slowly from 5 mb to about 4 mb at 20 GeV/c.[27i, 27j, 40]

Summary

In conclusion, the study of elastic scattering shows that both s- and t-channel effects are important. Resonances show their effect on the slope of the diffraction peak. We feel that a possible explanation for the behavior of the second maximum lies with the spin-flip amplitude for the P' Regge trajectory.

C. Three-Body States

In this section we give a description of the experimental results from Reactions (1) and (2),

$$\pi^- p \rightarrow n\pi^+\pi^-, \tag{1}$$

$$\pi^- p \rightarrow p\pi^0\pi^-. \tag{2}$$

Production scatter plots

In Figs. 28 and 29 we show Dalitz plots for both reactions at each of our six energies. The density of these plots is not constant, indicating strong final-state interactions, the most prominent feature being the band associated with the ρ meson at $m^2_{\pi\pi} \approx 0.56$ BeV^2. The density along the band itself is not constant and the question immediately arises whether the concentration of events, particularly at low $n\pi^+$ or $p\pi^0$ masses, is a property of the ρ-decay angular distribution or is due to the presence of πN resonances. This is a difficult question to settle satisfactorily. For the moment, we shall point out that when we add all six momenta together in Fig. 30, it is apparent that there is structure corresponding to bands in the πN systems. However, these are less intense than the $\pi\pi$ band. At the three higher energies, we see indications of the f^0 in the $\pi^+\pi^-$ system. In the combined data in Fig. 30, its presence is quite evident.

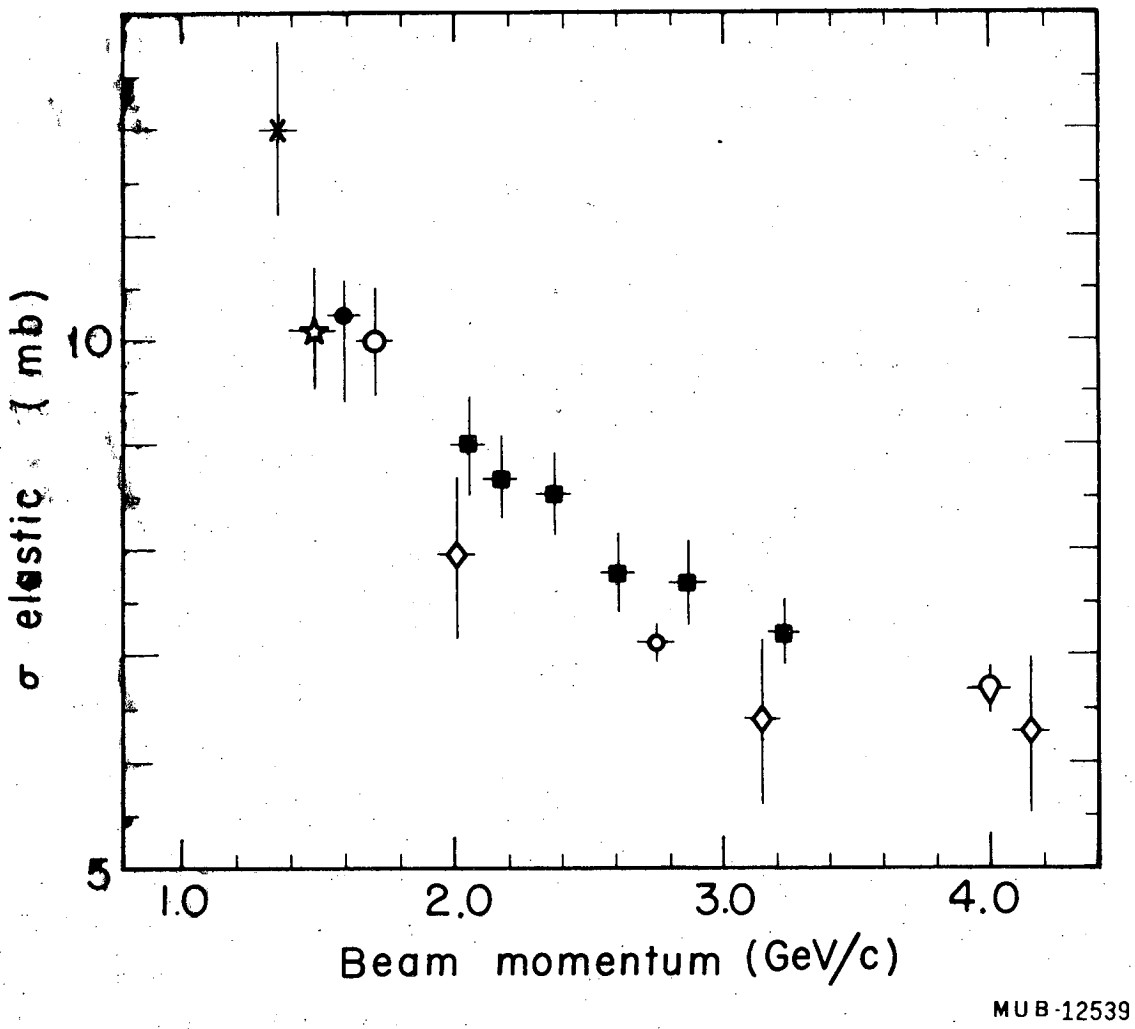

Fig. 27. Total elastic scattering cross section as a function of beam momentum. See Fig. 23 for key to symbols.

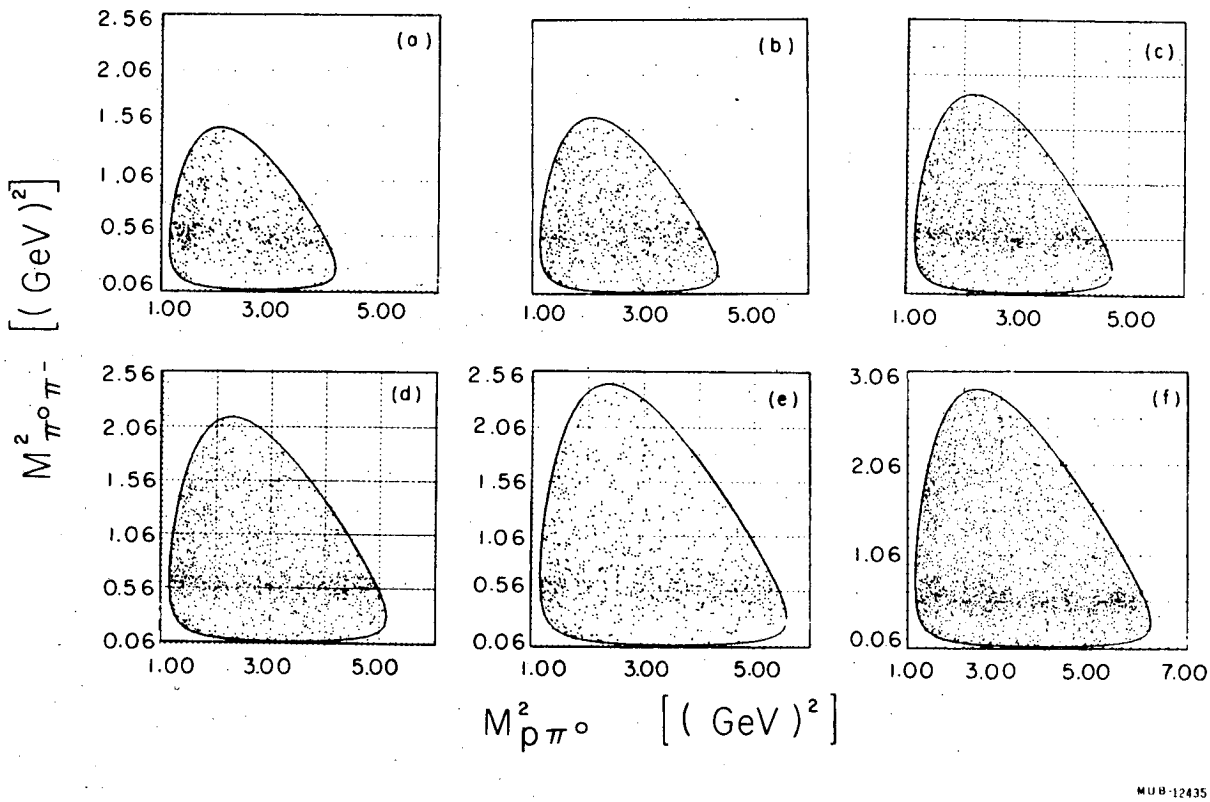

Fig. 28. Dalitz plots for the reaction $\pi^- p \rightarrow p\pi^0\pi^-$.

(a) 2.05 GeV/c
(b) 2.17 GeV/c
(c) 2.36 GeV/c
(d) 2.60 GeV/c
(e) 2.86 GeV/c
(f) 3.22 GeV/c

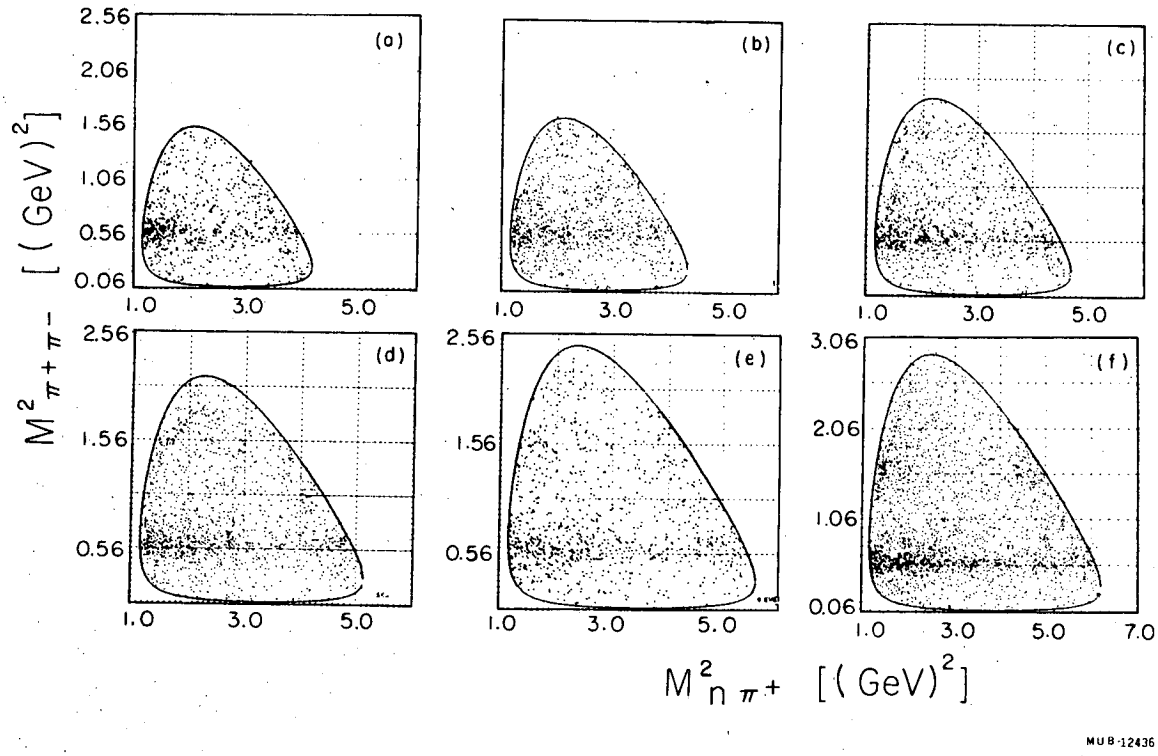

Fig. 29. Dalitz plots for the reaction $\pi^- p \rightarrow n\pi^+\pi^-$.

(a) 2.05 GeV/c
(b) 2.17 GeV/c
(c) 2.36 GeV/c
(d) 2.60 GeV/c
(e) 2.86 GeV/c
(f) 3.22 GeV/c

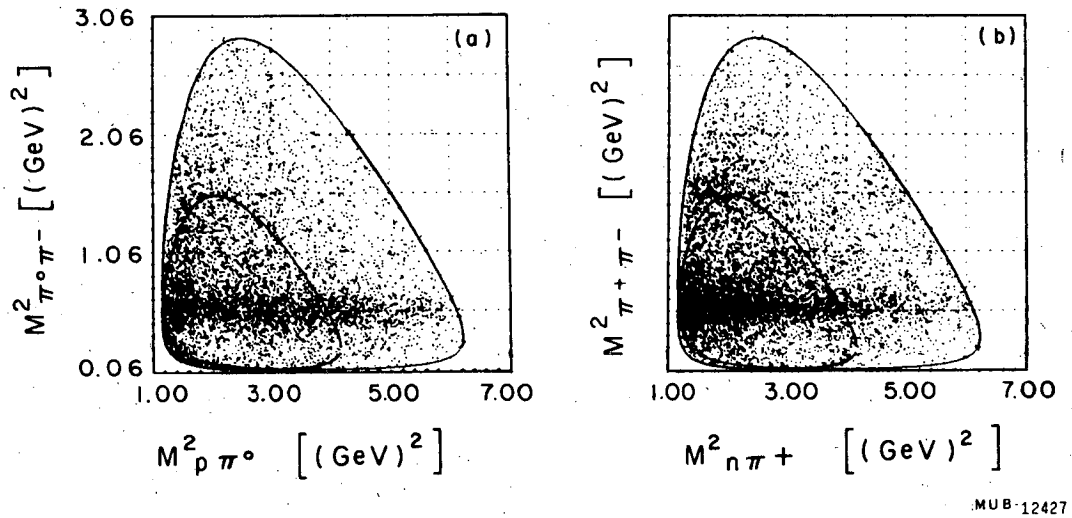

Fig. 30. Dalitz plots for all beam momenta.

(a) $\pi^- p \rightarrow p\pi^0\pi^-$

(b) $\pi^- p \rightarrow n\pi^+\pi^-$

Since the Dalitz plot suppresses all production-angle information, to reveal this we plot the data, in two dimensions, on a Chew-Low plot. Generally, this presupposes the importance of some particular Feynman exchange diagram. In our case, we plot the $\pi\pi$ effective mass against the momentum transfer squared between the initial and final nucleons. The pertinent diagram is that of one-pion exchange, OPE, Fig. B-1. Figures 31 and 32 show not only that the events cluster about the ρ mass, but also that they occur predominantly with $\Delta^2 \leq 20\ m_{\pi^0}^2$. Further, Δ^2 values less than $20\ m_{\pi^0}^2$ are in the physical region only if the beam momentum is greater than 2.36 GeV/c. Since it is apparent that the f^0, like the ρ, is made at low Δ^2 (see Fig. 64), it is obvious that only at energies above 3 GeV/c will the kinematics favor its production. Figure 31d suggests that in ρ^- production at 2.60 GeV/c there is a secondary clumping of events at about $50\ m_{\pi^0}^2$. The combined data at 2.75 and 3.0 GeV/c presented by Hagopian et al.[41] show a similar effect, and remark that a calculation by Jackson, based on a model in which ω exchange interferes with π^0 exchange, does not explain their effect. However, at 2.86 and 3.22 GeV/c in our data the effect is no longer seen, (Figs. 31e and 31f). (At 2.86 GeV/c, we show the effect of the contaminating elastic scatterings at low $\pi\pi$ mass. These have been removed in the other plots.) The combined energies show a further feature, in Fig. 33, that there is a general concentration of events along the lower edge of the plot. This allows us to refer with some justification to OPE outside the ρ region.

Δ^2 distributions

In Figs 34-39, we plot the Δ^2 distribution for all events and for the ρ region; we define the latter as $m^2_{\pi\pi}$ 0.41 to 0.76 $(\text{GeV})^2$. We have incorporated a crude test of the OPE energy dependence suggested by Alfred Goldhaber.[42] We multiply $d\sigma/d\Delta^2$ by the square of P_{lab}, the beam momentum--and the resulting quantity should be energy-independent. For ρ^- production, the height of the distribution (uncorrected for short proton tracks) varies between 28 and 38 mb. For ρ^0 production, the variation is greater, from 40 to 65 mb. We leave fitting the Δ^2 distribution to some model until the next section.

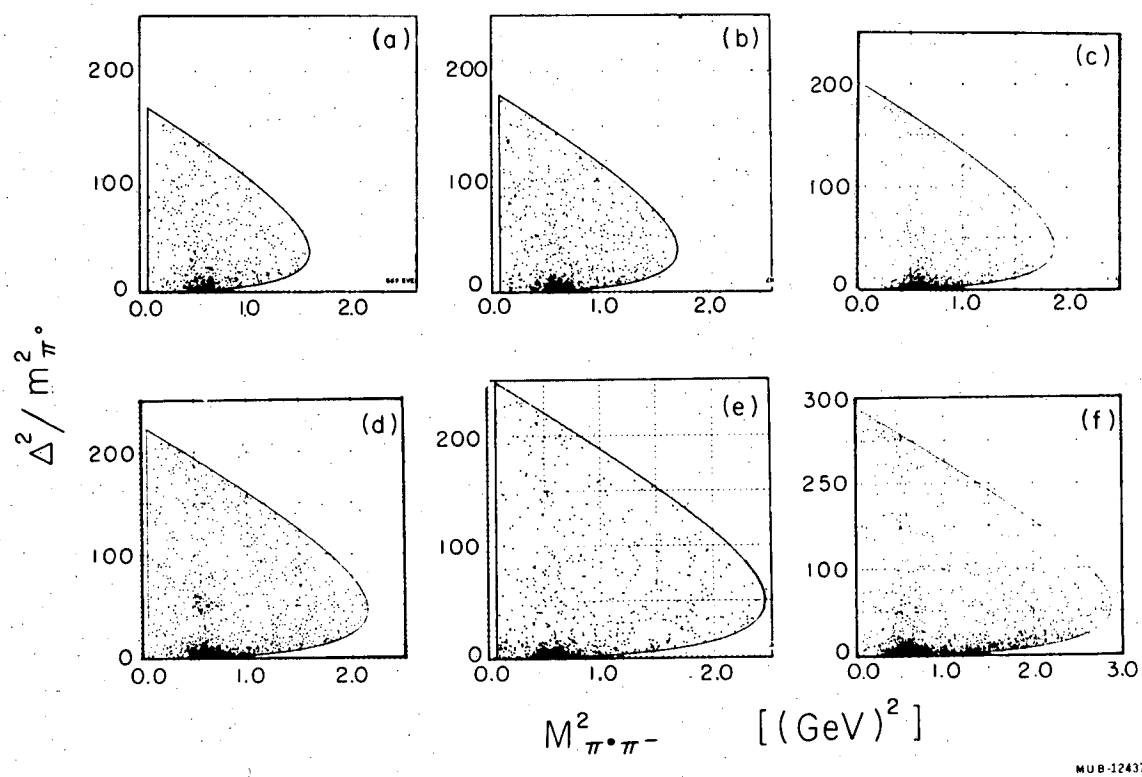

Fig. 31. Chew-Low plots for the reaction $\pi^- p \rightarrow p\pi^0 \pi^-$.

(a) 2.05 GeV/c
(b) 2.17 GeV/c
(c) 2.36 GeV/c
(d) 2.60 GeV/c
(e) 2.86 GeV/c
(f) 3.22 GeV/c

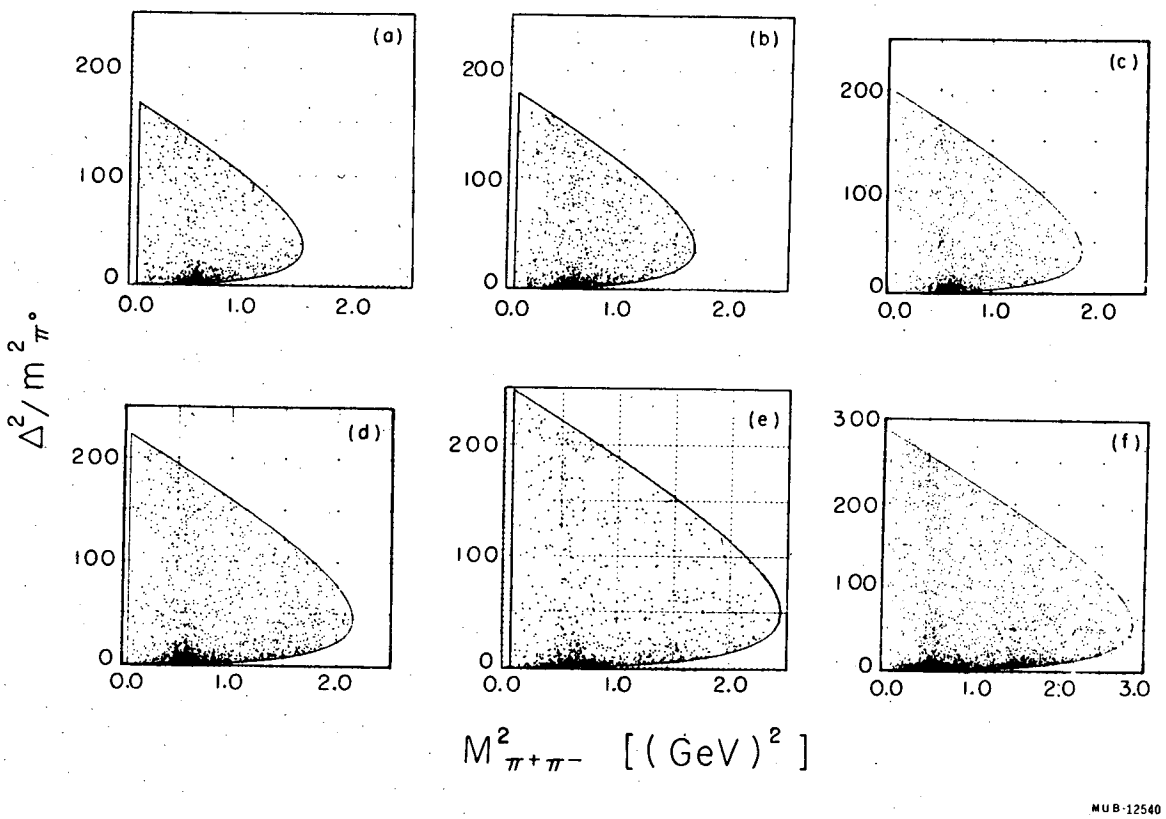

Fig. 32. Chew-Low plots for the reaction $\pi^- p \rightarrow n\pi^+\pi^-$.

(a) 2.05 GeV/c
(b) 2.17 GeV/c
(c) 2.36 GeV/c
(d) 2.60 GeV/c
(e) 2.86 GeV/c
(f) 3.22 GeV/c

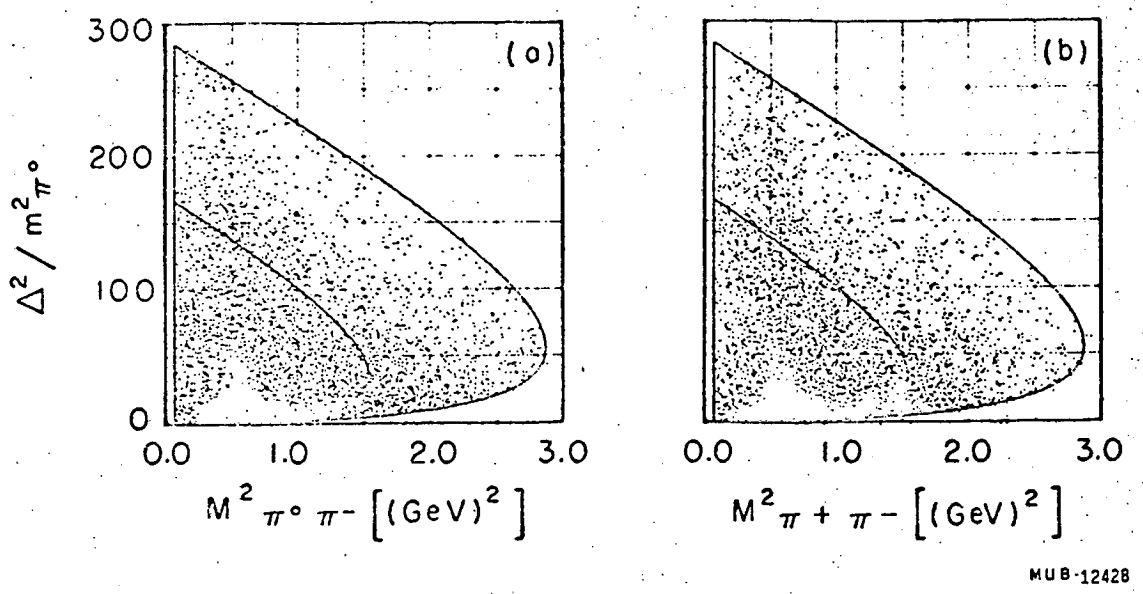

Fig. 33. Chew-plots for all beam momenta.

(a) $\pi^- p \rightarrow p\pi^0 \pi^-$

(b) $\pi^- p \rightarrow n\pi^+ \pi^-$

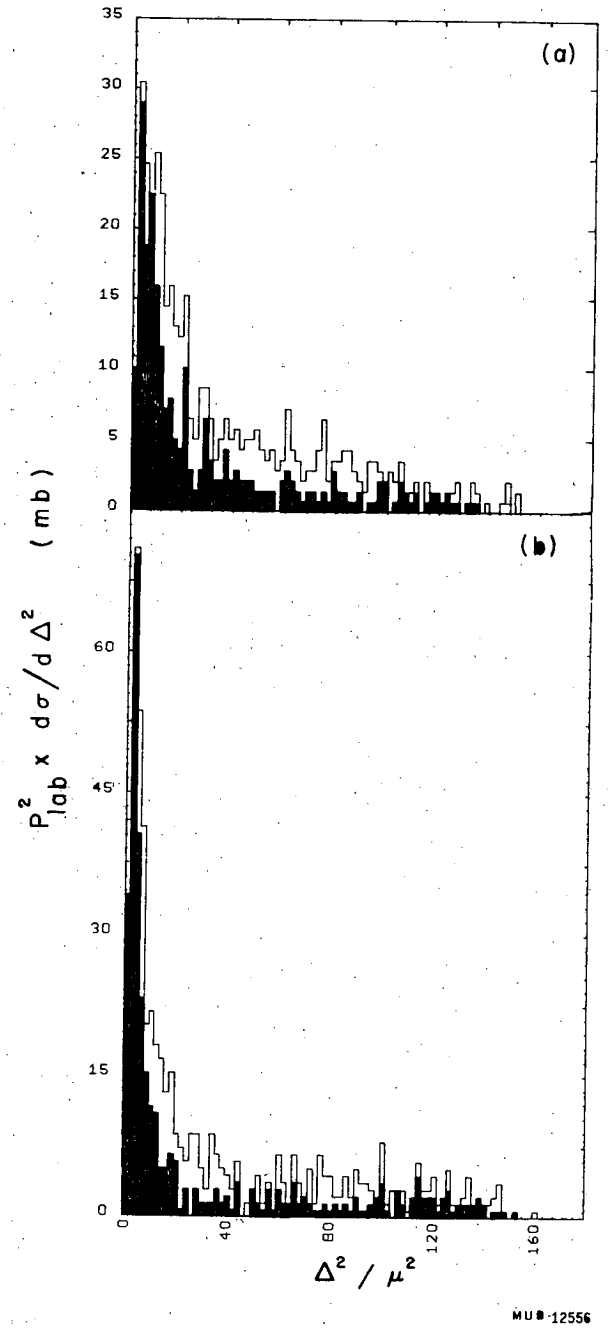

Fig. 34. 2.05-GeV/c Δ^2 distributions. Events shown as solid are in the ρ region, $M^2_{\pi\pi}$ 0.41 to 0.76 $(GeV)^2$.

(a) $\pi^- p \rightarrow p\pi^0 \pi^-$

(b) $\pi^- p \rightarrow n\pi^+ \pi^-$

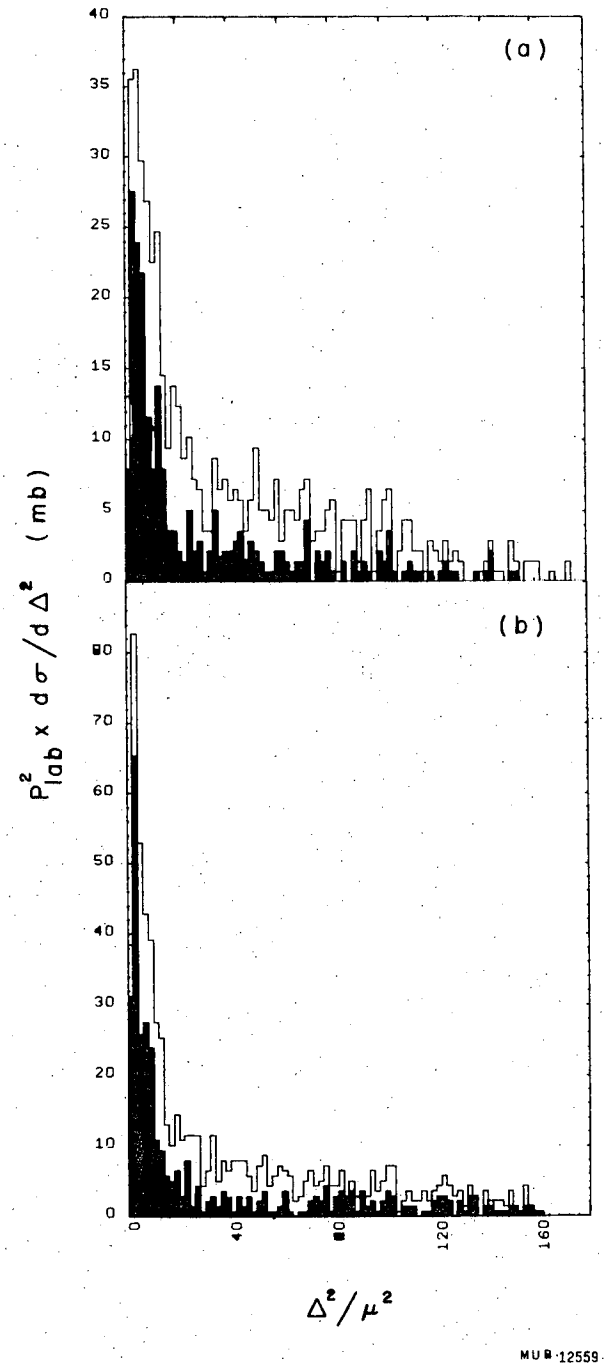

Fig. 35. 2.17-GeV/c Δ^2 distributions. Events shown as solid are in the ρ region, $M^2_{\pi\pi}$ 0.41 to 0.76 $(GeV)^2$.

(a) $\pi^- p \rightarrow p\pi^0\pi^-$

(b) $\pi^- p \rightarrow n\pi^+\pi^-$

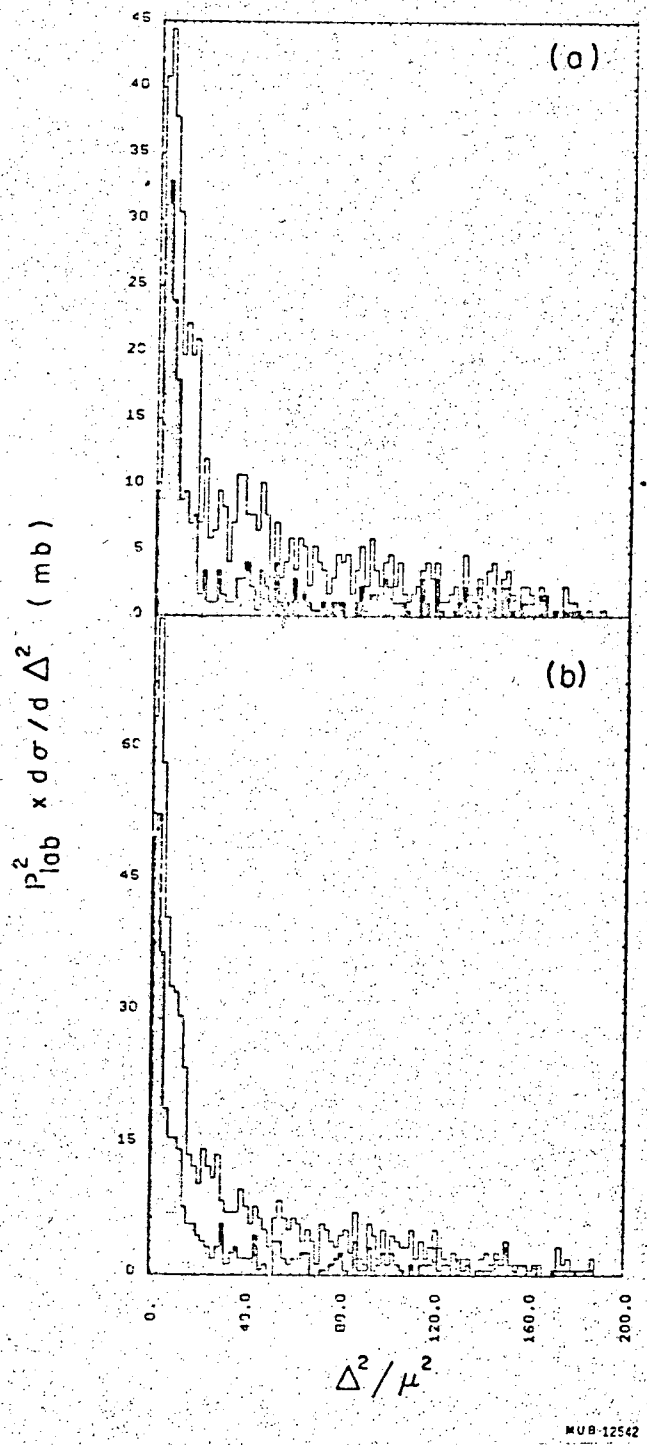

Fig. 36. 2.36-GeV/c Δ^2 distributions. Events shown as solid are in the ρ region, $M^2_{\pi\pi}$ 0.41 to 0.76 $(GeV)^2$.

(a) $\pi^- p \to p\pi^0\pi^-$

(b) $\pi^- p \to n\pi^+\pi^-$

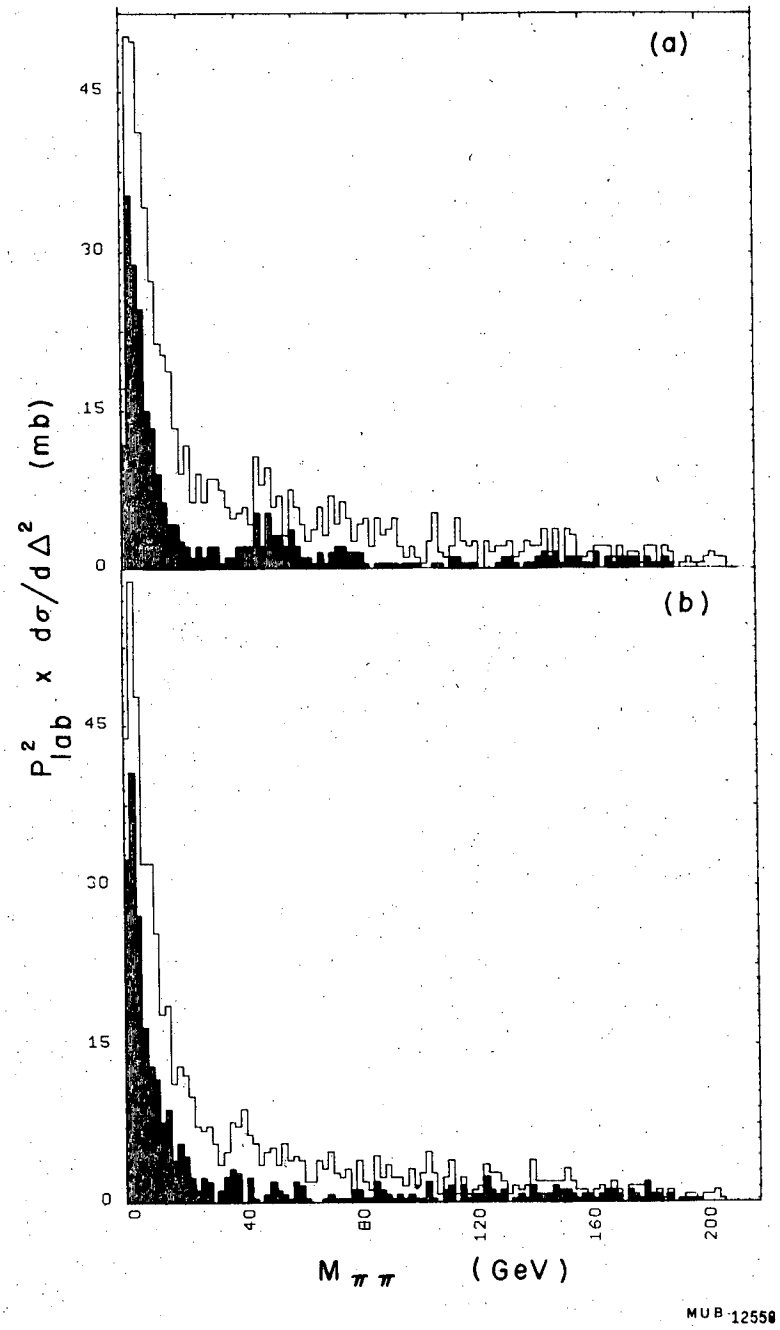

Fig. 37. 2.60-GeV/c Δ^2 distributions. Events shown as solid are in the ρ region, $M^2_{\pi\pi}$ 0.41 to 0.76 $(GeV)^2$.

(a) $\pi^- p \rightarrow p\pi^0\pi^-$

(b) $\pi^- p \rightarrow n\pi^+\pi^-$

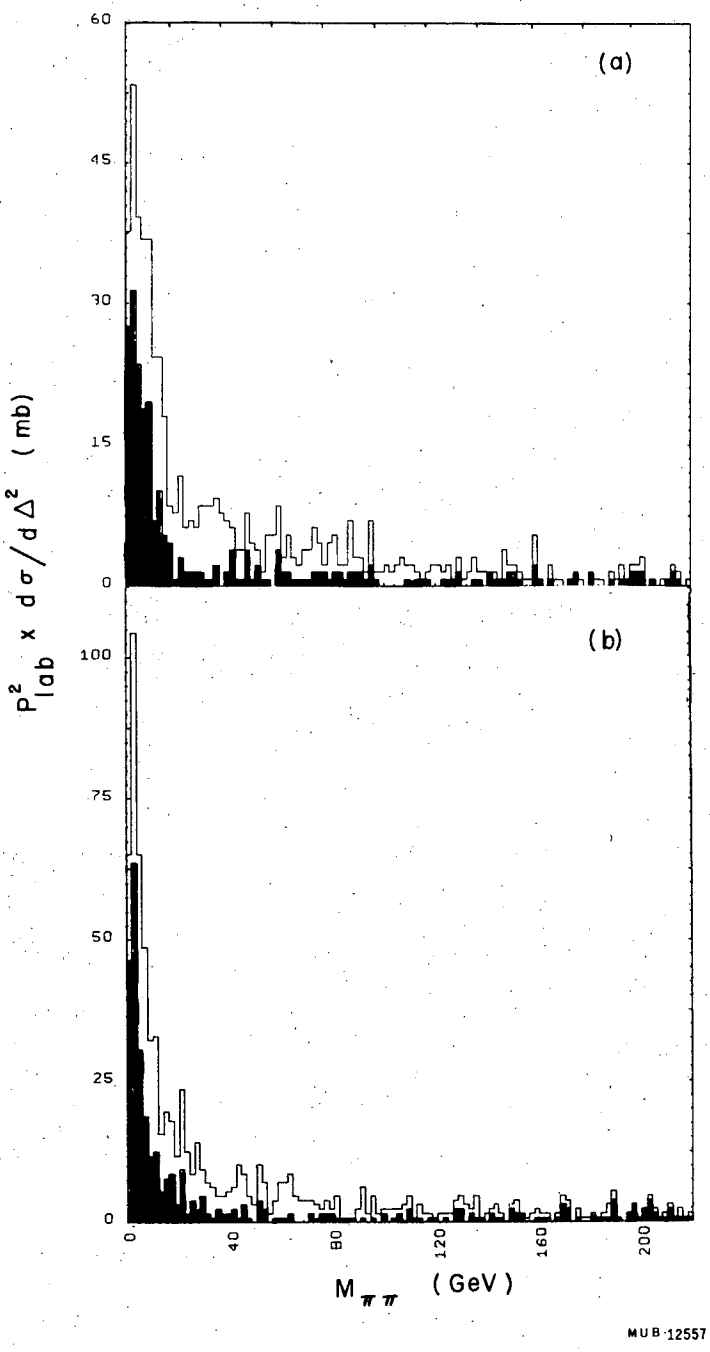

Fig. 38. 2.86-GeV/c Δ^2 distributions. Events shown as solid are in the ρ region, $M^2_{\pi\pi}$ 0.41 to 0.76 $(\text{GeV})^2$.

(a) $\pi^- p \rightarrow p\pi^0\pi^-$

(b) $\pi^- p \rightarrow n\pi^+\pi^-$

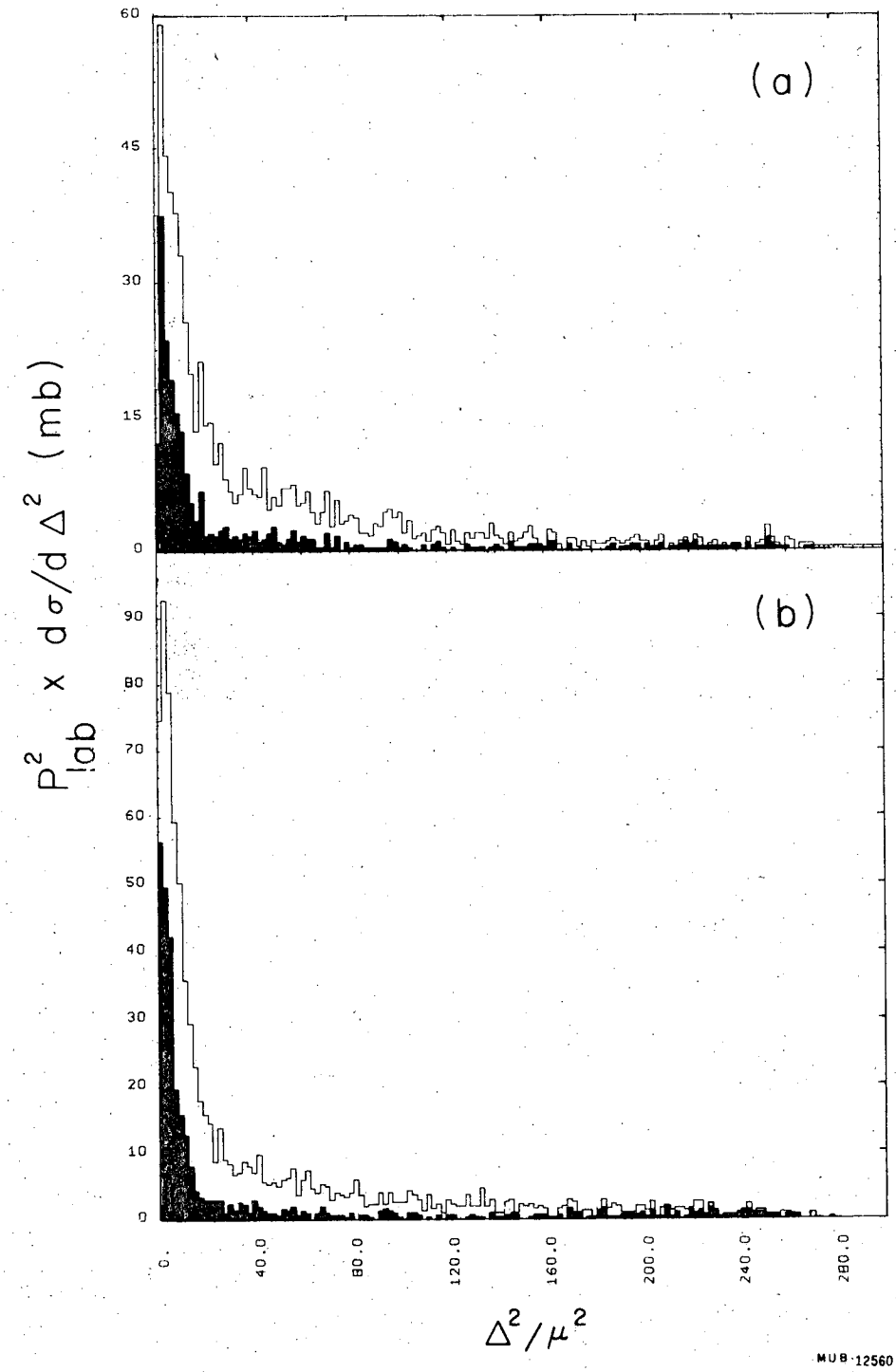

Fig. 39. 3.22-GeV/c Δ^2 distributions. Events shown as solid are in the ρ region, $M^2_{\pi\pi}$ 0.41 to 0.76 $(GeV)^2$.

$\pi\pi$ mass spectra

Figures 40 through 45 show the $\pi\pi$ effective mass spectra for both charge states at each energy. The shaded events are those with Δ^2 less than 20 $m_{\pi^0}{}^2$. The curves are least-squares fits, as determined by MINFUN,[43] to background and a p-wave Breit-Wigner resonant form. For the latter, we have used an integral over the relevant Δ^2 interval of the Chew-Low formula (Eq. B-25) with only the p-wave contributing. For the background we use phase space, except that for the events with a Δ^2 cut, we have modified it by the OPE pole term $\Delta^2/[\Delta^2 + \mu^2]^2$. We believe this is a more realistic description at low Δ^2 and accounts, in a simple-minded way, for any s-wave $\pi\pi$ interaction.

We remark that ρ production is the most important single effect present. At the higher energies, we see the effect of the f^0 above the curve. On Fig. 46 we have selected events with $\Delta^2 \leq 20\ m_{\pi^0}{}^2$ at 3.22 GeV/c and fitted the distribution to modified phase space and a d-wave Breit-Wigner. Our best fit of m_c = 1267 MeV and Γ_0 = 99 MeV is included in Fig. 45b. (Visual estimates for the f^0 production cros sections will be shown in Table X.)

We do not see enhancements outside these regions. At 3.22 GeV/c, we see a 3-standard-deviation one-bin fluctuation in the $\pi^0\pi^-$ distribution at 780 to 800 MeV. With the combined data in Fig. 47a, we see these events distort our peak from the Breit-Wigner shape assumed by our fits for the ρ^-. No evidence has ever been presented for any effect other than ρ^- production in this region, and we regard the excess of events at 795 MeV as not significant. In Fig. 47b we see a definite narrow peak centered about 780 MeV. It is tempting to associate these events with the 2π decay of the ω. We discuss this presently.

In Table VIII we tabulate the parameters and χ^2 probability for each of the 24 mass plots of Figs. 40 through 45. it is evident that by taking the weighted mean, we can determine the mass of the ρ^- and ρ^0 with some certainty. The widths and percentages of background required vary considerably. If statistics permit, a fit can be preferred with an

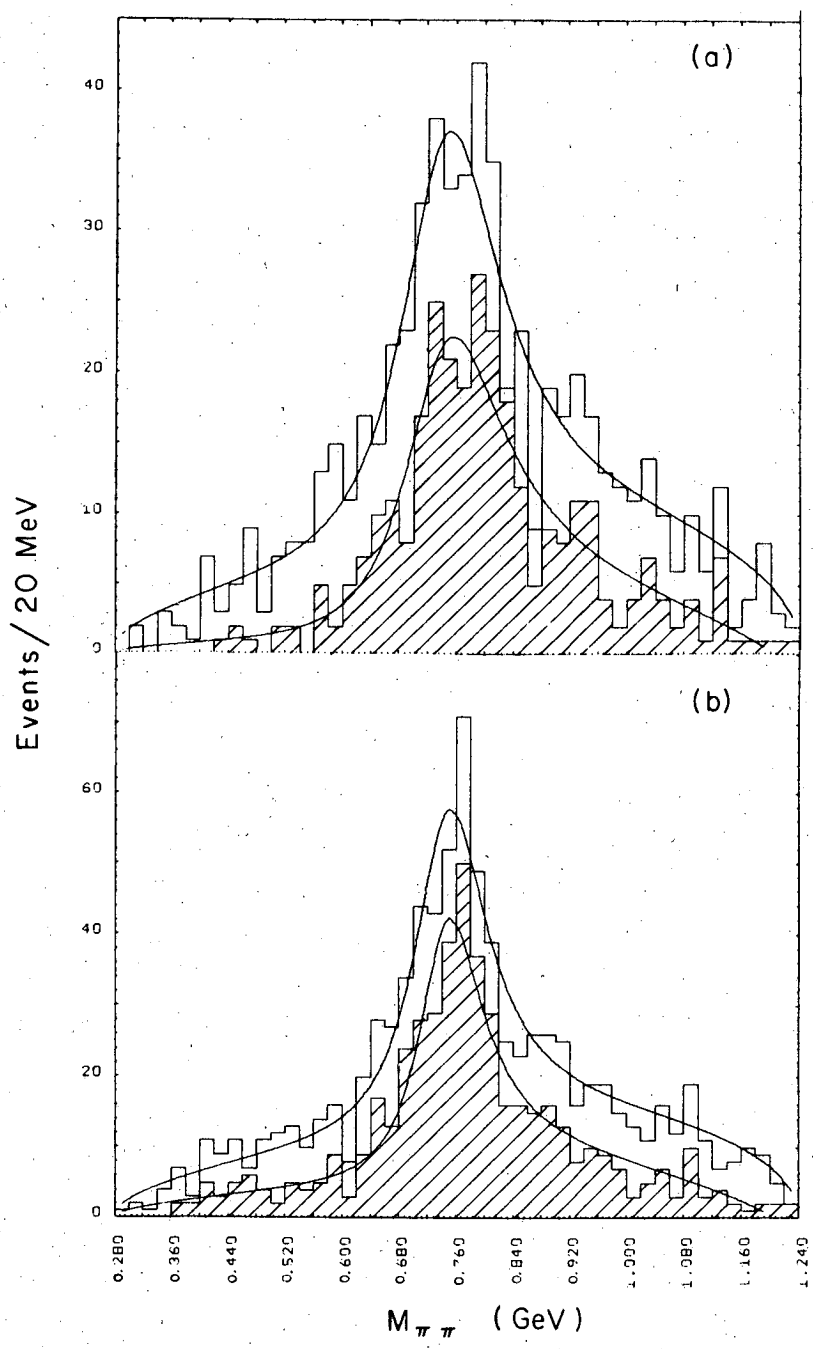

MUB-12532

Fig. 40. 2.05-GeV/c $\pi\pi$ invariant-mass spectra. Events shown shaded have $\Delta^2 \leq 20\, m_{\pi^0}{}^2$. Curves are best fits to phase space and a p-wave Breit-Wigner form.

(a) $p\pi^0\pi^-$, 624 events, 301 with $\Delta^2 \leq 20\, m_{\pi^0}{}^2$.
(b) $n\pi^+\pi^-$, 864 events, 480 with $\Delta^2 \leq 20\, m_{\pi^0}{}^2$.

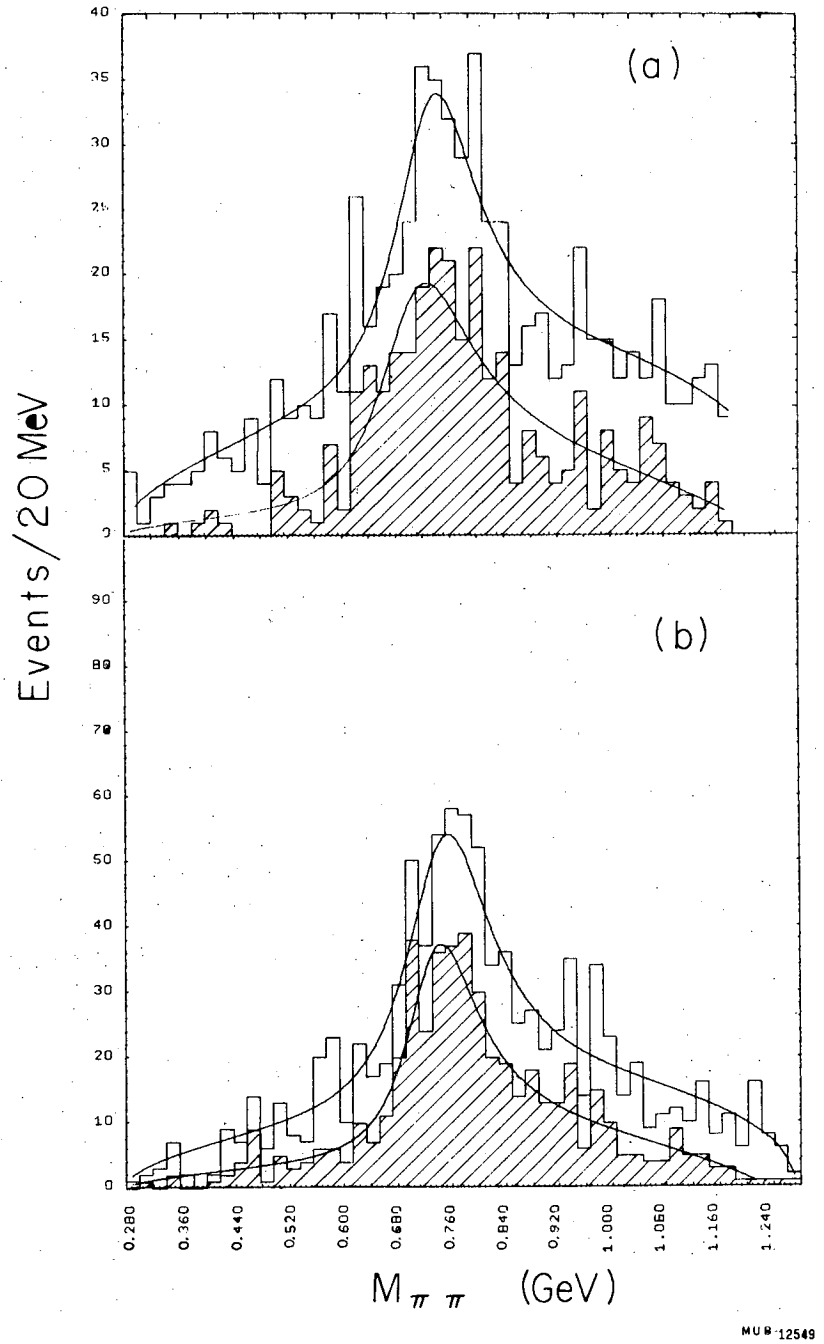

Fig. 41. 2.17-GeV/c $\pi\pi$ invariant-mass spectra. Events shown shaded have $\Delta^2 \leq 20\ m_{\pi^0}{}^2$. Curves are best fits to phase space and a p-wave Breit-Wigner form.

(a) $p\pi^0\pi^-$, 701 events, 300 with $\Delta^2 \leq 20\ m_{\pi^0}{}^2$.

(b) $n\pi^+\pi^-$, 951 events, 491 with $\Delta^2 \leq 20\ m_{\pi^0}{}^2$.

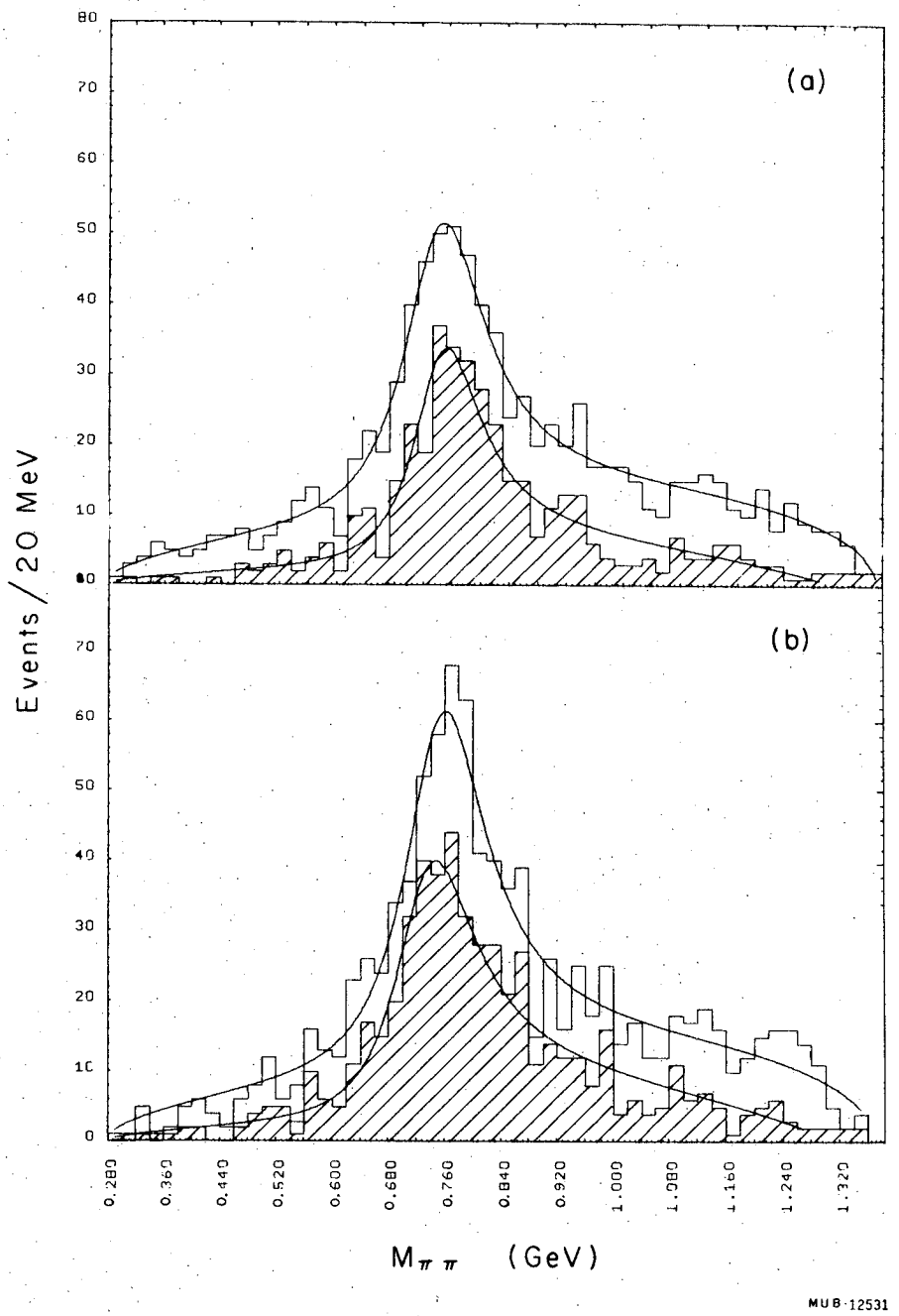

Fig. 42. 2.36-GeV/c $\pi\pi$ invariant-mass spectra. Events shown shaded have $\Delta^2 \leq 20\ m_{\pi^0}{}^2$. Curves are best fits to phase space and a p-wave Breit-Wigner form.

(a) $p\pi^0\pi^-$, 901 events, 405 with $\Delta^2 \leq 20\ m_{\pi^0}{}^2$.

(b) $n\pi^+\pi^-$, 1005 events, 539 with $\Delta^2 \leq 20\ m_{\pi^0}{}^2$.

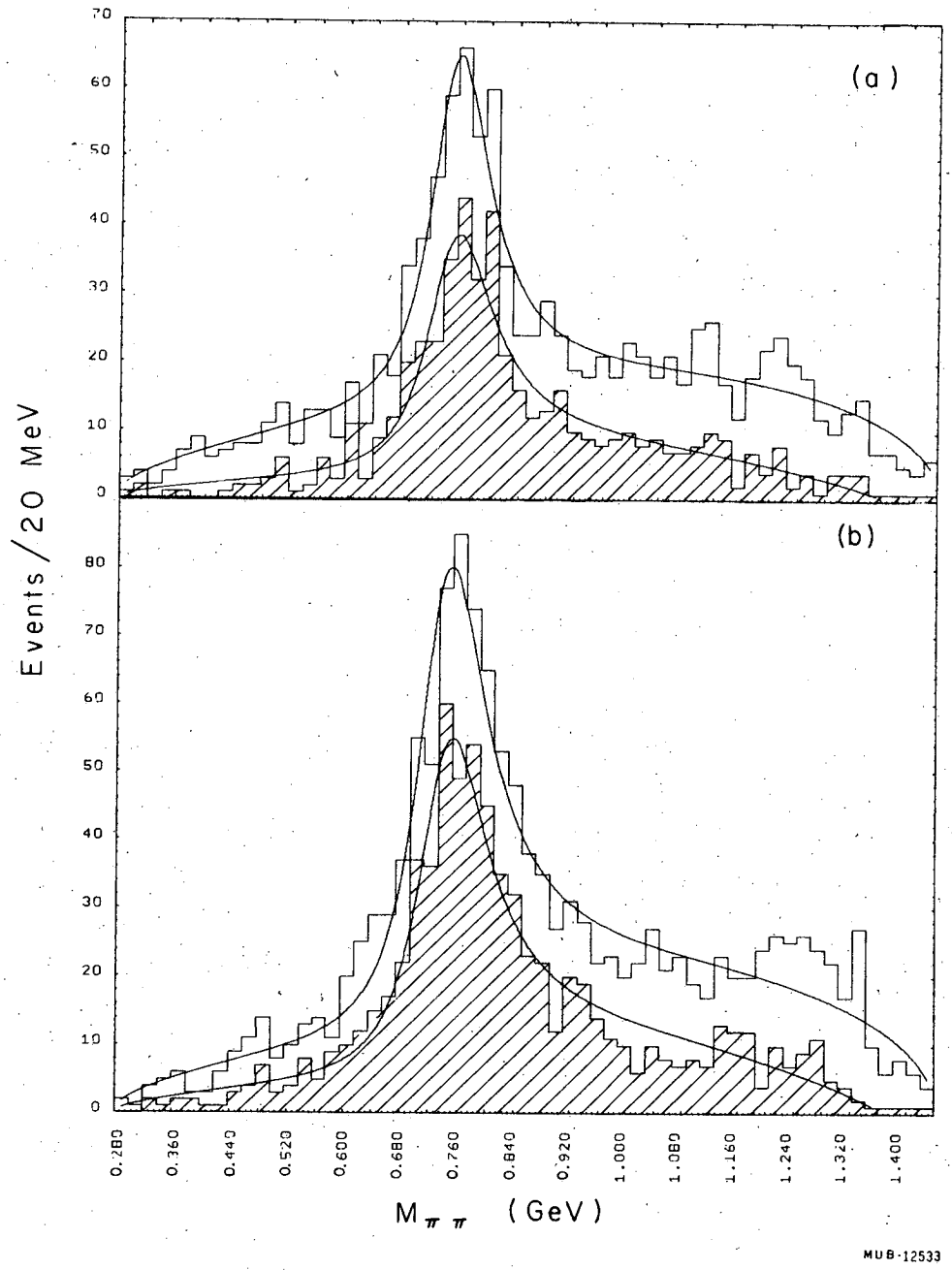

Fig. 43. 2.60-GeV/c $\pi\pi$ invariant-mass spectra. Events shown shaded have $\Delta^2 \leq 20\ m_{\pi^0}{}^2$. Curves are best fits to phase space and a p-wave Breit-Wigner form.

(a) $p\pi^0\pi^-$, 1122 events, 508 with $\Delta^2 \leq 20\ m_{\pi^0}{}^2$.

(b) $n\pi^+\pi^-$, 1418 events, 743 with $\Delta^2 \leq 20\ m_{\pi^0}{}^2$.

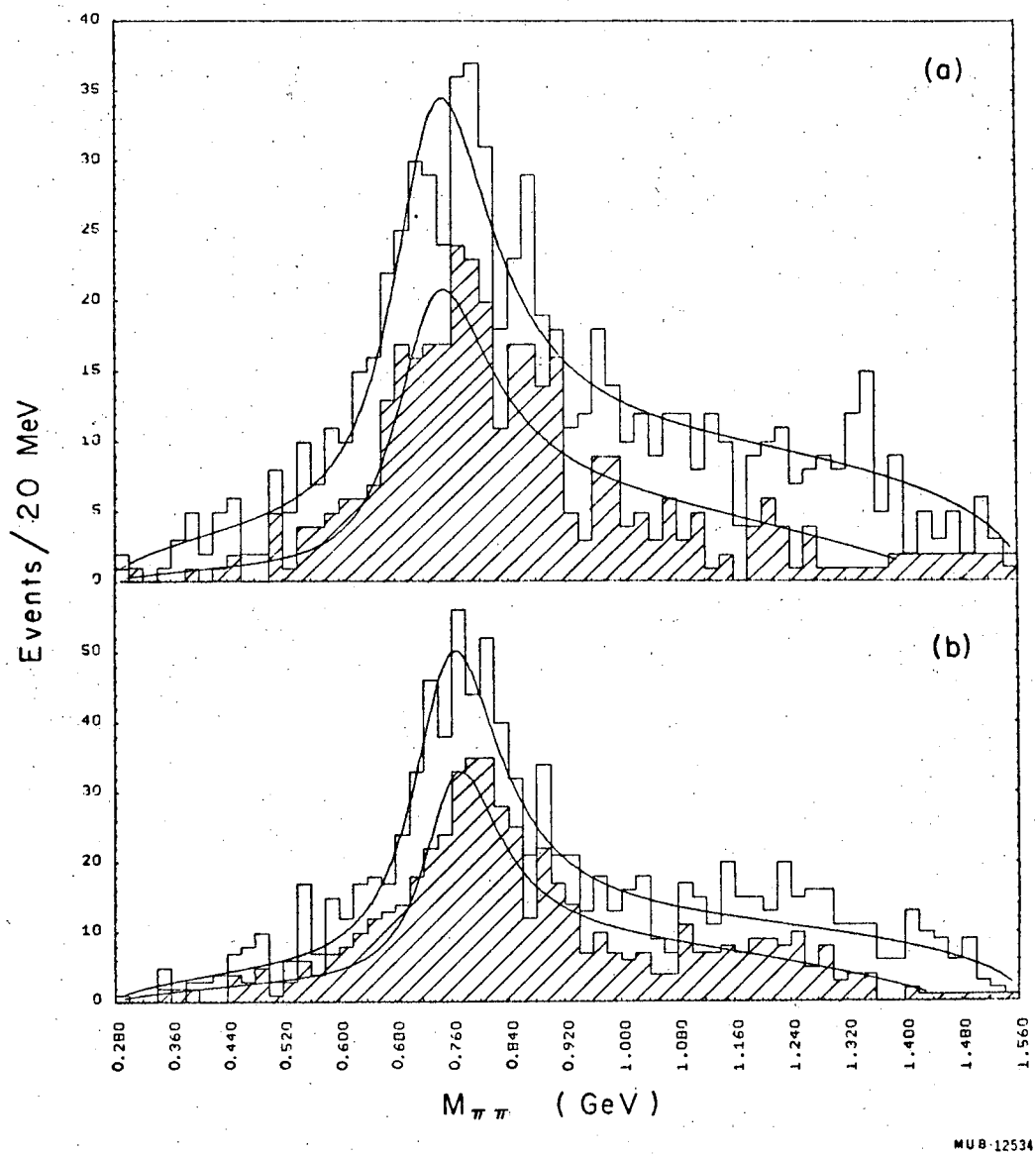

Fig. 44. 2.86-GeV/c $\pi\pi$ invariant-mass spectra. Shaded events have $\Delta^2 \leq 20\ m_{\pi^0}{}^2$. Curves are best fits to phase space and a p-wave Breit-Wigner form.

(a) $p\pi^0\pi^-$, 727 events, 348 with $\Delta^2 \leq 20\ m_{\pi^0}{}^2$.

(b) $n\pi^+\pi^-$ 982 events, 527 with $\Delta^2 \leq 20\ m_{\pi^0}{}^2$.

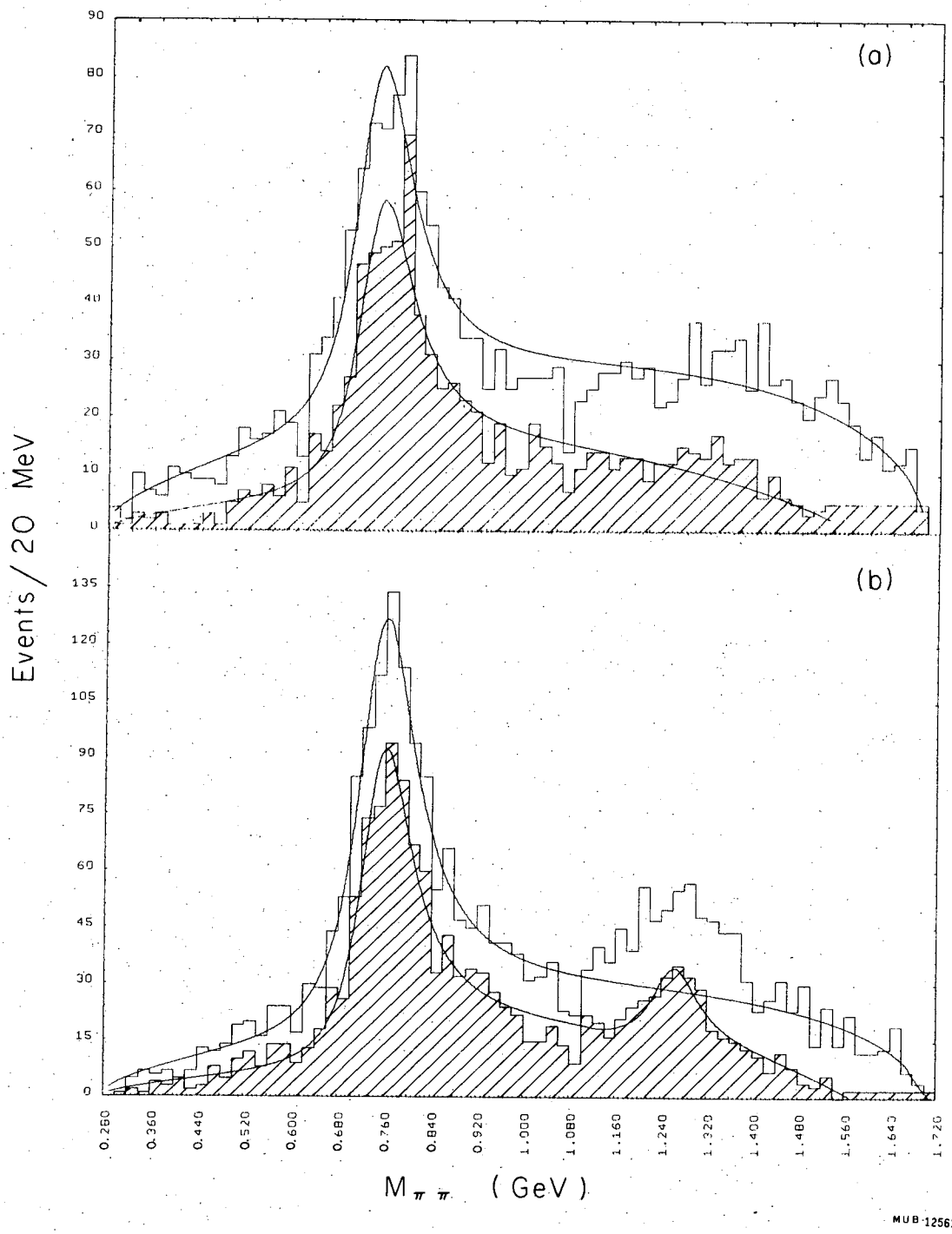

Fig. 45. 3.22-GeV/c $\pi\pi$ invariant-mass spectra. Events shown shaded have $\Delta^2 \leq 20\ m_{\pi^0}{}^2$. Curves are best fits to phase space and a p-wave Breit-Wigner form (and a d-wave Breit-Wigner form in 45b, for events shown shaded.

(a) $p\pi^0\pi^-$, 1939 events, 926 with $\Delta^2 \leq 20\ m_{\pi^0}{}^2$.

(b) $n\pi^+\pi^-$, 2540 events, 1416 with $\Delta^2 \leq 20\ m_{\pi^0}{}^2$.

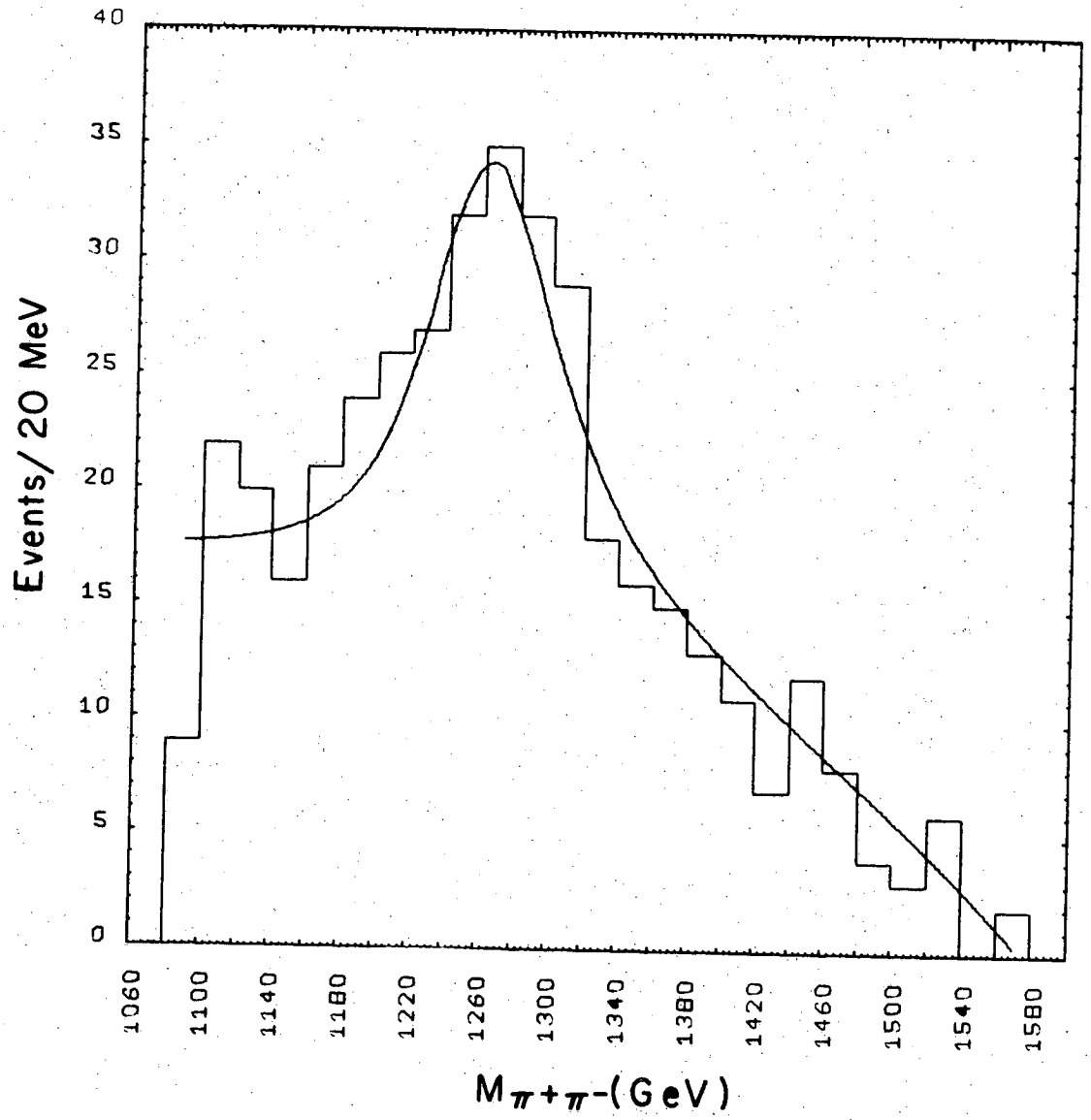

MUB-12331

Fig. 46. $\pi\pi$ invariant-mass spectrum at 3.22 GeV/c and $\Delta^2 \leq 20\, m_{\pi^0}^2$, showing fit to phase space and a d-wave Breit-Wigner form with m_c = 1267 MeV and Γ_0 = 99 MeV.

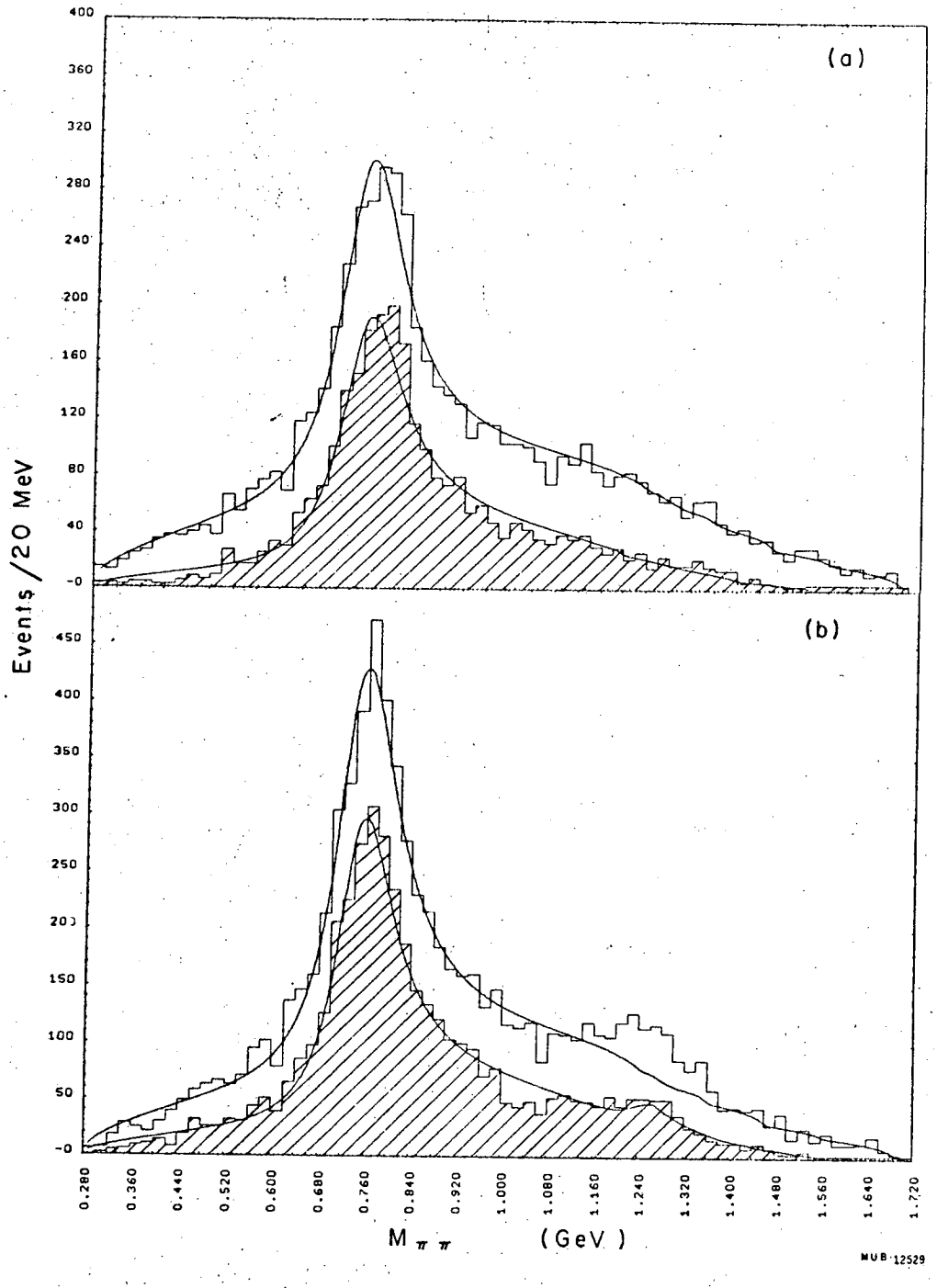

Fig. 47. $\pi\pi$ invariant-mass spectra for combined beam momenta 2.05 to 3.22 GeV/c. Curves are sums of the curves in Figs. 40 through 45.

(a) $p\pi^0\pi^-$, 6014 events, 2775 with $\Delta^2 \leq 20\ m_{\pi^0}{}^2$.

(b) $n\pi^+\pi^-$, 7760 events, 4207 with $\Delta^2 \leq 20\ m_{\pi^0}{}^2$.

Table VIII. Parameters of fits to mass and width of ρ.

Beam momentum (GeV/c)	$\pi^- p \to p\pi^0\pi^-$								$\pi^- p \to n\pi^+\pi^-$							
	All Δ^2				$\Delta^2 < 20\, m_{\pi^0}{}^2$				All Δ^2				$\Delta^2 < 20 m_{\pi^0}{}^2$			
	$P(\chi^2)$ %	Phase space %	m_ρ MeV	Γ_ρ MeV	$P(\chi^2)$ %	Phase space %	m_ρ MeV	Γ_ρ MeV	$P(\chi^2)$ %	Phase space %	m_ρ MeV	Γ_ρ MeV	$P(\chi^2)$ %	Phase space %	m_ρ MeV	Γ_ρ MeV
2.05	55.3	50.4	761.2	180.0	43.4	19.0	757.0	180.0	78.1	57.9	756.6	127.8	57.9	41.4	752.1	110.4
2.17	60.3	68.8	759.0	158.0	21.4	31.8	735.0	180.0	0.12	56.4	771.1	164.8	26.0	37.6	753.7	135.7
2.36	100.0	56.7	762.8	145.6	55.5	34.2	762.0	119.6	41.3	53.0	765.5	146.5	41.2	29.6	745.8	144.2
2.60	86.7	69.2	767.2	103.2	36.7	41.4	764.0	116.4	94.3	50.8	757.1	122.8	55.7	39.6	759.4	122.4
2.86	68.8	53.5	752.0	180.0	11.2	27.5	747.0	169.2	12.4	49.9	768.7	156.2	32.7	42.0	771.6	133.2
3.22	49.7	71.9	750.1	122.7	12.5	47.4	751.2	116.5	89.7	58.2	763.0	124.7	81.2	41.9	760.3	109.0
Combined		64.4	757.6 ± 6.6	139.5 ±15		37.2	753.5 ±10.5	137.1 ±20		54.9	763.3 ± 6.0	136.4 ±12		39.4	758.0 ± 7.5	122.2 ±15

unrealistically large width and correspondingly small amount of phase space. This occurs at energies 2.05, 2.17, and 2.86 GeV/c. We conclude that for the widths, the more extreme numbers tell us more about our statistics than they do about the ρ. It is amusing to note that widths as low as 77 MeV[44] and as high as 210 MeV[23] have been reported for the ρ.

In order to check the values of the mass and width of the ρ obtained for $\Delta^2 \leq 20\ m_{\pi^0}^2$ and to avail ourselves of the greater statistical accuracy afforded by combining the data at all energies, we also carried out the three-parameter fit with a background consisting of the sum of the six phase spaces weighted by the numbers of events at each momentum. The fitted curve for the ρ^- case is shown in Fig. 48. The mass and width agree well with the previous result (See Table IX). The parameters for the ρ^0 are also in agreement, but the probability is bad, 0.06%.

ρ Production cross section

To say something about the ρ production cross section it is important to be able to estimate the background. We have been circumspect about the numbers in Table VIII and have combined them judiciously with an eyeball estimate of the data to give the cross sections in Table X. In Fig. 49,[45] we plot the cross section for the total three-body Reactions (1) and (2) and for ρ production. Both cross sections are falling between 2 and 4 GeV/c. The quasi-two-body reaction $\pi^- p \rightarrow N\rho$ fulfills the OPE prediction that it should decrease like P_{lab}^{-2}. The dashed line which is to be regarded as a useful visual guide is $12/P_{lab}^2$ ($7/P_{lab}^2$) for the ρ^0 (ρ^-). The other OPE prediction of the ratio $(\sigma_{\rho^0}/\sigma_{\rho^-}) = 2$ is not realized.

Possible presence of ω

To investigate whether we are observing an effect of the ω, we have attempted a four-parameter fit based on an interference model due in part to Durand and Chiu.[46] Initial and final-state absorption admits the possibility of an interference between ρ exchange in ω production and π exchange in ρ production. They write down a formula giving the

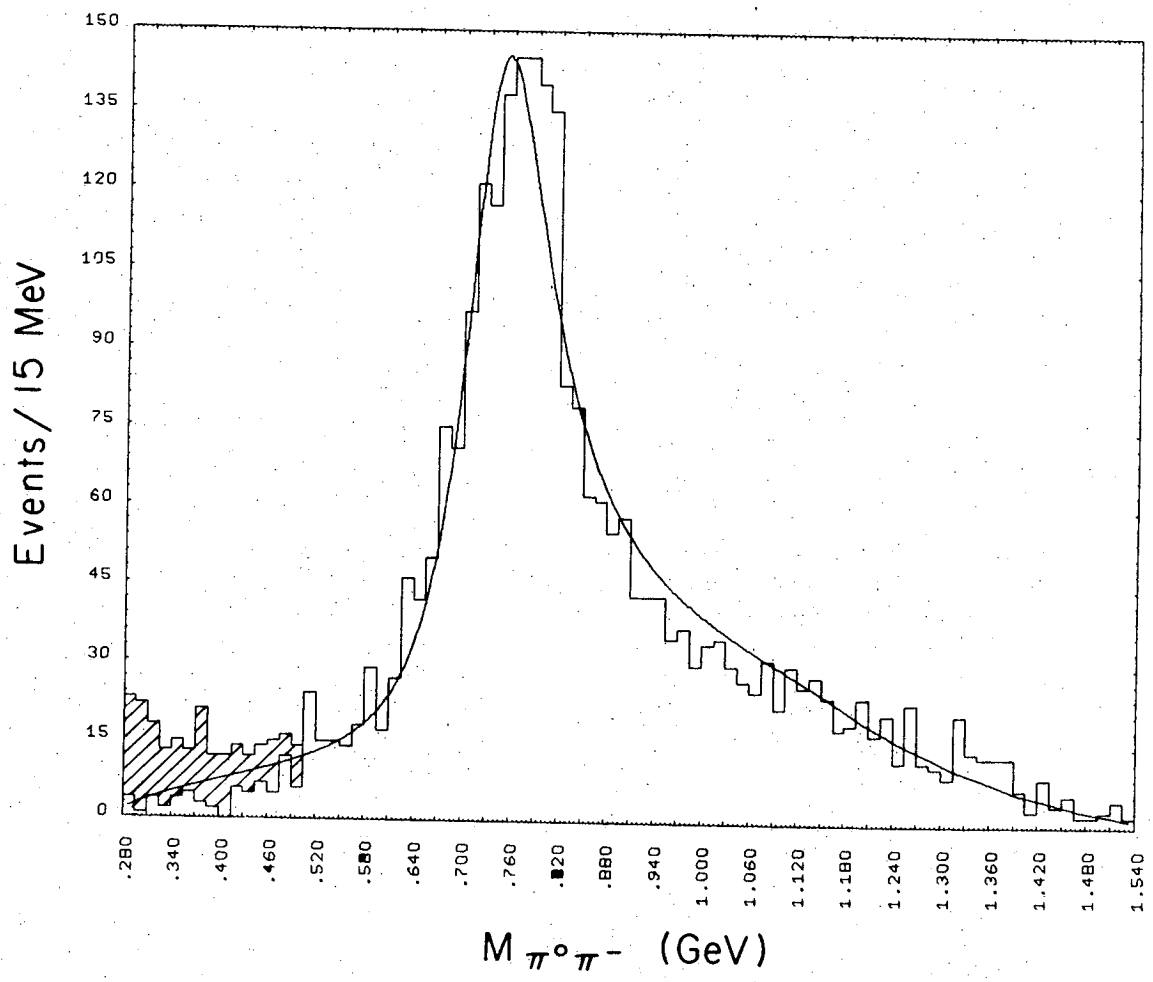

MUB-12332

Fig. 48. $\pi^0\pi^-$ invariant-mass spectrum for combined momenta 2.05 to 3.22 GeV/c and $\Delta^2 \leq 20\ m_{\pi^0}{}^2$. The events shown shaded are misfitted elastic scatterings which were removed by remeasurement. Curve is a three-parameter fit to 25% background and a p-wave Breit-Wigner form with $m_c = 750$ MeV and $\Gamma_0 = 137.5$ MeV.

Table IX. Mass and width of ρ.

Δ^2 Interval From Table VIII	ρ^- Background (%)	ρ^- m_ρ (MeV)	ρ^- Γ_ρ (MeV)	ρ^0 Background (%)	ρ^0 m_ρ (MeV)	ρ^0 Γ_ρ (MeV)	ρ^0 with ω interference Background (%)	ρ^0 with ω interference m_ρ (MeV)	ρ^0 with ω interference Γ_ρ (MeV)
All Δ^2	64.4	757.6	139.5	54.9	763.3	136.4	-	-	-
$\Delta^2 < 20$	37.2	753.5	137.1	39.4	758.0	122.2	-	-	-
$\Delta^2 < 20$	25.0	750.0	137.5	27.1	757.4	120.0	28.0	753.3	124.0
Δ^2 5-10	-	-	-	28.4	756.4	127.4	28.5	754.9	140.9
Low Δ^2	19.6	753.7	145.6	27.5	758.2	141.3	-	-	-

Table X. ρ and f^0 production cross sections.

Beam momentum (GeV/c)	σ_{ρ^-} (mb)		σ_{ρ^0} (mb)		σ_{f^0}[a] (mb)
	$\Delta^2 \leq 20$	All Δ^2	$\Delta^2 \leq 20$	All Δ^2	All Δ^2
2.05	1.2± 0.25	1.6± 0.4	1.8 ± 0.1	2.7± 0.4	–
2.17	1.1± 0.3	1.3 ± 0.3	1.75± 0.2	2.6 ± 0.4	–
2.36	1.0± 0.2	1.55± 0.1	1.45± 0.2	2.15± 0.15	0.15± 0.1
2.60	0.9± 0.1	1.15± 0.15	1.35± 0.1	2.05± 0.1	0.25± 0.13
2.86	0.7± 0.2	1.1 ± 0.2	1.05± 0.1	1.6 ± 0.1	0.20± 0.1
3.22	0.6± 0.05	0.75± 0.1	0.9 ± 0.1	1.1 ± 0.1	0.39± 0.05

[a] f^0 contains neutral mode $f^0 \rightarrow \pi^0 \pi^0$.

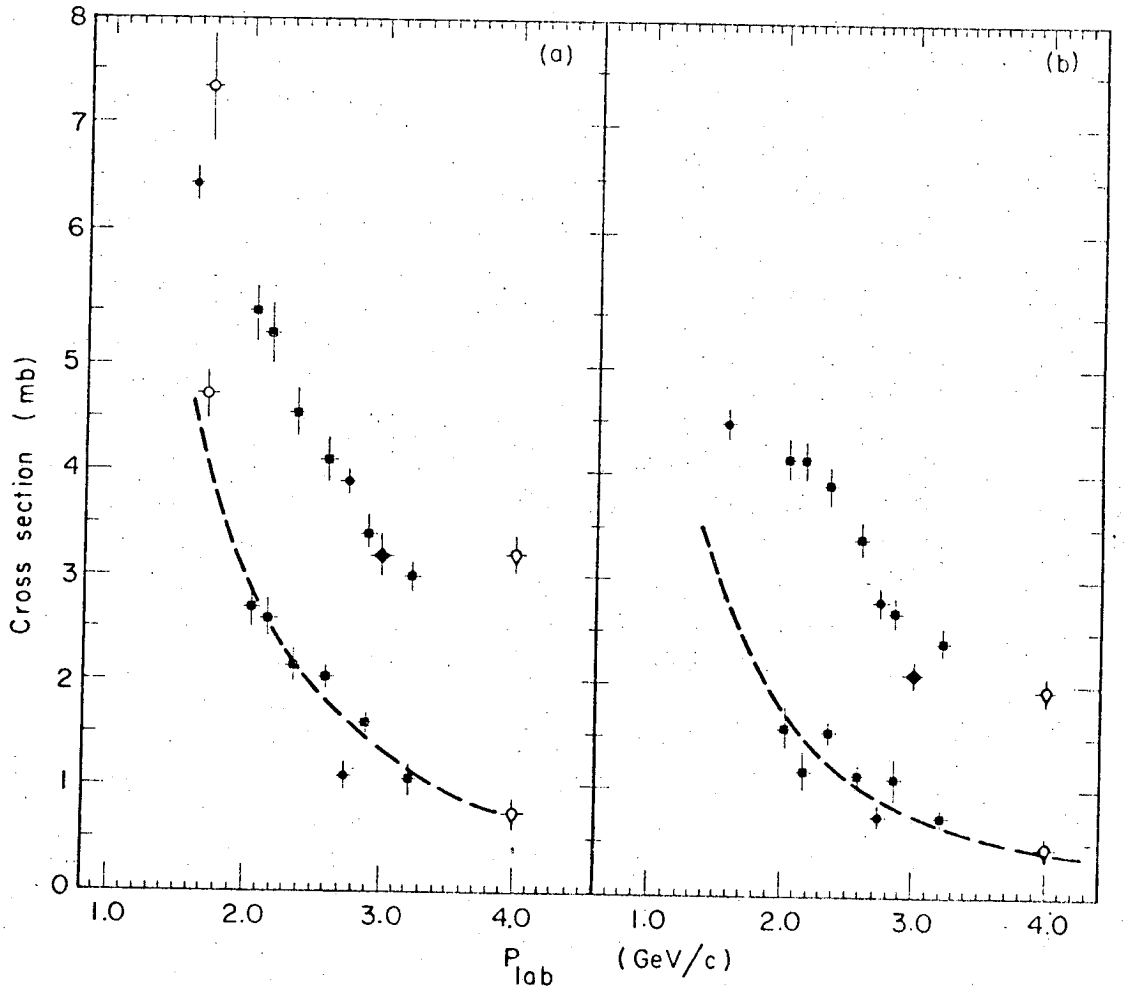

Fig. 49. Cross sections for the reaction $\pi^- p \to N\pi\pi$ and $\pi^- p \to N\rho$ as a function of beam momentum.

- ■ Present work, 2.05, 2.17, 2.36, 2.60, 2.86, 3.22 GeV/c.
- O Bacon et al., 1.70 GeV/c.
- ● S. O. B. B., 1.59, 2.75 GeV/c.
- ◆ Hagopian, 3.0 GeV/c.
- ◇ Bondar et al., 4.0 GeV/c.

(a) $\pi^- p \to n\pi^+\pi^-$, $\pi^- p \to n\rho^0$. Dotted line is $12/P^2_{lab}$.
(b) $\pi^- p \to p\pi^0\pi^-$, $\pi^- p \to p\rho^-$. Dotted line is $7/P^2_{lab}$.

dependence on $m_{\pi\pi}^2$ and Δ^2 containing three terms:

$$\frac{d^2\sigma}{dm^2 d\Delta^2} = \frac{m}{\pi[(m^2-m_\rho^2)^2 + m_\rho^2\Gamma_\rho^2]} \left\{ \Gamma_\rho \frac{d\sigma_\rho}{d\Delta^2} \right.$$

$$+ \frac{r\Gamma_\omega}{[(m^2-m_\omega^2)^2 + m_\omega^2\Gamma_\omega^2]} \frac{d\sigma_\omega}{d\Delta^2} [(m_\omega^2-m_\rho^2)^2 + m_\rho^2\Gamma_\rho^2]$$

$$+ \sqrt{r\Gamma_\rho\Gamma_\omega} \frac{d\sigma_{\rho\omega}}{d\Delta^2} \frac{(m^2-m_\omega^2)\sqrt{(m_\omega^2-m_\rho^2)^2 + m_\rho^2\Gamma_\rho^2}}{[(m^2-m_\omega^2)^2 + m_\omega^2\Gamma_\omega^2]} .$$

The first term is the contribution from pure ρ production. For $d\sigma_\rho/d\Delta^2$ we use the Chew-Low formula. The second term is pure ω production, where we assume the ω makes an electromagnetic transition to the ρ^0. The third term is the important one for the $\pi\pi$ mass spectrum, and can give rise to a large effect even if $r = \Gamma_{\omega \to 2\pi}/\Gamma_\omega$ is small. For $d\sigma_\omega/d\Delta^2$ we have used the experimental distribution published by Cohn, Bugg, and Condo.[47] We have used Fig. 1 of Ref. 47 to set $d\sigma_\omega/d\Delta^2$ equal to $d\sigma_\rho/d\Delta^2$ at $\cos\Theta_{cm} = 0.85$ at 3.22 GeV/c, and have taken $d\sigma_{\rho\omega}/d\Delta^2$ constant and equal to the same value. We have allowed the phase-space background, m_ρ, Γ_ρ, and r to vary. Our value for r is not to be interpreted as the $\omega \to 2\pi$ branching ratio, since it has the strongly energy-dependent variation of the $\pi N \to N\omega$ production cross section folded in. The order of magnitude needed for r is about 1%.

Figure 50 shows a fit to the $\pi^+\pi^-$ distribution, with $\Delta^2 \leq 20\, m_{\rho^0}^2$. It is not surprising that with one extra parameter we are able to make a better fit. Yet, in the above formula, the mass and width of the ω were fixed at 783 MeV and 12 MeV. The mass of the ρ^0 is about 4 MeV less, and the width is 20 MeV less than that required without the ω.

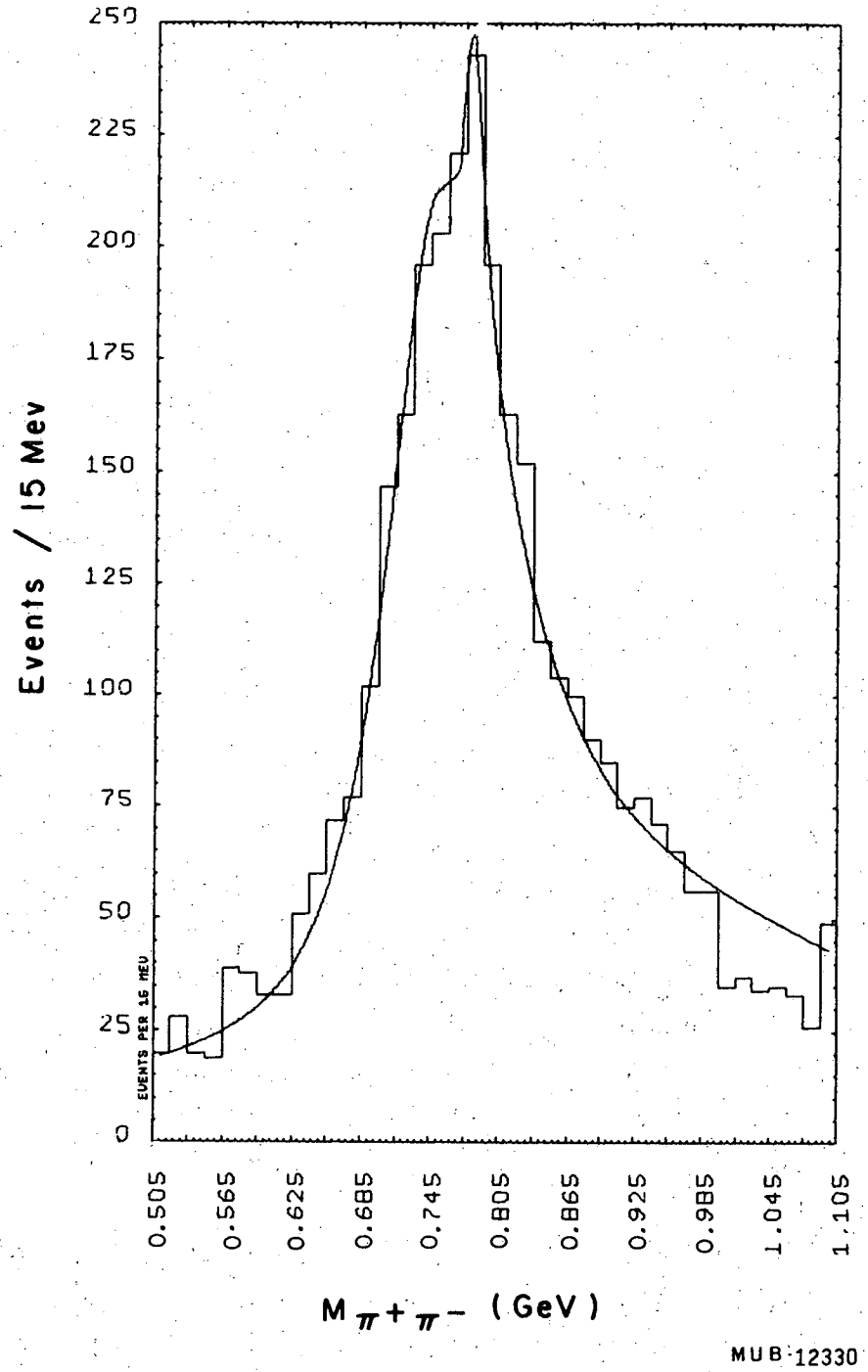

Fig. 50. $\pi^+\pi^-$ invariant-mass spectrum for combined momenta 2.05 to 3.22 GeV/c and $\Delta^2 \leq 20\, m_{\pi^0}{}^2$. The curve is a least-squares fit assuming interference of ρ^0 and ω production amplitudes.

By selecting events with Δ^2 in the range 5 to 10 $m_{\pi^0}{}^2$, we enhance the sharp peak at 780 MeV. Figure 51 shows a fit to the mass plot both with and without ω interference. If we choose events at the lower momenta only, the peak is still evident but does not account for most of the effect. Since the cross section is known to be larger at lower energies,[48] we would expect the narrow peaking to predominate at lower energies. According to the known Δ^2 distribution[47] for the ω, we should expect a genuine $\omega \rightarrow 2\pi$ peak to be even more distinguishable from the ρ in the Δ^2 region 10 to 20 $m_{\pi^0}{}^2$, but it is in fact absent, casting in doubt the interpretation, without some artificial restrictions, of the observed peaks as due to the ω.

Desai[49] considers that a better alternative is the presence of a 2^+ particle at $\approx$ 780 MeV. He is able to fit both the mass and decay angular distributions under these assumptions.

ρ Parameters

To determine the parameters of the ρ optimally, we do so where the OPE model should be most valid, at very low Δ^2. We choose as low a Δ^2 interval as possible without sacrificing statistical accuracy. With a yardstick of 1000 events, we pick 4 $m_{\pi^0}2$ for the ρ^0 and 6 $m_{\pi^0}{}^2$ for the ρ^-. These are shown in Figs. 52 and 53. We determine

for the ρ^0, $m_c = 758 \pm 5$ MeV, $\Gamma_0 = 141 \pm 10$ MeV,

for the ρ^-, $m_c = 754 \pm 5$ MeV, $\Gamma_0 = 146 \pm 10$ MeV.

We have summarized the data on the mass and width of the ρ in Table IX. We see no obvious dependence of m_ρ on Δ^2. The mass difference, $(M_{\rho^0} - m_{\rho^-})$ seems to be about 5 MeV. Both widths are of the order of 140 MeV. At certain Δ^2 regions there may be distorting effects, possibly due to the ω, which cause the observed ρ^0 width to be about 120 MeV.

Events at high Δ^2

In Fig. 54 we have plotted $m^2_{\pi\pi}$ against u, the square of baryonic momentum transfer between the beam pion and the final nucleon. This is the valid plot in case of baryon exchange, and has the effect of superimposing on one another the tails of the Δ^2 plots shown in

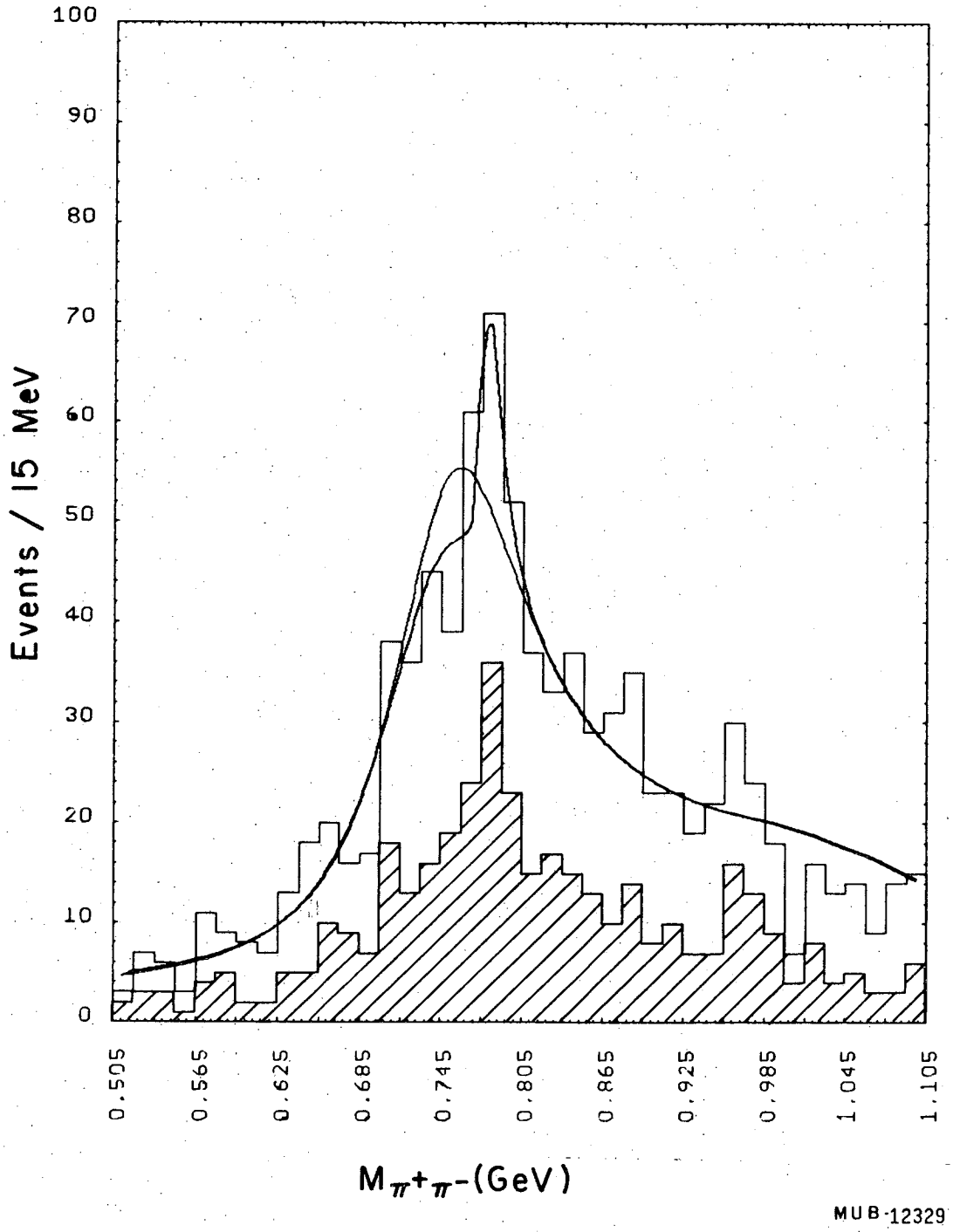

Fig. 51. $\pi^+\pi^-$ invariant-mass spectrum for combined momenta 2.05 to 3.22 GeV/c and Δ^2 in the range 5 to 10 $m_{\pi^0}{}^2$. The shaded events have incident beam momenta 2.05 to 2.36 GeV/c. The curves are fits to background and ρ^0 with and without ω interference.

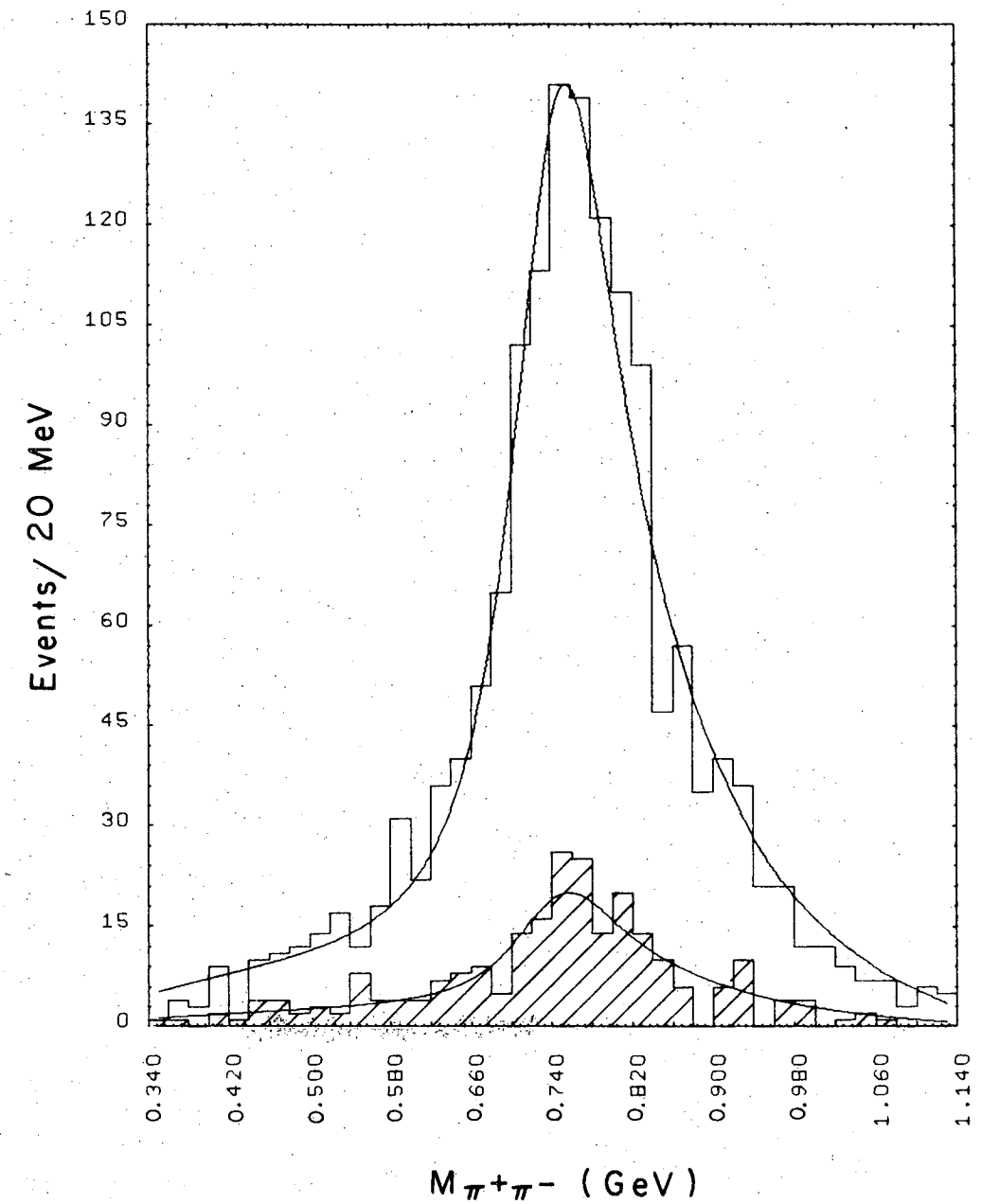

MUB-12429

Fig. 52. $\pi^+\pi^-$ invariant-mass spectrum for combined momenta 2.05 to 3.22 GeV/c and $\Delta^2 \leq 4 m_{\pi^0}{}^2$, 1500 events; 242 shaded events have $|\cos\theta| \leq 0.3$. Curves are three-parameter fits to 27.5% background and a p-wave Breit-Wigner form with m_c = 758 MeV and Γ_0 = 141 MeV.

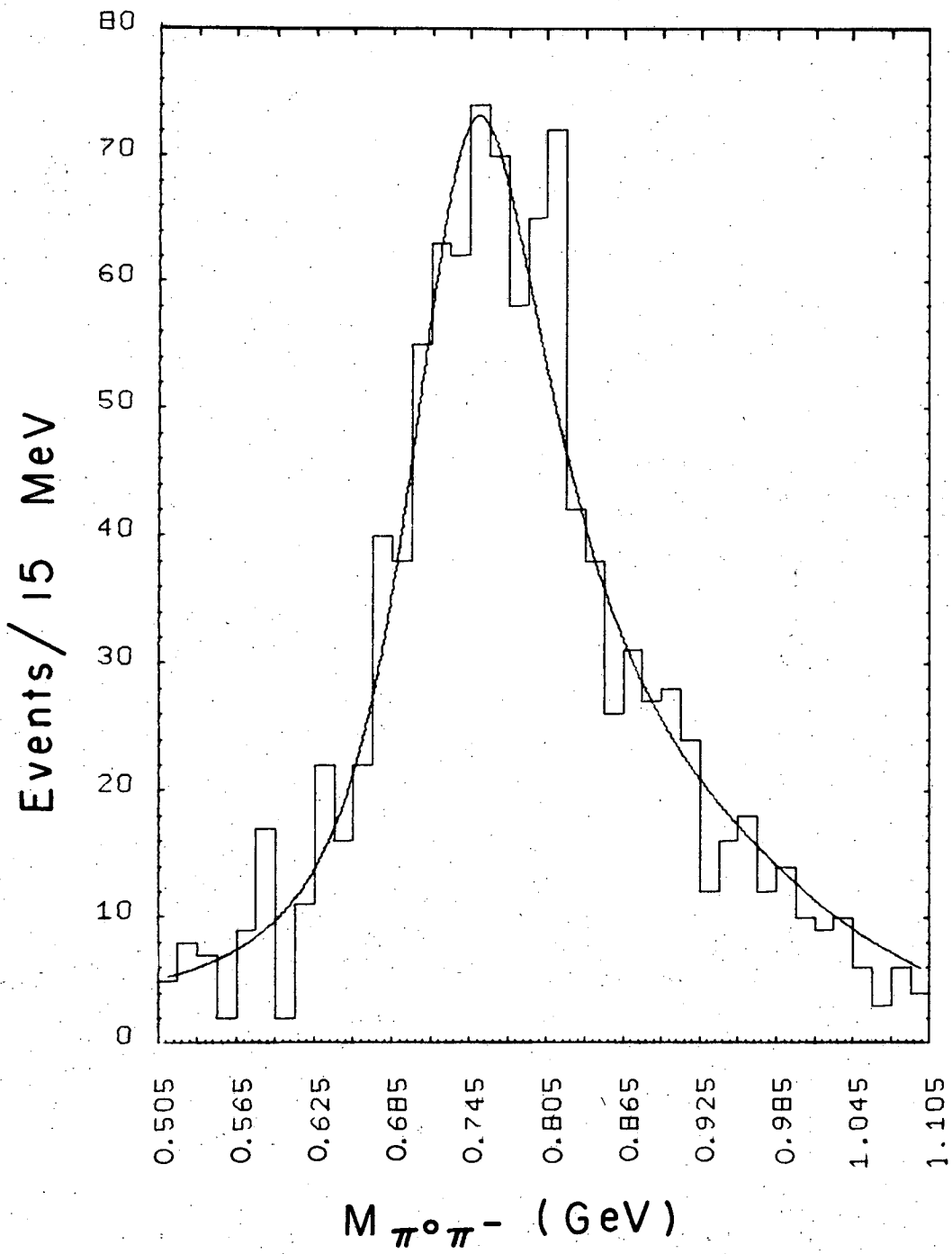

MUB-12537

Fig. 53. $\pi^0\pi^-$ invariant-mass spectrum for combined momenta 2.05 to 3.22 GeV/c and $\Delta^2 \leq 6\ m_{\pi^0}{}^2$, 1054 events. Curve is three-parameter fit to 19.6% background and a p-wave Breit-Wigner form with m_c = 754 MeV and Γ_0 = 146 MeV.

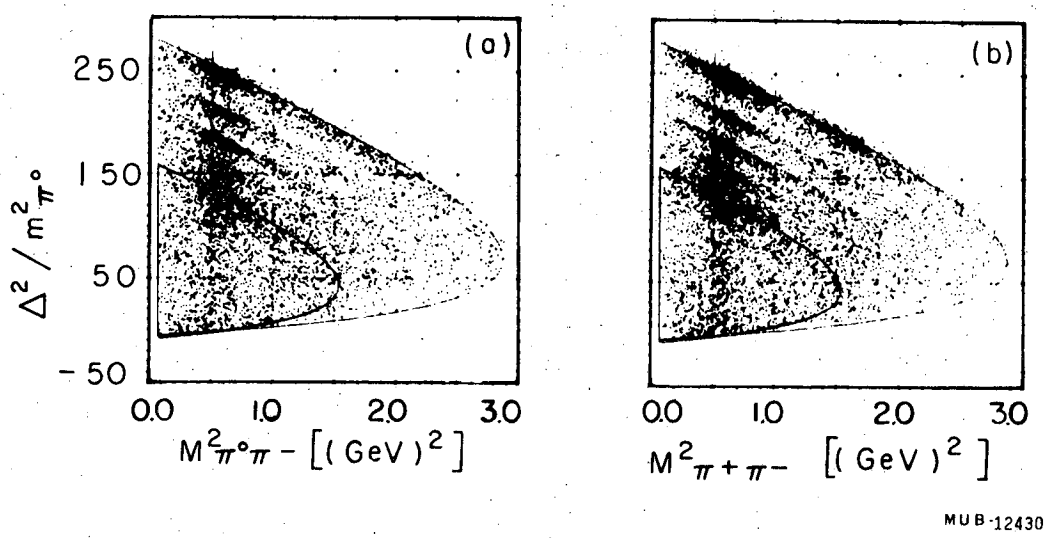

Fig. 54. Scatter plot of u, baryonic momentum transfer squared, against $m^2_{\pi\pi}$ for all beam momenta.

(a) $p\pi^0\pi^-$.

(b) $n\pi^+\pi^-$.

Figs. 34-39. Though no backwards peaking was observed in the Δ^2 distributions, it is clear that more $\pi^+\pi^-$ events in the ρ region are produced with high Δ^2 (or low u) than $\pi^0\pi^-$. An obvious question is whether these are really ω events. In Fig. 55 we show the mass plots for $u \leq 110\ m_{\pi^0}{}^2$. The charged events in Fig. 55a are consistent with weak ρ^- production. The narrow peak in the neutral combination is centered at the ρ^0. We have checked these events for possible biases, mismeasurement, or misidentification. There is no evidence for ω production in these events.

Nπ mass spectra

In Fig. 56 we show Dalitz plots for all data with Δ^2 less than $20\ m_{\pi^0}{}^2$. The density of points and character of the ρ and f^0 bands is unchanged, suggesting that these are not due to πN resonances. If we were producing the $\Delta^+(1238)$, we would expect twice as much intensity in $p\pi^0$ as in $n\pi^+$. Checking this in the presence of the ρ is difficult, but the indications are that the production of this state is not important. In fact, experiments in the same energy range, studying the reactions

$$\pi^+ p \rightarrow p\pi^+\pi^0$$

and

$$\pi^+ p \rightarrow n\pi^+\pi^+ ,$$

while showing substantial $\Delta^{++}(1238)$, show small amounts of $\Delta^+(1238) \rightarrow p\pi^0$ and very little of $\Delta^+(1238) \rightarrow n\pi^+$.[50-52] We conclude that the concentration of events is due to the way in which the $\pi\pi$ system tends to decay, with the final π^- continuing in the same direction as the beam π^-. This becomes more pronounced at higher $\pi\pi$ masses.

In Fig. 57 we show the Nπ effective-mass plots for all six energies combined. The background due to phase space is the same in all four plots. However, the forward outgoing π^- distorts the distribution, so that there is a tendency for high π^-p and π^-n and for low π^0p and π^+n effective masses. As we shall show, in Reaction (2) the $\pi^0\pi^-$ decay distribution up to the ρ region is symmetric, which is reflected in Fig. 57a at the low-mass end. This makes it difficult to say how much $\Delta^0(1238)$ is formed. It is also hard to say whether any

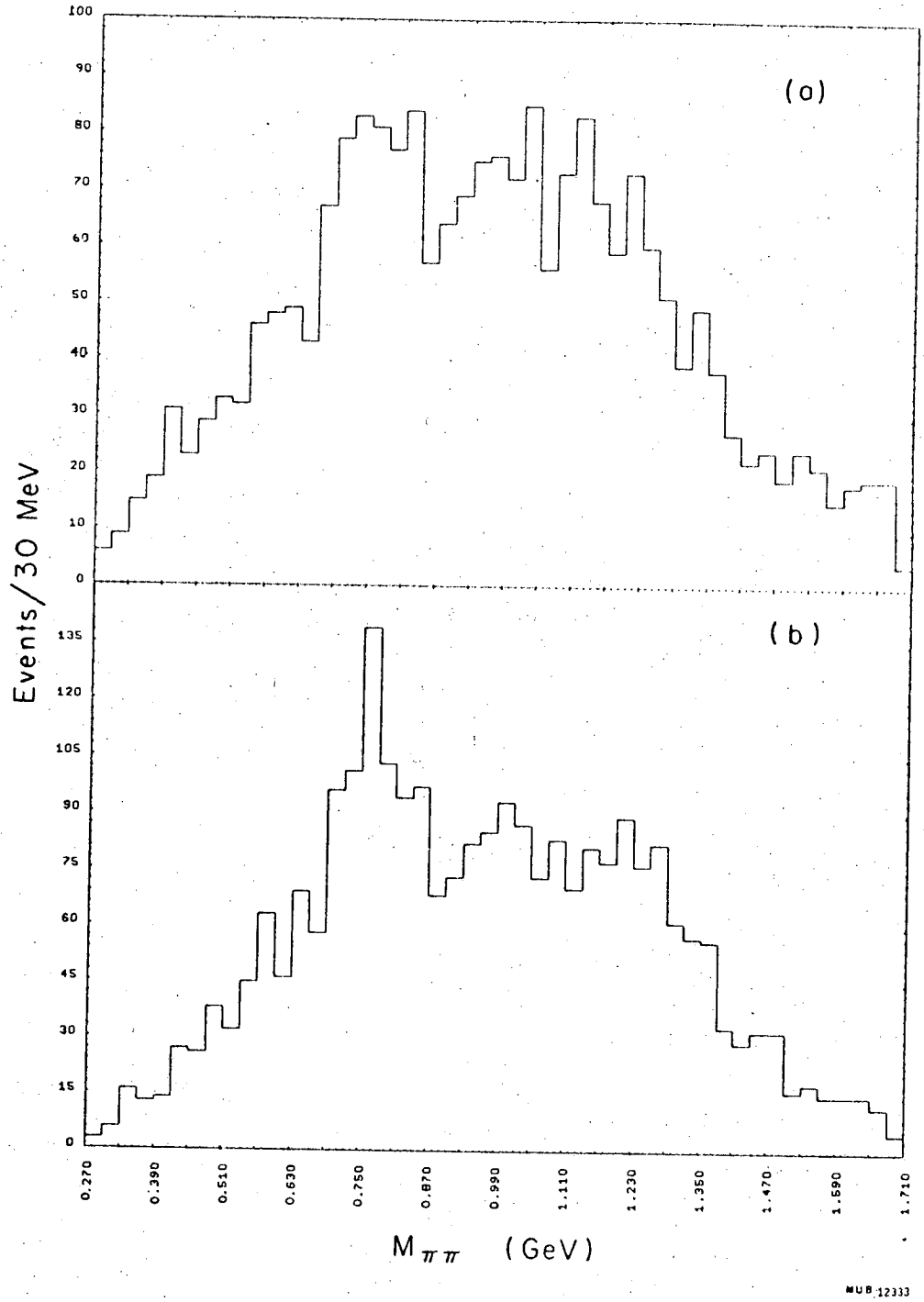

Fig. 55. $\pi\pi$ invariant-mass spectra for combined momenta 2.05 to 3.22 GeV/c and $u \leq 110\ m_{\pi^0}^2$.

(a) $p\pi^0\pi^-$, 2213 events.

(b) $n\pi^+\pi^-$, 2600 events.

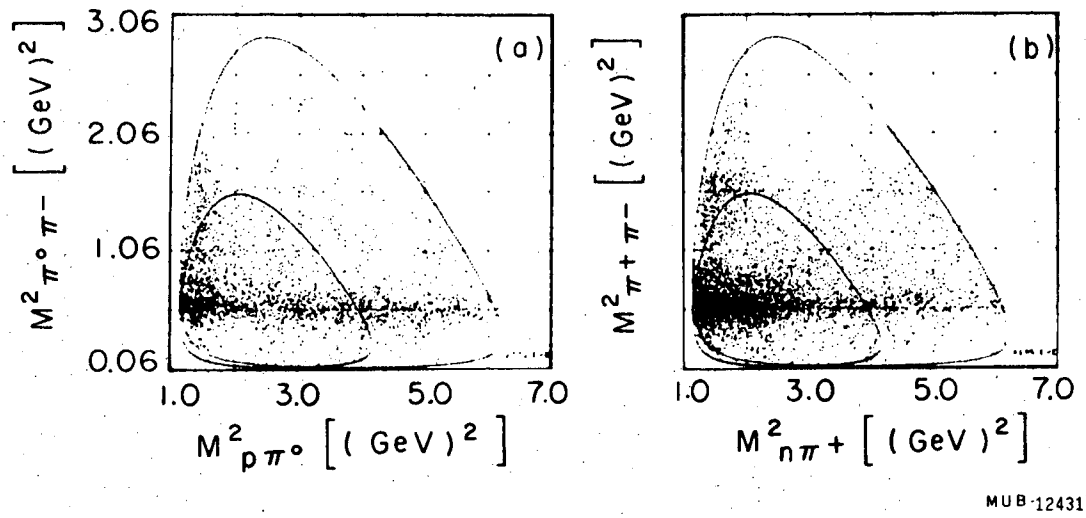

Fig. 56. Dalitz plots for all events with $\Delta^2 \leq 20\, m^2_{\pi^0}$.

(a) $p\pi^0\pi^-$.

(b) $n\pi^+\pi^-$.

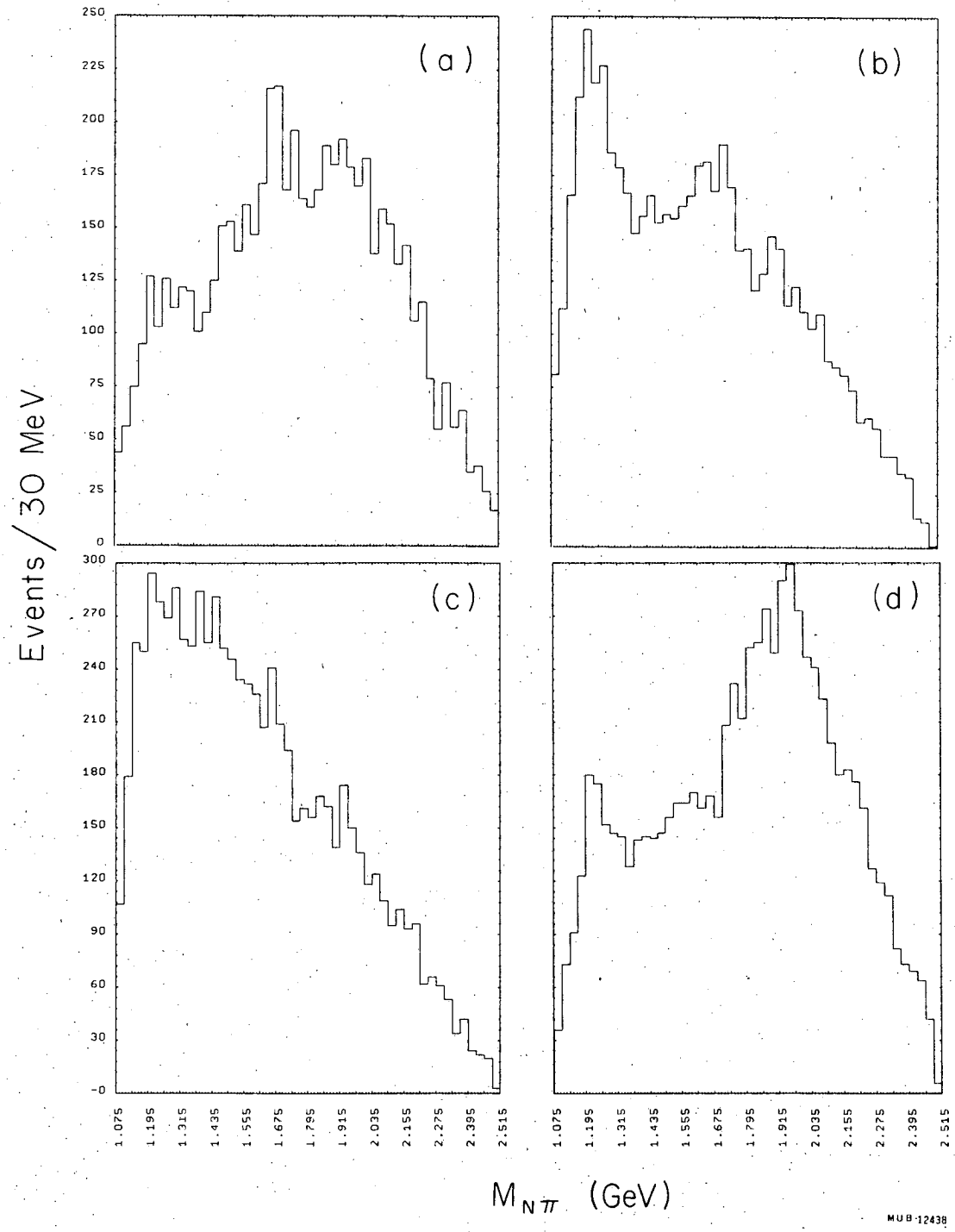

Fig. 57. Nπ invariant-mass spectra for combined momenta 2.05 to 3.22 GeV/c.

$\pi^- p \to p\pi^0 \pi$, (a) $p\pi^-$ combination,
(b) $p\pi^0$ combination.
$\pi^- p \to n\pi^+ \pi^-$, (c) $n\pi^+$ combination,
(d) $n\pi^-$ combination.

$\Delta^0(1920)$ is made. The most prominent feature in Fig. 57a is the formation of the $N^{*0}(1688)$. The $N^{*+}(1688)$ is also evident in the $p\pi^0$ and $n\pi^+$ distributions. There seems to be evidence for a small amount of $\Delta^+(1920)$ in these distributions. In Fig. 57d we have clear evidence of the $\Delta^-(1238)$. We have not considered the possibility of $N^*\rho$ interference in any of these processes.

If we examine these distributions at each individual momentum, considering only those peaks which emerge clearly above the background, despite the bad statistics we can estimate the production cross sections. These are shown in Table XI. Entries are left blank where either we have consistency with the absence of the resonance, or we are unable to estimate the effect above the background.

Decay angular distributions

We present here mainly a qualitative description of the decay angular distributions. In the next section their significance for the OPE model is discussed. The two decay angles are θ and ϕ. They are defined in Fig. 58: θ is the $\pi\pi$ scattering angle in the $\pi\pi$ rest frame. It is the polar angle that the outgoing π^- makes with the direction of the beam pion which we take as the Z axis; ϕ is the angle between the $\pi\pi$ scattering or decay plane and the production plane; $\phi = 0°$ occurs when the normals to the planes are parallel.

In Fig. 59 we select events in the ρ band, 650 to 850 MeV and plot Δ^2 vs $\cos\theta$. In the neutral case, we note a strong forwards-backwards asymmetry, which is largest at the lowest values of Δ^2. In contrast, the ρ^- plot is symmetric. Both tend to become isotropic as Δ^2 increases. It is evident that if we choose events with low Δ, less than $4\, m_{\pi^0}{}^2$, we will accentuate the characteristics of the angular distributions.

In Fig. 60 we plot $m_{\pi\pi}$ against $\cos\theta$. The charged combination in Fig. 60a is isotropic below 700 MeV. Above 800 MeV, there is a definite tendency for the π^- to go in the forward direction. In contrast, the neutral combination is always asymmetric. No further structure, e.g., a diagonal effect, is evident. The similar plots for ϕ,

Table XI. Isobar production cross sections.[a]

Beam momentum (GeV/c)	$\sigma_{N^{*+}(1688)\to n\pi^+}$ (mb)	$\sigma_{\Delta^-(1238)\to n\pi^-}$ (mb)	$\sigma_{N^{*+}(1688)\to p\pi^0}$ (mb)	$\sigma_{N^{*0}(1688)\to p\pi^-}$ (mb)
2.05	—	0.35± 0.1	—	—
2.17	—	0.15± 0.05	—	0.25± 0.1
2.36	0.07± 0.05	0.10± 0.05	—	0.25± 0.1
2.60	0.1 ± 0.05	0.17±0.05	0.07± 0.05	0.05± 0.05
2.86	—	0.1 ± 0.05	—	—
3.22	—	0.05± 0.02	—	0.06± 0.02

a. Entries are left blank if there is no obvious N^* enhancement or if it is impossible to separate it from the effect of the ρ - decay distribution.

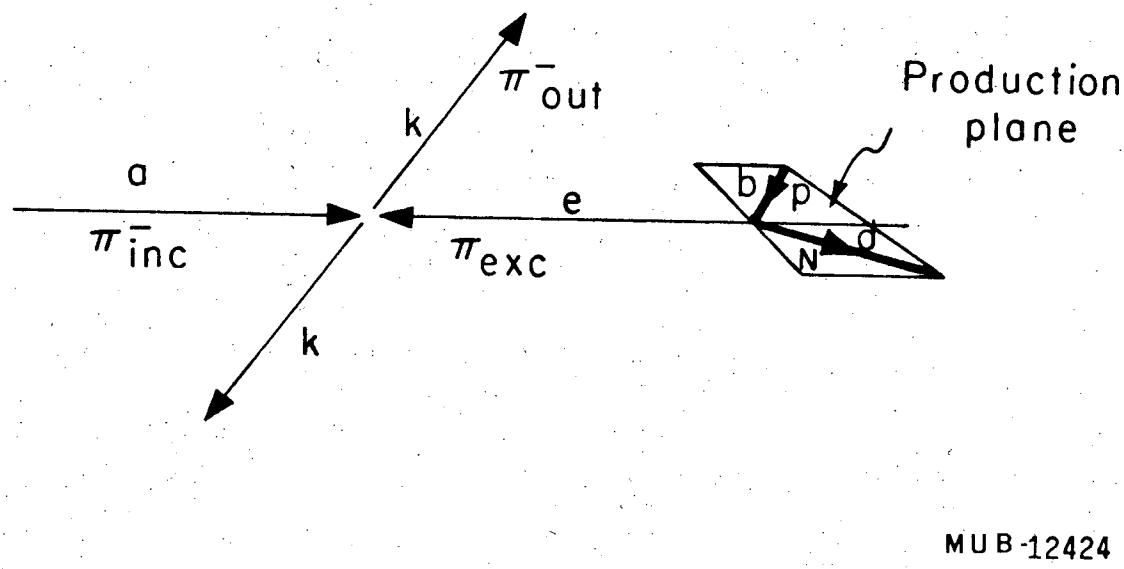

Fig. 58. Definition of $\pi\pi$ decay angles ϕ and θ ; ϕ is angle in $\pi\pi$ rest frame between decay and production planes; θ is angle between outgoing and incident π^-.

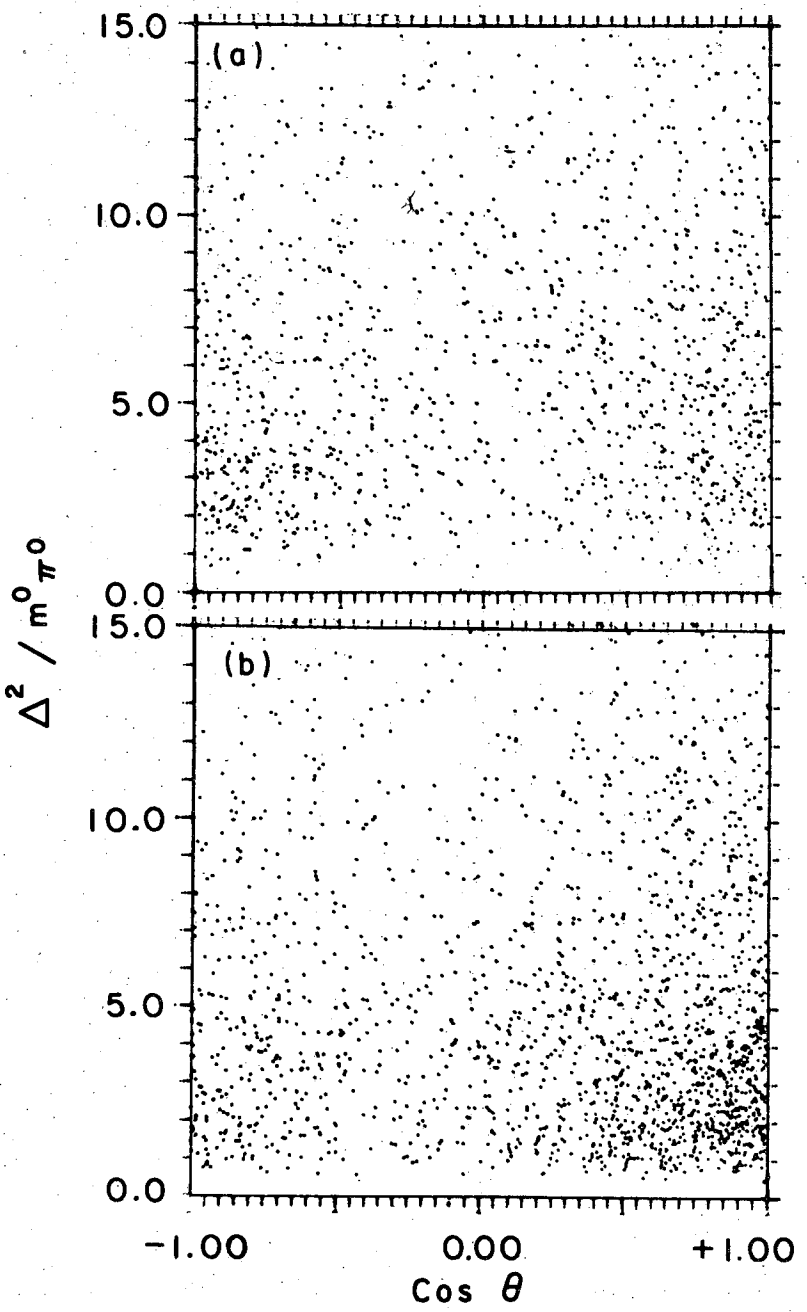

MUB-12328

Fig. 59. Scatter plot of Δ^2 vs $\cos\theta$ for ρ, $m_{\pi\pi}$ 680 to 850 MeV.
(a) ρ^-, 1197 events.
(b) ρ^0, 1806 events.

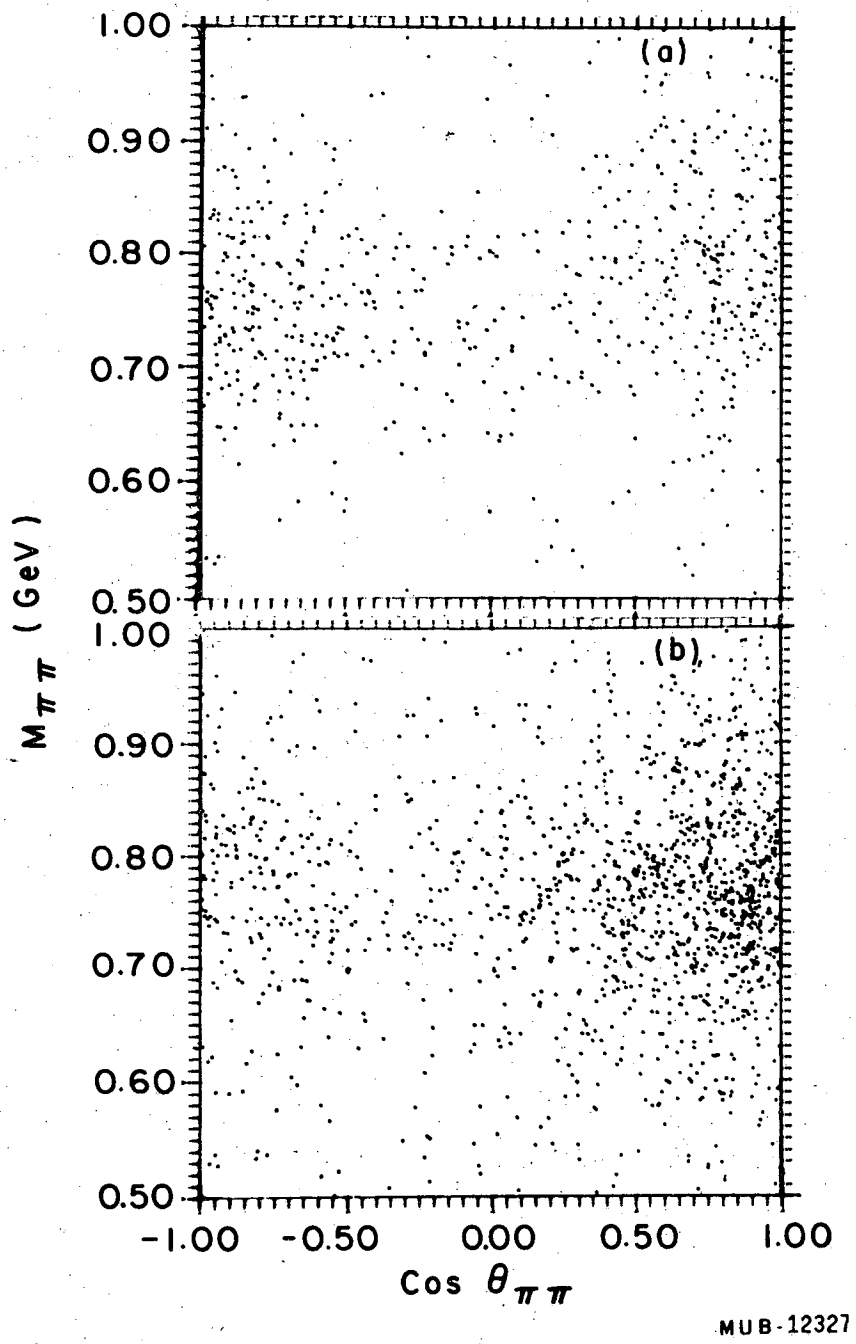

Fig. 60. Scatter plot of $M_{\pi\pi}$ vs $\cos\theta$ for events with $\Delta^2 \leq 4\, m_{\pi^0}{}^2$.

(a) $p\pi^0\pi^-$, 663 events

(b) $n\pi^+\pi^-$, 1500 events.

Fig. 61, show that it is isotropic in the charged combination but appears to have some asymmetry in the region of the ρ^0. In Fig. 62, we have selected various mass bands for events with $\Delta^2 \leq 10\ m_{\pi^0}{}^2$ and plotted the $\pi^0\pi^-$ $\cos\theta$ distributions. The curves are least-squares fits to a sum of Legendre polynomials, $\sum_{i=0}^{n} a_i P_i(\cos\theta)$. Because of their orthogonality, if we attempt a higher-order fit--i.e., $n \rightarrow n+1$--the various a_i, $i = 0 \cdots n$ do not change appreciably. This makes it easier to decide when the higher-order fit is preferable. In Table XII we have summarized the coefficients needed for the $\pi^+\pi^-$ distributions in Fig. 63.

The new features which emerge are that order 2 is good up to 1 GeV and is in accordance with the p wave's being resonant in the region 700 to 800 MeV. We note that A_0 has the same behavior as A_2, but as we show in the next section, this is not evidence for either an s-wave resonance or a background that peaks at the ρ. The $\pi^+\pi^-$ distribution is symmetric in the 1020- to 1110-MeV band. We show a fourth-order fit. The probability for second order is 2%, but since the next band contains a large amount of P_4, coming presumably from the f^0, we do expect some d-wave to be coming in. The $\pi^+\pi^-$ band containing the f^0 is shown with a sixth-order fit. The probability for fourth order is less than 1%. Experiments with higher-energy π^- beams--for example, Biswas et al.[53] at 8 GeV/c--show evidence that for $\pi\pi$ masses above 1600 MeV most of the events have the outgoing π^- going forward. At these energies $\pi\pi$ scattering becomes diffractive, which implies that several partial waves are contributing. We believe that the existence of f-waves in the region 1110 to 1380 MeV is thus not unreasonable. We are reinforced in this belief by the unimportance of the $\Delta^+(1238)$ in our events and by the fact that in Ref. 53 it seems to be entirely absent. The $\pi^0\pi^-$ distribution has a 28% probability for a sixth-order fit, but only 7% for second or fourth order. For consistency, we show the sixth-order fit.

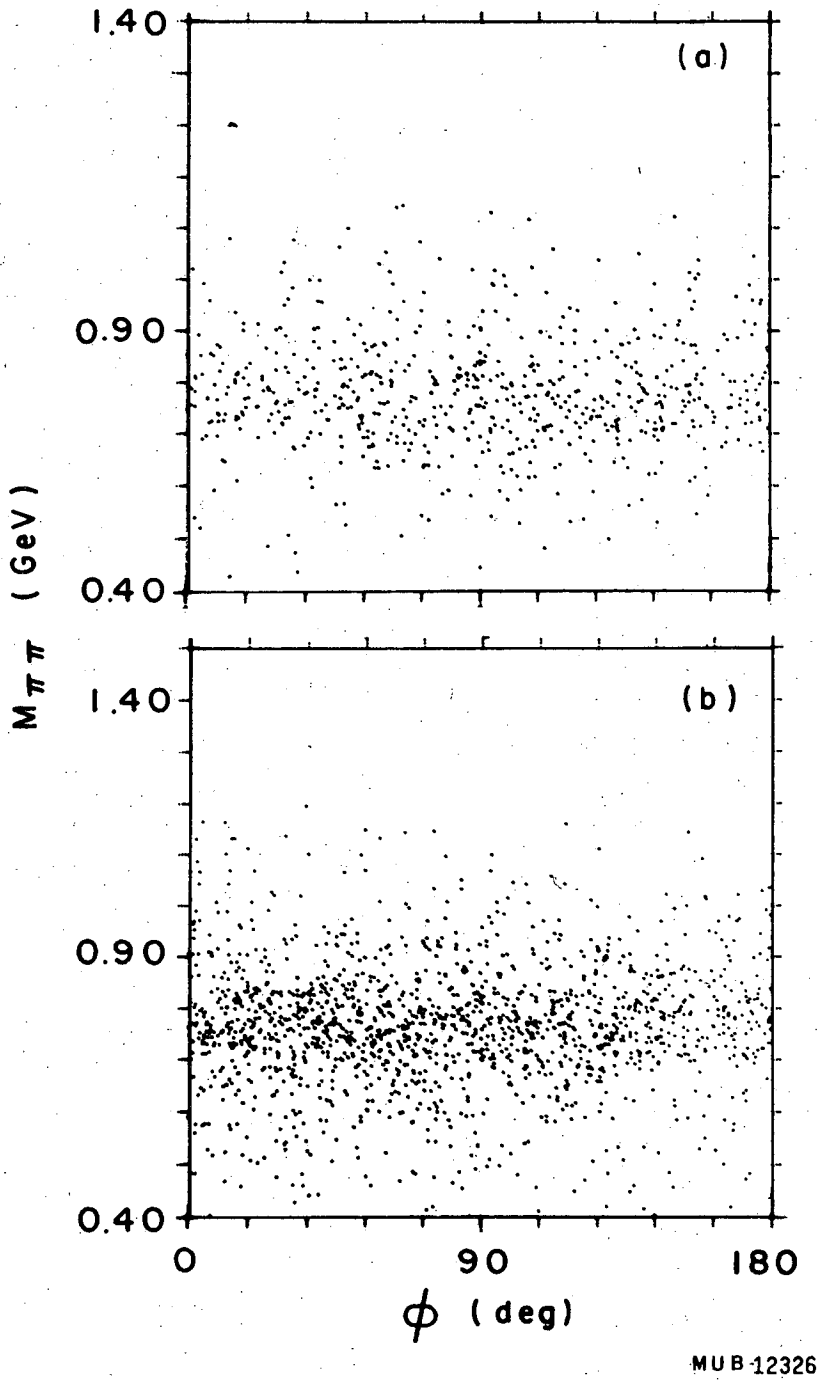

Fig. 61. Scatter plot of $M_{\pi\pi}$ vs ϕ (Treiman-Yang angle) for events with $\Delta^2 \leq 4 m_{\pi^0}^2$.
(a) $p\pi^0\pi^-$, 663 events.
(b) $n\pi^+\pi^-$, 1500 events.

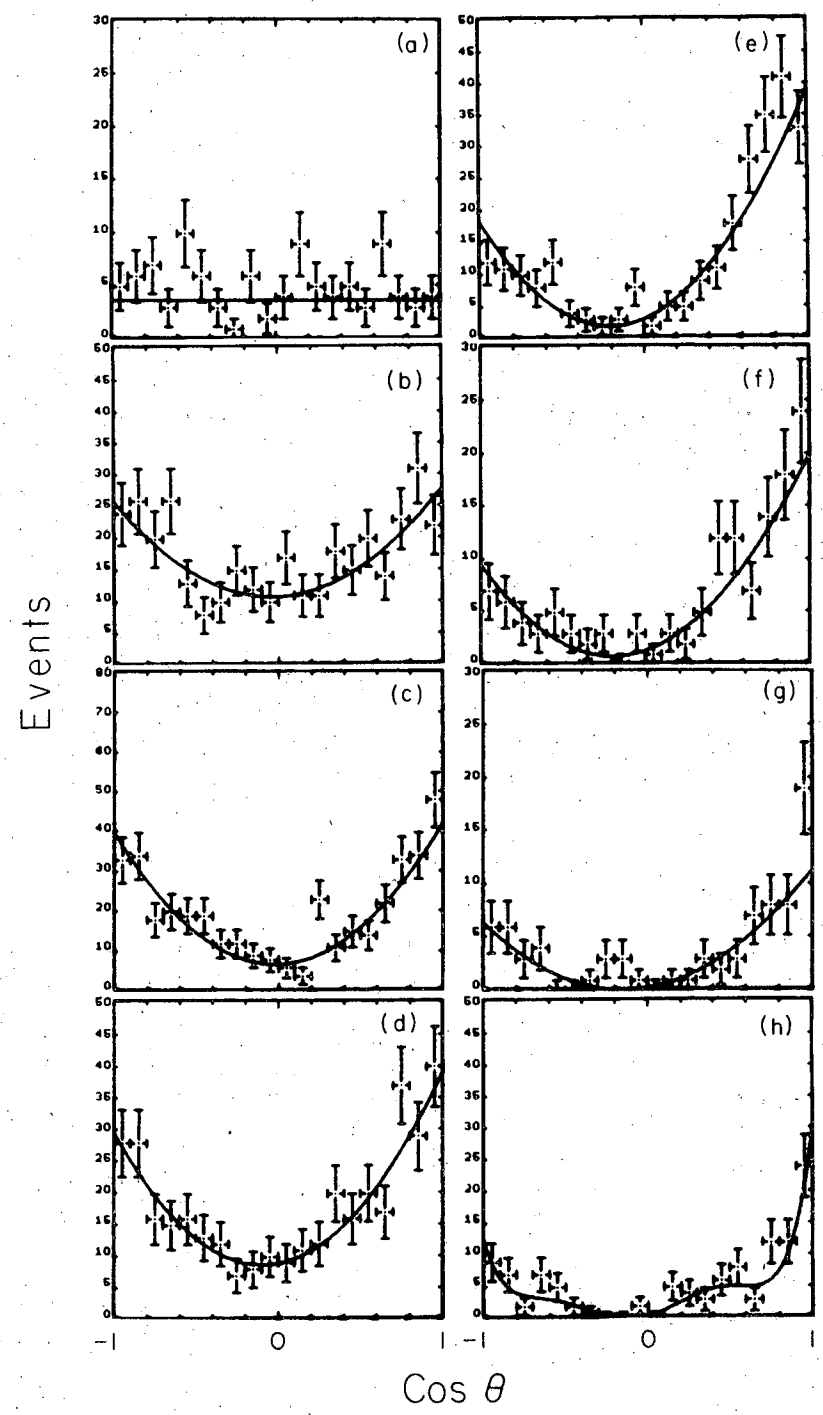

Fig. 62. Distributions of $\cos\theta$ for $p\pi^0\pi^-$ events with $\Delta^2 \leq 10 m_{\pi^0}^2$, showing least-squares fits to sum of Legendre polynomials.

(a) $M_{\pi\pi}$, 360-600 MeV, 99 events.
(b) $M_{\pi\pi}$, 600-720 MeV, 346 events.
(c) $M_{\pi\pi}$, 720-780 MeV, 394 events.
(d) $M_{\pi\pi}$, 780-840 MeV, 364 events.
(e) $M_{\pi\pi}$, 840-930 MeV, 260 events.
(f) $M_{\pi\pi}$, 930-1020 MeV, 134 events.
(g) $M_{\pi\pi}$, 1020-1110 MeV, 79 events.
(h) $M_{\pi\pi}$, 1110-1380 MeV, 112 events.

Table XII. Values of a_i in expansion $\frac{dN}{d\cos\theta} = \sum_{i=0}^{N} a_i P_i(\cos\theta)$ of $\pi\pi$ decay angular distributions.

Mass interval (GeV)	$\pi^0\pi^-$								$\pi^+\pi^-$							
	$P(\chi^2)$ (%)	a_0	a_1	a_2	a_3	a_4	a_5	a_6	$P(\chi^2)$ (%)	a_0	a_1	a_2	a_3	a_4	a_5	a_6
0.36-0.51	16.4	3.7 ±0.4							57.1	4.4 ±0.5	4.0 ±0.8	0.0 ±0.9				
0.51-0.60	37.2	16.4 ±0.9	1.4 ±1.7	10.9 ±2.2					45.3	6.3 ±0.6	5.8 ±1.0	3.0 ±1.4				
0.60-0.72	15.2	19.6 ±1.0	1.9 ±1.9	23.3 ±2.3					39.8	24.9 ±1.1	27.3 ±2.1	20.7 ±2.3				
0.72-0.78	87.8	17.2 ±0.9	5.4 ±1.8	17.4 ±2.3					0.3	30.7 ±1.2	27.1 ±2.4	29.9 ±2.9				
0.78-0.84	26.6	12.0 ±0.8	11.1 ±1.7	17.6 ±1.7					31.5	27.8 ±1.2	24.3 ±2.3	35.1 ±2.7				
0.84-0.93	60.1	6.0 ±0.6	5.6 ±1.1	9.1 ±1.2					88.6	21.0 ±1.0	21.0 ±2.0	24.9 ±2.4				
0.93-1.02	47.3	3.3 ±0.4	2.7 ±0.8	5.8 ±1.1					34.3	11.4 ±0.5	10.1 ±1.5	15.9 ±1.7				
1.02-1.11	28.3	4.9 ±0.5	4.5 ±1.1	9.6 ±1.5	3.0 ±1.8	4.9 ±1.9	4.1 ±1.8	4.7 ±1.9	10.1	5.2 ±0.5	0.5 ±1.2	10.1 ±1.5	-1.0 ±1.4	4.6 ±1.6		
1.11-1.38									2.8	12.9 ±0.8	15.8 ±2.0	3.2 ±2.6	15.5 ±2.8	20.1 ±3.2	6.6 ±2.7	3.9 ±2.9

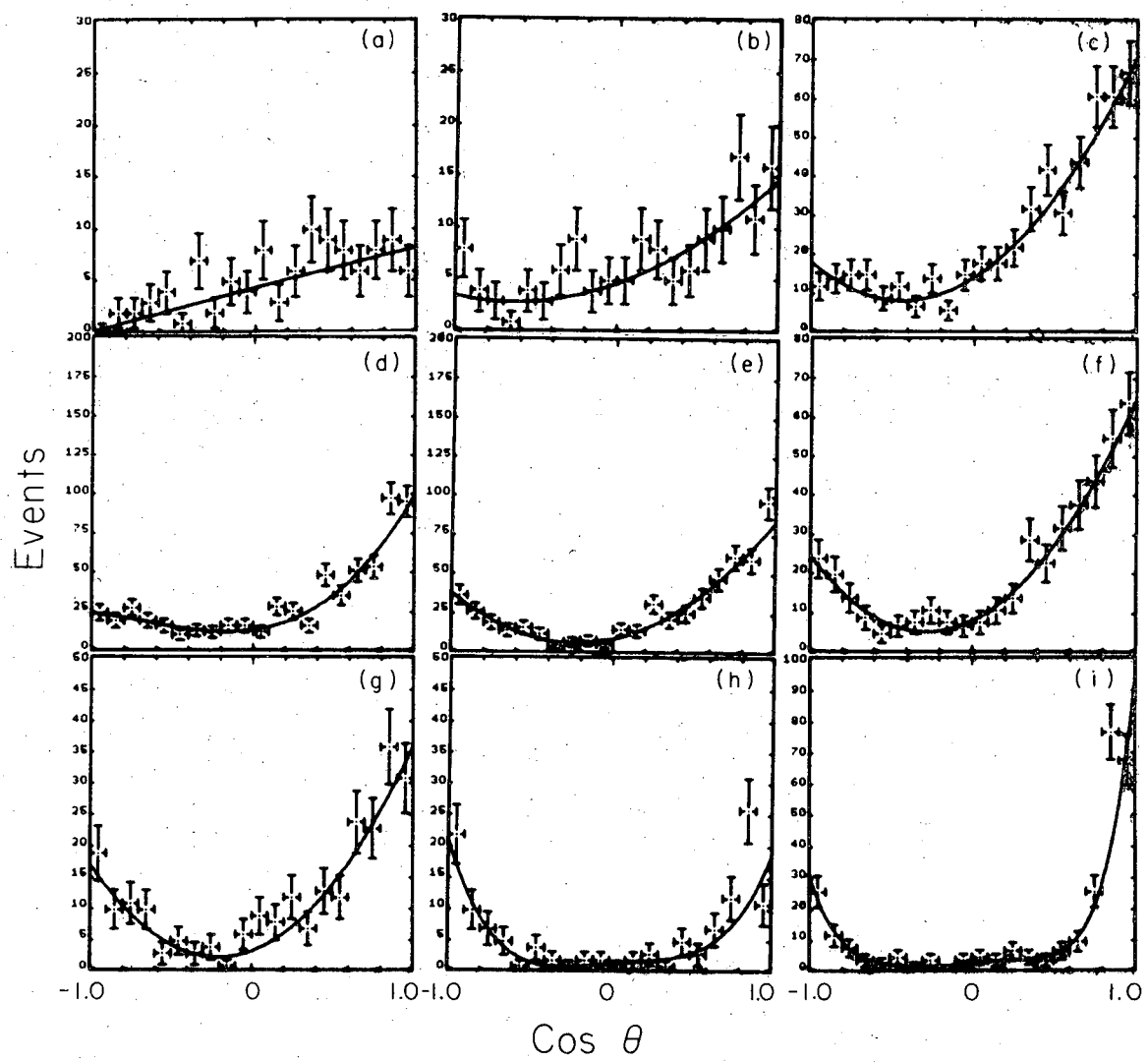

MUB 12546

Fig. 63. Distributions of $\cos\theta$ for $n\pi^+\pi^-$ events with $\Delta^2 \leq 10\, m_{\pi^0}{}^2$, showing least-squares fits to sum of Legendre polynomials.

(a) $M_{\pi\pi}$, 360-510 MeV, 103 events.
(b) $M_{\pi\pi}$, 510-600 MeV, 143 events.
(c) $M_{\pi\pi}$, 600-720 MeV, 515 events.
(d) $M_{\pi\pi}$, 720-780 MeV, 652 events.
(e) $M_{\pi\pi}$, 780-840 MeV, 572 events.
(f) $M_{\pi\pi}$, 840-930 MeV, 431 events.
(g) $M_{\pi\pi}$, 930-1020 MeV, 247 events.
(h) $M_{\pi\pi}$, 1020-1110 MeV, 127 events.
(i) $M_{\pi\pi}$, 1110-1380 MeV, 282 events.

Density matrix elements for the ρ

By expanding the $\cos\theta$ distribution as a sum of Legendre polynomials, we have in fact found the $m = 0$ multipole moments. We can extend this to the ρ and expand

$$\frac{d\sigma}{d\Omega_{\pi\pi}} = \frac{d^2\sigma}{d\cos\theta\, d\phi}$$

as a sum of spherical harmonics and determine the various $\langle Y_l^m \rangle$ from

$$\langle Y_l^m \rangle = \int d\Omega_{\pi\pi} \frac{d\sigma}{d\Omega_{\pi\pi}} Y_l^m(\theta,\phi).$$

To relate this to the well-known density matrix expansion of the angular distribution, which we discuss in the next section, we make use of the Clebsch-Gordan series,[54] which we write in the form

$$\frac{4\pi}{\sqrt{(2l+1)(2l'+1)}} Y_l^m(\theta,\phi)\, Y_{l'}^{*m'}(\theta,\phi)$$

$$= \sum_j \langle l\,-m,\, l'm' \,|\, j\; m'-m\rangle \langle l\,-m, l'm' | j0\rangle \sqrt{\frac{4\pi}{(2j+1)}}\, Y_j^{m'-m}(\theta,\phi).$$

We may derive the density matrix elements from a linear combination of the multipole moments.

f^0 production and decay distributions

In Fig. 64 we present the Δ^2 distribution for f^0 production, where we have selected events with the mass between 1140 and 1340 MeV. Figure 65 shows a scatter plot of ϕ and $\cos\theta$. The asymmetry and strong polar effect in $\cos\theta$ are obvious. The distribution in ϕ seems to be isotropic, exhibiting little correlation with $\cos\theta$. We contrast this with similar plots for the ρ (see Figs. 68 and 69). To describe the decay of a spin-2 particle, eight independent density matrix elements, $\rho^{(2)}_{mm'}$, are required. We have not attempted to determine them.

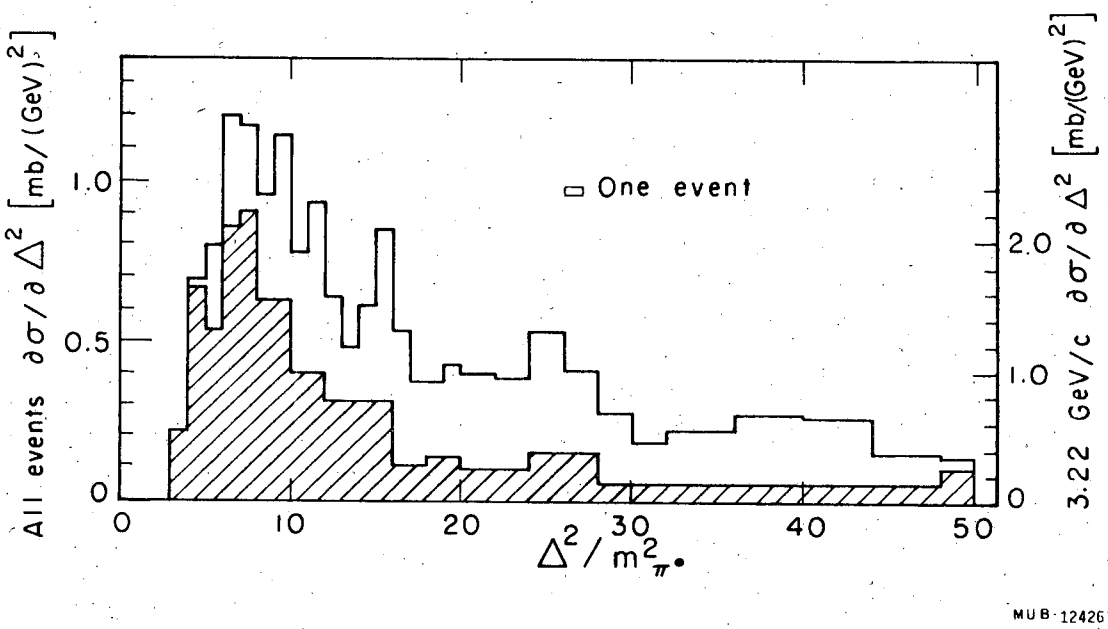

Fig. 64. f^0 ($M_{\pi\pi}$ 1140 to 1340 MeV), Δ^2 distribution. Events shown shaded are at 3.22 GeV/c.

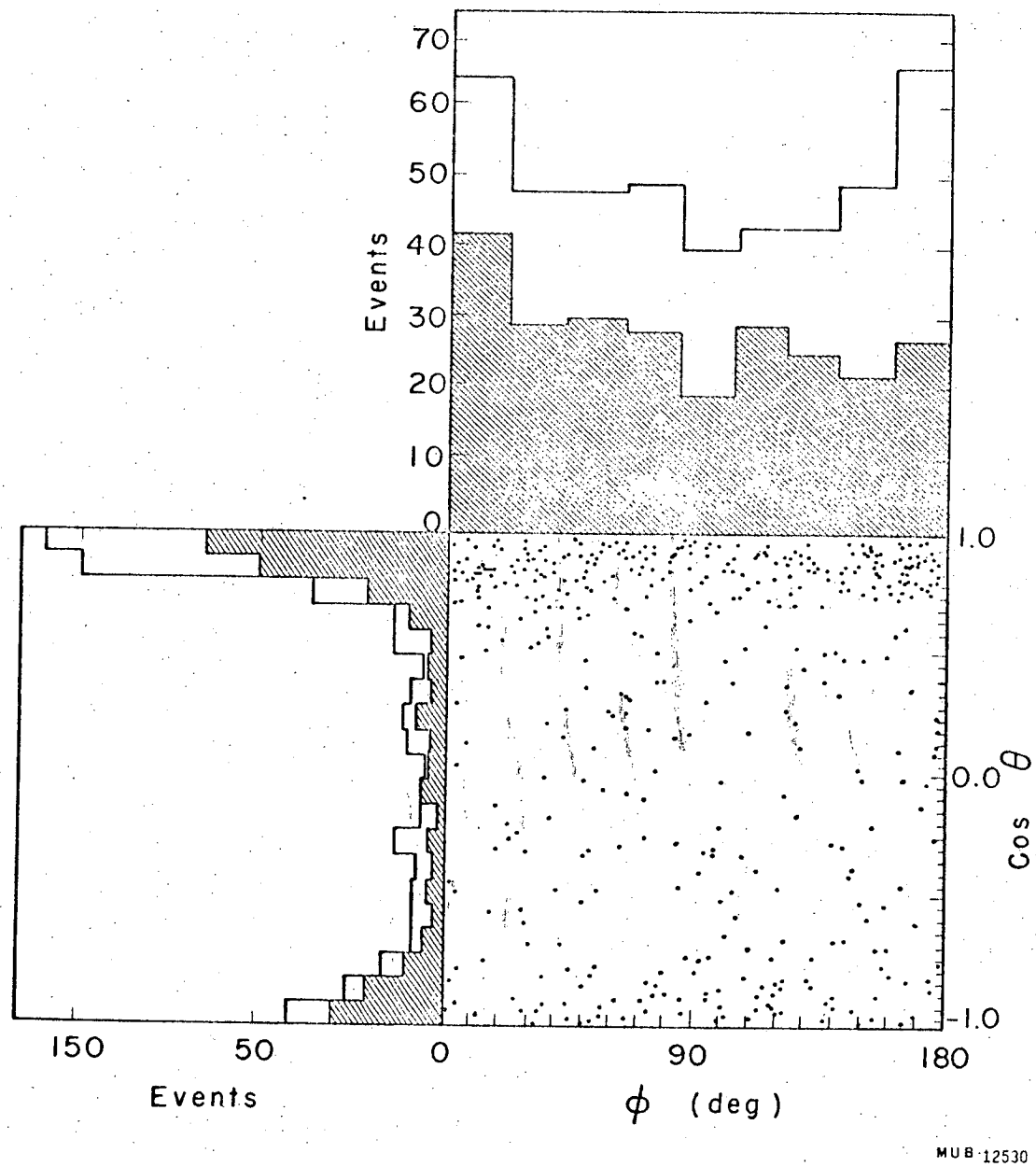

Fig. 65. Scatter plot of $\cos\theta$ vs ϕ for f^0 ($M_{\pi\pi}$ 1140 to 1340 MeV) and projected distributions of $\cos\theta$ and ϕ. Events shown shaded (260) are at 3.22 GeV/c. Total events, 459.

We conclude this descriptive section with an overall survey of the data contained in Figs. 66 and 67. This method of displaying data, due to Dr. Vasken Hagopian, shows the variation of the cross section with $m_{\pi\pi}$, Δ^2, $\cos\theta$, and ϕ. A quantitative description in terms of the OPE model as a function of these quantities is contained in the next section, which goes far towards explaining the observed distributions.

D. $\pi\pi$ Scattering and the Absorption Model

Discussion of peripheral interactions

We have shown in the preceding section that the reactions

$$\pi^- p \to n\pi^+\pi^- , \tag{1}$$

$$\pi^- p \to p\pi^0\pi^- \tag{2}$$

are dominated by production of the ρ meson. Taken over all available values of momentum transfer, the quasi-two-body reaction $\pi^- p \to N\rho$ is 1/3 to 1/2 of the three-body reaction. At low momentum transfer, $\Delta^2 \leq 5\, m_{\pi^0}^2$, the ratio rises to about 80%. The ρ is thus typically formed at low values of Δ^2 and the reaction $\pi^- p \to N\rho$ is characteristically a peripheral interaction. This leads one quite naturally to a model in which the reaction proceeds predominantly by OPE. The present form of the OPE model has been refined since its inception, but not beyond recognition.

A peripheral interaction is characterized by small momentum transfers. The colliding systems see each other only through a comparatively long-range interaction; the reaction takes place mainly through the high-angular-momentum components in a partial-wave expansion of the scattering amplitude. All these effects are characteristic of a reaction in which a single virtual particle is exchanged by the colliding systems. In general, in an inelastic reaction, one would like to select the exchanged virtual particle to correspond with the smallest momentum transfer between an incident and an outgoing particle. (However, in ρ^0 production, due to the special circumstances of the ρ^0 asymmetry, the smallest momentum transfer is usually between the π^- incident and π^- outgoing, and not between the two nucleons.)

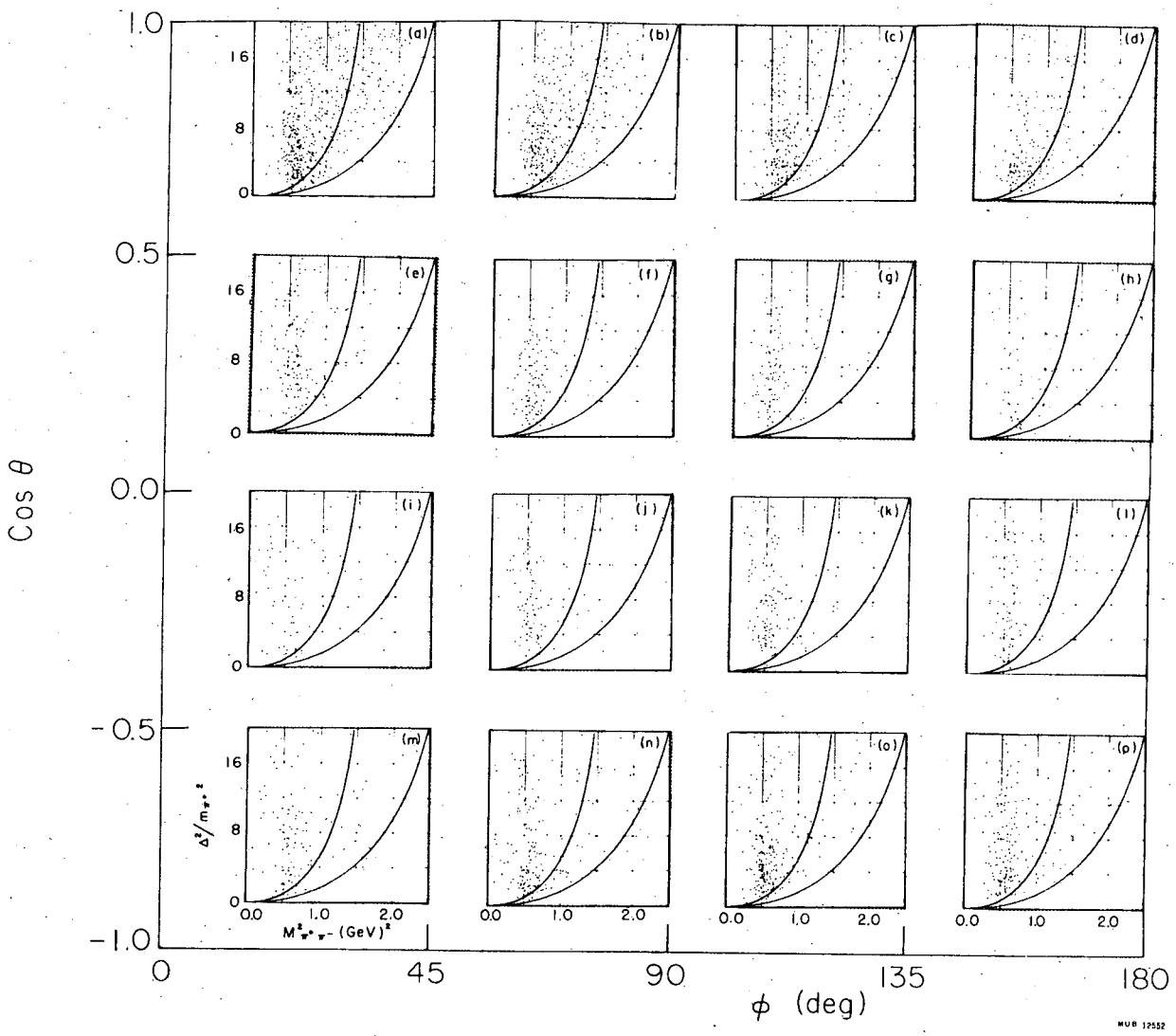

Fig. 66. $\Delta^2 - M_{\pi^0\pi^-}$ distributions for various $(\cos\theta - \phi)$ intervals, $\pi^- p \rightarrow p\pi^0\pi^-$.

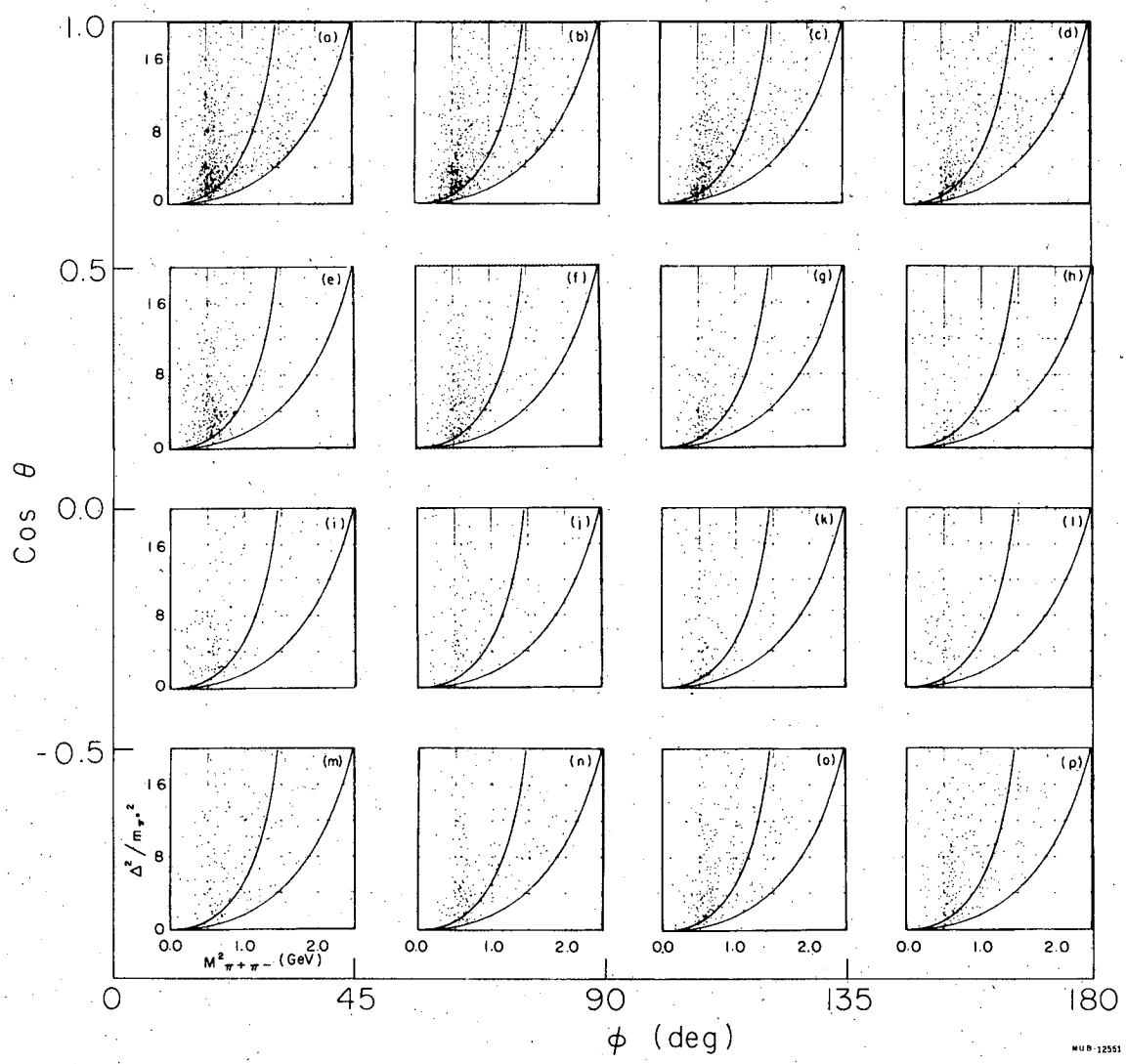

Fig. 67. Δ^2 - $M_{\pi^+\pi^-}$ distributions for various ($\cos\theta$-ϕ) intervals, $\pi^- p \rightarrow n\pi^+\pi^-$.

Chew and Low,[55] by considering the proximity to the physical region of the pole in the one-particle exchange amplitude, proposed a method of extrapolation from the physical to the unphysical region. Such an extrapolation was tried by Carmony.[56] Since the extrapolation procedure needs good statistics, and as a degree of arbitrariness was involved in its use,[57] it was found more convenient to extend the Chew-Low formula (see Appendix B) to the physical region of low momentum transfer. In the parlance of Ferrari and Selleri,[58] this is the pole approximation. Their contribution was twofold. In Ref. 59 Selleri makes the reasonable assumption that the effect of the virtual particles being off the mass shell--i.e., that $\Delta^2 \neq -\mu^2$, is not to alter the π-π phase shifts but to modify the π-π scattering amplitude by what is, in effect, a kinematic factor. In practical terms the Chew-Low formula for

$$\frac{\partial^2 \sigma}{\partial \omega^2 \partial \Delta^2}$$

becomes modified by a factor

$$\left[\frac{a\omega}{k}\right]^2 ,$$

where a_ω is the momentum of the beam pion in (for our case) the $\pi\pi$ rest system, and k the momentum of the decay pions. Jackson and Pilkuhn[60] derive $\partial\sigma/\partial\Delta^2$ for various types of meson exchange. The off-mass-shell factor occurs naturally from the coupling at the upper--i.e., three-meson--vertex. The second proposal of Selleri[59] is the controversial one. If, for simplicity, we examine pseudoscalar exchange, we see that

$$\frac{\partial \sigma}{\partial \Delta^2} \sim [F(\Delta^2)]^2 \, a_\omega^2 \, \frac{\Delta^2}{[\Delta^2 + \mu^2]^2} ,$$

where $F(\Delta^2)$ is some form factor which arises when the exchanged particle is off its mass shell; $(F(-\mu^2) = 1$. Also,

$$a_\omega = \frac{1}{2\omega} \sqrt{[\Delta^2 + (m_a + \omega)^2]\,[\Delta^2 + (m_a - \omega)^2]} ,$$

which, for large Δ^2, $\sim\Delta^2$. [m_a is the mass of the beam pion.] Hence $\frac{\partial\sigma}{\partial\Delta^2}$, for large Δ^2, increases with Δ^2. An ℓ-wave resonance according to this formulation will have a differential cross section as a function of Δ^2 that goes like $\Delta^{2\ell}$. To maintain some sort of agreement with experiment, for pseudoscalar exchange producing a vector meson, $F(\Delta^2)$ must necessarily go as $1/\Delta^2$. Thus there arises the famous form factor,[61]

$$F(\Delta^2) = 0.72/\left[1+\frac{\Delta^2+\mu^2}{4.73\,\mu^2}\right] + 0.28/\left[1+\left[\frac{\Delta^2+\mu^2}{32\,\mu^2}\right]^2\right],$$

which previous experiments[21, 23, 52] have shown gives good agreement for the differential cross section of the reaction $\pi^- p \to N\rho$. Since, for vector exchange and most other processes, besides ρ production, more drastic and arbitrary form factors are required--such as exponential factors whose effect really masks out the basic peripheral mechanism and which do alter the one-particle exchange model out of recognition--doubt has been cast not only on the whole business of form factors, mainly because their behavior is different from what is expected from a form factor, but also on exchange models in general.

Angular correlations

Treiman and Yang[62] pointed out that for all processes going by one-pion exchange there could be no correlation between the production plane of the process and the decay plane of the π-π systen as seen in the π-π rest frame because the exchanged particle is spinless and cannot, therefore, transmit any angular momentum information from one vertex to another.

While all the above is perfectly true, it remained for Jackson[63] to point out that although the Treiman-Yang angle can be defined in more than one way, what is really being described is the azimuthal angular dependence of the scattering of the incident beam particle by the exchanged particle. For OPE it is just π-π scattering. In the π-π rest frame the contribution to the magnetic quantum number m

and along the incident π direction comes from the orbital angular momentum, the incident pion, and the exchanged pion; $m = 0$. There is no azimuthal angular dependence for simple π-π scattering. For other exchange processes things are obviously more complicated. Gottfried and Jackson[64, 65] considered this problem and showed how the angular decay correlations gave information as to the angular momentum and parity properties of the exchanged system. In this work they first introduced the now familiar expression for the density matrix of the decaying system.

For the process $\pi N \rightarrow N\pi\pi$, the particles that can be exchanged are few. They can have only negative G parity. For $\pi^- p \rightarrow p\pi^0\pi^-$ the exchanged particle has to have zero charge. The possible candidates are π^0, ω, and A_2^0: For $\pi^- p \rightarrow n\pi^+\pi^-$ there is no available vector particle, and only the π^- and A_2^- can be exchanged. In the Δ^2 distributions for ρ^- production, Figs. 34 through 39, apart from the small effect at 2.60 GeV/c we observed no obvious secondary maximum that could be linked to ω exchange. They are qualitatively similar to the $\rho^0\Delta^2$ distributions. As to A_2 exchange, according to the principle of Occam's razor, there is no need to invoke its presence until one is forced to. In any case, experimental agreement with the predictions of the exchange model decreases as the spin of the exchanged particle increases.[66]

So, for $\pi p \rightarrow N\pi\pi$ we are in the fortunate position of having to consider only OPE. For ρ production, the angular distribution should have $\rho_{00}^{(1)} = 1$, and anything else should be zero. The decay angular distribution should be, apart from the background, $\cos^2\theta$ in the polar angle and flat in the azimuthal angle, ϕ.

Experimentally, the $\cos\theta$ distributions (Figs. 59, 60, 62, and 63) show the presence of a linear term, which suggests an interference. We shall return to this. The distributions in ϕ, Fig. 61, tend to be flat, except for some asymmetry near the ρ^0 and a slight but definite accumulation near 90° for the ρ^-. It would seem that the Treiman-Yang condition for OPE is fulfilled. However, only when we make a scatter

plot of the scattering angle versus azimuthal angle does the surprising fact emerge that there is definite structure in the Treiman-Yang angle, Figs. 68 and 69. The description of the reaction as involving π-π scattering must be modified. Is it possible to keep the peripheral model, preserve the concept of exchanging a pion, and yet explain the presence of nonzero magnetic quantum numbers along the incident beam direction? Before attempting to answer this we should note that no ad hoc form factor will give rise to the observed nonzero elements in the density matrix.

Absorption

Beginning about 1962 a phenomenological theory has grown up known loosely as the absorption correction to peripheral interactions.[67] It seeks to correct the defects, as outlined above, of the one-meson exchange model. The basic idea is the following. The peaking of the reaction cross section at low Δ^2 tells us that predominantly high-angular-momentum states are involved. The one-meson-exchange diagram involves mainly the high-angular-momentum states, but the observed differential cross section is even more peripheral. The wrong distribution of angular momentum states is being loaded into the matrix element. We must invoke another physical method of cutting down the low-angular-momentum states. In concept, the answer is easy. The lower the angular momentum, the larger is the cross section for non-peripheral processes and the lower the available cross section for any given peripheral process. The presence of highly inelastic channels depletes further the low-angular-momentum amplitudes, and the result is a sharpening of the Δ^2 distribution. It also results as we shall demonstrate later, in a depolarization of the angular momentum states of the resonance. Thus the absorption model has the required ingredients to explain the deviations from the predictions of the unmodified OPE model.

In most of the formulations of the absorption model the relationship between the absorbed amplitude and the unmodified Born amplitude is given by

	0	1	0	-1
0	0.05	-0.01	0.07	*
1	*	*	-0.12	0.04
0	*	*	0.72	*
-1	*	*	*	*

$M\pi^0\pi^-$ 650 - 850 MeV.

$\Delta^2 \leq 15\ \mu^2$.

$\pi^- p \to p\,\pi^0\,\pi^-$ 2.05 - 3.22 GeV/c

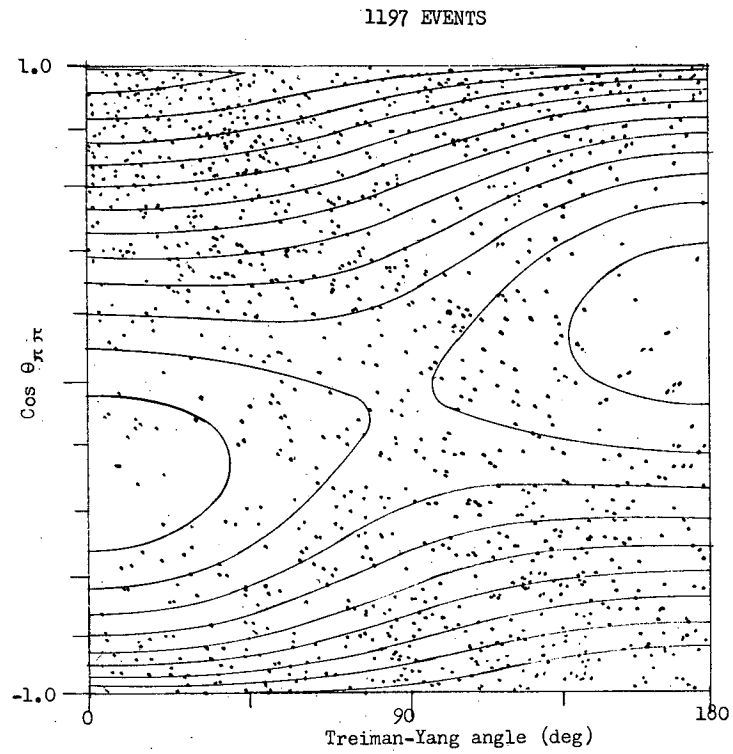

MUB-12621

Fig. 68. Scatter plot of $\cos\theta$ vs ϕ for ρ^-. Contour lines correspond to density matrix shown, which is calculated from the absorption model with C = 1.15 and A = 10 $(\mathrm{GeV})^{-2}$. A T = 2, $\pi\pi$ s-wave scattering length of -0.55 fermi is included in the calculation.

	0	1	0	-1
0	0.08	-0.04	0.21	*
1	*	*	-0.12	0.04
0	*	*	0.69	*
-1	*	*	*	*

$M\ \pi^+\pi^-$ 650 - 850 MeV.

$\Delta^2 \leq 15\ \mu^2$

$\pi^- p \to n\ \pi^+\pi^-$ 2.05 - 3.22 GeV/c

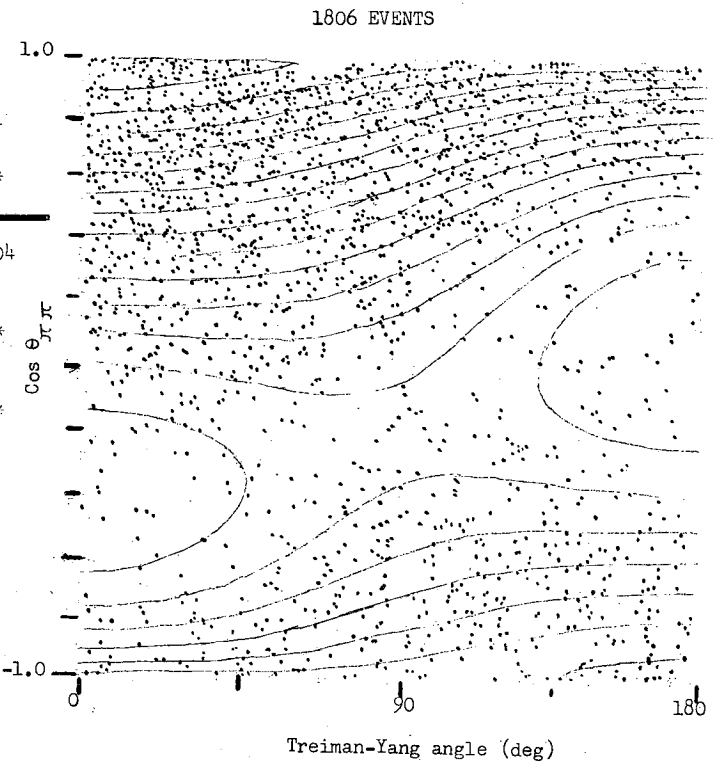

MUB-12622

Fig. 69. Scatter plot of $\cos\theta$ vs ϕ for ρ^0. Contour lines correspond to density matrix shown, which is calculated from the absorption model with C = 1.15 and A = 10 $(\text{GeV})^{-2}$. A δ_0^0 which increases from 40° to 100° in the mass interval 650 to 850 MeV is included in the calculation.

$$F_{fi}^{j} = \sqrt{S_{ff}^{j}}\; B_{fi}^{j} \sqrt{S_{ii}^{j}} \;,$$

Where S_{ff}, S_{ii} represent the S matrix for elastic scattering in the initial and final states, and the j is a label to represent the components in a partial-wave expansion. For these S-matrix elements, by assuming a Gaussian dependence for the elastic differential cross section

$$\frac{d\sigma}{d\Omega} \sim e^{-A\Delta^2}$$

and that the elastic amplitudes are imaginary, we can write the elastic amplitude as

$$f\,[\Delta, q] = i\,\frac{\sigma_T q}{4\pi}\, e^{\left[-\frac{1}{2} A \Delta^2\right]} \;,$$

and carry out a Fourier-Bessel transform to obtain

$$\sqrt{S^j} = 1^{iX} = 1 - \frac{\sigma_T}{4\pi A}\; e^{\frac{-[j - j_{mm}-]^2}{2Aq^2}} \;.$$

When this expression is put into the above formula for the absorbed amplitudes we see how the partial-wave amplitudes get reduced and how the reduction is greatest in the s- and p-wave components.

It is agreed that the formula for absorption gives generally good agreement with experiment, but it has so far been impossible to derive the formula rigorously. To mention just one inconsistency, the formula can be derived in nonrelativistic quantum mechanics by use of the Schrödinger equation and the concept of potentials; in this case a necessary condition is that the range of the exchange potential should be less than the extent of the absorption region, whereas this is precisely not so, and the best agreement with theory, OPE, maximally violates the condition. We shall not discuss the theoretical bases for absorption nor discuss the commonly presented development of the theory as it is applied to experiment by Gottfried and Jackson and by Durand and Chiu, but will make reference to a different presentation of an absorption calculation by Robert Huff.

Above we decomposed the amplitude into partial waves and introduced the absorption at each value of the c.m. angular momentum, making explicit the varying absorption with the c.m. angular momentum. In Huff's formalism the absorption is introduced into a framework built round the canonical conjugate variable to angular momentum, namely, angle.

Without analyzing any inherent virtues of this "linear momentum representation" which might make it a more suitable vehicle on which to mount an absorption calculation, we could make two simple observations. The expressions for the absorption came from the elastic scattering differential cross section, and are thus explicitly functions of the scattering angle. Secondly, the summing over all intermediate states at which the reduction of amplitude is made consists of integrating over all values of the c.m. scattering angle. As a procedure this seemed more accurate and simpler than the approximations involved in the angular momentum approach, in which the summation over j gets replaced by an integration over impact parameter, and the rotation coefficients of the first and second kinds, $d^j_{\mu\lambda}(\Theta)$, $e^j_{\mu\lambda}(z)$, by Bessel and Hankel functions, respectively. However Durand and Chiu[68] and Högaasen et al.[66] have shown that it is possible and fairly straightforward to perform an exact summation. Further, to evaluate an integral numerically on the computer involves a summation, and as it turned out in the Huff approach, a double integral comes into absorbed matrix element [see Eqs. (C-34)-(C-36)]. As regards computing procedure, the advantages of the Huff procedure are not so attractive as they initially seemed. As in the angular momentum approach, there are two parameters for the absorption, a total cross section σ_T from which we derive the forward scattering amplitude, and an exponential elastic scattering slope A. In Appendix C we have included, by courtesy of Dr. Huff, a full exposition of the absorption calculation in the linear momentum representation. In it we arrive at formula (C-34),

$$F_{\mu\lambda}[\Theta] = B_{\mu\lambda}[\Theta] - \int d\cos\ \Theta_i\, B_{\mu\lambda}[\Theta_i]\, Q^0\,[\Theta,\Theta_i],$$

which relates the Born helicity amplitude to the absorbed amplitude. Q^0 is itself an integral,

$$Q^0 \sim \int d\Phi_i R[\Theta_{i0}]\ f[\Theta, \Theta_i, \Phi_i],$$

where f is a function of the angles such that $|f|^2 = 1$ and

$$R[\Theta_{i0}] \sim e^{-Aqq'[1-\cos\Theta_{i0}]},$$

where Θ_{i0} is the angle between the direction of Θ, the c.m. scattering angle, and the intermediate scattering angle $\hat{\Omega}_i = [\Theta_i, \Phi_i]$.

We see that the maximum contribution to Q^0 comes from the region where Θ and $\hat{\Omega}_i$ are collinear, i.e., $\Theta_{i0} = 0$. The effect of the integral operator on $B_{\mu\lambda}(\Theta)$ is to generate a new function, which is a smoothed-out version of $B_{\mu\lambda}(\Theta)$. Subtracting a smoothed-out version of itself from $B_{\mu\lambda}(\Theta)$ gives rise to the collimation effect. Where $B_{\mu\lambda}(\Theta)$ is already smooth--i.e., at high Δ^2-- the two functions are similar and the difference is small. At low Δ^2, where $B_{\mu\lambda}(\Theta)$ has a peak and a large derivative, the two functions are dissimilar and their difference is large.

Depolarization

It is obvious from the discussion above how the differential cross section as a function of Δ^2 gets modified. What is not so obvious and what should be demonstrated is how the depolarization of the π-π states comes about. We shall discuss this first purely in terms of production of the ρ meson, but by then it will become more transparent how to account for interference effects and still adhere to the absorption model.

For unmodified OPE we can write, for the invariant $\pi\pi$ scattering amplitude,

$$\mathcal{J}_{\pi\pi} = 8\pi\omega f(\theta)$$

$$= 8\pi \frac{\omega}{k} \sum_l [2l+1]\, e^{i\delta_l} \sin\delta_l \left[\frac{a\omega}{k}\right]^l P_l[\cos\theta],$$

where we have pedantically included the off-the-mass-shell correction, $\left[\frac{a\omega}{k}\right]^l$.

Restricting the summation to $l = 1$ gives the p-wave scattering amplitude

$$\mathcal{J}_{\pi\pi} = 8\pi \frac{\omega}{k} \; 3 e^{i\delta_1} \sin\delta_1 \left[\frac{a_\omega}{k}\right] \cos\theta$$

$$= 8\pi \frac{\omega}{k} \sqrt{12\pi} \; e^{i\delta_1} \sin\delta_1 \left[\frac{a_\omega}{k}\right] Y_0^1 [\theta, \phi]$$

$$= A_0^1 \, Y_0^1 [\theta, \phi],$$

which gives rise to the δ decay angular distribution

$$W(\theta, \phi) = 3/4\pi \cos^2\theta.$$

Here $\rho_{00}^{(1)} = 1$ and all other density matrix elements vanish. The discussion so far has all taken place in the $\pi\pi$ rest frame. However, absorption effects are calculated in the overall c.m. frame in a helicity representation, since we compute the effect of initial- and final-state absorption on amplitudes that connect the various helicity eigenstates. Hence it is instructive to transform the $\pi\pi$ scattering amplitude and density matrix to this same overall c.m. frame.

If Θ is the c.m. scattering angle, and Ψ is the angle between the incident beam pion and the direction of the ρ meson and incident pion in the ρ rest frame, we have the following relationship arising from the Lorentz transformation from one frame to the other:

$$\sin\Psi = \frac{q}{a_\omega} \sin\Theta ,$$

$$\cos\Psi = \frac{E_\omega}{\omega} [\cos\Theta - \alpha] \frac{q}{a_\omega} ,$$

$$\text{where } \alpha = \frac{q' E_a}{q E_\omega} ,$$

where the symbols are defined in Appendix B.

The ρ amplitudes transform like a vector under Lorentz transformation,

i.e., $\mathcal{A}^1_m \to d^1_{\mu m}(-\Psi)\,\mathcal{A}^1_m = \hat{\mathcal{A}}^1_\mu$,

$$\rho^{(1)}_{00} \to d^1_{\mu 0}(-\Psi)\, d^1_{0\mu'}(-\Psi) = \hat{\rho}^{(1)}_{\mu\mu'} ,$$

where $\hat{\mathcal{A}}^1_\mu$ and $\hat{\rho}^{(1)}_{\mu\mu'}$ are the $\pi\pi$ scattering amplitudes and density matrix in a helicity representation.

The Born helicity amplitudes for the OPE process contain the factor $\hat{\mathcal{A}}^1_\mu$, where μ denotes the ρ helicity, as well as the contribution from the $NN\pi$ vertex and the propagator. When we Lorentz-transform back to the $\pi\pi$ c.m. we rotate the matrix elements by the angle Ψ, and arrive back with only $\mathcal{A}^1_0$ nonzero and $\rho^{(1)}_{00} = 1$. However, any tampering such as that outlined in Appendix B due to absorption, or what have you, of the helicity amplitudes followed by the rotation will certainly give nonzero $\mathcal{A}_1$, $\mathcal{A}_{-1}$ amplitudes as well as nonvanishing off-diagonal density matrix elements.

The effect of the absorption, which we take as the model producing this depolarization, may be represented by writing the invariant amplitudes for the ρ as

$$\mathcal{A}^1_m = 8\pi \frac{\omega}{k} \sqrt{12\pi}\; e^{i\delta_1} \sin\delta_1 \frac{a_\omega}{k}\, C_{1m} ,$$

where $|C_{1m}| \leq 1$ and $T_r\,[C_{1m}\, C^*_{1m'}] \leq 1$.

The question arises as to the significance of amplitudes with nonzero m. For genuine π-π scattering there can be no terms with $m \neq 0$. But the effect of the initial- and final-state absorption on the process, looked at as $\pi\pi$ scattering, is that the incident wave can no longer be thought of as a plane wave. The presence of the proton in the initial state causes an asymmetry in space, giving rise to the dependence on azimuthal angle ϕ.

The extension of these ideas to other partial waves is now seen to be trivial.

For the invariant scattering amplitude we have

$$\mathcal{T}_{\pi\pi} = \sum_{l}\sum_{m} \mathcal{A}^{l}_{m}\, Y^{l}_{m}(\theta,\phi),$$

where $$\mathcal{A}^{l}_{m} = 8\pi\frac{\omega}{k}\sqrt{4\pi}\sqrt{2l+1}\; e^{i\delta_l}\sin\delta_l\left[\frac{a_c}{k}\right]^{l} C_{lm},$$

and the density matrix

$$\rho^{(l,l')}_{mm'} = \frac{\mathcal{A}^{l}_{m}\,\mathcal{A}^{l'*}_{m'}}{T_r\left[\mathcal{A}^{l}_{m}\mathcal{A}^{l'*}_{m'}\right]},$$

where in the computation of the bilinear form the summation over nucleon helicities in the OPE model is also implied.

One could proceed from here to treat the angular distributions

$$W(\theta,\phi) = \sum_{l}\sum_{m} \rho^{(l,l')}_{mm'}\, Y^{l}_{m}(\theta,\phi)\, Y^{l'}_{m'}(\theta,\phi)$$

and fit them with a reasonable set of parameters as follows. The elements of the density matrix are determined by the average value of the various phase shifts over the mass interval considered and the amount of absorption, which depends on the Δ^2 interval and is reflected in the values of the C_{lm}'s. A suitable parameterization would then be a set of phase shifts--some of which may have been determined previously by other means--and a set of values for C_{lm}. This would be a most general sort of parameterization, and makes no assumptions as to the nature of the cause of the depolarization. For the events of interest in this experiment this was not done, but a more ambitious parameterization was attempted based on the absorption model.

As we have outlined already, the effect of the absorption model is to give depolarization of the $\pi\pi$ angular momentum states. It requires two parameters, which implicitly determine the C_{lm}'s. The phase shifts still remain to be determined.

To write down the Born helicity amplitudes, as is done in Appendix B, is perfectly straightforward, and follows from the foregoing discussion. What is not clear conceptually is the physical meaning of an absorption modification to such an amplitude. A given helicity amplitude relates to a OPE process where the two final pions are in some angular momentum and isospin state. Such a three-body final state will have a final-state interaction, but we are presented with an imponderable if we attempt to describe it. Omnes,[69] however, in talking about eigenstates of the S matrix (see Appendix C), maintains that his treatment of absorption is "not restricted to the case in which the final system of particles excluding the nucleon can be treated as a particle." Accordingly we have gone ahead and used the same formalism irrespective of the nature of the $\pi\pi$ final state and, as it turns out, have even used the same parameters A, C. The two absorption parameters might change as the mass of the $\pi\pi$ system varies, but we have suppressed this degree of freedom. We note, however, that the parameter $\gamma = 1/2_{qq'}A$ is a function of $\pi\pi$ mass.

In effect the fit is a phase-shift analysis of π-π scattering, where we have corrected the OPE model by absorption. The question may be asked: if the main interest is really the determination of the phase shifts, is the introduction of absorption really necessary or does it obfuscate the issue? It has been stated[70] that the dependence on the azimuthal angle is not large and, in any case, is of such a symmetry as to cancel out its effect. While this may or may not be true, we make the point that a fit that includes the extra information in the ϕ dependence and which does not introduce too many extra parameters is to be preferred to one that makes an assumption that is blatantly partially wrong. We make two further points. To investigate the behavior of the s-wave phase shift we direct our attention, in the main, to the (F-B)/(F+B) asymmetry in the $\cos\theta$ distribution. For a given set of s and p phase shifts the value of the observed asymmetry depends on the absorption--the maximum asymmetry being observed when there are no absorption effects. Lastly, any fit to the data in terms of a power-series

expansion of the decay angular distribution in $\cos\theta$ that makes no reference to the depolarization will yield some false conclusions. Let us illustrate this point by reference to Fig. 70. This shows data with $|\cos\theta| \leq 0.3$ and $\Delta^2 \leq 4\mu^2$. We see enhancements in the mass distribution in the region of the ρ^0 and the ρ^-. The presence of these events can easily and naturally be accounted for by the absorption. The elements of the density matrix, $\rho_{11}^{(1)}$ and $\rho_{-1,-1}^{(1)}$, are nonzero. However, according to the simple OPE model, the probability for finding events with $|\cos\theta| \leq 0.3$ is very small, and explanations outside the model must be sought. Resort can be made to a background term (see Fig. 9 of Ref. 71) or some other resonance in the region, Ref. 72. If we return briefly to the effect of absorption on the s-p interference it is possible to show that a phase-shift analysis based on a power series in $\cos\theta$ will come up with the wrong value of the phase shifts if absorption is neglected.

Including the interference terms, we have

$$\int_0^{2\pi} W(\theta,\phi)\, d\phi =$$

$$\frac{1}{2}\rho_{00}^{(0)} + \frac{3}{2}\left[\rho_{00}^{(1)}\cos^2\theta + \rho_{11}^{(1)}\sin^2\theta\right] + \sqrt{3}\,\rho_{00}^{(1,0)}\cos\theta$$

$$\rho_{00}^{(0)} + \rho_{00}^{(1)} + 2\rho_{11}^{(1)} = 1.$$

As we have stated earlier, the density matrix elements and, in particular, $\rho_{00}^{(1,0)}$, depend on the phase shifts and the C_{lm}'s.

Ignoring the C_{lm}'s is tantamount to putting in a different value for δ_l.

We may write

$$C_{lm}\, e^{i\delta_l} \sin\delta_l = \eta_l\, e^{i\delta_l'} \sin\delta_l' \quad ,$$

where if we have $C_{lm} = |C_{lm}|\, e^{i\chi}$,

$$\delta_l' = \delta_l + \chi$$

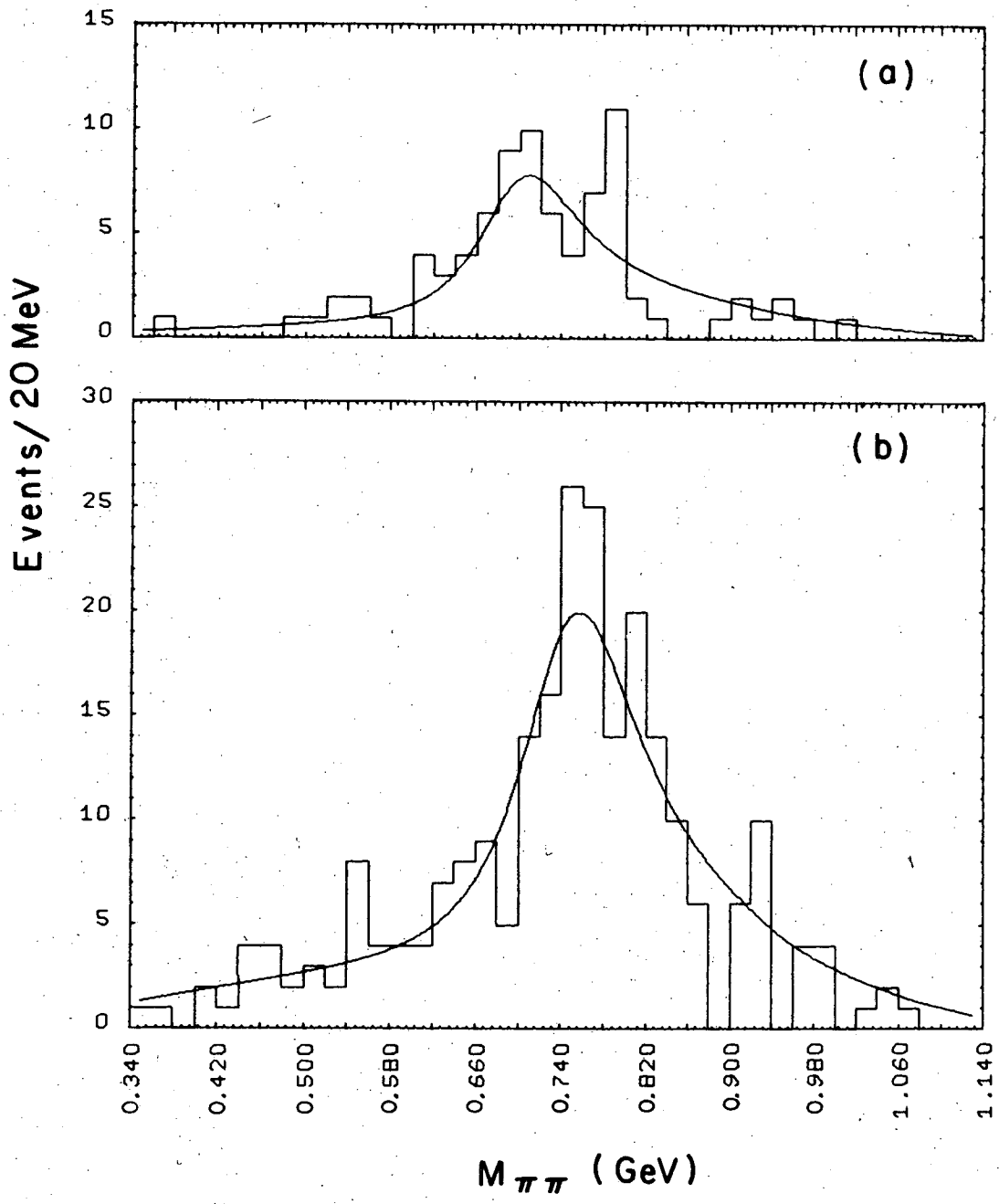

MUB-12325

Fig. 70. $\pi\pi$ invariant-mass spectra with $\Delta^2 \leq 4\, m_{\pi^0}{}^2$ and $|\cos\theta| < 0.3$, showing the presence of the depolarization in the p wave. Curves are p-wave resonances and background.
(a) $p\pi^0\pi^-$
(b) $n\pi^+\pi^-$.

and

$$\eta_1 = \frac{\sin[\delta_1 + \chi]}{|C_{1m}| \sin \delta_1} ,$$

η_1 could fake an inelasticity, but it is possible for $|\eta_1| > 1$.

In the absorption model treatment, following Gottfried and Jackson,[73] we have assumed a purely imaginary elastic scattering amplitude. Thus our C_{1m}'s are real. Any phase shifts we may determine will also suffer, in part, by including any phase that the actual absorption may introduce and that we have neglected.

Fit to the data

We have set up a very elaborate model with which to compare our experimental data. As a model it is the only one that predicts the sort of angular correlations that are observed. There are two parameters in the absorption theory which we must somehow choose, if we can, so that the model will give good quantitative agreement with experiment. We must also do the same with the phase shifts, but in this case we can make some simplifying assumptions. For the range of $\pi\pi$ effective mass that we are dealing with, $m_{\pi\pi} \leq 1.5$ GeV, it seems reasonable to consider five phase shifts, $\delta_1^I = \delta_1^1$, δ_0^0, δ_0^2, δ_2^0, and δ_2^2. Two of the phase shifts are associated with peaks in the mass spectrum, and we use this to represent them by a Breit-Wigner formula. There are grounds for believing that δ_2^2 is small,[52,72] with the same sign as δ_0^2. In our fits to the $\pi^0\pi^-$ $\cos\theta$ distributions (Fig. 62) we did not need P_4 below $m_{\pi\pi} = 1$ GeV. In this section we have considered its effect to be less than the approximations of the theory as applied to this sample of data. δ_0^2 itself is represented by the Chew-Mandelstam effective range formula[74]

$$\cos \delta_0^2 = \frac{\omega}{k} \frac{1}{2a_0^2 \mu} + \alpha,$$

where

$$\alpha = \frac{2}{\pi} \log_e \left[\frac{k + \frac{1}{2}\omega}{\mu} \right] .$$

This leaves δ_0^0; we defer discussion of this until we consider the ρ^0 in detail.

In a three-body final state, there are five independent scalar invariants that we can construct from the various initial and final momenta of the particles. We can keep any four fixed and obtain the differential cross section with respect to the fifth. In this work, the obvious variables to choose have been ω^2, Δ^2, $\cos\theta$, and ϕ. The fifth variable is the total c. m. energy, $E_{c.m.}$. The OPE model tells us exactly how $E_{c.m.}$ comes into the matrix element. At low beam energies, 2 GeV/c or less, certain low values of Δ^2 will not be available for ω above a certain value. However, the major dependence on $E_{c.m.}$ comes in through the flux factor, $1/\mathcal{F}^2$. With the introduction of absorption, further c. m. energy-dependent effects could be introduced by allowing σ_T and A, the two absorption parameters, to vary with $E_{c.m.}$. We know, however, from Table VI that the absorption parameters vary slowly in this region for $\pi^- p$. We therefore regard σ_T and A as independent of beam energy, and in our parameterization they are averaged over the span of beam momenta 2.05 to 3.22 GeV/c. We have already shown in Table IX and in Figs. 34 through 39 and 48 that there is general agreement with the OPE energy dependence, and in particular the factor $2.5 = [3.215/2.05]^2$ between the two extreme energies. Accordingly in our treatment of the data we have lumped all six beam energies together.

Determination of parameters

We use the following values for the mass and width of the ρ found at low Δ^2 in the previous section:

for the ρ^0, $m_c = 758 \pm 5$ MeV, $\Gamma_0 = 141 \pm 10$ MeV;

for the ρ^-, $m_c = 754 \pm 5$ MeV, $\Gamma_0 = 146 \pm 10$ MeV.

For the f^0 we found

$m_c = 1267 \pm 10$ MeV, $\Gamma_0 = 99 \pm 10$ MeV.

The phase shifts are then related by formula (B-26), where

$$\Gamma^{(l)} = \Gamma_0^{(l)} \left[\frac{a_\omega}{a_c}\right]^{2l+1} \frac{m_c}{\omega} .$$

With respect to the determination of the other phase shifts and the absorption parameters, two alternative procedures suggest themselves. In the first, we could consider both final states, $\pi^- p \to p\pi^0\pi^-$ and $\pi^- p \to n\pi^+\pi^-$, together. As we have demonstrated earlier, the ratio of ρ^0 to ρ^- production is not in accord with the OPE prediction of 2:1. We would be obliged to use the model to explain the discrepancy by using different absorption parameters for the ρ^- and the ρ^0. We would prefer to test the theory in this experiment and leave this particular question until more light can be shed on it by other sorts of experiments, e.g., actual form-factor effects. The other advantage that might accrue to us is that we would be treating the T = 2, s-wave $\pi\pi$ interaction simultaneously. However, the gain from including the extra information in the $\pi^+\pi^-$ distributions would be more than offset by the fact that in the $\pi^+\pi^-$ case the T = 2 interaction contributes to the s-wave amplitude coherently with the T = 0 interaction, whose effect is difficult enough to describe properly and which is, in actuality, our main interest.

We therefore followed the second procedure, which avoids these pitfalls, and study the two final states separately. Ideally, to get at the T = 2 interaction we would like to study $\pi^+\pi^+$ or $\pi^-\pi^-$ states, e.g., $\pi^- p \to \Delta^{++}(1238)\,\pi^-\pi^-$, to determine the behavior of the s- and d-wave T = 2 phase shifts. However, in this experiment we use the $p\pi^0\pi^-$ final state, not only to find the ρ absorption parameters but also a_0^2, the T = 2, s-wave scattering length in the Chew-Mandelstam formula. We then use these parameters in considering the $n\pi^+\pi^-$ final state.

We undertook a maximum-likelihood fit to the $p\pi^0\pi^-$ data with results that were only partially successful. Events were chosen with $\Delta^2 \leq 20\,\mu^2$. For each event the probability of its occurrence was constructed by computing $\partial^4\sigma/\partial\omega^2\partial\Delta^2\partial\Omega_{\pi\pi}$, using absorbed OPE helicity amplitudes, and was normalized by dividing by the integral of the rate over the physical limits of Δ^2, ω^2, and $\Omega_{\pi\pi}$. For the integral we used one setting of beam momentum interval. For the rate itself we used the five measured quantities $E_{c.m.}$, ω^2, Δ^2, $\cos\theta$, and ϕ of the event in question.

The actual mechanics of the program were as follows. A maximum value of Δ^2 was read into the computer. The input file containing the events, ordered by increasing momentum transfer, was then read in until the maximum value of Δ^2 was reached. For each event the five kinematic quantities were read in and stored together with a weight. This weight compensates for the scanning bias against protons with low momentum transfer, and is calculated from the beam azimuthal distribution of elastic scatterings (q. v.). With this set of parameters we compute the integral over the relevant area of the Chew-Low plot for all six beam-momentum settings. We then calculate the probabilities of events in the sample and form the logarithm of the likelihood function. We also calculate the probabilities with parameters incremented by small amounts to obtain numerically the first and second derivatives of the likelihood function. This part of the program is due to Dr. Philippe Eberhard, and seeks a maximum likelihood by a Newtonian method. It should be obvious that demands on storage space and the complexities in the computation of the rate--which involves a double integral--make it absolutely essential for the calculation to be done on a big fast computer. In December 1965 a CDC 6600 was delivered to the Laboratory. Without it, this maximum-likelihood method could not have been carried out.

Because of the ordering of events, the preliminary runs with a restricted sample involved small values of Δ^2, where the model should be most applicable. With 1300 events and $\Delta^2 \leqslant 6\mu^2$, a maximum likelihood was found with

$$C = 1.82, \; A = 2.23 \; (\mathrm{GeV})^{-2}, \; a_0^2 = 0.55 \text{ fermi}.$$

A subsequent run with provision for a noninterfering phase-space background gave

$$10\% \text{ phase space}, \; C = 1.69, \; A = 2.48 \; (\mathrm{GeV})^{-2}.$$

As regards the scattering length, on the basis of the fits with the above sets of parameters and the set to follow, we feel that a good value is $a_0^2 = -0.55 \pm 0.05$ fermis.

Taken over the whole sample of 2775 events, $\Delta^2 \leq 20\ \mu^2$, the parameters $C = 1.82$, $A = 2.23$ were consistent with a maximum in the overall likelihood. However, the likelihood was much smaller and not consistent with a mere doubling of events. The reason appears to be that we are attempting to describe simultaneously differential cross sections with respect to angle and Δ^2 (the distribution in ω^2 is taken care of by the resonant form), and the likelihood method is most sensitive to the angular distributions. The data are concentrated at low values of Δ^2 before the parameters, as it were, have got a chance to start attenuating the differential cross section, and so their values are, in the main, set by the angular distributions at the lowest Δ^2. In short, it was found that to match the experimental falloff in $\rho_{00}^{(1)}$ the parameters were driven to the values given above, with the consequence for the Δ^2 distribution that it did not fall off fast enough (see Fig. 71). The angular distributions are fitted very well with this choice of parameters, perhaps better than similar fits by Jackson. However, in the density matrix expansion the absolute cross section is divided out, and although one feels that the fit to the density matrix elements is the sensitive test of the absorption theory, in view of the distressing disagreement of the Δ^2 distribution, these parameters were rejected.

By inspection of the behavior of the Δ^2 distribution and density matrix elements for various values of the absorption parameters, it became evident that we could not reproduce both simultaneously. However, a choice of $C = 1.15$ and $A = 10\ (\mathrm{GeV})^{-2}$--corresponding to the solid curve in Fig. 71--reproduces well the observed Δ^2 distribution for the ρ^-. There is no arbitrary normalization. We have taken $G^2/4\pi = 15$ to yield an absolute calculation.[75]

The situation with respect to the density matrix elements is, of course, less satisfactory (Fig. 72). The calculated curves have the general features of the data, of which there are enough statistics to show how the density matrix elements do vary with Δ^2, but quantitative agreement is absent. In the regions of low Δ^2, the calculated density matrix elements differ by less than 10% from the observed values. At values

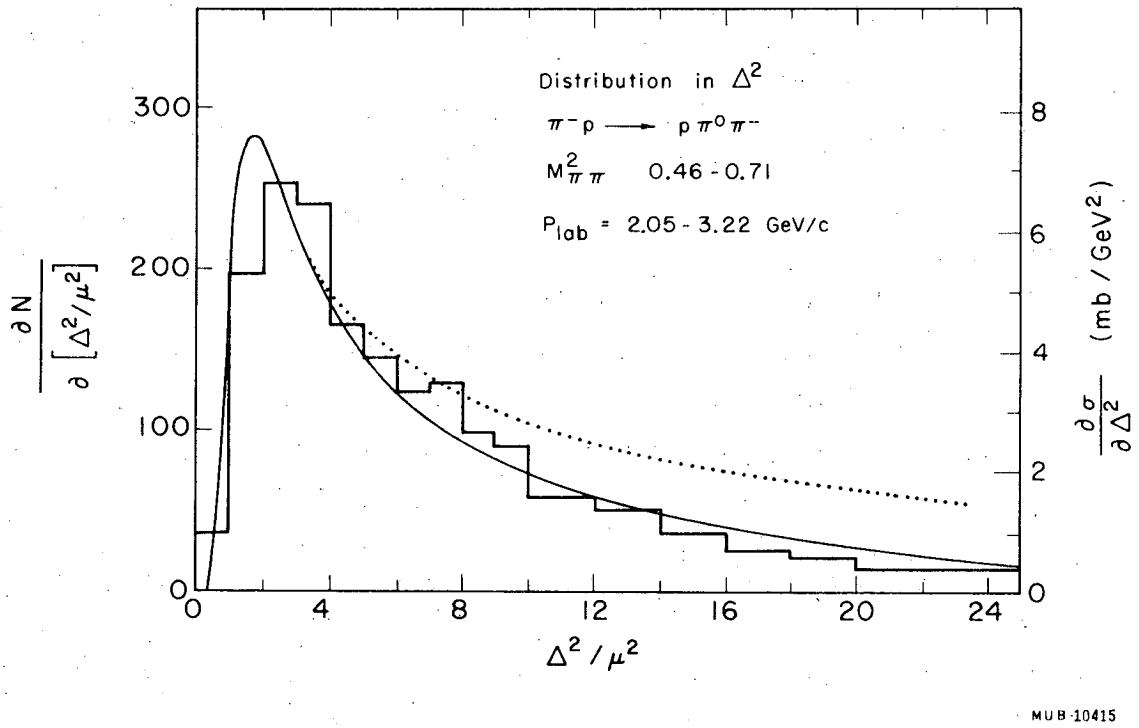

Fig. 71. Δ^2 distribution for ρ^-. Dotted line is from OPE absorption calculation, with C = 1.82 and A = 2.23 $(GeV)^{-2}$. Solid line is from OPE absorption calculation with C = 1.15 and A = 10 $(GeV)^{-2}$.

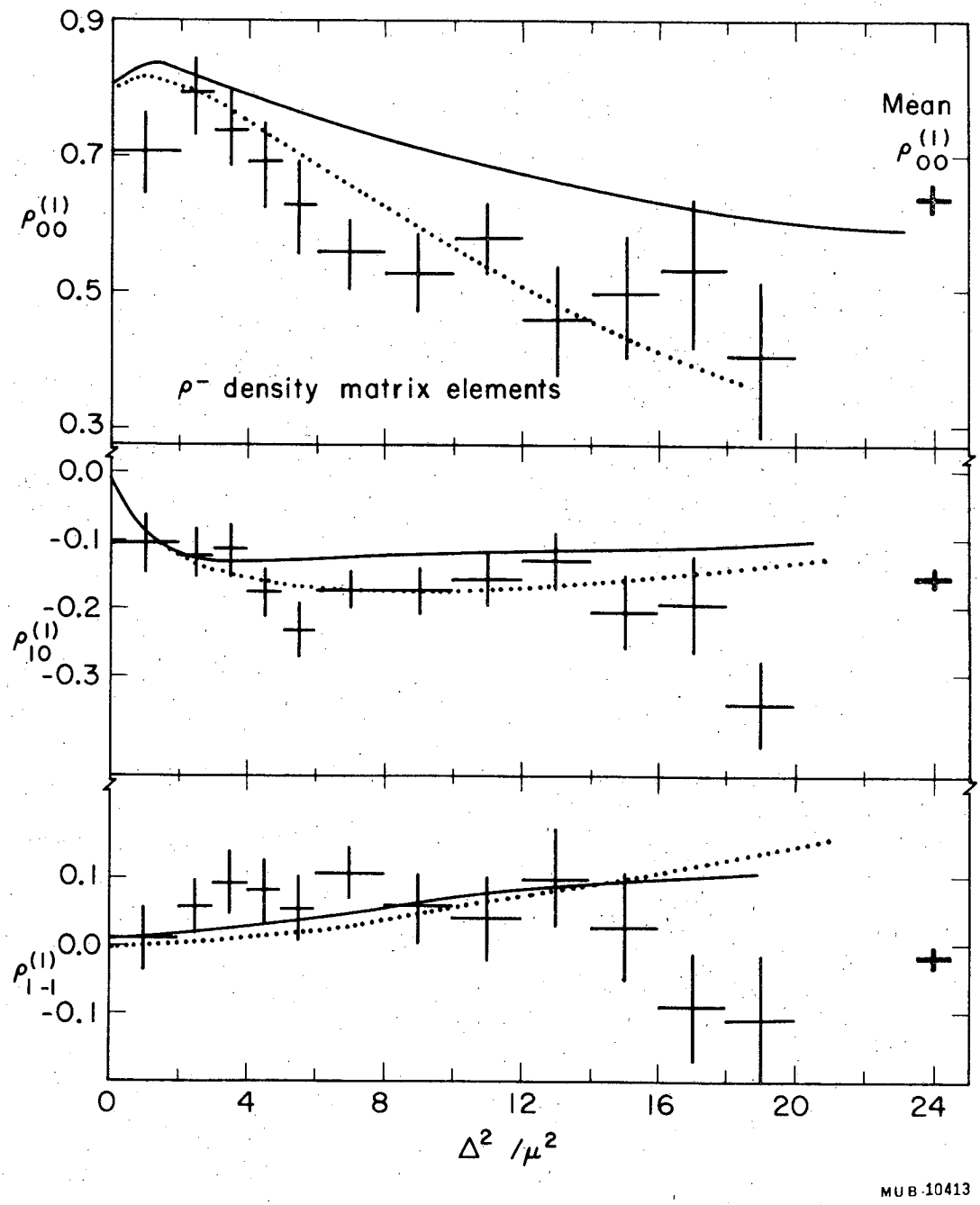

Fig. 72. ρ^- density matrix elements as a function of Δ^2. Dotted lines are from OPE absorption calculation with C = 1.82 and A = 2.23 $(\mathrm{GeV})^{-2}$. Solid lines are from OPE absorption calculation with C = 1.15 and A = 10 $(\mathrm{GeV})^{-2}$.

of $\Delta^2 \geqslant 15\ \mu^2$, the observed points contain the effect of background and are less than the actual density matrix elements for the ρ^- at these values of Δ^2. Since the disagreement is least where the greater part of the data is, i.e., at low Δ^2, we have used this new pair of absorption parameters in all further calculations.

The implications for the phase-shift determination are reflected in the (F-B)/(F+B) asymmetry. In Fig. 73 we plot the $\pi^0\pi^-$ asymmetry as calculated with the new parameters and $a_0^2 = -0.55$ fermi. We see that the effect is to slightly overestimate the asymmetry--certainly in the ρ region. We shall return to this in considering the asymmetry in the ρ^0. The other feature of some importance in Fig. 73 is that below 700 MeV, the $\cos\theta$ distribution is substantially symmetric. This is in disagreement with other groups; some discussion of this is found in Ref. 76. The calculated asymmetry is negative in this region. However, we would mention that only 55 events--i.e., 2.5%--are to be found below 620 MeV, therefore, statistically, the disagreement is not serious. The fit to the scattering length is determined by the increasing asymmetry through the ρ region. The addition of some d wave may help to reduce the interference, but this is unlikely at the low values of $\pi\pi$ mass, where the discrepancy is observed.

Before proceeding further, let us examine the parameters we have obtained and compare them with those obtained by other authors. Although Durand and Chiu[68] and Jackson and co-workers[66,73,77] use the angular momentum approach, our parameters can be used in their formulation. Durand and Chiu use the parameter ν, where $\nu = \sqrt{1/2A}$ and $C = 1$. At 4 GeV/c, for $\pi^- p \rightarrow \rho^- p$, they use $\nu = 0.24$ GeV. With $A = 10\ (\mathrm{GeV})^{-2}$ our value of ν is 0.224. In Refs. 77 and 78 the parameters $C\pm$ and $\gamma\pm$ are defined for the initial and final states: C- is 1, maximal absorption, and $\gamma-/\gamma+ = 0.75$; γ is related to A via the relation

$$\gamma = 1/2Aq^2 .$$

Our parameters give an effective exponential elastic scattering slope and an effective total cross section of 57 mb, which we take to be

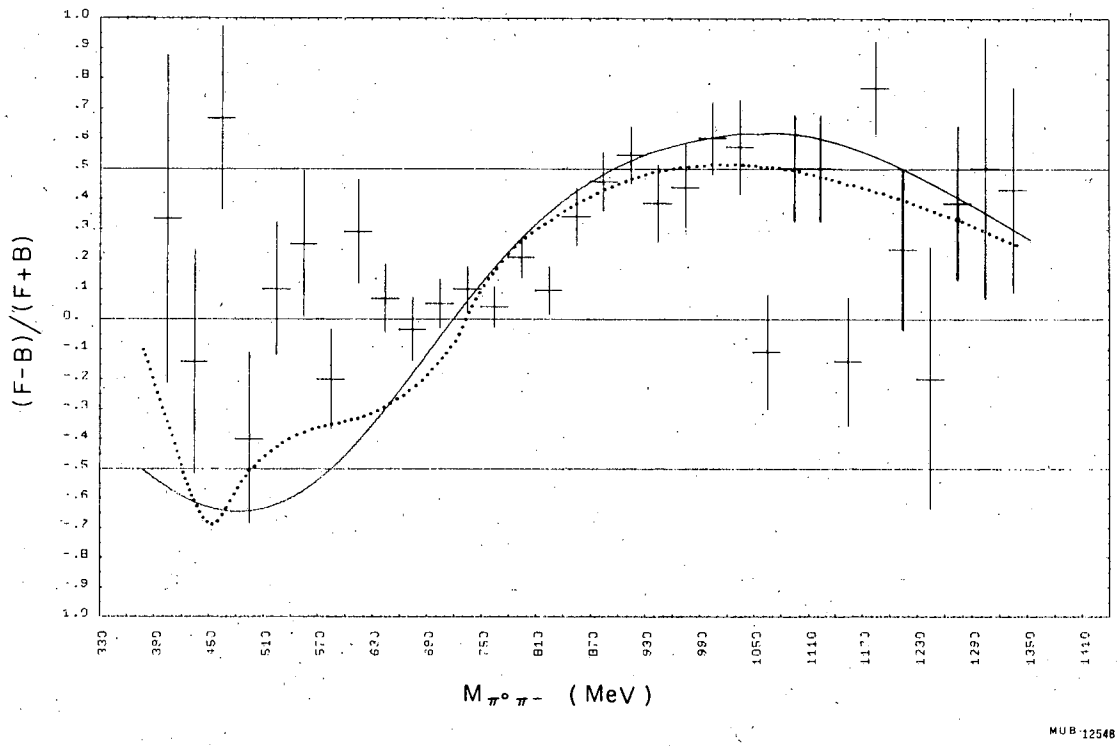

Fig. 73. (F - B)/(F + B) asymmetry for $\pi^0\pi^-$ system with $\Delta^2 \leq 10\ m_{\pi_0}^2$. Solid curve is from OPE absorption calculation with C = 1.15, A = 10 $(GeV)^{-2}$ and a_0^2 = - 0.55 fermi. Dotted line is from the unmodified OPE calculation of Wolf, Ref. 72.

the geometric means of these quantities for the initial and final states. This gives $A_- = 12.5$ to 13 $(\mathrm{GeV})^{-2}$ and $\sigma^{TOT}_{\rho^- p}$ 90 to 100 mb, and therefore

$$\frac{\gamma_-}{\gamma_+} = \frac{A_+ q^2}{A_- q'^2} \approx \frac{8 \times 1.15^2}{12.5} = 0.85.$$

Lastly, we would like to comment on the values of A_- and $\sigma^{TOT}_{\rho^- p}$. Recent experiments with ρ^0 photoproduction[79] seem to suggest that the exponential diffraction slope is of the order of 10 to 15 $(\mathrm{GeV})^{-2}$. Drell and Trefil,[80] on examining the energy and momentum dependence of coherent ρ^0 photoproduction as a function of the atomic number of the target nuclei, present an argument to show that at 4 GeV/c the $\rho^0 N$ total cross section lies between 66 and 94 mb. Both these findings seem to suggest that our choice of parameters is not unreasonable.[81]

<u>$n\pi^+\pi^-$ final state</u>

We pretend to understand the absorptive effects in the ρN case and the behavior of the T = 2 s-wave phase shift, and now we turn our attention to the ρ^0. There is a case to be made for using different absorption parameters in the $\rho^0 n$ case, since this is a different final state from $\rho^- p$, but the state of the art does not really warrant it. The question arises as to the absorptive effects in the s and d waves. Since the T = 2 s wave is small, we used the same absorption parameters as in the ρ^-. For the s-wave T = 0 interaction, the two obvious alternatives are to use no absorption or the same parameters. We used the latter and were guided to this choice by the fact that the ρ^0 asymmetry decreases as Δ^2 increases in the range 0 to 10 μ^2, where we do not expect background to be important; see Fig. 74, also Ref. 70, Fig. 3, where the same effect is seen in good agreement with our data. The implications of this are that the s-wave interaction falls off relative to the p-wave as Δ^2 increases. The s wave has no off-the-mass-shell correcting term $(a_\omega/k)^1$, and so the Δ^2 distribution is dominated by the propagator term $1/[\Delta^2+\mu^2]^2$. If the p wave gets absorbed and the s wave does not, the least we can expect is that the asymmetry remain roughly

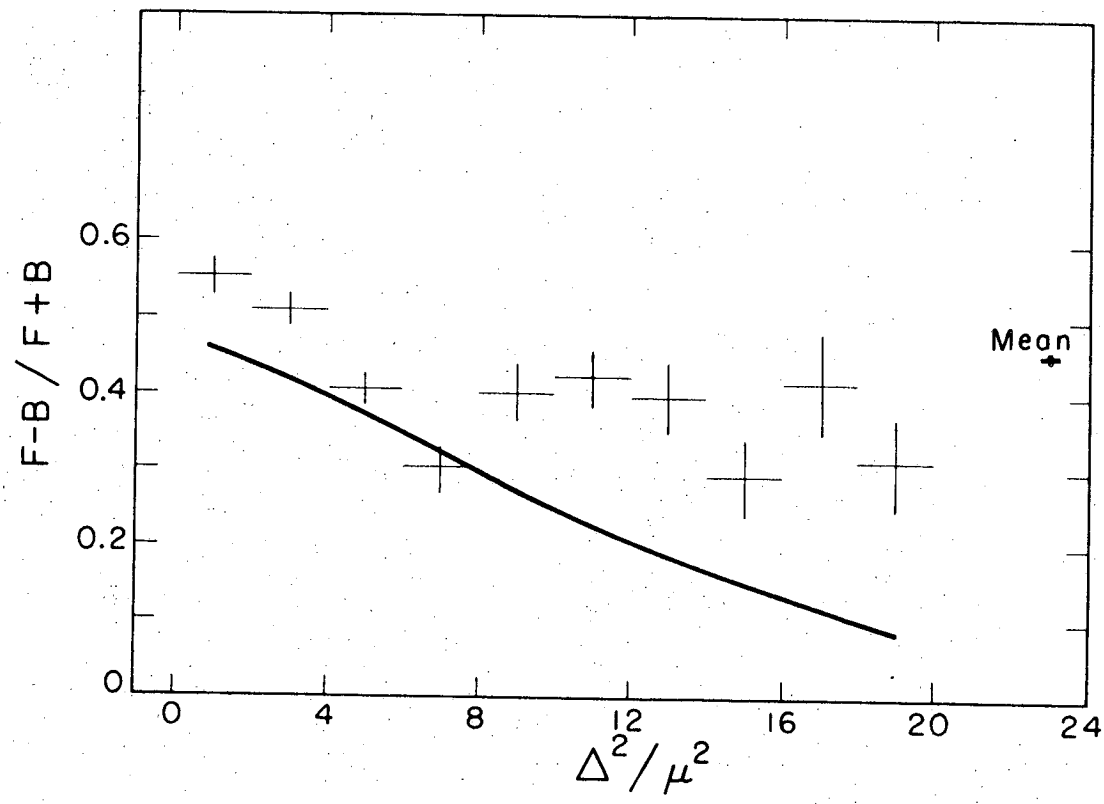

MUB-12432

Fig. 74. (F - B)/(F + B) asymmetry for ρ^0 as a function of Δ^2. Curve shows predictions of OPE absorption model with equal absorption in the s and p waves.

constant. Since the reverse is seen, we believe our choice is qualitatively correct.

We have alluded many times to the steady and strong asymmetry in the $\pi^+\pi^-$ decay angular distribution. The suggestion that this is due to a strong T = 0 s-wave amplitude is not a new one;[82] we should like to investigate the statement[83] that this amplitude is, in fact, necessarily resonant. Hagopian et al.,[84] on the basis of equatorial $|\cos\theta| \leq 0.3$, events at low $\Delta^2 \leq 4\mu^2$, with something like 45% of the statistics in this experiment, aver that they see an indication of this scalar particle. Feldman et al.[85] see a peak in the $\pi^0\pi^0$ effective-mass distribution at 700 MeV in a spark chamber experiment to study $\pi^- p \rightarrow n\pi^0\pi^0$, but only at one beam energy, 1.52 GeV/c.

To determine the T = 0, s-wave phase shift, δ_0^0, twelve values of $m_{\pi\pi}$ were chosen, with five concentrated in the mass interval 670 to 800 MeV. Associated with these ten points were ten values of δ_0^0. A quadratic expression in δ_0^0 was put through any three adjacent points, and gave δ_0^0 at any other mass value. In this way, we ensured a smooth and continuous variation in δ_0^0. The maximum-likelihood fit indicated that δ_0^0 increased slowly through 90° in the region of the ρ^0.

With this information, we can compute the Δ^2 distribution and density matrix elements for the ρ^0 and take into account the strong s-wave contribution.

In the Δ^2 distribution, Fig. 75, to which the s-wave contributes about 8% of the cross section, we have normalized arbitrarily to the area between 5 and 20 μ^2. The absorption calculation gives a slower falloff in the cross section than is observed, casting in doubt our assumption for $\rho^0 n$ of the same absorption parameters as $\rho^- p$.

The effect of the s wave on the density matrix elements will be to reduce the pure spin-1 components--since we are normalizing by a cross section that contains more s wave--but our measured $\rho_{00}^{(1)}$ will have the effect of the s-wave cross section added to it (see earlier). Thus Fig. 76 is similar to that for the ρ^- density matrix elements, Fig. 72.

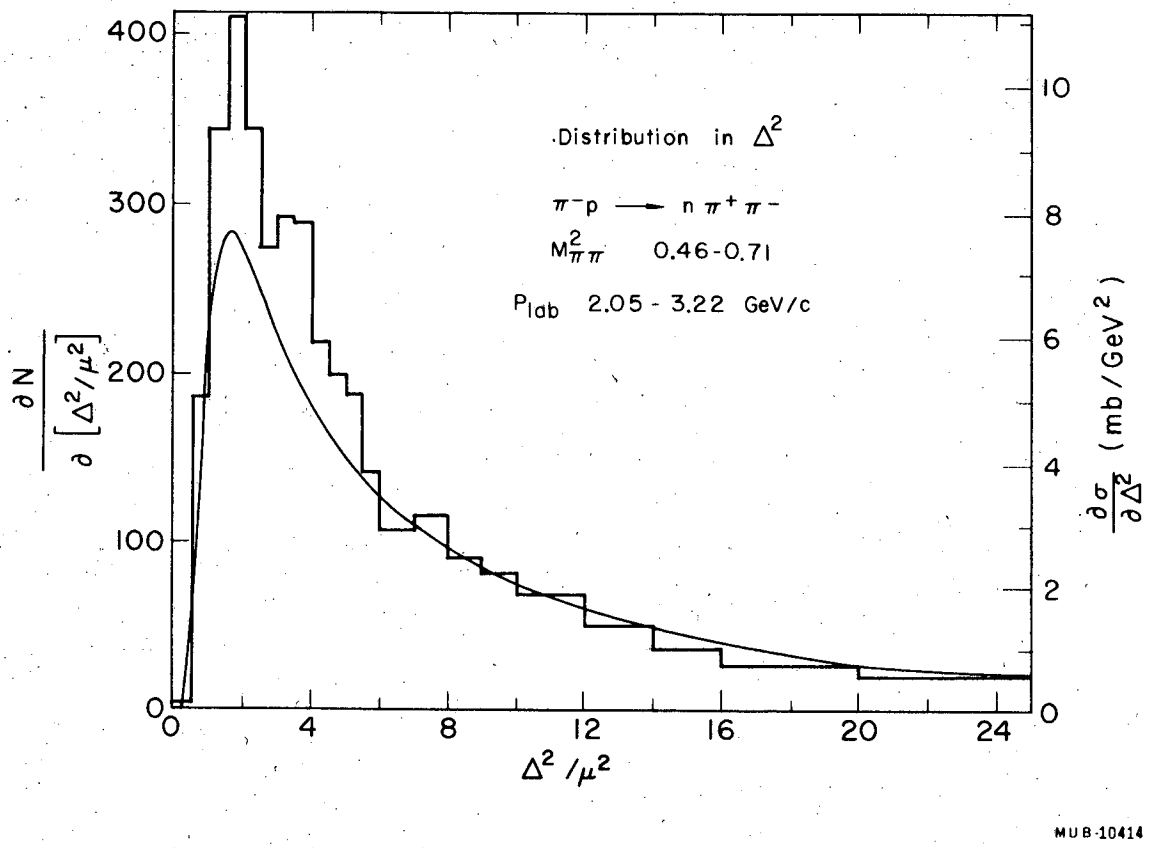

Fig. 75. Δ^2 distribution for ρ^0. Curve is from OPE absorption calculation with C = 1.15 and A = 10 $(\text{GeV})^{-2}$ --normalized to tail of distribution.

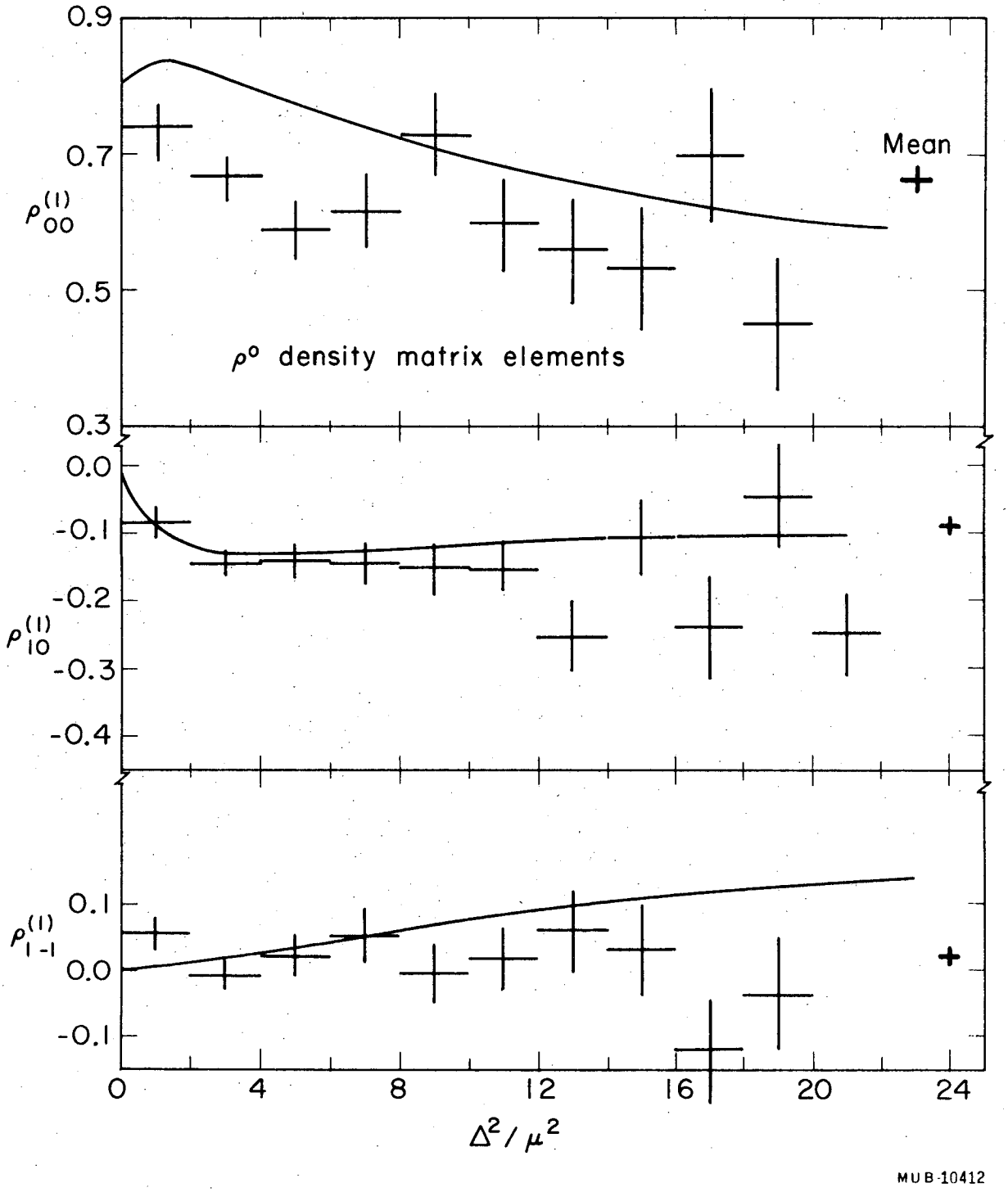

Fig. 76. δ^0 density matrix elements as a function of Δ^2. Curves show predictions of OPE absorption calculation with C = 1.15 and A = 10 $(\mathrm{GeV})^{-2}$.

In Fig. 69 we showed a scatter plot of $\cos\theta$ vs ϕ for the ρ^0 as compared with the ρ^-, Fig. 68. The elements of the density matrix were calculated from the model and averaged over the mass and Δ^2 interval, and used to calculate the contour curves. In both cases, good agreement is obtained. By projecting the distributions on both axes, we obtain the angular distributions shown in Figs.77 and 78. The agreement with thoery is good.

Figure 69 is very similar to that shown by Durand and Chiu[83] and by Derado et al.[86] Further, our calculated density matrices are very similar to those calculated by Durand and Chiu and quoted by Derado et al. From these plots alone, it is very hard to give preference to a theory with a resonant δ_0^0, as Durand and Chiu maintain, or to one that merely has it climb slowly through 90° near the ρ, since we are averaging mass-dependent effects, and both theories agree that δ_0^0 is 90° near the ρ^0.

We may use the calculated density-matrix elements to show that in the ρ region and $\Delta^2 \leqslant 15$, taking events with $|\cos\theta| \leqslant 0.3$ will reduce the cross section to 1/7, of which the s wave is just 1/6. Hence, considering equatorial events, although we gain a factor of two in the s-wave cross section, is still not sufficient to distinguish it from the p-wave cross section. (We may mention here that without absorption we expect the "equatorial" cross section to be about 6% of the total, of which 58% would be s wave.) With a Δ^2 limit of 4 μ^2 the proportion of s wave is enhanced to 25%, at most, of the equatorial events.

To determine the phase shifts outside the ρ region, we evaluated the (F-B)/(F+B) asymmetry as a function of mass, varying our input δ_0^0 at the 12 fixed points, until it most closely resembled the experimental points. The result is shown in Fig. 79, and δ_0^0 itself is shown on Fig. 80. Except for the region 620 to 700 MeV, we are able to fit the asymmetry from about 400 MeV up to 1000 MeV. Above 1000 MeV we have arbitrarily let the T = 0, s-wave amplitude vanish. Patently, we do not reproduce the asymmetric decay of the f^0.

In the region immediately below 700 MeV, no value of δ_0^0 is able to generate the large asymmetry, about 0.5, in this region. To make

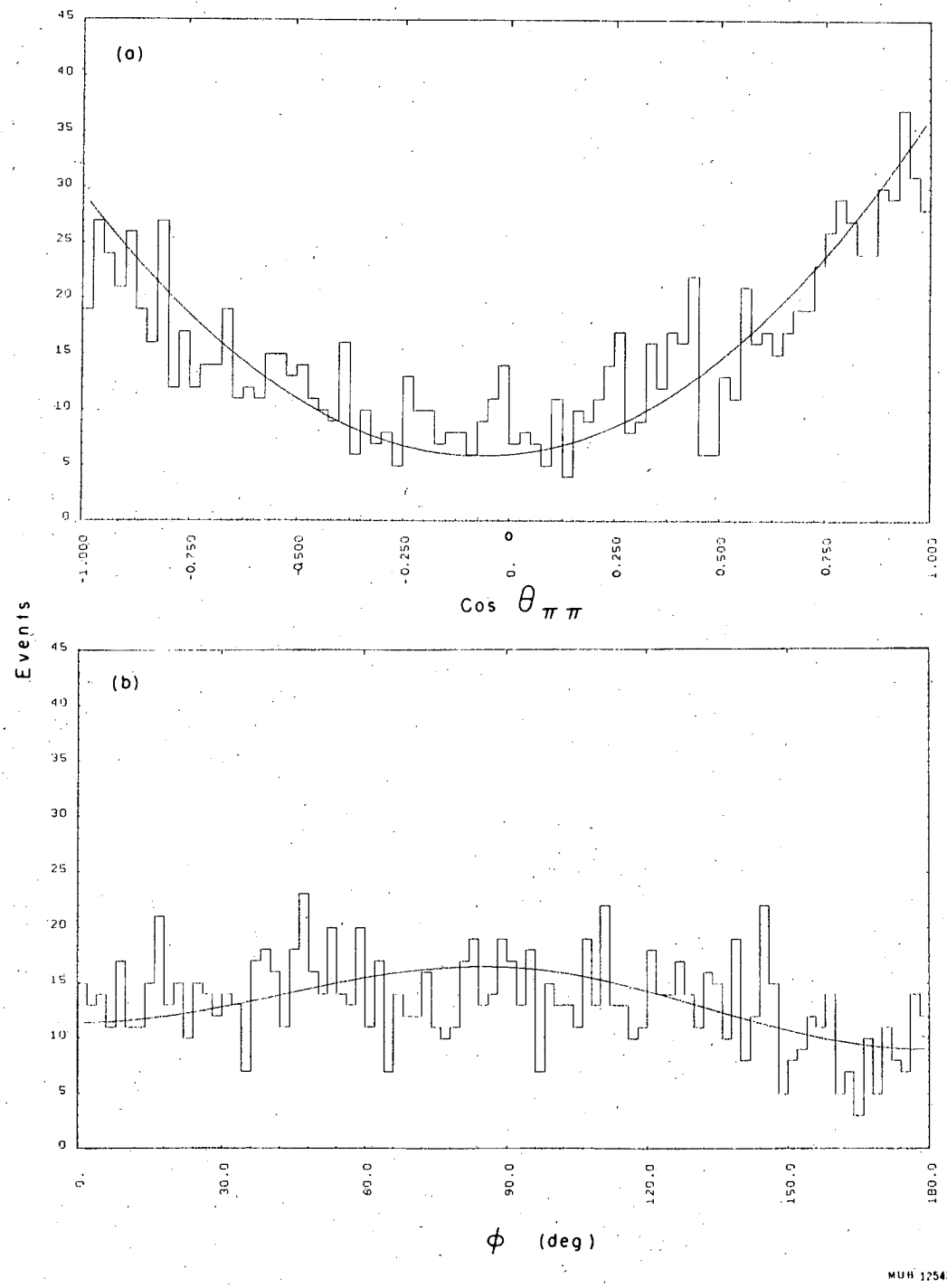

Fig. 77. Distribution of $\cos\theta$ and ϕ for ρ^-. Curves are from density matrix displayed in Fig. 68.

(a) $\cos\theta$, $P(\chi^2) = 0.5\%$.

(b) ϕ, $P(\chi^2) = 13\%$.

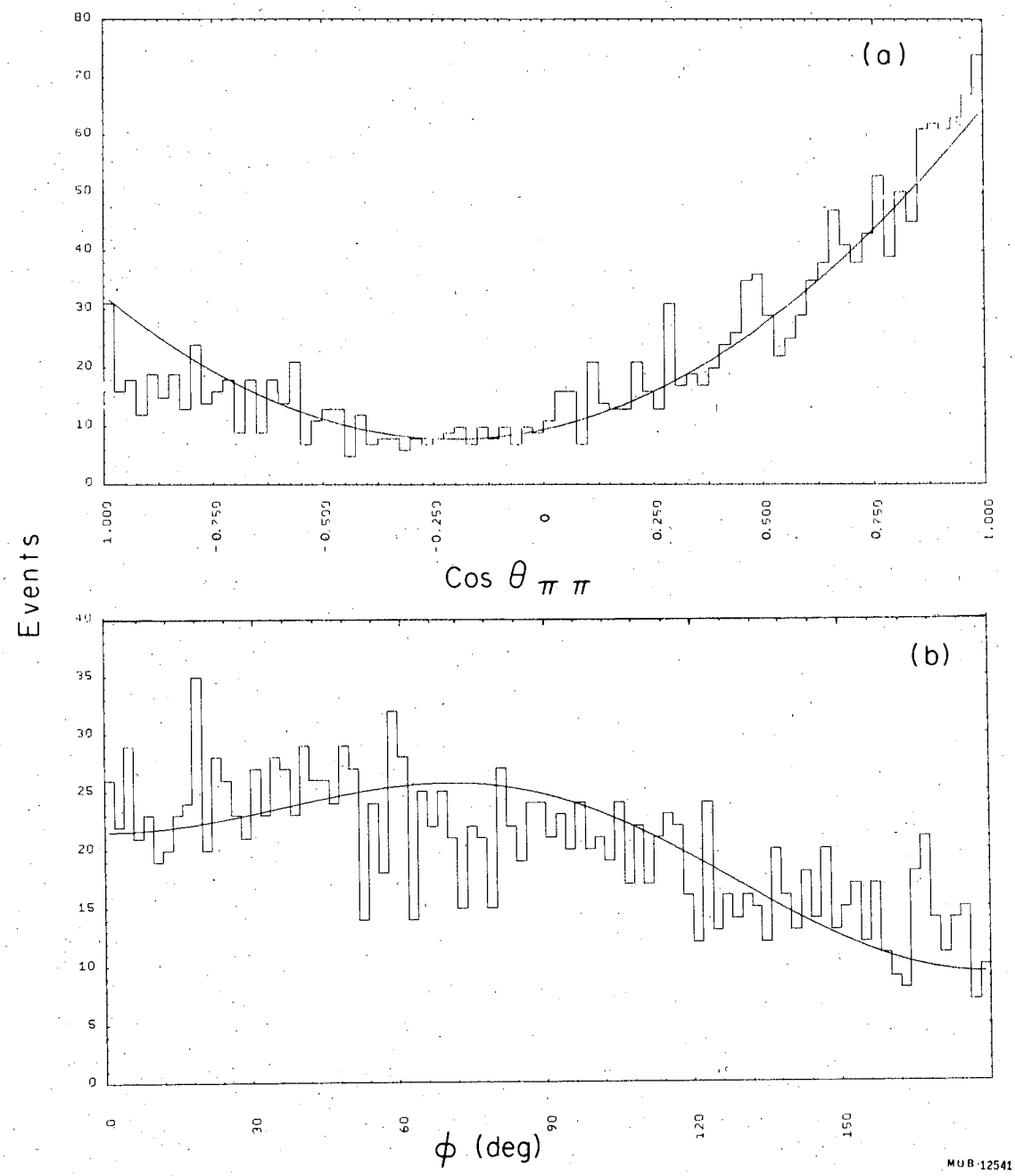

Fig. 78. Distribution of $\cos\theta$ for ρ^0. Curves are from density matrix displayed in Fig. 69.

(a) $\cos\theta$, $P(\chi^2) = 2\%$.

(b) ϕ, $P(\chi^2) = 17.5\%$.

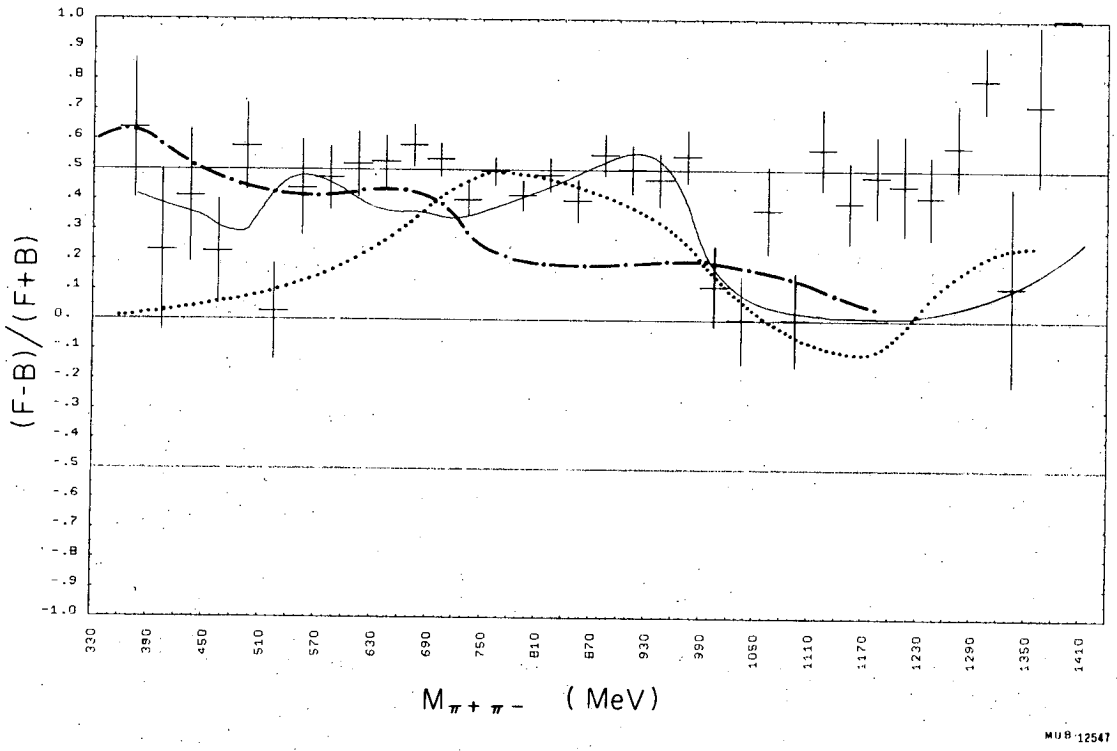

Fig. 79. (F - B)/(F+ B) asymmetry for the $\pi^+\pi^-$ system, with $\Delta^2 \leq 10\,\mu_{\pi^0}^2$. Solid line is from absorption calculation using the δ_0° shown in Fig. 80. Dashed line is calculation with same absorption parameters, but with a resonant δ_0° having $m_\rho = 730$ MeV and $\Gamma = 90$ MeV. Dotted line is from unmodified OPE calculation of Wolf, Ref. 72, with $\Delta^2 = 15\,\mu^2$.

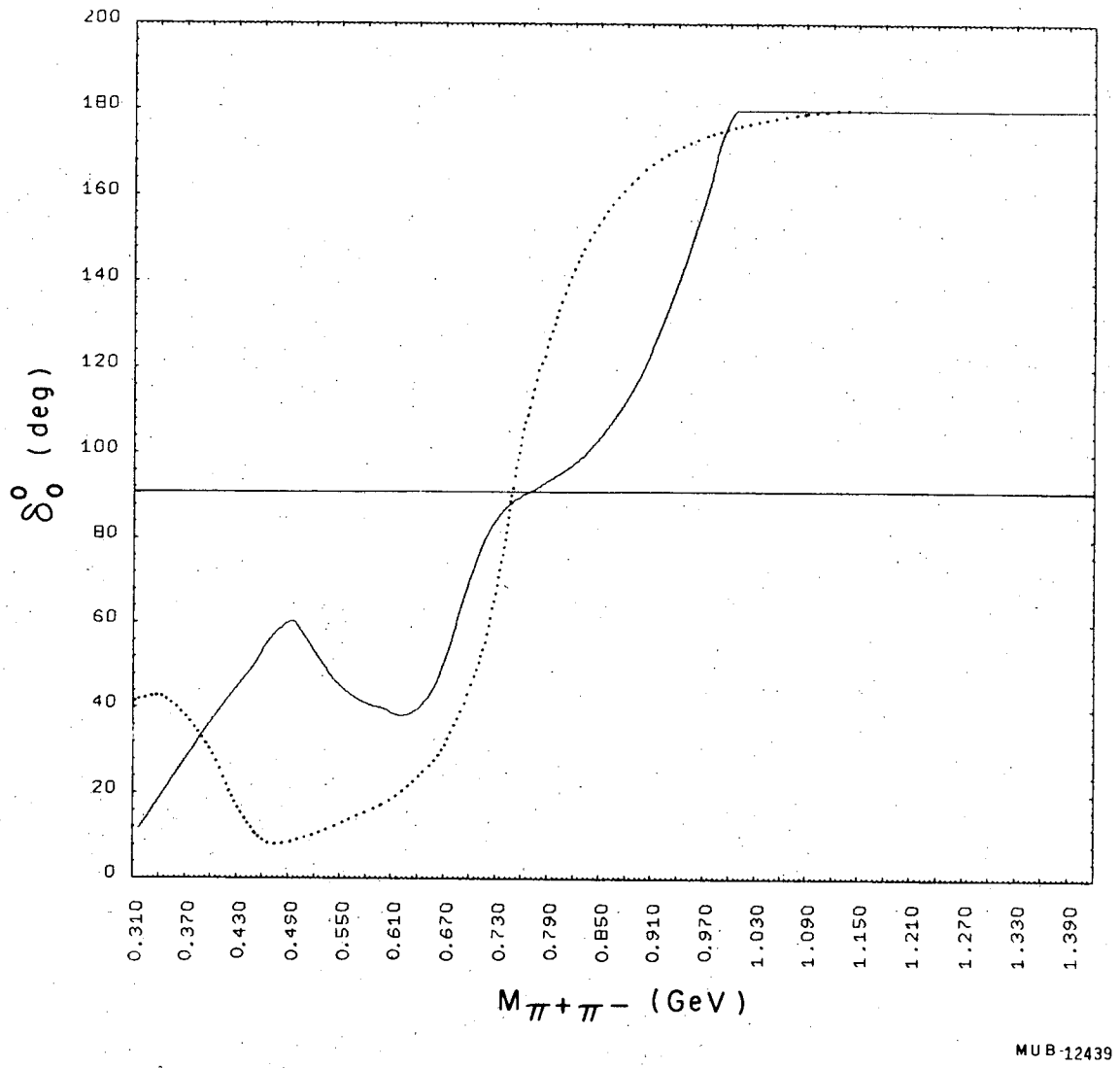

Fig. 80. Behavior of δ°_{0} used to fit (F - B)/(F + B) asymmetry in Fig. 79. Dotted line is solution of Wolf, Ref. 72.

this clear, the following calculation is in order. Ignoring the T = 2 contribution, we can express the asymmetry in terms of the phase shifts,

$$\frac{F - B}{F + B} = \frac{2 \sin \delta_0^0 \sin \delta_1 \cos(\delta_0^0 - \delta_1)}{3 \sin^2 \delta_1 + \frac{4}{9} \sin^2 \delta_0^0} .$$

For a given value of δ_1 this is approximately a maximum for $(2\delta_0^0 - \delta_1) = \frac{\pi}{2}$. Thus for $\delta_1 = \frac{\pi}{2}$, $\delta_0^0 = \frac{\pi}{2}$ will give a maximum asymmetry of 18/31 = 0.58. At $m_{\pi\pi} \approx 670$ MeV, δ_1 is about 40°. Taking $\delta_0^0 = 65°$ gives an asymmetry of 0.64. However, in OPE these would be the values obtained only at the pole $\Delta^2 = -\mu^2$. As we have shown, the asymmetry decreases with Δ^2, so that at the ρ^0, averaged over 0 to 10 μ^2, it falls from 0.58 to 0.39. At $m_{\pi\pi} \approx 670$ MeV the maximum asymmetry we can generate in the calculation is about 0.45. We do not pretend to understand the data in this interval and would not like to advance any one hypothesis over another, whether it be an upward fluctuation in the data (we are in disagreement with Jones et al.[70]), lack of absorptive effects in this region, or other $\pi\pi$ interactions that have not been considered.

In the f^0 region we predict zero asymmetry, since we do not have enough p-wave amplitude if a ρ Breit-Wigner form is used. We must invoke either f waves or a p-wave amplitude independent of the ρ. Our arguments in the previous section seem to favor the former.

With a slow increase of δ_0^0 through 90° we can reproduce the increasing asymmetry up to 900 MeV and account satisfactorily for the decrease to zero at 1100 MeV. Because of the approximations and inaccuracies we have introduced with our absorption model we believe that we have estimated the right order of magnitude of the absorptive effects, but the δ_0^0 could change by ±15°. In the region an error of ±8° would be more suitable.

If one makes the transformation $\delta_0^0 \to \frac{\pi}{2} - [\delta_0^0 - \delta_1]$ the asymmetry does not change. In the expression for maximum asymmetry this is associated with the solution $(2\delta_0^0 - \delta_1) = \frac{-\pi}{2}$. Near the ρ the two solutions are similar. Outside the ρ the transformed solution will have a

more complicated behavior than the present solution. In theory, a determination of the s-wave cross section will distinguish between the two. In Ref. 76, the attempt was made to do this, but between 400 and 500 MeV, δ_1 is small and both solutions are near 45°.

We should therefore like to present our solution for the behavior of δ_0^0 as a plausible one and to point out that the resonance invoked by Durand and Chiu [83] (see Fig. 79), is not only unnecessary but also incapable of fitting our data. We may measure the slope

$$\frac{d\delta_0^0}{dk}$$

and say whether δ_0^0 is changing fast enough through $\pi/2$ for it to be called resonant.[87] At the ρ,

$$\left|k\frac{d\delta_0^0}{dk}\right| \approx 0.42,$$ and so we aver that δ_0^0 is slowly varying and not resonant.

Lastly we should like to remark that although we let δ_0^0 increase from 0 at threshold, we could have let it decrease from π, as Chew has suggested.[88] This would be in disagreement with the positive asymmetry below 400 MeV shown by the data, since a decreasing phase shift would make the asymmetry change sign. However, there are only 20 to 30 events in this sample below 400 MeV, and Jones et al.[70] with a total of more than 1100 events below 450 MeV find a negative asymmetry.

In summary, we have shown that the absorption model gives qualitative and reasonable-to-good quantitative agreement to the experimental data. Possibly, we have introduced too much absorption into the s-wave amplitudes. The Huff formalism does not seem to generate so much "absorption" as the angular momentum approach. With our absorptive corrections in, we are in agreement with other workers on the magnitude and sign of the T = 2, s-wave $\pi\pi$ interaction, and have shown that the T = 0 s-wave phase shift is 90° near the ρ but not resonant.

E. Missing-Mass Hypotheses

In Fig. 81 we show the missing-mass plot for Reaction (5),

$$\pi^- p \rightarrow \pi^- p + \text{m.m.}$$

We have summed over all energies and selected events with $\Delta^2 \geqslant 0.3$ $(\text{GeV})^2$ in order to reduce the background in the region of the η. The η signal at each energy is not strong. In Fig. 81 we also show the mass plot at 2.86 GeV/c, where η production seemed to be higher. In Table XIII we present our estimates of η production at each energy.

In Fig. 82a, b, c, we show the mass spectrum for the combination π^- (m.m.) at 2.60, 2.86, and 3.22 GeV/c for all momentum transfer and for $\Delta^2 \leqslant 0.65$ $(\text{GeV})^2$. As the beam energy increases, the peak of the four-body phase space with no Δ^2 cut goes from about 1250 MeV at 2.60 GeV/c to about 1450 MeV at 3.22 GeV/c. Consequently, although the presence of the A_2,[89, 90] with mass and width in agreement with those of Refs. 89 and 90, is evident in all three plots, it is very hard to estimate it above background at the two lower energies. With the Δ^2 cut from 0 to 0.65 $(\text{GeV})^2$, the background is flatter and the A_2 effect is enhanced, although at 2.86 GeV/c (Fig. 82b) our statistics are poorer and we can say only that the histogram is consistent with the presence of the A_2. In Table XIII, we present cross sections for the reaction $\pi^- p \rightarrow p A_2^-$ based on estimates of the number of A_2^-'s produced at 2.36 to 3.22 GeV/c. At 3.22 GeV/c we note that the estimate for A_2^- production, $A_2^- \rightarrow \rho^- \pi^0$ of 0.15 mb, is in good agreement with that of Chung for $A_2^- \rightarrow \rho^0 \pi^-$.[89] The equal branching ratio of $A_2^- \rightarrow \rho^0 \pi^-$, $A_2 \rightarrow \rho^- \pi^0$ has been reported previously in Ref. 91.

The A_1 is not apparent in the mass spectra with no cut. With the cut, we cannot rule out the presence of a shoulder near 1100 MeV. However, our histograms are different from those for the $\pi^+ \pi^- \pi^-$ combination[89, 90, 92] with $\Delta^2 \leqslant 0.65$ $(\text{GeV})^2$, and we are in disagreement with Ref. 92, which sees a definite narrow peak at 1100 MeV in $\pi^-_{\text{m.m.}}$.

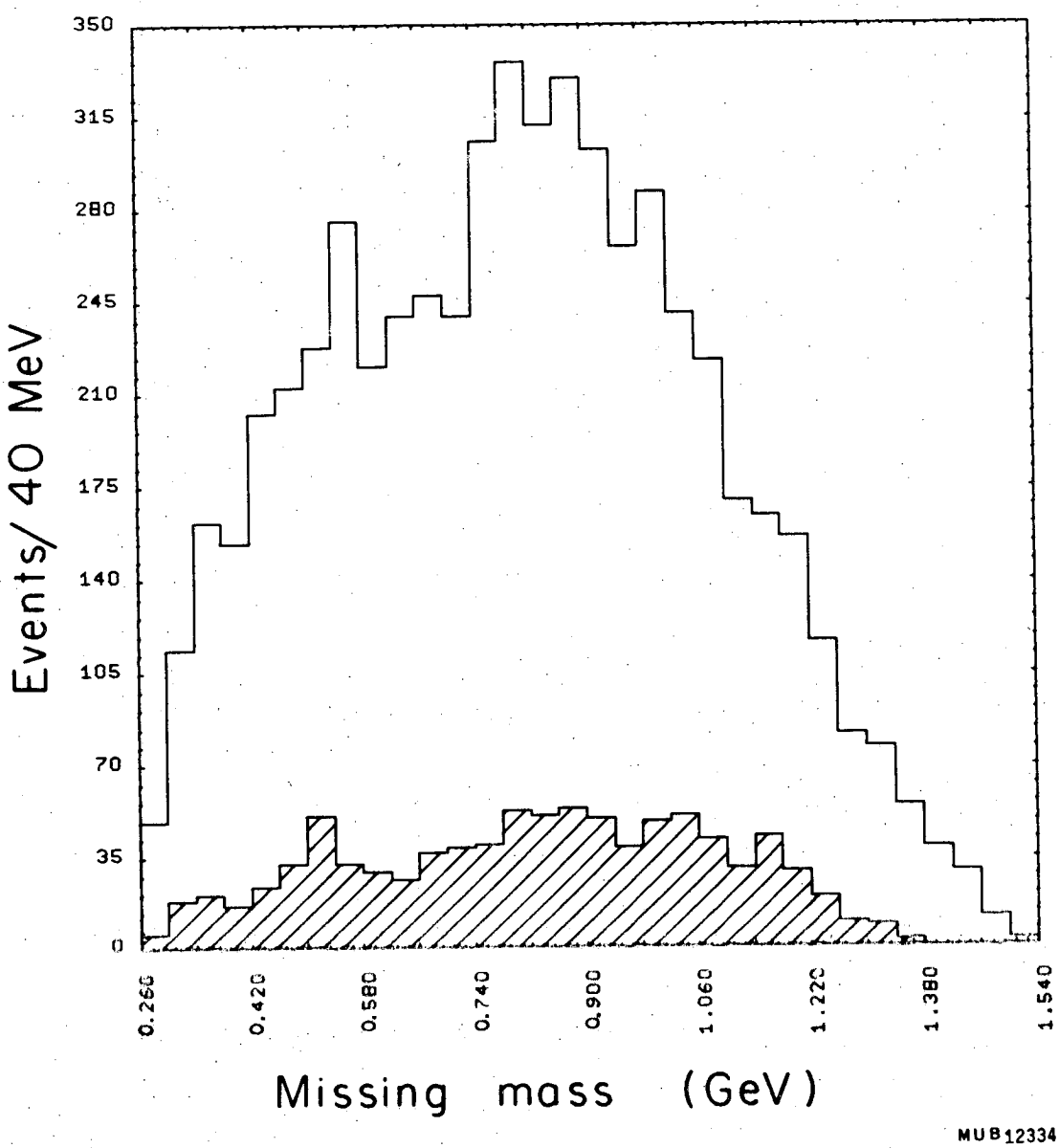

Fig. 81. Distribution of missing mass in the reaction $\pi^- p \rightarrow \pi^- p$ + missing mass at 2.05 to 3.22 GeV/c and $\Delta^2 > 0.3$ GeV^2. Shaded events are 2.86 GeV/c only.

Table XIII. η and A_2 production cross sections in in $\pi^- p \rightarrow \pi^- p$ + neutrals.

Beam Momentum (GeV/c)	σ_η (μb)	σ_{A_2} (μb)
2.05	0±85	-
2.17	165± 75	-
2.36	105± 50	60± 40
2.60	150± 60	145± 50
2.86	235± 90	350± 100
3.22	140± 65	300± 75

σ_{A_2} is production cross section for $\pi^- p \rightarrow p A_2^-$,

σ_η is production cross section for $\pi^- p \rightarrow \pi^- p \eta$.

Both cross sections include corrections for modes not seen in this experiment.

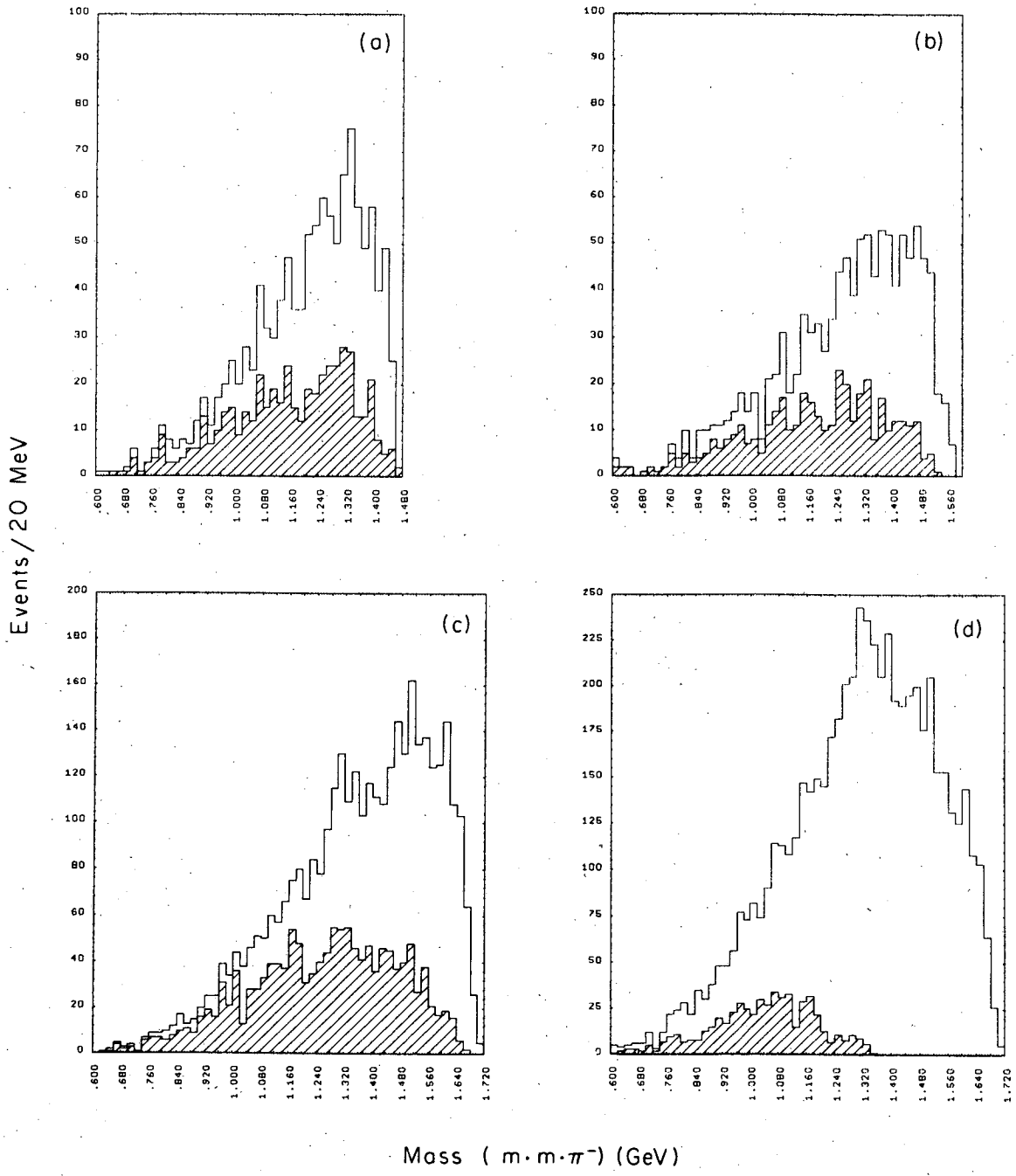

Fig. 82. Distribution of (π^-p missing mass) in the reaction $\pi^-p \rightarrow \pi^-p$ + missing mass.
(a) 2.60 GeV/c; events shown shaded have $\Delta^2 < 0.65(\text{GeV})^2$.
(b) 2.86 GeV/c; events shown shaded have $\Delta^2 < 0.65(\text{GeV})^2$.
(c) 3.22 GeV/c; events shown shaded have $\Delta^2 < 0.65(\text{GeV})^2$.
(d) 2.60 to 3.22 GeV/c. Events shown shaded have $\Delta^2 < 0.15\,(\text{GeV})^2$.

By making the cut Δ^2 0.15 to 0.65 $(\mathrm{GeV})^2$, not shown, we find the A_2 is unaffected but the events at 1100 MeV are depleted. In Fig. 82d we add the data at 2.60 to 3.22 GeV/c. The A_2 is prominent. However, by making the cut $\Delta^2 \leq 0.15\ (\mathrm{GeV})^2$, we see a strong peaking at 1100 MeV. To give an unambiguous interpretation of this is almost impossible. References 89 and 90 have shown that the A_1 effect may be explained in good part by a OPE diagram where there is $\pi\pi$ scattering at one vertex and πp scattering at the other. The situation for us, in that case, is very similar. The $\pi^0\pi^-$ scattering is dominated by the ρ^- and we have $\pi^0 p$ scattering. The amplitude for $\pi^0 p \rightarrow \pi^0 p$ is the mean of $\pi^- p \rightarrow \pi^- p$ and $\pi^+ p \rightarrow \pi^+ p$. We should therefore expect an A_1 enhancement at low Δ^2. Since this is a dynamic effect, depending on various amplitudes, we do not expect any constant ratio for an A_1 going to $\pi^0\pi^0\pi^-$ and A_1 going to $\pi^+\pi^-\pi^-$. The worsened mass resolution will also tend to wash out any broad A_1 peak.

In summary, we find evidence for the production of the A_2 resonant state. We see no strong A_1 effect. This supports the view that the A_1 is not a resonant state. The excess of events at low Δ^2 near 1100 MeV, while consistent with phase-space predictions, may be interpreted as a kinematic effect of the ρ^- and $\pi^0 p$ diffractive scattering.

ACKNOWLEDGMENTS

Thanks are due to Professor Luis W. Alvarez, without whose encouragement and prior work this experiment could not have been conducted, and to Professor Arthur H. Rosenfeld, who made it possible for me to come from England to join the Alvarez Group.

I have received good guidance and advice from Professor Donald H. Miller, for which I am grateful. Professor Gerson Goldhaber has always taken a keen interest in this study. Conversations with Professor Walter Selove and Monique Neveu-René were very helpful.

My appreciation also goes to the operating crews of the Bevatron and the 72-inch hydrogen bubble chamber, and to the many members of the Alvarez Scanning and Measuring Group as well as to the stalwart members of the $\pi 72$- $\pi 63$ Data Processing Library.

To all these people and to the various members of the Alvarez Group, too numerous to mention by name, who have aided me and answered my many questions, I express my gratitude.

This experiment was done under the auspices of the U. S. Atomic Energy Commission.

APPENDIX A

Relation between Proton Momentum and its Scattering Angle in the Laboratory System

The effective mass squared of the resulting particles accompanying the recoil proton in a $\pi^- p$ collision is given by

$$\omega^2 = (E_{in} - E_p)^2 - (P_{in} - P_p)^2,$$

where the notation is obvious.

We compute this in the laboratory frame of reference:

$$\omega^2 = m_{in}^2 + m_p^2 - 2E_{in}E_p + 2P_{lab}\,P_p \cos\Theta_{lab},$$

where Θ_{lab} is the lab scattering angle of the proton.

Since m_{in}^2 is the square of the overall c.m. energy,

$$m_{in}^2 = m_\pi^2 + m_p^2 + 2E_\pi m_p;$$

$$\therefore \quad \omega^2 - m_\pi^2 = 2m_p^2 - 2E_{in}E_p + 2E_\pi m_p + 2P_{lab}P_p \cos\Theta_{lab}.$$

Let us write $$E_p = m_p + T_p$$

and

$$E_{in} = m_p + E_\pi;$$

$$\therefore \quad \omega^2 - m_\pi^2 = 2P_{lab}P_p \cos\Theta_{lab} - 2T_p\,[E_\pi + m_p].$$

Nonrelativistically, i.e., $P_p \lesssim 400$ MeV/c,

we may write $$T_p = P_p^2 / 2m_p,$$

$$\therefore \quad \omega^2 - m_\pi^2 = 2P_{lab}P_p \cos\Theta_{lab} - \frac{P_p^2}{m_p}[E_\pi + m_p].$$

For elastic scattering only, the left-hand side vanishes and we have

$$\cos\Theta_{lab} = \frac{P_p[E_\pi + m_p]}{2P_{lab}\,m_p}.$$

The curves for $\omega \neq m_\pi$ for $P_{lab} = 1.59$ GeV/c are shown in Ref. 93.

APPENDIX B

Helicity Amplitudes for One-Pion Exchange

We generally follow Jackson and Pilkuhn[60] and Gottfried and Jackson[73] in the definitions of the symbols used, except that we use E_a, $E_b \cdots$ for a_0, $b_0 \cdots$. For momentum transfer squared, we use $\Delta^2 = -t$. (See Fig. B-1.)

The invariant amplitude for the process is

$$\mathcal{M}_p = G\,\bar{u}_{j'}(d)\,\gamma_5\,u_j(b)\,\frac{F[\Delta^2]}{\mu^2+\Delta^2}\,\mathcal{J}_{\pi\pi}\,; \tag{B-1}$$

μ is the mass of the exchanged pion. $F(\Delta^2)$ is some form factor, taken here as unity. $\mathcal{J}_{\pi\pi}$ is the invariant $\pi\pi$ scattering amplitude. Equation (B-1) should be compared with Jackson and Pilkuhn's formula (8),[60]

$$\mathcal{J}_{\pi\pi} = \sum_{l} \mathcal{A}^{l}_{0}\, Y^{l}_{0}[\theta,\phi]\,, \tag{B-2}$$

partial-wave expansion in $\pi\pi$ rest frame,

where $$\mathcal{A}^{l}_{0} = 8\pi\omega\sqrt{4\pi}\sqrt{2l+1}\,\frac{e^{i\delta l}\sin\delta_l}{k}\left[\frac{a_\omega}{k}\right]^{l} \tag{B-3}$$

is the lth partial-wave amplitude, ω is the mass of the $\pi\pi$ system and E_ω the energy in the c.m. system, k is the momentum of the decay pions in the $\pi\pi$ rest frame, $\hat{\Omega}_{\pi\pi} = (\theta,\phi)$ $\pi\pi$ decay angles, a_ω is the momentum of m_a, the incident beam pion, in the $\pi\pi$ rest frame, and is thus both a function of Δ^2 and ω:

$$a_\omega = \frac{1}{2\omega}\sqrt{(\Delta^2+(m_a+\omega)^2)(\Delta^2+(m_a-\omega)^2)}\,. \tag{B-4}$$

To compensate for the exchanged pion's being off the mass shell, $\mathcal{A}^{l}_{0}$ becomes a function of Δ^2 via the factor $[\frac{a_\omega}{k}]^{l}$.[59] Below, we shall try to justify the presence of this factor.

We now wish to write Eq. (B-1) explicitly in the overall c.m. frame and in a helicity representation.[94]

Nucleon Helicities

The four different expressions for $\bar{u}_{j'} \gamma_s u_j$, according as the initial and final nucleon spin projections are parallel or antiparallel to their momenta directions, now follow.

λ_d, Final Nucleon	λ_b, Initial Nucleon	$G\, u_{j'} \gamma_s u_j$
$\frac{1}{2}$	$\frac{1}{2}$	$G\,\xi_- \cos\frac{\Theta}{2}$
$\frac{1}{2}$	$-\frac{1}{2}$	$G\,\xi_+ \sin\frac{\Theta}{2}$
$-\frac{1}{2}$	$\frac{1}{2}$	$G\,\xi_+ \sin\frac{\Theta}{2}$
$-\frac{1}{2}$	$-\frac{1}{2}$	$-G\,\xi_- \cos\frac{\Theta}{2}$

(B-5)

Here Θ is the c.m. scattering angle, and

$$\xi_\pm = q\sqrt{\frac{E_d + m_d}{E_b + m_b}} \pm q'\sqrt{\frac{E_b + m_b}{E_d + m_d}}$$

$$= \sqrt{(E_d + m_d)(E_b - m_b)} \mp \sqrt{(E_b + m_b)(E_d - m_d)}\,. \qquad \text{(B-6)}$$

We note here that averaging over the initial nucleon helicities and summing over final nucleon helicities gives

$$\xi_+^2 \sin^2\frac{1}{2}\Theta + \xi_-^2 \cos^2\frac{1}{2}\Theta = [(m_b - m_d)^2 + \Delta^2]\,. \qquad \text{(B-7)}$$

Dipion Contribution

Spin amplitudes undergo a unitary transformation as one goes from one Lorentz frame to another. This can be expressed as a rotation through some angle of the amplitudes. Using helicity amplitudes makes it simple for us to see what angle this is. We know that under a Lorentz transformation along the helicity direction, i.e., in the direction of the momentum of the particle, the helicity states are unchanged. Suppose we have some z axis defined in the particle's rest frame; we will obtain the helicity states by rotating the axes in such a way that the new z axis is the direction along which the particle will move, i.e., the direction of the Lorentz transofrmation. Thus, generally, the angle in question is the one between the directions of the Lorentz transformations as seen from the rest frame of the particle.

For us, the "particle" is the dipion system and the angle is between the axis in the rest frame, which is the incident beam direction, and the $\pi\pi$ momentum direction in the c.m. frame. The angle is Ψ (see Fig. B-2), where

$$a_\omega \sin\Psi = q \sin\Theta ,$$

$$a_\omega \cos\Psi = q\,[\cos\Theta - \alpha]\,\frac{E_\omega}{\omega} , \qquad \text{(B-8)}$$

$$\alpha = \frac{q' E_a}{q E_\omega} . \qquad \text{(B-9)}$$

However, since we are, in fact, rotating the axes, the argument in the rotation matrices will be $-\Psi$.

In the $\pi\pi$ rest frame, the partial-wave amplitudes are

$$\mathcal{A}^1_m(\Delta^2) = \mathcal{A}^1_0(\Delta^2)\,\delta_{m0} , \qquad \text{(B-10)}$$

where $\mathcal{A}^1_0$ is given by (B-3).

In the helicity representation, therefore,

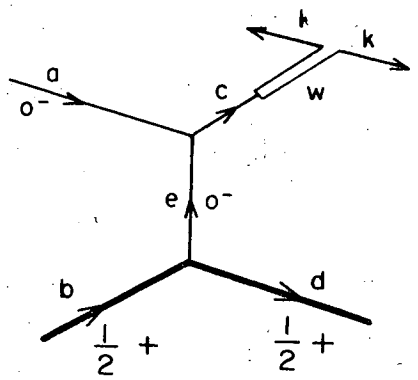

Fig. B-1. Feynman diagram, in the Born approximation, for OPE process. Notation follows that of Jackson and Pilkuhn.

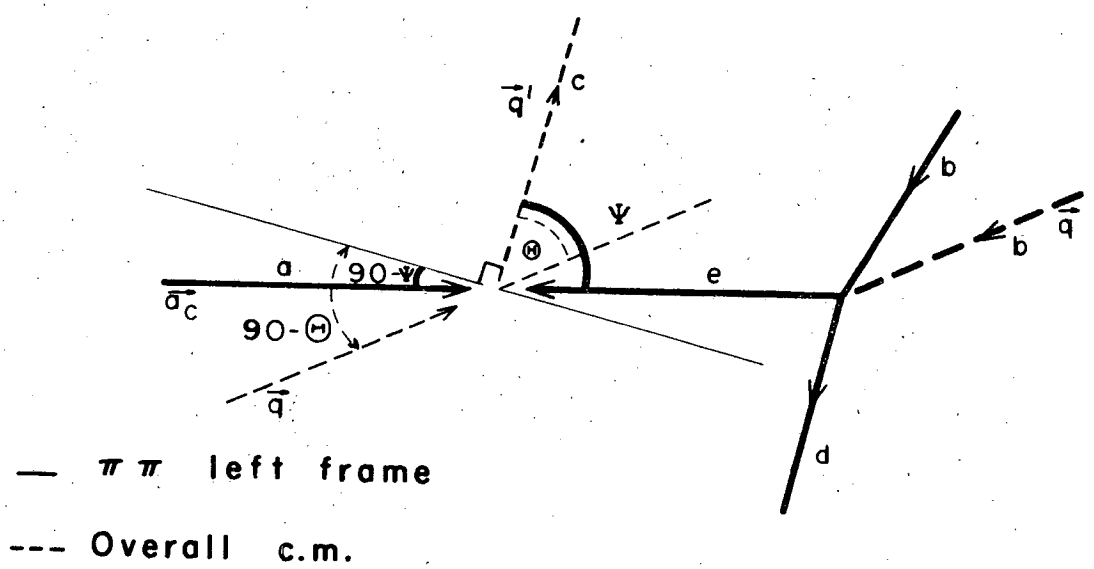

MUB-12538

Fig. B-2. Relation between particle directions in overall c.m. and ππ rest frame.

$$\hat{\mathcal{A}}^{l}_{m'}(\Delta^2) = d^{l}_{m'm}(-\Psi)\mathcal{A}^{l}_{m}(\Delta^2)$$

$$= d^{l}_{m'0}(-\Psi)\mathcal{A}^{l}_{0}(\Delta^2)$$

$$= \sqrt{\frac{4\pi}{2l+1}}\, Y^{l}_{m'}(-\Psi, 0)\mathcal{A}^{l}_{0}(\Delta^2). \qquad \text{(B-11)}$$

OPE Helicity Amplitudes

Let the helicity projections of the four particles be

$$\lambda_a,\ \lambda_b,\ \lambda_c(\lambda_\omega),\ \lambda_d,$$

with $\lambda = \lambda_a - \lambda_b,\ \mu = \lambda_c - \lambda_d$,

and let us write $B^{(l)}_{\mu\lambda}$ for the OPE helicity amplitude, where the $\pi\pi$ system is in an angular momentum state l:

$$B^{(l)}_{\mu\lambda} = G \begin{bmatrix} \xi_- \cos\frac{\Theta}{2} & \xi_+ \sin\frac{\Theta}{2} \\ \xi_+ \sin\frac{\Theta}{2} & -\xi_- \cos\frac{\Theta}{2} \end{bmatrix} \frac{F[\Delta^2]}{\mu^2+\Delta^2}\hat{\mathcal{A}}^{l}_{m'} \ . \qquad \text{(B-12)}$$

We write down some selected $B^{(l)}_{\mu\lambda}$:

$$B^{(0)}_{-1/2,1/2} = \langle 0+ \,|\, B^{(0)} \,|\, - \rangle$$

$$= G\xi_+ \sin\frac{\Theta}{2}\, \frac{F[\Delta^2]}{\mu^2+0^2}\, 8\pi\, \frac{\omega}{k}\, e^{i\delta_0} \sin\delta_0, \qquad \text{(B-13a)}$$

$$B^{(1)}_{-1/2,-1/2} = \langle 0+ \,|B^{(1)}|\, + \rangle$$

$$= G\xi_- \cos\frac{\Theta}{2}\, \frac{F[\Delta^2]}{\mu^2+\Delta^2}\, 8\pi\, \frac{\omega}{k}\, 3e^{i\delta_1} \sin\delta_1 \left[\frac{a_\omega}{k}\right]\cos\Psi\ , \qquad \text{(B-13b)}$$

$$B^{(1)}_{3/2,-1/2} = \langle 1- \,|B^{(1)}|\, + \rangle$$

$$= G\xi_+ \sin\frac{\Theta}{2}\, \frac{F[\Delta^2]}{\mu^2+\Delta^2}\, 8\pi\, \frac{\omega}{k}\, 3e^{i\delta_1} \sin\delta_1 \left[\frac{a_\omega}{k}\right] \frac{\sin\Psi}{\sqrt{2}}\ , \qquad \text{(B-13c)}$$

$$B^{(2)}_{-1/2,-1/2} = \langle 0+ | B^{(2)} | + \rangle$$

$$= G\xi_- \cos\frac{\Theta}{2} \frac{F[\Delta^2]}{\mu^2+\Delta^2} 8\pi \frac{\omega}{k} 5\, e^{i\delta_2} \sin\delta_2 [\frac{a_\omega}{k}]^2 \frac{3\cos^2\Psi - 1}{2} , \tag{B-13d}$$

$$B^{(2)}_{3/2,-1/2} = \langle 1- | B^{(2)} | + \rangle$$

$$= G\xi_+ \sin\frac{\Theta}{2} \frac{F[\Delta^2]}{\mu^2+\Delta^2} 8\pi \frac{\omega}{k} 5e^{i\delta_2} \sin\delta_2 [\frac{a_\omega}{k}]^2 \sqrt{\frac{3}{8}} \sin 2\Psi , \tag{B-13e}$$

$$B^{(2)}_{5/2,1/2} = \langle 2- | B^{(2)} | - \rangle$$

$$= -G\xi_- \cos\frac{\Theta}{2} \frac{F[\Delta^2]}{\mu^2+\Delta^2} 8\pi \frac{\omega}{k} 5e^{i\delta_2} \sin\delta_2 [\frac{a_\omega}{k}]^2 \frac{\sqrt{3}}{2} \sin^2\Psi . \tag{B-13f}$$

Having obtained these OPE amplitudes in the helicity representation, we are at will to alter them by some mechanism, for example, absorption. Then, in order to get decay angular distributions, we go back to the $\pi\pi$ rest frame, i.e., we perform the inverse rotation through the angle Ψ. Then we construct the bilinear forms from $\mathcal{M}_p \mathcal{M}_p^*$ sum, and average over nucleon helicities, and we arrive at the density matrix elements,

i.e.,

$$\rho = \frac{\sum_{\lambda_b, \lambda_d} B_{\mu\lambda}^{(l)} B_{\mu'\lambda'}^{*(l')}}{Tr\left[\sum_{\lambda_b, \lambda_d} B_{\mu\lambda}^{(l)} B_{\mu'\lambda'}^{*(l')}\right]} . \tag{B-14}$$

Cross Sections

In this section, we derive expressions for

$$\frac{\partial^2\sigma}{\partial\omega^2 \partial\Delta^2} \text{ and } \frac{\partial^3\sigma}{\partial\Omega_{\pi\pi} \partial\Delta^2}$$

and show the connection with the Chew-Low formula and the formulae of Jackson and Pilkuhn and of Högaasen et al.

The cross section is given by

$$d\sigma = \frac{[2\pi]^4}{4\mathcal{F}}\left[\frac{1}{2}\sum_{jj'}|\mathcal{M}_p|^2\right]d\rho\ ; \tag{B-15}$$

$\mathcal{F}$ is the flux, $\mathcal{F}^2 = (a\cdot b)^2 - (m_a m_b)^2$

$$= [a_{lab}\, E_b^{lab}]^2 = [q\, E_{cm}]^2, \tag{B-16}$$

$d\rho$ is the three-body phase space (Lorentz invariant).
With normalization of states,

$$\langle \vec{k}'E'/\vec{k}E\rangle = 2\sqrt{EE'}\,\delta_{EE'}\,(2\pi)^3\,\delta(\vec{k}-\vec{k}')$$

$$\rightarrow d\rho = \prod_i\left[\frac{1}{(2\pi)^3}\,\delta(p_i^2 - m_i^2)\,d^4k_i\right]\delta^4(k_{in}-k_{out}) \tag{B-17}$$

$$= \prod_i\left[\frac{1}{(2\pi)^3}\,\frac{d\vec{k}_i}{2E_i}\right]\delta^4(k_{in}-k_{out}). \tag{B-18}$$

We choose to write $d\rho$ in a form which shows that we are considering the three-body as the product of two two-body phase spaces:

$$d\rho = \frac{1}{(2\pi)^9}\left[\frac{k}{4\omega}\,d\Omega_{\pi\pi}\,d\omega^2\right]\left[\frac{q}{4E_{cm}}\,d\Omega\right]$$

$$= \frac{1}{(2\pi)^9}\left[\frac{k}{4\omega}\,d\cos\theta\,d\phi\,d\omega^2\right]\left[\frac{\pi}{4\mathcal{F}}\,d\Delta^2\right], \tag{B-19}$$

$$\frac{1}{2}\sum_{jj'}|\mathcal{M}_p|^2 = G^2\left[\frac{F[\Delta^2]}{\mu^2+\Delta^2}\right]^2\left[\xi_+^2\sin^2\frac{\Theta}{2} + \xi_-^2\cos^2\frac{\Theta}{2}\right], \tag{B-20}$$

which by (B-2), (B-3), and (B-7)

$$= G^2 \left[\frac{F[\Delta^2]}{\mu^2+\Delta^2} \right]^2 [(m_b - m_d)^2 + \Delta^2]$$

$$\times\ 64\pi^2 \frac{\omega^2}{k^2} 4\pi \sum_{ll'} \left[\sqrt{(2l+1)(2l'+1)} \left[\frac{a_\omega}{k} \right]^{l+l'} \right. \tag{B-21}$$

$$\left. \times \sin\delta_l \sin\delta_{l'}\, e^{i(\delta_l - \delta_{l'})}\, Y_l^0(\theta,\phi)\, Y_{l'}^{0*}(\theta,\phi) \right].$$

(The absorption model introduces partial-wave amplitudes with $m \neq 0$. We can replace the summation in the last expression by

$$\sum_{ll'} \left[\sqrt{(2l+1)(2l'+1)} \left[\frac{a_\omega}{k} \right]^{l+l'} \sin\delta_l \sin\delta_{l'} \right.$$

$$\left. \times \sum_{mm'} C_{lm} C_{l'm'}^{*}\, Y_l^m(\theta,\phi)\, Y_{l'}^{m'*}(\theta,\phi) \right], \tag{B-21a}$$

and the following discussion proceeds analogously.)

For convenience, let us consider first one partial wave, and then we have, from Eq. (B-15),

$$d\sigma^{(l)} = \frac{(2\pi)^4}{4\mathcal{J}} G^2 \left[\frac{F[\Delta^2]}{\mu^2+\Delta^2} \right]^2 [(m_b - m_d)^2 + \Delta^2]$$

$$\times\ 64\pi^2 [2l+1]^2 \sin^2\delta_l \frac{\omega^2}{k^2} \left[\frac{a_\omega}{k} \right]^{2l} [P_l(\cos\theta)]^2$$

$$\times \frac{\pi}{(2\pi)^9} \frac{k}{16\omega} \frac{1}{\mathcal{J}} d\Omega_{\pi\pi}\, d\omega^2\, d\Delta^2, \tag{B-22}$$

$$\therefore \quad \frac{\partial^4 \sigma^{(1)}}{\partial \Omega_{\pi\pi} \partial \omega^2 \partial \Delta^2} = \frac{64\pi^2}{(2\pi)^5} \frac{\pi}{64 \mathcal{F}^2} G^2 \left[\frac{F[\Delta^2]}{\mu^2+\Delta^2} \right]^2 [(m_b-m_d)^2+\Delta^2]$$

$$\times (2l+1)^2 \sin^2 \delta_l \frac{\omega^2}{k^2} \left[\frac{a_\omega}{k} \right]^{2l} [P_l[\cos\theta]]^2$$

$$= \frac{1}{2\mathcal{F}^2} \left[\frac{G^2}{4\pi} \right] \left[\frac{F[\Delta^2]}{\mu^2+\Delta^2} \right]^2 [(m_b-m_d)^2 + \Delta^2] \frac{k}{\omega} (2l+1) \sin^2 \delta_l \frac{\omega^2}{k^2} \left(\frac{a_\omega}{k} \right)^{2l}$$

$$|Y_0^l(\theta, \phi)|^2 . \tag{B-23}$$

Evaluating this expression at $\Delta^2 = -\mu^2$, we make the "pole approximation," and by summing over l, we derive the Chew-Low formula.[55] At $\Delta^2 = -\mu^2$, $F[\Delta^2] = 1$ and $a_\omega = k$, since the exchanged pion is now considered to be on its mass shell;

$$\therefore \quad \frac{\partial^2 \sigma^{(1)}}{\partial \Omega_{\pi\pi} \partial \omega^2 \partial \Delta^2} = \frac{1}{2\mathcal{F}^2} \left[\frac{G^2}{4\pi} \right] \frac{[(m_b-m_d)^2+\Delta^2]}{[\mu^2+\Delta^2]^2} \omega k (2l+1)$$

$$\frac{\sin^2 \delta_l}{k^2} |Y_0^l(\theta, \phi)|^2 , \tag{B-24}$$

$$\therefore \quad \frac{\partial^2 \sigma}{\partial \omega^2 \partial \Delta^2} = \frac{1}{8\pi \mathcal{F}^2} \left[\frac{G^2}{4\pi} \right] [(m_b-m_d)^2+\Delta^2] \omega k \frac{\sigma_{\pi\pi}}{[\mu^2+\Delta^2]^2} . \tag{B-25}$$

To connect formula (B-23) with expressions for the production of vector[60] and 2^+ mesons[66] by pion exchange, we have to show the relationship between the phase shift δ_l and the coupling constant $g^{(l)}$.

For those phase shifts that are resonant at $\omega = m_c$, we can write down the Breit-Wigner form for the scattering amplitude,

$$e^{i\delta_l} \sin\delta_l = \frac{\Gamma^{(l)} m_c}{[(\omega^2 - m_c^2) - i\, \Gamma^{(l)} m_c]} , \tag{B-26}$$

$$\therefore \quad \frac{1}{\pi} \int \sin^2\delta \, d\omega^2 = \Gamma^{(l)} m_c \, . \tag{B-27}$$

Instead of this last equation, let us define $\Gamma^{(l)}$ in

$$\frac{1}{\pi} \int \frac{\omega}{k} \left[\frac{a_\omega}{k}\right]^{2l} \sin^2\delta \, d\omega^2 = \frac{m_c}{k_c} \left[\frac{a_c}{k_c}\right]^{2l} \Gamma^{(l)} m_c \tag{B-28}$$

here a_c and k_c are the values of a_ω and k at $\omega = m_c$.

We can also describe the resonant particle as decaying into two pseudoscalar particles by the coupling

$$\frac{g^{(l)}}{m_c^{l-1}} \, (a-e)^l : t_l, \tag{B-29}$$

where $(a-e)^l$ is a tensor of the lth rank, formed from the four-vector $(a-e)$, i.e., a "raw" tensor in the Zemach[95] sense, and t_l is a symmetric traceless polarization tensor describing the spin states of a spin-l particle.

The t_l's are not unit tensors, but have the normalization[96]

$$\eta_l = t_l : t_l = \frac{[2l-1]!!}{l!} \, . \tag{B-30}$$

With expression (B-29) for the coupling, we derive the partial decay rate into two particles of momentum k_c:

$$\Gamma^{(l)} = \frac{g^{(l)2}}{4\pi} \left[\frac{4k_c^2}{m_c^2}\right]^l \frac{k_c}{2[2l+1]} \, . \tag{B-31}$$

In Table B-I we summarize these results for $l = 0, 1$, and 2. Note that for $l = 2$, our normalization differs from that of Högaasen et al.,[66] with consequences for the definition of $g^{(2)}$.

In the evaluation of (B-29), for the various spins and helicities in Table B-I, we have transformed the momenta into the $\pi\pi$ rest frame. This is because the polarizations are then formed from three-vectors, i.e., they have no "time" components. In this way, we relate to the previous work, where we transformed the spin states from the $\pi\pi$ rest frame to the c.m. frame using the matrices $d^l(-\Psi)$, which depend on the same Lorentz transformation.

Polarization tensors, OPE amplitudes in a helicity representation and decay rates for $l = 0$, 1 and 2

Table B-I.

l	$\eta_l = \frac{[2l-1]!!}{l!}$	t_l in $\pi\pi$ rest frame	$\frac{g^{(l)}}{m_c} i^{l-1} [a-e]^l : t_l$	$\Gamma^{(l)} = \frac{g^{2(l)}}{4\pi} [\frac{2a_c}{m_c}]^{2l} \frac{a_c}{4(2l+1)}$
0	1	1	$g^{(0)} m_c$	$\frac{g^{2(0)}}{4\pi} \frac{a_c}{2}$
1	1	$\vec{\epsilon}^{(1)} = \begin{cases} \epsilon^{(+)} = \frac{-1}{\sqrt{2}}[\hat{x} + i\hat{y}] \\ \epsilon^{(0)} = \hat{z} \\ \epsilon^{(-)} = \frac{1}{\sqrt{2}}[\hat{x} - i\hat{y}] \end{cases}$	$g^{(1)}[a-e]_\mu \epsilon^{(\lambda)}_\mu = \begin{cases} g^{(1)}\sqrt{2}\, q \sin\Theta \\ 2g^{(1)} q[\cos\Theta - a]\frac{E_c}{m_c} \\ -g^{(1)}\sqrt{2}\, q \sin\Theta \end{cases}$	$\frac{g^{2(1)}}{4\pi} \frac{2}{3} \frac{a_c^3}{m_c^2}$
2	$\frac{2}{3}$	$t_2 = \begin{cases} \sqrt{\frac{3}{2}}\, \epsilon^{(+)}\epsilon^{(+)} \\ \sqrt{\frac{3}{2}}\, [\epsilon^{(+)}\epsilon^{(0)} + \epsilon^{(0)}\epsilon^{(+)}] \\ \frac{1}{2}[\epsilon^{(+)}\epsilon^{(-)} + \epsilon^{(-)}\epsilon^{(+)}] \\ + \epsilon^{(0)}\epsilon^{(0)} \\ \sqrt{\frac{3}{2}}\, [\epsilon^{(0)}\epsilon^{(-)} + \epsilon^{(-)}\epsilon^{(0)}] \\ \sqrt{\frac{3}{2}}\, \epsilon^{(-)}\epsilon^{(-)} \end{cases}$	$\frac{g}{m_c}[a-e] : t_2 : [a-e] =$ $m = 2 - \sqrt{\frac{3}{2}}\, 2\frac{g^{(2)}}{m_c} q^2 \sin^2\Theta$ $m = 1 - 2\sqrt{6}\frac{g^{(2)}}{m_c} q^2 \sin\Theta[\cos\Theta - a]\frac{E_c}{m_c}$ $m = 0 - \frac{g^{(2)}}{m_c} q^2[(\cos\Theta - a)^2 (\frac{E_c}{m_c})^2$ $- \frac{1}{2}\sin^2\Theta]$	$\frac{g^{2(2)}}{4\pi} \frac{8}{5} \frac{a_c^5}{m_c^4}$

From (B-28) and (B-31) we see that we can derive $g^{(l)}$ from

$$\frac{1}{\pi}\int \frac{\omega}{k}\left[\frac{a_\omega}{k}\right]^{2l} \sin^2\delta \, d\omega^2 = \frac{m_c^{\,2}}{k_c}\left[\frac{a_c}{k_c}\right]^{2l} \frac{g^{(l)^2}}{4\pi}\left[\frac{4k_c^{\,2}}{m_c^{\,2}}\right]^{l} \frac{k_c}{2(2l+1)} ,$$

i.e.,

$$= \frac{1}{m_c^{\,(2l-2)}} \frac{g^{(l)^2}}{4\pi} . \qquad \text{(B-32)}$$

Let us return now to Eq. (B-23), integrate over ω^2, and use the last equation:

$$\frac{\partial^3\sigma^{(l)}}{\partial\Omega_{\pi\pi}\partial\Delta^2} = \frac{\pi}{4\mathcal{J}^2}\left[\frac{G^2}{4\pi}\right]\left[\frac{F[\Delta^2]}{\mu^2+\Delta^2}\right]^2 [(m_c-m_d)^2+\Delta^2]$$

$$\times \frac{g^{(l)^2}}{4\pi} \frac{(4a_c^{\,2})^l}{m_c^{\,(2l-2)}} \left|Y_l^0(\theta,\phi)\right|^2. \qquad \text{(B-33)}$$

For l = 1, this is identical with Jackson and Pilkuhn,[60] Eq. (10). For l = 2--apart from the different normalization factor of 3/2--this is Eq. (2.4) of Högaasen et al.[66]

With this identification, we have attempted to show that, because of the nature of the coupling of a spin-l particle to two pseudoscalars--Eq. (B-29)--the inclusion of the kinematic off-the-mass-shell factor $\left[\frac{a_c}{k_c}\right]^l$ in the partial-wave expansion formulae is justified.

APPENDIX C

Absorption Calculation in a Linear Momentum Representation

This unpublished work is entirely due to Dr. Robert Huff, and is included here with his kind permission.

Omnes[69] introduces the concept of eigenstates of the S matrix $|\alpha\rangle$, $|\beta\rangle \cdots$ to be contrasted with the physically observable states $|a\rangle$, $|b\rangle \cdots$:

$$|a\rangle = u_{a\alpha}|\alpha\rangle \qquad \text{(summation convention)}, \tag{C-1a}$$

$$|\alpha\rangle = \bar{u}_{\alpha a}|a\rangle \tag{C-1b}$$

where u is a unitary matrix;

$$S|\alpha\rangle = e^{2i\delta_\alpha}|\alpha\rangle, \tag{C-2}$$

where δ_α is the real eigen-phase-shift.

The relationship between F, the absorbed matrix, and B, the Born matrix, is given in the eigenstate representation by

$$\langle\beta|F|\alpha\rangle = e^{i(\delta\beta+\delta\alpha)}\langle\beta|B|\alpha\rangle. \tag{C-3}$$

Thus

$$\langle b|F|a\rangle = \sum_{\alpha,\beta} \bar{u}_{\beta b} u_{\alpha a} \langle\beta|F|\alpha\rangle \tag{C-4a}$$

$$= \sum_{a',b',\alpha,\beta} e^{i(\delta\beta+\delta\alpha)} \bar{u}_{\beta b'} u_{\beta b'} u_{\alpha a} \bar{u}_{\alpha a'} \langle b'|B|a'\rangle \tag{C-4b}$$

$$= \sum_{a'b'} \hat{S}_{bb'} \langle b'|s|a'\rangle \hat{S}_{a'a}, \tag{C-4c}$$

where

$$\hat{S}_{a'a} = \sum_{\alpha} \bar{u}_{\alpha a'} u_{\alpha a} e^{i\delta\alpha} = \langle a'|S^{1/2}|a\rangle, \tag{C-5a}$$

and

$$\hat{S}_{bb'} = \sum_{\beta} \bar{u}_{\beta b} u_{\beta b'} e^{i\delta\beta} = \langle b|S^{1/2}|b'\rangle. \tag{C-5b}$$

Hence we have the matrix relation

$$\boxed{F = S^{1/2} B S^{1/2}.} \tag{C-6}$$

In the usual angular momentum representation, the physical states $|a\rangle$, $|b\rangle$ are labeled $|i, J, M, \lambda_1, \lambda_2\rangle$ and $|f, J, M, \lambda_3, \lambda_4\rangle$ for the initial and final states; J, M refer to the c.m. angular momentum; λ_n are the helicities of the four particles in the quasi-two-body reaction; all the other quantum numbers, including the c.m. energy, are contained in the labels i and f: $\lambda = \lambda_1 - \lambda_2$, $\mu = \lambda_3 - \lambda_4$.

With this representation, Eq. (C-6) takes the form

$$\langle f J M \lambda_3 \lambda_4 | F | i J M \lambda_1 \lambda_2 \rangle =$$

$$\sum_{\lambda'_n} \langle f J M \lambda_3 \lambda_4 | S^{1/2} | f J M \lambda_3' \lambda_4' \rangle \langle f J M \lambda_3' \lambda_4' | B | i J M \lambda_1' \lambda_2' \rangle$$

$$\times \langle i J M \lambda_1' \lambda_2' | S^{1/2} | i J M \lambda_1 \lambda_2 \rangle . \tag{C-7}$$

However, in a linear momentum representation, the physical states are $|f, \Omega_f, \lambda_3, \lambda_4\rangle$ and $|i, \Omega_i, \lambda_1, \lambda_2\rangle$, where Ω = direction $[\Theta, \Phi]$. We note the relationships

<u>Orthonormality</u>

$$\int d\Omega \sum_{\lambda_1 \lambda_2} |\Omega \lambda_1 \lambda_2\rangle\langle \lambda_1 \lambda_2 \Omega| = 1 \tag{C-8a}$$

$$= \sum_{J M \lambda_1 \lambda_2} |J M \lambda_1 \lambda_2\rangle\langle J M \lambda_1 \lambda_2|; \tag{C-8b}$$

<u>Connection between two representations</u>

$$\langle \Omega \lambda_1 \lambda_2 | J M \lambda_1' \lambda_2' \rangle = \delta_{\lambda \lambda_1'} \delta_{\lambda_2 \lambda_2'} \sqrt{\frac{2J+1}{4\pi}} \mathcal{D}^{J*}_{M\lambda}(\hat{\Omega}) \tag{C-9}$$

[see Jacob and Wick[94] Eq. (24)].

Relation (C-6) in this representation becomes

$$\boxed{\begin{aligned}&\langle f\Omega\,\lambda_3\lambda_4\,|F|\,i\,0\,\lambda_1\lambda_2\rangle = \\ &\int d\Omega_f d\Omega_i \sum_{\lambda'_n} \langle f\Omega\,\lambda_3\lambda_4\,|S^{1/2}|\,f\Omega_f\,\lambda_3'\lambda_4'\rangle \\ &\times\langle f\Omega_f\lambda_3'\,\lambda_4'\,|B|i\Omega_i\lambda_1'\lambda_2'\rangle\,\langle i\Omega_i\,\lambda_1'\lambda_2'\,|S^{1/2}|\,i0\lambda_1\lambda_2\rangle\end{aligned}} \qquad \text{(C-10)}$$

We now try to simplify the above equation. Using Eq. (C-9), we have

$$\langle f\,\Omega_f\,\lambda_3\lambda_4\,|B|\,i\Omega_i\,\lambda_1\lambda_2\rangle =$$

$$\sum_{JM} \langle f\,J\,M\lambda_3\lambda_4\,|B|\,i\,J\,M\,\lambda_1\lambda_2\rangle \frac{2J+1}{4\pi}\,\mathcal{D}^{J*}_{M\mu}(\hat{\Omega}_f)\,\mathcal{D}^{J}_{M\lambda}(\hat{\Omega}_i)$$

$$= \sum_{J} \langle f\,J\,M\lambda_3\lambda_4\,|B|\,i\,J\,M\lambda_1\lambda_2\rangle \frac{2J+1}{4\pi}\,\mathcal{D}^{J*}_{\lambda\mu}[\hat{\Omega}_i^{-1}\Omega_f]\ , \qquad \text{(C-11)}$$

where we have used the unitarity and group properties of the $\mathcal{D}$'s and also the fact that $\langle f\,J\,M\lambda_3\lambda_4\,|B|\,J\,M\lambda_1\lambda_2\rangle$ is independent of M.

Let us write the Euler angles for the rotation

$$\hat{\Omega}_i^{-1}\Omega_f = [\Phi_{if}, \Theta_{if} - \Psi_{if}]\ : \qquad \text{(C-12)}$$

$$\mathcal{D}^{J*}_{\lambda\mu}[\Omega_i^{-1}\Omega_f] = e^{i\lambda\Phi_{if}}\,d^{J}_{\lambda\mu}[\Theta_{if}]\,e^{-i\mu\Psi_{if}}\ . \qquad \text{(C-13)}$$

But we have, again using relation (C-9)

$$\langle f\Theta_{if}\lambda_3\lambda_4\,|B|\,i\,0\lambda_1\lambda_2\rangle =$$

$$\sum_{J} \langle f\,J\,M\lambda_3\lambda_4\,|B|\,i\,J\,M\lambda_1\lambda_2\rangle \frac{2J+1}{4\pi}\,d^{J}_{\lambda\mu}[\Theta_{if}]\,. \qquad \text{(C-14)}$$

Thus $\langle f\Omega_f \lambda_3\lambda_4 |B| i\Omega_i \lambda_1\lambda_2 \rangle =$

$$e^{i\lambda\Phi_{if}} e^{-i\mu\Psi_{if}} \langle f\Theta_{if}\lambda_3\lambda_4 |B| i0\lambda_1\lambda_2\rangle \ . \tag{C-15}$$

In Appendix D we quote Huff to show

$$\eta_{if} = e^{1/2_i[\Phi_{if} - \Psi_{if}]} = \frac{\cos\frac{\Theta_i}{2}\cos\frac{\Theta_f}{2} + \sin\frac{\Theta_i}{2}\sin\frac{\Theta_f}{2}\, e^{i[\Phi_i - \Phi_f]}}{\cos\frac{\Theta_{if}}{2}} \tag{C-16a}$$

$$\beta_{if} = e^{1/2_i[\Phi_{if} + \Psi_{if}]} = \frac{\cos\frac{\Theta_i}{2}\sin\frac{\Theta_f}{2}\, e^{i\Phi_f} - \sin\frac{\Theta_i}{2}\cos\frac{\Theta_f}{2}\, e^{i\Phi_i}}{\sin\frac{\Theta_{if}}{2}} \ . \tag{C-16b}$$

It will be useful to relate matrix elements which differ by having the angles Ω_f and Ω_i interchanged. To obtain this we start from

$$\mathcal{D}^{J*}_{\lambda\mu}[\hat{\Omega}_f^{-1}\hat{\Omega}_i] = \mathcal{D}^{J}_{\mu\lambda}[\hat{\Omega}_i^{-1}\Omega_f] = e^{-i\mu\Phi_{if}} e^{i\lambda\Psi_{if}} d^J_{\mu\lambda}(\Theta_{if}) \ . \tag{C-17}$$

But $\quad d^J_{\mu\lambda}(\Theta_{if}) = (-1)^{\lambda-\mu} d^J_{\lambda\mu}(\Theta_{if});$ (C-18)

we then have

$$\mathcal{D}^{J*}_{\lambda\mu}[\hat{\Omega}_f^{-1}\Omega_i] = (-1)^{\lambda-\mu} e^{i\lambda\Psi_{if} - i\mu\Phi_{if}} d^J_{\lambda\mu}[\Theta_{if}]$$

$$= [-1]^{\lambda-\mu} e^{i[\lambda+\mu][\Phi_{if} - \Psi_{if}]} \mathcal{D}^{J*}_{\lambda\mu}[\hat{\Omega}_i^{-1}\Omega_f] \ . \tag{C-19}$$

Thus $\quad \langle f\Omega_f\lambda_3\lambda_4 |B| i\Omega_i\lambda_1\lambda_2\rangle$

$$=(-1)^{\lambda-\mu} e^{i[\lambda+\mu][\Phi_{if}-\Psi_{if}]} \langle f\Omega_i\lambda_3\lambda_4 |B| i\Omega_f\lambda_1\lambda_2\rangle \ . \tag{C-20}$$

For the special case of $\Omega_i = 0$

$$\langle f\Omega_f \lambda_3\lambda_4 | B | i\,0\,\lambda_1\lambda_2\rangle = (-1)^{\lambda-\mu}\langle f\,0\,\lambda_3\lambda_4 | B | i\Omega_f\lambda_1\lambda_2\rangle . \qquad \text{(C-21)}$$

We apply these relations to $BS^{1/2}$, using $\lambda' = \lambda_1' - \lambda_2'$, $\mu' = \lambda_3' - \lambda_4'$:

$$\langle f\Omega_f \lambda_3'\lambda_4' | BS^{1/2} | i\,0\,\lambda_1\lambda_2\rangle$$
$$= [-1]^{\lambda-\mu'}\langle f\,0\,\lambda_3'\lambda_4' | BS^{1/2} | i\Omega_f\lambda_1\lambda_2\rangle$$

$$=[-1]^{\lambda-\mu'}\int d\Omega_i \sum_{\lambda_1'\lambda_2'} \langle f\,0\,\lambda_3'\lambda_4' | B | i\Omega_i\lambda_1'\lambda_2'\rangle\langle i\Omega_i\lambda_1'\lambda_2' | S^{1/2} | i\Omega_f\lambda_1\lambda_2\rangle$$

$$= \int d\Omega_i \sum_{\lambda_1'\lambda_2'} \langle f\Omega_i\lambda_3'\lambda_4' | B | i\,0\,\lambda_1'\lambda_2'\rangle\langle i\Omega_i\lambda_1'\lambda_2' | S^{1/2} | i\Omega_f\lambda_1\lambda_2\rangle(-1)^{\lambda-\lambda'}. \qquad \text{(C-22)}$$

We can now write the full absorbed matrix element of Eq. (C-10),

$$\langle f\Theta\lambda_3\lambda_4 | F | i0\,\lambda_1\lambda_2\rangle =$$

$$\int d\cos\Theta_i \sum_{\lambda_n'} \langle f\Theta_i\lambda_3'\lambda_4' | B | i0\lambda_1'\lambda_2'\rangle Q(\Theta,\Theta_i), \qquad \text{(C-23)}$$

where

$$Q[\Theta,\Theta_i] = \int d\Phi_i\, d\Omega_f [-1]^{\lambda-\lambda'} e^{i\Phi_i[\lambda'-\mu']}$$

$$\times \langle f\Theta\lambda_3\lambda_4 | S^{1/2} | f\Omega_f\lambda_3'\lambda_4'\rangle\langle i\Omega_i\lambda_1'\lambda_2' | S^{1/2} | i\Omega_f\lambda_1\lambda_2\rangle . \qquad \text{(C-24)}$$

Define $S^{1/2} = 1 - R \rightarrow$ (C-25)

$$Q[\Theta,\Theta_i] = \delta\lambda_1\lambda_1'\,\delta\lambda_2\lambda_2'\,\delta\lambda_3\lambda_3'\,\delta\lambda_4\lambda_4'\,\delta[\cos\Theta - \cos\Theta_i]$$
$$-Q_f[\Theta,\Theta_i]\,\delta\lambda_1\lambda_1'\,\delta\lambda_2\lambda_2' - Q_i[\Theta,\Theta_i]\,\delta\lambda_3\lambda_3'\,\delta\lambda_4\lambda_4'$$
$$+ Q_{if}[\Theta,\Theta_i], \qquad \text{(C-26)}$$

where

$$Q_f[\Theta,\Theta_i] = \int d\Phi_i \, e^{i\Phi_i[\lambda-\mu']} \langle f\Theta\lambda_3\lambda_4 | R | f\Omega_i \lambda_3'\lambda_4' \rangle , \qquad \text{(C-27a)}$$

$$Q_i[\Theta,\Theta_i] = \int d\Phi_i (-1)^{\lambda-\lambda'} e^{i\Phi_i[\lambda'-\mu]} \langle i\Omega_i \lambda_1'\lambda_2' | R | i\Theta\lambda_1\lambda_2 \rangle , \qquad \text{(C-27b)}$$

and

$$Q_{if}[\Theta,\Theta_i] = \int d\Phi_i \, d\Omega_f [-1]^{\lambda-\lambda'} e^{i\Phi_i[\lambda'-\mu']} \times$$

$$\langle f\Theta\lambda_3\lambda_4 | R | f\Omega_f \lambda_3'\lambda_4' \rangle \langle i\Omega_i \lambda_1'\lambda_2' | R | i\Omega_f \lambda_1\lambda_2 \rangle . \qquad \text{(C-27c)}$$

To simplify further these R matrix elements with $\hat{\Omega} = [0, \Theta, 0]$,

(C-28a)

we define $\hat{\Omega}_i^{-1} \hat{\Omega} = [\Phi_{i0}, \Theta_{i0}, -\Psi_{i0}]$, (C-28b)

$$\hat{\Omega}_f^{-1} \hat{\Omega} = [\Phi_{f0}, \Theta_{f0}, -\Psi_{f0}] ; \qquad \text{(C-28c)}$$

$$\therefore \quad \cos\Theta_{i0} = \cos\Theta_i \cos\Theta + \sin\Theta_i \sin\Theta \cos\Phi_i , \qquad \text{(C-29a)}$$

$$\eta_{i0} = e^{1/2 i[\Phi_{i0} - \Psi_{i0}]} = \frac{\cos\frac{\Theta_i}{2} \cos\frac{\Theta}{2} + \sin\frac{\Theta_i}{2} \sin\frac{\Theta}{2} e^{i\Phi_i}}{\cos\frac{\Theta_{i0}}{2}} ,$$

(C-29b)

$$\beta_{i0} = e^{1/2 i[\Phi_{i0} + \Psi_{i0}]} = \frac{\cos\frac{\Theta_i}{2} \sin\frac{\Theta}{2} - \sin\frac{\Theta_i}{2} \cos\frac{\Theta}{2} e^{i\Phi_i}}{\sin\frac{\Theta_{i0}}{2}} ,$$

(C-29c)

and similarly for

$$\cos\Theta_{f0}, \ \eta_{f0}, \text{ and } \beta_{f0}.$$

We simplify our notation.

$$F_{\mu\lambda}(\Theta) = \langle f\Theta\lambda_3\lambda_4 \,|F|\, i0\lambda_1\lambda_2 \rangle , \tag{C-30}$$

$$R_{f\mu}(\Theta) = \langle f\Theta\lambda_3\lambda_4 \,|R|\, f0\lambda_3'\lambda_4' \rangle , \tag{C-31a}$$

$$R_{i\lambda}(\Theta) = \langle i\Theta\lambda_1'\lambda_2' \,|R|\, i0\lambda_1\lambda_2 \rangle , \tag{C-31b}$$

and similarly for $B_{\mu\lambda}(\Theta)$.

Specifically we consider the two matrix elements in Eq. (C-27c), but the discussion proceeds analogously for (C-27a) and (C-27b). Hence, applying Eq. (C-15), we have

$$\langle f\Theta\lambda_3\lambda_4 \,|R|\, f\Omega_f\lambda_3'\lambda_4' \rangle = e^{i\mu'\Phi_{f0} - i\mu\Psi_{f0}} R_{f\mu}[\Theta_{f0}] ,$$

and by Eq. (C-16), $= \eta_{f0}^{\mu'+\mu}\beta_{f0}^{\mu'-\mu} R_{f\mu}[\Theta_{f0}]$. (C-32a)

By Equation (C-20) we have

$$(-1)^{\lambda-\lambda'}\langle i\Omega_i\lambda_1'\lambda_2' \,|R|\, i\Omega_f\lambda_1\lambda_2 \rangle = e^{-i[\lambda+\lambda'][\Phi_{if} - \Psi_{if}]}$$

$$\times \langle i\Omega f\lambda_1'\lambda_2' \,|R|\, i\Omega_i\lambda_1\lambda_2 \rangle ,$$

and again by Eq. (C-15) $= e^{-i\lambda'\Phi_{if} + i\lambda\Psi_{if}} R_{i\lambda}[\Theta_{if}]$, (C-32b)

and again by Eq. (C-16) $= \bar{\eta}_{if}^{\lambda+\lambda'}\beta_{if}^{\lambda-\lambda'} R_{i\lambda}[\Theta_{if}]$. (C-32c)

Therefore we have, for Eqs. (C-27)

$$Q_f[\Theta,\Theta_i] \int d\Phi_i\, e^{i\Phi_i[\lambda-\mu']}\eta_{i0}^{\mu'+\mu}\beta_{i0}^{\mu'-\mu} R_{f\mu}[\Theta_{i0}] , \tag{C-33a}$$

$$Q_i[\Theta,\Theta_i] = \int d\Phi_i\, e^{i\Phi_i[\lambda'-\mu]}\,\bar{\eta}_{i0}^{\lambda+\lambda'}\beta_{i0}^{\lambda-\lambda'} R_{i\lambda}[\Theta_{i0}] , \tag{C-33b}$$

$$Q_{if}[\Theta,\Theta_i] = \int d\Phi_i d\Omega_f\, e^{i\Phi_i[\lambda'-\mu']}\,\eta_{f0}^{\mu'+\mu}\beta_{f0}^{\mu'-\mu}\bar{\eta}_{if}^{\lambda+\lambda'}\beta_{if}^{\lambda-\lambda'} R_{f\mu}[\Theta_{f0}]\, R_{i\lambda}[\Theta_{if}]$$

(C-33c)

In Eq. (C-23), as well as the integration over all values of $\cos\Theta_i$, there is a summation over all intermediate helicities λ_n'; assuming that only the nonhelicity flip terms contribute is not a bad approximation, since the major contribution to elastic scattering is in the forward direction, where any helicity flip terms are already falling off to zero, at least in the πN state.

Accordingly, Eq. (C-23) becomes

$$\boxed{F_{\mu\lambda}[\Theta] = B_{\mu\lambda}[\Theta] - \int d\cos\Theta_i \, B_{\mu\lambda}[\Theta_i] \, Q^0[\Theta,\Theta_i] \quad ,} \tag{C-34}$$

where

$$Q^0(\Theta,\Theta_i) = Q_f^0(\Theta,\Theta_i) + Q_i^0(\Theta,\Theta_i) - Q_{if}(\Theta,\Theta_i) \ , \tag{C-35}$$

$$Q_f^0[\Theta,\Theta_i] = \int d\Phi_i \ e^{i\Phi_i[\lambda-\mu]} \eta_{i0}^{2\mu} R_{f\mu}[\Theta_{i0}] \ , \tag{C-36a}$$

$$Q_i^0[\Theta,\Theta_i] = \int d\Phi_i \ e^{i\Phi_i[\lambda-\mu]} \bar{\eta}_{i0}^{\ 2\lambda} R_{i\lambda}[\Theta_{i0}] \ , \tag{C-36b}$$

$$Q_{if}^0[\Theta,\Theta_i] = \int d\Phi_i \, d\Omega_f \ e^{i\Phi_i[\lambda-\mu]} \eta_{f0}^{2\mu} \bar{\eta}_{if}^{2\lambda} R_{f\mu}[\Theta_{f0}] R_{i\lambda}[\Theta_{if}] . \tag{C-36c}$$

We now make our final simplifications. Under the substitution

$$\Theta \to \Theta_f, \quad \Phi_i \to \Phi_i - \Phi_f,$$

$$\eta_{i0} \to \eta_{if} \quad \text{and} \quad \Theta_{i0} \to \Theta_{if}.$$

Hence, replacing Φ_i by $\Phi_i + \Phi_f$ in the expression (C-36c) for Q_{if}, we obtain

$$Q_{if}^0[\Theta,\Theta_i] = \int d\cos\Theta_f Q_f^0[\Theta,\Theta_f] \, Q_i^0[\Theta_f,\Theta_i] \ . \tag{C-37}$$

Further, since $\Theta_{i0} \to \Theta_{i0}$ and $\eta_{i0} \to \bar{\eta}_{i0}$ under the substitution (Eq. C-29), we may write

$$\boxed{\begin{aligned} Q_f^0[\Theta,\Theta_i] &= 2\int_0^\pi d\Phi_i\, R_{f\mu}[\Theta_{i0}]\, \mathrm{Re}[e^{i\Phi_i[\lambda-\mu]}\,\eta_{i0}^{2\mu}]\ , \qquad \text{(C-38a)} \\ Q_i^0[\Theta,\Theta_i] &= 2\int_0^\pi d\Phi_i\, R_{i\lambda}[\Theta_{i0}]\, \mathrm{Re}[e^{-i\Phi_i[\lambda-\mu]}\,\eta_{i0}^{2\lambda}]\ . \qquad \text{(C-38b)} \end{aligned}}$$

The question remains, what function do we use for $R_{f\mu}$ and $R_{i\lambda}$?

Following a suggestion by Huff, we talk about an effective scattering amplitude T, which gives rise to an effective elastic cross section which may possibly behave like , the geometric mean of the initial- and final-state elastic scattering (for some justification of this approach, see Appendix E:)

$$\text{i.e.,}\quad \frac{\partial\sigma_{el}}{\partial\Omega} = \frac{4\pi^2}{qq'}\,|T|^2; \qquad \text{(C-39)}$$

if we assume T is purely imaginary by the optical theorem, we have

$$T = \frac{iqq'}{8\pi^2}\,\sigma_T\, e^{-Aqq'[1-\cos\Theta]}\ . \qquad \text{(C-40)}$$

Knowing the relationship of T to the S matrix and with the definition of R in Eq. (C-25), to first order we have

$$\boxed{R[\Theta] = \frac{qq'}{16\pi^2}\,\sigma_T\, e^{-Aqq'[1-\cos\Theta]}} \qquad \text{(C-41)}$$

Here q, q' are initial and final c.m. momenta; σ_T, A are two absorption parameters, an effective total cross section and an effective elastic scattering exponential slope. We may define

$$C = \frac{\sigma_T}{4\pi A} \qquad \text{(C-42)}$$

and

$$\gamma = \frac{1}{2Aqq'}\ , \qquad \text{(C-43)}$$

and

$$\therefore\quad R[\Theta] = \frac{C}{8\pi\gamma}\, e^{-1/2\gamma[1-\cos\Theta]}\ . \qquad \text{(C-44)}$$

For consistency we have $C \leqslant 8\pi\gamma$.

To find what corresponds to maximal absorption, we use the orthonormality relations (C-8a) and (C-9) to find the absorption in the s wave. In fact, this is just the average absorption over all angles,

i.e., $$R^{(0)} = 1 - \frac{1}{4\pi}\int 2R[\Theta]\, d\Omega\,, \tag{C-45}$$

which, from (C-44), is $$1 - C[1 - e^{-1/4\gamma^2}], \tag{C-46}$$

which brings us back to Jackson's condition of $C \leq 1$. We obtain fits with $1 < C < 8\pi\gamma$, because our difinition of R is true only to first order, since

$$R = \sqrt{1 - T} = 1 - \frac{1}{2}T - \frac{1}{8}T^2 - \frac{1}{16}T^3 \cdots\,, \tag{C-47}$$

and therefore the values of C that we derive compensate for our neglect of higher-order terms.

For computing the absorbed amplitude from the Born amplitude, the term $Q^0_{if}[\Theta, \Theta_i]$ was dropped, since it involves a quadruple integral. Its effect is second order, tending to reduce the absorption. The steps involved in obtaining $F_{\mu\lambda}[\Theta]$ are the following

1. For a given value of production angle Θ and mass of the $\pi\pi$ system, we evaluate $B_{\mu\lambda}[\Theta]$ for a given initial and final helicity state.
2. We now vary Θ_i, "the intermediate scattering angle," between 0 and 180° and evaluate $B_{\mu\lambda}[\Theta_i]$.
3. For a given value of Θ and Θ_i we vary Φ_i between 0 and 180° and evaluate $\cos\Theta_{i0}$, $\eta_i^{2\mu}$, and $e^{i\Phi_i[\lambda-\mu]}$ as well as $R[\Theta_{i0}]$.
4. The results of step 3 give rise to the integral over Φ_i, and yield $Q_i^0[\Theta, \Theta_i]$ and $Q_f^0[\Theta, \Theta_i]$.
5. We multiply Q_i^0 and Q_f^0 by $B_{\mu\lambda}[\Theta_i]$ and evaluate the integral over $\cos\Theta_i$. The integrand subtracted from $B_{\mu\lambda}[\Theta]$ gives $F_{\mu\lambda}[\Theta]$.

APPENDIX D

Determination of η_{if}, β_{if}

We examine the relation

$$\mathcal{D}(\Phi_{if}, \Theta_{if}, -\Psi_{if}) = \mathcal{D}^{-1}(\hat{\Omega}_i)\,\mathcal{D}(\hat{\Omega}_f)$$

for $J = 1/2$, obtaining

$$e^{-\frac{1}{2}i\Phi_{if}\sigma_z}\, e^{-\frac{1}{2}i\Theta_{if}\sigma_y}\, e^{\frac{1}{2}i\Psi_{if}\sigma_z}$$

$$= e^{-\frac{1}{2}i\Phi_i\sigma_z}\, e^{\frac{1}{2}i\Theta_i\sigma_y}\, e^{\frac{1}{2}i\Phi_i\sigma_z}\, e^{-\frac{1}{2}i\Phi_f\sigma_z}\, e^{-\frac{1}{2}i\Theta_f\sigma_y}\, e^{\frac{1}{2}i\Phi_f\sigma_z}.$$

Defining $\eta_{if} \equiv e^{\frac{1}{2}i[\Phi_{if} - \Psi_{if}]}$ and $\beta_{if} \equiv e^{\frac{1}{2}i[\Phi_{if} + \Psi_{if}]}$,

and using $e^{\frac{1}{2}i\Theta\sigma_y} = \cos\frac{1}{2}\Theta + i\sigma_y \sin\frac{1}{2}\Theta$,

we have

$$\begin{bmatrix} \bar{\eta}_{if}\cos\frac{\Theta_{if}}{2}, & -\bar{\beta}_{if}\sin\frac{\Theta_{if}}{2} \\ \beta_{if}\sin\frac{\Theta_{if}}{2} & \eta_{if}\cos\frac{\Theta_{if}}{2} \end{bmatrix}$$

$$= \begin{bmatrix} \cos\frac{\Theta_i}{2} & e^{-i\Phi_i}\sin\frac{\Theta_i}{2} \\ -e^{i\Phi_i}\sin\frac{\Theta_i}{2} & \cos\frac{\Theta_i}{2} \end{bmatrix}$$

$$\times \begin{bmatrix} \cos\frac{\Theta_f}{2} & -e^{-i\Phi_f}\sin\frac{\Theta_f}{2} \\ e^{i\Phi_f}\sin\frac{\Theta_f}{2} & \cos\frac{\Theta_f}{2} \end{bmatrix}.$$

Thus

$$\eta_{if} \cos \frac{\Theta_{if}}{2} = \cos \frac{\Theta_i}{2} \cos \frac{\Theta_f}{2} + \sin \frac{\Theta_i}{2} \sin \frac{\Theta_f}{2} e^{i[\Phi_i - \Phi_f]},$$

$$\beta_{if} \sin \frac{\Theta_{if}}{2} = \cos \frac{\Theta_i}{2} \sin \frac{\Theta_f}{2} e^{i\Phi_f} - \sin \frac{\Theta_i}{2} \cos \frac{\Theta_f}{2} e^{i\Phi_i}.$$

These equations give η_{if} and β_{if} once we determine $\cos \Theta_{if}$. But $\cos \Theta_{if} = \cos \Theta_i \cos \Theta_f + \sin \Theta_i \sin \Theta_f \cos [\Phi_i - \Phi_f]$.

APPENDIX E

Effective Scattering Amplitude

In the angular momentum approach, it is straightforward to use an "intermediate" S matrix whose partial-wave components $\hat{S}^{(J)}$ are the geometric means of the initial- and final-state S matrices, i.e., $\hat{S}^{(J)} = (S^{(J)}_{f\mu}\, S^{(J)}_{i\lambda})^{1/2}$, which is exactly what we need in the absorption formulas.

There is no corresponding averaging in the linear momentum approach. Starting from $\partial\sigma^{elastic}_{f\mu}/\partial\Omega$ and $\partial\sigma^{elastic}_{i\lambda}/\partial\Omega$, we cannot arrive at some intermediate $R(\Theta)$ that relates to $\partial\sigma^{eff}/\partial\Omega$.

Define $\langle \Omega\, \lambda_3\, \lambda_4 \,|\hat{S}|\, \Omega'\lambda_3\, \lambda_4\rangle$

$$= \sum_{J,\,M} \frac{2J+1}{4\pi}\, \hat{S}_J\, \mathcal{D}^{J*}_{M\mu}(\hat{\Omega})\, \mathcal{D}^{J}_{M\mu}(\hat{\Omega}')$$

with $\hat{S}^{(J)} = (S^{(J)}_{f\mu}\, S^{(J)}_{i\lambda})^{1/2}$ (see Eq. C-11).

But, from the orthonormality relation (C-8a),

$$\int d\Omega''\langle \Omega\lambda_3\, \lambda_4|\hat{S}|\,\Omega''\,\lambda_3\,\lambda_4\rangle\langle\Omega''\,\lambda_3\,\lambda_4|\hat{S}|\,0\lambda_3\,\lambda_4\rangle$$

$$= \sum_{J,\,M} \frac{2J+1}{4\pi}\,(\hat{S})^2\, \mathcal{D}^{J*}(\hat{\Omega}).$$

However,

$$\int d\,\Omega''\,\langle f,\ \Omega\,\lambda_3\,\lambda_4|S|f,\ \Omega''\,\lambda_3\,\lambda_4\rangle$$

$$\langle i,\ \Omega''\,\lambda_1\,\lambda_2\,|S|\,i,\ 0\,\lambda_1\,\lambda_2\rangle$$

$$= \sum_{J,\,M,\,J'} \frac{2J+1}{4\pi}\,\frac{2J'+1}{4\pi}\, S^{(J)}_{f\mu}\, S^{(J')}_{i\lambda}$$

$$\times\, \mathcal{D}^{J*}_{M\mu}(\hat{\Omega})\int \mathcal{D}^{J}_{M\mu}(\hat{\Omega}'')\, \mathcal{D}^{J'*}_{\lambda\lambda}(\hat{\Omega}'')\, d\Omega''$$

$$= \sum_{JJ'} \frac{2J+1}{4\pi}\, S^{(J)}_{f\mu}\, S^{(J')}_{i\lambda}\, \mathcal{D}^{J*}_{\mu\mu}(\hat{\Omega})$$

$$\times \left[\frac{2J'+1}{2}\int d[\cos\Theta'']\, d^{J}_{\mu\mu}[\Theta'']\, d^{J'}_{\lambda\lambda}[\Theta'']\right].$$

If $\mu = \lambda$, the integral in brackets reduces to $\delta_{JJ''}$, but otherwise the linear momentum relation analagous to $[S^{(J)}]^2 = S^{(J)}_{f\mu} S^{(J)}_{i\lambda}$ does not hold, i.e.,

$$\int d\Omega'' \left|\Omega'' \lambda_3 \lambda_4\right\rangle\left\langle\Omega'' \lambda_3' \lambda_4'\right| = 1$$

only if

$$\lambda_3 - \lambda_4 = \lambda_3' - \lambda_4'.$$

We know the initial-state absorption from $\pi^- p$ elastic scattering, but since the final-state scattering is unknown, nothing is gained if we try to parameterize in terms of the final-state absorption parameters. It is better to go directly to the intermediate function $R(\Theta)$ and parameterize that.

FOOTNOTES AND REFERENCES

1. Lyndon M. Hardy, Analysis of Strange Particle Resonant States from $\pi^- p$ Interactions (Ph. D. Thesis), UCRL-16788, July 1966.
2. Richard I. Hess, Analysis of $K\bar{K}$ Pairs from $\pi^- p$ Interactions (Ph. D. Thesis), UCRL-16832, July 1966.
3. G. Alexander, O. I. Dahl, L. Jacobs, G. R. Kalbfleisch, D. H. Miller, A. Rittenberg, J. Schwartz, and G. Smith, Phys. Rev. Letters 9, 400 (1962).
4. David J. Crennell, George R. Kalbfleisch, K. W. Lai, J. Michael Scarr, Thomas G. Schumann, Ian O. Skillicorn, and Medford S. Webster, Phys. Rev. Letters 16, 1025 (1966).
5. M. Hutchinson and N. Joseph, LYRIC II--A Program Used to Perform Library Functions for a Large Bubble Chamber Experiment, Alvarez Group Programming Memo P-123, May 1965.
6. S. Penny, LINGO, Alvarez Group Programming Memo P-7, Jan. 1962.
7. A good summary of measuring machines and data analysis programs as used in this experiment is to be found in A. H. Rosenfeld and W. E. Humphrey, Ann. Rev. Nucl. Sci. 13, 103 (1963).
8. Margaret H. Alston et al., PANAL, Alvarez Group Programming Memo 358, Feb. 1963.
9. George R. Kalbfleisch et al., DST-EXAM and π63, K63 Data Analysis Systems, Alvarez Group Programming Memo P-54, May 1964.
10. Lynn Champomier, Fortran Program SUMX, UCRL-11222, April 1964.
11. A good discussion of this is to be found in Appendix A of Ronald R. Ross, Elastic and Charge-Exchange Scattering of K^- Mesons in Hydrogen (Ph. D. Thesis), UCRL-9749, June 1961.
12. This is due to Orin I. Dahl and is described in Ref. 9.
13. A. Citron, W. Galbraith, T. F. Kycia, B. A. Leontić, R. H. Phillips, and A. Rousset, Phys. Rev. Letters 13, 205 (1964).

14. A. N. Diddens, E. Lillethun, A. E. Taylor, T. G. Walker, and A. M. Wetherell, Phys. Rev. Letters 9, 108 (1962).

15. Inadvertently in the π 72 experiment, only stopping protons were measured on two rolls of the 2.36 GeV/c film. This has been taken into account in the determination of the partial cross sections.

16. P. J. Duke et al., Phys. Rev. Letters 15, 468 (1965); also Rutherford Laboratory, N. I. R. N. S. preprint RPP/H/8.

17. A. Yokosawa, Phys. Rev. Letters 16, 1019 (1966).

18. M. L. Perl and M. C. Corey, Phys. Rev. 136, B 787 (1964).

19. L. M. Simmons, Phys. Rev. Letters 12, 229 (1964).

20. We are aware of the comments made by Chinowsky et al., Phys. Rev. 139, B 1411 (1966), that a maximum-likelihood method which takes account of errors in the measurement of Δ^2 is preferable to a least-squares fit. In the Δ^2 region that we are considering, the measurements are mainly determined by the ranges of the protons, and we are not convinced that the errors lead to any bias in the estimate of A.

21. J. Alitti et al., Nuovo Cimento 29, 515 (1963).

22. M. L. Perl, L. W. Jones, and G. C. Ting, Phys. Rev. 132, 1252 (1963).

23. L. Bondár et al., Nuovo Cimento 31, 729 (1964).

24. See, for example, G. Höhler, G. Ebel, and J. Giesecke, Z. Physik 180, 430 (1964).

25. Robert J. Esterling, Roger E. Hill, Norman E. Booth, S. Suwa, and A. Yokosawa, $\pi^- p$ Elastic Scattering between 1.7 and 2.5 GeV/c, Enrico Fermi Institute Report #EFINS 66-29.

26. For a good description of Regge poles with a comprehensive list of references, a set of lecture notes by R. J. N. Phillips for the 1966 Erice Summer School is recommended, A. E. R. E., Harwell preprint HL66/2798, July 1966. An earlier summary is by Elliot Leader, Rev. Mod. Phys. 38, 476 (1966)

27. The sources for the other points on this figure are:

a. × L. Bertanza et al., Nuovo Cimento 19, 467 (1961).

b. ☆ M. Chrétien, J. Leitner, N. P. Samios, M. Schwartz, and J. Steinberger, Phys. Rev. 108, 381 (1957).

c. ● S.O.B.B., Ref. 21.

d. O D. D. Allen, G. P. Fisher, G. Godden, J. B. Kopelman, L. Marshall, and R. Sears, Phys. Letters 21, 468 (1966).

e. △ Ref. 25.

f. ◇ D. E. Damouth, L. W. Jones, and M. L. Perl, Phys. Rev. Letters 11, 287 (1963). See also Technical Report #11, University of Michigan, June 1963; Ref. 18, and Martin J. Perl, Yong Yung Lee, and Erwin Marquit, Phys. Rev. 138, B 707 (1965).

g. ▽ C. T. Coffin, N. Dikmen, L. Ettlinger, D. Meyer, A. Saulys, K. Terwilliger, and D. Williams, Phys. Rev. Letters 15, 838 (1965).

h. ◊ Ref. 23.

i. ▷ D. Harting et al., Nuovo Cimento 38, 60 (1965).

j. ◁ S. Brandt et al., Phys. Rev. Letters 10, 413 (1963).

28. It is tempting to associate the background with the Regge contribution. It is evident from the signature factor $\xi(t)$ that the P is predominantly imaginary, with only a small negative real part away from $t = 0$. The real amplitude can arise only from the P' or from the tails of resonances at lower energies.

29. Gerald R. Lynch (Lawrence Radiation Laboratory, Berkeley, California), private communication, July 1966.

30. Charles G. Wohl, Frank T. Solmitz, and M. Lynn Stevenson, Phys. Rev. Letters 17, 107 (1966).

31. P. Sonderegger, J. Kirz, O. Guisan, P. Falk-Vairant, C. Bruneton, P. Borgeaud, A. V. Stirling, C. Caverzasio, J. P. Guillard, M. Yvert, and B. Amblard, Phys. Letters 20, 75 (1966).

32. H. Brody, R. Lanza, R. Marshall, J. Niederer, W. Selove, M. Schochet, and R. Van Berg, Phys. Rev. Letters 16, 828, 968 (1966).

33. Roger J. N. Phillips and William Rarita, Phys. Rev. 139, 1336 (1965).

34. Dr. Charles Chiu, who is making a detailed Regge pole analysis of πN elastic scattering and charge-exchange differential cross sections and polarizations, drew the author's attention to this point. His work indicates a large slope for $\alpha_{P'}(t)$.

35. Shigeki Suwa, Akihiko Yokosawa, Norman E. Booth, Robert J. Esterling, and Roger E. Hill, Phys. Rev. Letters 15, 560 (1965).

36. L. Holloway, Bull. Am. Phys. Soc. 11, 118 (1966); also Paul D. Grannis, Michel J. Hansroul, and Owen Chamberlain (Lawrence Radiation Laboratory), private communication.

37. L. A. Ettlinger, C. T. Coffin, F. N. Dikmen, D. I. Meyer, A. Saulys, K. M. Terwilliger, and David G. Williams, Bull. Am. Phys. Soc. 11, 416 (1966).

38. The slope obtained agrees well with that needed by Victor Flores-Maldonado, 1.4, to account for the pp and $\bar{p}p$ differential cross sections using a P, P', and ω Regge pole model. High-Energy $\bar{p}p$ and pp Differential Cross Sections and Residue Functions from Regge Poles, UCRL-16873 and to be published (Physics Letters).

39. Janos Kirz (Lawrence Radiation Laboratory), private communication, August 1966.

40. K. J. Foley et al., Phys. Rev. Letters 11, 425 (1963).

41. V. Hagopian, W. Selove, J. Alitti, J. P. Baton, and M. Neveu-René, Phys. Rev. 145, 1128 (1966).

42. Alfred S. Goldhaber, Phys. Rev. 134, B 600 (1964).

43. W. E. Humphrey, A General Minimizing Routine--MINFUN, Lawrence Radiation Laboratory Alvarez Group Programming Memo P-6, Sept. 1962.

44. D. D. Carmony, D. N. Hoa, R. L. Lander, Ng-h. Xuong, and P. Yager, One-Pion Production by π^+ in Hydrogen at 3.54 GeV/c. A Study of the Position and Width of the ρ Meson, talk given by O. Piccioni at XII Intern. Conf. on High Energy Physics (Atomizdat, Moscow, 1966).

45. The sources for the other points on this figure are:

a. O T. C. Bacon, W. J. Fickinger, D. G. Hill, H. W. K. Hopkins, D. K. Robinson, and E. O. Salant, in Proceedings of the Second Athens Topical Conference on Resonant Particles, Ohio University, Athens, Ohio, Aug. 1965.

b. ◉ Ref. 21 and Baton et al., Nuovo Cimento 35, 713 (1965).

c. ◇ Vasken Hagopian, The Reaction $\pi^- p \rightarrow \pi + \pi +$ Nucleon at 3 BeV/c (Ph. D. Thesis), Department of Physics, University of Pennsylvania, 1963; also private communication.

d. ◇ Ref. 23.

46. Loyal Durand, III, and Yam Tsi Chiu, Phys. Rev. Letters 14, 1039 (1965).

47. H. O. Cohn, W. M. Bugg, and G. T. Condo, Phys. Letters 15, 344 (1965). Normalizing the number of ρ^0's and ω seen in this experiment to the ρ^0 cross section that we have obtained at 3.22 GeV/c, i.e., ≈1 mb, we estimate that the ω production cross section is about 200 μb.

48. See, for example, Ref. 45a, where the cross section for ω production in $\pi^+ n \rightarrow p\omega$ is given as 2 mb. This is 10 times the figure in the preceding reference.

49. Bipin R. Desai and P. G. O. Freund, Phys. Rev. Letters 16, 622 (1966); also private communication, May 1966.

50. F. E. James and Henry L. Kraybill, Phys. Rev. 142, 896 (1966).

51. Cynthia Alff-Steinberger et al., Phys. Rev. 145, 1072 (1966).

52. N. Armenise et al., Nuovo Cimento 37, 361 (1965).

53. N. N. Biswas, N. M. Cason, I. Derado, V. P. Kenney, J. A. Poirier, W. D. Shepard, and E. H. Synn, Dipion Resonance Production in 8-GeV/c $\pi^- p$ Interactions, University of Notre Dame preprint, Notre Dame, Indiana, July 1966.

54. M. E. Rose, Elementary Theory of Angular Momentum (John Wiley and Sons, Inc., New York, 1957), Section 14, Equation 4.25.

55. G. F. Chew and F. E. Low, Phys. Rev. 113, 1640 (1959).

56. Duane D. Carmony, The Pion-Pion Cross Section by the Chew-Low Method (Ph. D. Thesis), UCRL-9886, Oct. 1961.

57. According to Durand and Chiu (Ref. 68) the introduction of absorption effects into the reaction causes the extrapolation procedure to fail.

58. E. Ferrari and F. Selleri, Suppl. Nuovo Cimento 24, 453 (1962). In this paper, Ferrari and Selleri show that, away from the pole, the $\pi\pi$ interaction contributes the factor $\left|\frac{a_\omega}{k}\right| (\partial\sigma[\omega_1\Delta^2]/\partial\Omega_{\pi\pi})$ since the incident (outgoing) pions have momentum $a_\omega(k)$; $\partial\sigma[\omega_1\Delta^2]/\partial\Omega_{\pi\pi}$ depends on the off-mass-shell partial-wave amplitudes $A_0^1(\Delta^2)$ in our notation, i.e., $\partial\sigma(\omega_1\Delta^2)/\partial\Omega_{\pi\pi}) = (k/a_\omega)|A_0^1(\Delta^2)|^2$. However, they leave unanswered the question of how $A_0^1(\Delta^2)$ is a function of Δ^2. This is done in Ref. 59.

59. F. Selleri, Phys. Letters 3, 76 (1962).

60. J. D. Jackson and H. Pilkuhn, Nuovo Cimento 33, 906 (1964).

61. E. Ferrari and F. Selleri, Nuovo Cimento 21, 1028 (1961); U. Amaldi and F. Selleri, Nuovo Cimento 31, 360 (1964).

62. S. B. Treiman and C. N. Yang, Phys. Rev. Letters 8, 140 (1962).

63. J. D. Jackson, Nuovo Cimento 34, 1644 (1964).

64. K. Gottfried and J. D. Jackson, Phys. Letters 8, 144 (1964).

65. K. Gottfried and J. D. Jackson, Nuovo Cimento 33, 309 (1964).

66. H. Högaasen, J. Högaasen, R. Keyser, and B. E. Y. Svensson, Nuovo Cimento 42, 323 (1966).

67. For a handy summary of the successes and failures of the absorption model, which also lists references and the various approaches taken by theorists, see J. D. Jackson's article in the 1965 Les Houches Summer School lectures. It also contains his article in Rev. Mod. Phys., Ref. 78.

68. Loyal Durand, III, and Yam Tsi Chiu, Phys. Rev. 139, B 646 (1965); Loyal Durand, III, and Yam Tsi Chiu, Phys. Rev. 137, B 1530 (1965).

69. R. Omnes, Phys. Rev. 137, B 649 (1965).

70. L. W. Jones, D. O. Caldwell, B. Zacharov, D. Harting, E. Bleuler, W. C. Middelkoop, and B. Elsner, Phys. Letters 21, 590 (1966).

71. J. P. Baton and J. Reignier, Nuovo Cimento 36, 1149 (1965).

72. Günter Wolf, DESY preprint 65/13; see also Phys. Letters 19, 328 (1965).

73. K. Gottfried and J. D. Jackson, Nuovo Cimento 34, 735 (1964).

74. G. F. Chew and S. Mandelstam, Phys. Rev. 119, 467 (1960); see also J. D. Jackson and G. L. Kane, Nuovo Cimento 23, 444 (1962).

75. In fact, the Δ^2 distribution, as calculated with C = 1.15 and A = 10 $(\mathrm{GeV})^{-2}$, has the same shape as that calculated with the Ferrari-Selleri form factor,

$$F[\Delta^2] = 0.72/\left[1 + \frac{\Delta^2 + \mu^2}{4.73\,\mu^2}\right] + 0.28/\left[1 + \left(\frac{\Delta^2 + \mu^2}{32\,\mu^2}\right)^2\right],$$

up to about Δ^2 = 15 to 20 μ^2, differing by a factor of 3/2 in magnitude and falling off faster beyond this point.

76. Laurance D. Jacobs and W. Selove, Phys. Rev. Letters 16, 669 (1966).

77. J. D. Jackson, J. T. Donohue, K. Gottfried, R. Keyser, and B. E. Y. Svensson, Phys. Rev. 139, B428 (1965).

78. J. D. Jackson, Rev. Mod. Phys. 37, 484 (1965).

79. The reports on recent work done at CEA and DESY exist mainly in preprint form. Reference is made to them, and the connection between photoproduction and vector meson scattering cross sections is shown in Marc Ross and Leo Stodolsky, Photon Dissociation Model for Photo-Vector Meson Production, Brookhaven National Laboratory Report BNL-10146, April 1966.

80. S. D. Drell and J. S. Trefil, Phys. Rev. Letters 16, 552, 832 (1966).

81. It is interesting to note that at 2.60 GeV/c, Flatté obtains $C_- = 1.2$ for the process $K^-p \to \Lambda\omega$, corresponding to a $\sigma^{tot}_{\Lambda\omega} \approx 80$ mb: Stanley Martin Flatté, The Reaction $K^-p \to \Lambda\omega$ from 1.2 to 2.7 BeV/c: The Absorption Model with Strange Meson Exchange (Ph. D. Thesis), UCRL-16648, March 1966.

This report was prepared as an account of Government sponsored work. Neither the United States, nor the Commission, nor any person acting on behalf of the Commission:

A. Makes any warranty or representation, expressed or implied, with respect to the accuracy, completeness, or usefulness of the information contained in this report, or that the use of any information, apparatus, method, or process disclosed in this report may not infringe privately owned rights; or

B. Assumes any liabilities with respect to the use of, or for damages resulting from the use of any information, apparatus, method, or process disclosed in this report.

As used in the above, "person acting on behalf of the Commission" includes any employee or contractor of the Commission, or employee of such contractor, to the extent that such employee or contractor of the Commission, or employee of such contractor prepares, disseminates, or provides access to, any information pursuant to his employment or contract with the Commission, or his employment with such contractor.